Free-Carrier Pump/Probe Spectroscopy

NOVEL FREE-CARRIER PUMP/PROBE TECHNIQUES FOR THE CHARACTERIZATION OF SILICON

BY KEVIN M.W. BOYD, B.ENG

A Thesis Submitted to the School of Graduate Studies in Partial Fulfilment of the Requirements for the Degree Doctor of Philosophy

McMaster University DOCTOR OF PHILOSOPHY (2018)

Hamilton, Ontario (Engineering Physics)

TITLE: Novel Free-Carrier Pump/Probe Techniques for the Characterization of Silicon

AUTHOR: Kevin M.W. Boyd, B.Eng (McMaster University)

SUPERVISOR: Professor Rafael N. Kleiman

NUMBER OF PAGES: xxii, 242

Abstract

Two novel pump/probe techniques have been developed for measuring the recombination lifetime in crystalline silicon wafers. The first technique, single-beam pump/probe, uses one laser as both pump and probe. The second technique, quasi-steady state free-carrier absorption, measures lifetime under quasi-steady state conditions. These techniques are supported by a general mathematical model that predicts the experimental signal accounting for the 3D charge-carrier transport and recombination within the semiconductor. The predictions of the model are validated experimentally, and quantitative agreement is found between the model and experimental results for both techniques. The recombination lifetime measured by these techniques is verified independently using a standard pump/probe method, and the results are in agreement with this work. Single-beam pump/probe is a first-time demonstration of a technique capable of measuring lifetime in silicon using a single laser beam. It dramatically simplifies traditional pump/probe measurements by completely eliminating the second laser beam. QSS-FCA is the first quasi-steady state technique that can be calibrated *in situ* without the requirement of a calibrated reference wafer. The calibration constant is the free-carrier absorption cross section of silicon, which is a material constant. QSS-FCA is able to measure this cross section to a higher precision than what has been reported in the literature. Precise measurement of this constant opens up the possibility of studying more fundamental physics of silicon using QSS-FCA.

Acknowledgements

A Ph.D is a long and trying experience, and is not something that can be done alone. I would like to thank my supervisor Rafael Kleiman, who has provided invaluable guidance along my six year journey through graduate school. His open mindedness and the autonomy he gave me to pursue all of my crazy ideas meshed perfectly with my often scatterbrained work ethic. Never once did he tell me an idea was too outlandish, or dismiss an idea outright without sound physical reasoning. I would not have flourished as I have under the supervision of any another professor. I would also like to thank to thank the other members of my supervisory committee, Professor Adrian Kitai, and Professor Daniel Cassidy. I chose them to be on my committee based on my experiences as an undergraduate student. I have had both Dr. Kitai and Dr. Cassidy instructors for multiple courses, and I always learned a great deal from them.

I would like to thank my family; my father Mike, my mother Kelly, my brother Nick, my sister Sam, my Granny and Grandma, and our many cats and dogs. I could not have done this without their love and support. Spending time at home with everyone was a much needed reprieve from the frustrations of laboratory research. I appreciate all of their support over these years, and for believing in me. They don't understand any of the science behind what I do, but they assume I do it well and that is good enough for me.

I would like to thank Shahram Tavakoli and Doris Stevanovic for all their hard work and guidance over the years on the experimental side of my research work. Experimental work in the CEDT laboratories would be impossible with their dedicated stewardship. Shahram's savant-like understanding of everything mechanical, and Doris' extensive experience and knowledge make for a formidable team. Any time I needed help setting up an experiment, or learning how to use a piece of equipment, Shahram and Doris were always available for help. I and all of the other graduate students owe them a great deal of gratitude for their efforts. I'd also like to thank Zhilin Peng and Jacek Wojcik for their help along the way as well.

I want to thank George Chiran for all of the work he has done for the optical characterization lab, and for the help he has provided me. His meticulousness can sometimes be frustrating, but it is

Contents

List of Figures

List of Tables

List of Abbreviations and Symbols

FCA   Free-Carrier Absorption

MFCA   Modulated Free Carrier Absorption

QSSPC   Quasi-steady state photoconductance

QSS-FCA   Quasi-steady state free-carrier absorption

SRV   Surface Recombination Velocity

QSS   Quasi-steady state

NIR   Near-infrared

UV   Ultraviolet

PU   Pump

PR   Probe

τ Effective Recombination Lifetime

τ_n Series effective lifetime

τ_n' Frequency-dependent series effective lifetime factor

τ_D Diffusion Time Constant

τ_b Bulk Recombination Lifetime

τ_{qss} Steady-state lifetime

τ_{3D} 3D effective lifetime

τ_r Radial diffusion lifetime

τ_{rad} Radiative recombination lifetime

τ_{SRH} Shockley-Read-Hall Lifetime

τ_{Aug} Auger recombination lifetime

τ_s Surface recombination lifetime

S Surface recombination velocity

D Diffusion coefficient

w Laser beam $1/e^2$ radius

$\mathfrak{T}$ Generalized Lifetime

A_n^{lc} Luke and Cheng coefficient (n is a summation index in this context)

A_n^{ax} Coefficient for even term in axial component of 3D solution (n is a summation index)

B_n^{ax} Coefficient for odd term in axial component of 3D solution (n is a summation index)

n Excess electron (or free-carrier) density

p Excess hole density

$\mathcal{D}$ Diffusive factor

r Radial cylindrical coordinate

z Axial cylindrical coordinate

$\mathfrak{R}$ Multiple-reflections correction factor

R Fresnel reflectance coefficient

T Fresnel transmittance coefficient

q	Elemental charge
λ	Wavelength
W	Wafer thickness
μ_n	Electron mobility
μ_p	Hole mobility
n	Refractive index
ε_0	Permittivity of free space
c	Speed of light
σ_{FCA}	Free-carrier absorption cross section
α	Band-to-band absorption coefficient
α_{FCA}	Free-carrier absorption coefficient
α_n	Luke and Cheng transcendental factor (n is a summation index)
β_n	Luke and Cheng transcendental factor (n is a summation index)
β_{bb}	Band-to-band absorption factor
β_{FCA}	Free-carrier absorption factor
g_0	Reflection-corrected photon flux density
ξ	3D Frequency-dependent factor
$\Gamma(0, x)$	Upper incomplete gamma function
P_0	Incident power

n_ω Time-dependent free-carrier density for harmonically varying optical excitation

$\mathcal{S}$ Single beam or dual-beam signal

$\mathcal{S}_\omega$ Raw single beam pump/probe signal with sample in place

$\mathcal{S}_b$ Raw single beam pump/probe signal with sample removed

Declaration of Academic Achievement

All of the mathematical models and derivations in this thesis are my own, unless stated otherwise. These models were developed with the guidance and support of Dr. Rafael Kleiman. I designed and built the experimental apparatus that was used in this work, and automated the collection of data using a computer program written in the Python programming language.

Dedication

This thesis is dedicated to my family, who are as loving as they are dysfunctional. To Jessica, who understands me better than I understand myself. To Sophie, our beloved black Labrador retriever who left us before her time; I'll never know a kinder, gentler soul than yours.

"…but all the compliments I received from MM.Arago, Laplace, and Biot never gave me as much pleasure as the discovery of a theoretical truth and the confirmation of my calculations by experiment."

— Augustin-Jean Fresnel

1 Introduction

In this dissertation I develop two novel experimental techniques for measuring the recombination lifetime in crystalline silicon wafers using free-carrier pump/probe spectroscopy. The recombination lifetime of a semiconductor provides valuable information about its electronic properties [1]. In silicon, where recombination is typically dominated by an impurity-assisted process, lifetime measurements can be used to assay the semiconductor. This information is extremely important to the field of photovoltaics, where high material purity and long recombination lifetimes are necessary for achieving high conversion efficiency between sunlight and electric current [2]. In a generic pump/probe lifetime measurement in silicon, free[1] electron/hole pairs (*free-carriers)* are pumped by a laser source with energy greater than the semiconductor's bandgap. The free-carrier density is probed by measuring the free-carrier induced absorption of a second laser beam. When the pump is modulated harmonically and the modulation frequency is varied, the probe signal traces out a Lorentzian response function which can be fitted to extract the recombination lifetime. This is the principle behind Modulated Free-Carrier Absorption (MFCA), which is a standard pump/probe lifetime measurement technique in silicon. The techniques that I develop in this dissertation improve upon MFCA. The first technique, single-beam pump/probe, uses the same laser beam for both pump and probe, eliminating the second laser beam from the MFCA apparatus. The second technique, quasi-steady state free-carrier absorption (QSS-FCA), measures the lifetime using a single datapoint collected at low-frequency, eliminating the requirement of sweeping the modulation frequency and alleviating the bandwidth requirements of the instrument.

---

[1] An electron or hole is "free" when it is not bound to a single atom and can move freely about the semiconductor lattice. Electrons in the conduction band and holes in the valence band are free. The term *free-carriers* is used to refer these carriers throughout this work.

The single-beam pump/probe technique I have developed is a dramatic simplification of the dual-beam configuration that is used in traditional laser-based pump/probe measurements. The main challenge in the implementation of any pump/probe study is the alignment of the pump and probe beams on the sample under study. High-precision alignment is necessary when the beam diameters are small, which is the case for pump/probe measurements on silicon[2] [3]. Alignment challenges can be surmounted on a laboratory bench where the experimenter has direct access to the sample stage and visual feedback on the positions of the pump and probe beams. However, for pump/probe systems designed to monitor semiconductor processing *in situ*, the alignment of the pump and probe beams could be considerably more complicated. Consider for example a pump/probe study designed to monitor a semiconductor undergoing chemical vapor deposition (CVD) of a dielectric film *in situ*. Both pump and probe beams have to be coupled through a window on the CVD reaction chamber and aligned to precisely the same spot on the sample, and then the probe has to be coupled out of the system and into a detector. If the beams are propagated over a long distance, high-stability optics are required to maintain alignment precision. Temperature changes and gases inside the CVD apparatus can potentially cause misalignment via refraction of the pump and probe beams. Reducing a pump/probe experiment to a single beam provides an extraordinary amount of flexibility in the implementation of the pump/probe measurement since simultaneous alignment of the pump and probe beams is automatic. The combined pump/probe beam simply has to strike the sample under study, and be collected by a detector. Even in the simplest cases, it will always be easier to align a single beam on a sample than two simultaneously.

QSS-FCA is a dual-beam pump/probe technique that directly simplifies MFCA by reducing the MFCA measurement to a single datapoint collected at low frequency. Traditional MFCA measures the lifetime via the *frequency dependence* of the MFCA signal, as will be discussed in Chapters 2 & 3. Alternatively, since the amplitude of the free-carrier population is directly proportional to the

---

[2] In the case of semiconductor pump/probe measurements, the beam diameters are on the order of millimeters or less

lifetime at low-frequency, the lifetime may be deduced from the *amplitude* of the MFCA signal collected at low-frequency. This reduces the MFCA technique to a single datapoint measurement. Measurement of the free-carrier amplitude is the basis for steady-state and quasi-steady state[3] (QSS) lifetime measurement techniques, which will be reviewed in Chapter 2. The advantage of QSS lifetime techniques is that they operate at low frequency so the bandwidth requirements of the experimental apparatus are modest. The disadvantage is that they require calibration in order to map the amplitude signal that is measured experimentally to the lifetime. The typical approach to calibration is to use a reference wafer of known doping type and density to create a mapping between free-carrier density and the signal measured from the apparatus. The free-carrier density is proportional to the recombination lifetime, so if the apparatus can measure the free-carrier density it can measure lifetime. As will be discussed later in this work, there are several issues associated with the use of a reference sample for calibration, and the accuracy of the free-carrier density measurement after calibration is not guaranteed. I demonstrate a superior calibration method whereby the amplitude of the signal is measured simultaneously with the lifetime measured via MFCA. This creates a direct mapping between the signal amplitude and lifetime of the semiconductor, instead of an indirect mapping to carrier density. It turns out the unknown factor that is deduced is the free-carrier absorption cross section σ_{FCA} of the semiconductor, which is a material constant. Since the calibration factor is a material constant, it is independent of the experimental geometry. This is in contrast to the most prominent QSS technique, quasi-steady state photoconductance (QSSPC), where the calibration factor includes geometrical factors that are not readily modelled. The consequence of this is that semiconductor wafers under test must be located in precisely the same position as the reference wafer was during calibration; this restriction does not apply to QSS-FCA. In addition to simplifying the measurement of lifetime in silicon, the QSS-FCA technique provides a direct means of quantifying σ_{FCA} to a high precision. As will be

---

[3] "Quasi-steady state" refers to the case where the pump power is not constant in time but is modulated slowly enough that the free-carrier population is always in equilibrium with it.

discussed in Chapter 7, the literature values for σ_{FCA} have a considerable amount of spread and have high measurement uncertainty ($\sim 50\%$). In accordance with this high uncertainty there is also considerable disagreement regarding the underlying physical models that govern σ_{FCA}. With my QSS-FCA technique, σ_{FCA} can be measured to a high degree of precision. Thus QSS-FCA provides a tool for probing more fundamental physics in silicon via σ_{FCA}. Ideas for studies are proposed later on in this work.

In order to theoretically describe the pump/probe techniques that I have developed, a model is required which captures all of the physics relevant to a lifetime measurement experiment. Since the probe signal is proportional to the free-carrier density, any effects that change this density are required to understand the results of a pump/probe experiment. The free-carrier density is described by the 3D continuity equation, which is a differential equation that accounts for the diffusion, generation and recombination of charge-carriers inside of a differential volume of a semiconductor slab. In this work I provide a general solution to the 3D continuity equation, which yields an equation that describes the free-carrier density as a function of 3D position and time in the semiconductor. This equation is analytic and algebraically succinct. It is almost completely closed form, except for a transcendental root that must be evaluated under certain conditions. From this equation, I develop a general model that predicts the probe signal from a pump/probe experiment of largely arbitrary configuration. The pump and probe powers, modulation frequencies, beam radii, and wavelength are all model parameters that can be specified by substituting the relevant quantities into the equation. The semiconductor under study can have an arbitrary thickness, surface reflection, bulk recombination lifetime, surface recombination velocity, and diffusion coefficient. Due to the model's generality, the probe signal from a vast variety of experiments can be predicted. The primary assumption for the model is that the pump and probe beams have Gaussian intensity profiles and are overlapped at their centres on the sample. This essentially covers almost all pump/probe experiments that use laser beams.

The content of this dissertation is outlined as follows. In Chapter 2 I review the literature behind lifetime measurements in silicon. Radio-frequency (RF), microwave, and free-carrier pump/probe

based lifetime measurements are examined, with free-carrier pump/probe techniques covered in depth. As well, I examine the small body of the literature around single-beam pump/probe techniques. In Chapter 3 I discuss the background theory that is relevant to this work. The various mechanisms that contribute to the overall recombination in a semiconductor are discussed, with emphasis given to the mechanisms relevant to silicon. The exact 1D solution to the continuity equation governing charge carrier transport and recombination in a semiconductor is examined in both the time and frequency domain. The generic signal that is acquired in a lifetime measurement is examined from a theoretical point of view, and related to this solution. In Chapter 4 I describe the experimental apparatus that is used in this work, which is divided into a pump, probe and detection branch. The components that comprise each branch and the methodology used to acquire data are discussed. I also tabulate the properties of the silicon wafers that have been studied in this work. In Chapter 5 I derive the generalized pump/probe equation, and examine several special cases based on common pump/probe configurations. In Chapters 6 and 7 I develop the single-beam pump/probe and QSS-FCA techniques. For both techniques I derive a model describing the signal measured, and then provide experimental validation of the model. It is shown that the lifetime measured by these techniques is consistent with the standard MFCA technique. In Chapter 8 I provide concluding remarks summarizing the accomplishments in this dissertation and my contribution to knowledge, as well as provide ideas for future work.

2 Literature Review

2.1 Overview of Lifetime Measurement in Silicon

Recombination in a semiconductor involves an electron in the conduction band getting captured by a hole in the valence band. In thermal equilibrium the rate of recombination of these free-carriers is balanced by their rate of thermal generation, and there is no net exchange of electrons in the conduction band and holes in the valence band. When the population of the free-carriers is increased, for example by absorption of light with energy greater than the bandgap, the rate of recombination is increased above the rate of thermal generation and there is a net decay of the free-carrier population over time. The average time it takes for an electron-hole population to decay is known as the *recombination lifetime*. In indirect bandgap semiconductors such as silicon, the lifetime is related to the purity of the material with higher purity material characterized by longer lifetimes. This information is invaluable to the photovoltaics community. The photovoltaics industry has grown at a remarkable rate over the last decade, often outpacing expert predictions. This growth was made possible, in part, by a dedicated supply line of solar-grade silicon feedstock. Solar-grade silicon is a cheaper alternative to the material used by the integrated circuits community, though the cost reduction comes at the expense of greater chemical contamination and degraded lifetime. Lifetime measurements are then critical for assessing the quality of incoming feedstock prior to photovoltaic device fabrication, or to improve the process used to create solar-grade silicon.

Lifetime measurements in silicon are ideally performed in a non-contact geometry (*i.e.* the wafer is not directly contacted with metal leads or a probe). This prevents contamination when performing the measurement, which is especially crucial if the wafer is to be subjected to high processing temperatures afterwards. As discussed in Chapter 1, lifetime measurements involve the excitation of excess free-carriers and the monitoring of their decay back to thermal equilibrium values. The excitation of free-carriers is performed by optical injection, where an optical source with energy above the bandgap of the semiconductor ($\lambda < 1100$ nm in silicon) is absorbed to

promote electrons and holes across the bandgap into conduction states. The free-carrier population is then measured using either photoconductivity, optical-free carrier absorption, or photoluminescence [4]. Lifetime is extracted from either the steady-state or quasi-steady state population of free-carriers [5], [6], or from their decay in either the time [3], [7] or frequency [8], [9] domains. The decay of the free-carriers back to equilibrium usually follows a decaying exponential in the time domain (or equivalently a Lorentzian in the frequency domain), and the lifetime is extracted by fitting this decay curve to a simple exponential or Lorentzian parameterized by a time constant that is equal to the recombination lifetime. The main advantage of decay techniques is that they rely only on the relative-and not absolute-amplitude of the free-carrier population. The main disadvantage is that the measurement apparatus requires bandwidth comparable to the inverse of the lifetime. For silicon, where practical lifetimes may be on the order of microseconds, the measurement apparatus requires bandwidth in the hundreds of kHz range. Conversely, QSS measurements are inherently low frequency and have very modest bandwidth requirements. However, these measurements rely on the absolute amplitude of the free-carrier population, so they are subject to calibration error. QSS measurements are typically calibrated using reference samples with known properties, so their accuracy is limited to the accuracy and validity of the calibration. In time-domain studies, the pump-side bandwidth requirements are met by using a pulsed-laser for the free-carrier excitation. For example, Kunst [10] and Linross [3] use a pulsed Nd:YAG laser with pulse-widths of 15, and 300 ns, respectively. This excitation can be considered instantaneous with respect to the recombination lifetime in silicon. In frequency-domain studies, the excitation source is modulated harmonically from low-to-high frequencies in order to map out the frequency-response of the semiconductor under test. To achieve high excitation bandwidths, fast laser diodes [9] or electro-optic modulators are used [8]. For both time and frequency-domain studies, high detection bandwidth is achieved by using fast diodes and high bandwidth oscilloscopes and lock-in amplifiers.

7
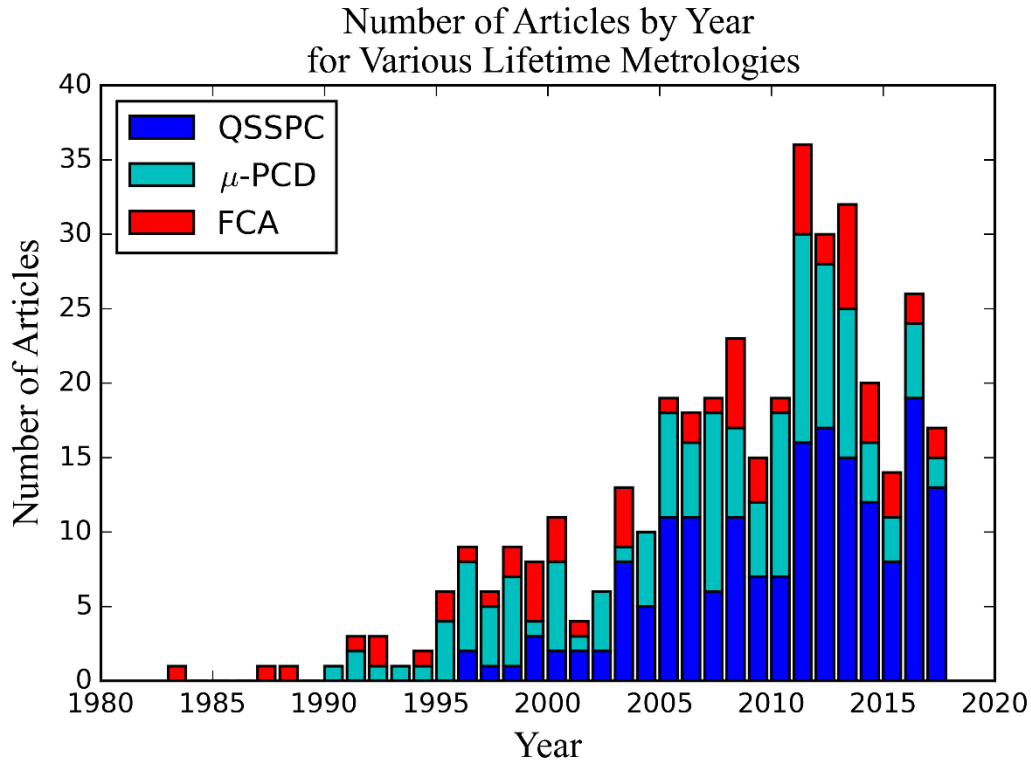
Figure 2.1: Number of Articles per Year for Various Lifetime Metrologies. Three common techniques for lifetime measurements are considered in this plot: QSSPC, u-PCD, and FCA. Data is obtained from Web of Science analytics.

The three most important techniques for lifetime measurement in silicon are quasi-steady state photoconductance (QSSPC), microwave photoconductance decay (μ-PCD) and pump/probe infrared free-carrier absorption [4]. The main difference between the techniques is the physical quantity used to sense the free-carrier density of an optically excited silicon wafer. The former two methods use RF and microwave-frequency measurements of photoconductivity, while the latter uses the FCA of an infrared probe beam. Figure 2.1 shows a plot of the total number of articles published by year related to the three lifetime metrologies. Papers developing the theory and implementation of the techniques, as well as papers applying the techniques to scientific studies are included. It can be seen that QSSPC and μ-PCD dominate the lifetime literature, compared to FCA. In the following section I review all three lifetime metrologies. Since the focus of this

dissertation is on pump/probe FCA, I review the corresponding literature in detail. QSSPC and μ-PCD are discussed briefly, with several references provided to the interested reader.

2.2 Silicon Lifetime Measurements based on RF/Microwave Photoconductivity

Under optical excitation the free-carrier density of a silicon wafer increases, which corresponds to an increase in the conductivity (lowering of electrical resistance) of the wafer. This *photoconductivity* may be sensed using RF/microwave-based measurements. Photoconductivity-based measurements have been the mainstay of silicon lifetime characterization for decades. In fact, commercial instruments for measuring lifetime in silicon in a non-contact mode are exclusively based on photoconductivity measurements[4]. One of the earliest photoconductivity-based techniques is *time-resolved microwave conductivity*, or as it is known today, *microwave photoconductance decay* (μ-PCD) [10]. In this technique, the semiconductor is placed inside of a microwave cavity. Microwaves are passed through a circulator and are brought incident upon the semiconductor. A pulsed laser with pulse-width much less than the lifetime of the wafer excites electron-holes pairs in the sample, increasing its photoconductivity. The increase in photoconductivity causes the wafer to become more metallic, and thus more reflective to microwaves. Reflected microwaves pass through a circulator and are detected. The decay of the excited electron-hole pairs back to equilibrium is monitored over time via the change in reflectance as the photoconductivity of the wafer decays back to equilibrium values. The decay constant, equal to the recombination lifetime, is extracted on an oscilloscope.

The first measurements of lifetime using microwaves were reported at least as far back as 1959 [11], though it wasn't until later on that the method became more widely used. Kunst and Beck

---

[4] Sinton Instruments (formerly Sinton Consulting) provides a series of lifetime measurement tools based upon QSSPC. SEMIlab provides a system that implements the μ-PCD technique. Freiberg Instruments provides tools that implements microwave-detected photoconductivity, which is related to μ-PCD. Each of these companies have tools for benchtop laboratory measurements as well as in-line characterization, all targeting photovoltaic applications. To my knowledge there are no commercial instruments for lifetime measurement based upon free-carrier pump/probe.

provided one of the first quantitative analyses of the measurement of charge carrier kinetics [10] using microwave conductivity measurements. In their work they derive a relationship between the change in conductivity due to optical excitation, and the change in reflectivity of microwave power. In general, the microwave reflectivity is a highly non-linear function of conductivity. In order to be useful as a relative measurement, the change in microwave reflectivity for a given change in conductivity should be linearly proportional to each other. This limits μ-PCD measurements to the small signal domain where the conductivity change is small enough that a first-order approximation to the change in reflectivity is valid. This is a significant complication when using μ-PCD as a tool for lifetime defect spectroscopy. Lifetime is a function of the injected free-carrier density, and lifetime spectroscopy for defect analysis requires measuring lifetime over a wide range of carrier injection levels [1]. Since μ-PCD is non-linear for large perturbations of the conductivity (*i.e.* large changes in carrier concentration), it cannot be used to directly measure lifetime at high carrier concentrations. To circumvent this, μ-PCD apparatuses use a bias lamp to set a steady-state carrier concentration above the equilibrium level, and then a small perturbation is made on top of this steady-state concentration using a pulsed laser. This maintains linearity between the reflected microwave power and the conductivity, allowing the lifetime to be extracted for large carrier concentrations.

Another prominent lifetime measurement tool based on the principle of photoconductivity is *Quasi-Steady State Photoconductance* (QSSPC) [5]. As the name suggests, this approach is a quasi-steady state technique and it extracts lifetime by measuring the absolute amplitude of photoconductivity in quasi-steady state, which is directly related to the free-carrier density via the carrier mobility. Though the relationship between photoconductivity and carrier density is non-linear, it is well known and independent of the measurement apparatus. QSSPC measures the conductivity of the wafer using an RF inductance bridge [1]. A metal coil is placed in close proximity to the wafer under test and an RF current is fed through the coil. The alternating magnetic field of the coil induces eddy currents in the wafer. The loss of energy due to the induction of eddy currents is proportional to the wafer's conductivity. The excitation source in QSSPC is a flash lamp with a slowly decaying optical power, the decay being slow enough that

the wafer's excess free-carrier population is always in equilibrium with the excitation (hence the reason the technique is referred to as *quasi*-steady state). The photoconductivity is monitored as the lamp power decays, and with knowledge of the excitation rate the lifetime may be extracted.

This dissertation is primarily focused on free-carrier absorption-based lifetime measurements. I have discussed the principles behind the µ-PCD and QSSPC techniques for the sake of completeness, and to give context to the lifetime metrologies that I have developed in this work. For further reading on µ-PCD and its applications, the curious reader may consult Refs [14]–[21]. For QSSPC, [1], [22]–[28].

2.3   Review of Free-Carrier Absorption Characterization Work in Silicon

In this section I review FCA-based lifetime measurement techniques, covering time-domain, frequency-domain, and steady/quasi-steady state methodologies. As is the case with microwave-based lifetime measurement techniques, the earliest work dates back to the 1950s but it wasn't until the 1990s where these techniques started gaining popularity. The growth in popularity coincides with the increasing feasibility of silicon photovoltaics as the cost of silicon decreased [29]. The technique itself has not evolved much since the early days of its implementation, though the technology used in its implementation has improved. Therefore most of this review focuses on the applications of the technique to silicon lifetime measurement, and the useful quantities that can be extracted.

Before reviewing the literature, it is instructive to discuss the generic experimental geometry used in pump/probe FCA measurements, and what is actually measured. Free-carriers are generated by an optical source, and measured by monitoring the transmission of an infrared light source through a chunk of semiconductor material. The pump and probe sources are typically configured so that the probe examines an area of uniform pump intensity, and thus uniform carrier density. This is achieved by making the pump beam radius much larger than the probe radius. Free-carriers absorb the infrared light source in proportion to their density, which provides a direct probe of the free-

carrier population. This population changes due to generation and recombination of free-carriers, and from that the recombination the lifetime of the semiconductor can be measured.

Frequency-domain FCA is typically referred to as *modulated free-carrier absorption* (MFCA), and involves exciting the sample with a modulated optical source and demodulating the resultant probe signal and extracting the lifetime from signal's frequency-dependence. One of the earliest FCA work was a frequency-domain approach that was the precursor to the modern MFCA technique [30], [31]. Huldt [30] examined the lifetime of near-intrinsic germanium. A tungsten strip lamp was used as the pump, and the probe beam was derived from a monochromator set to emit light at a wavenumber of $900 \ \text{cm}^{-1}$. The pump was mechanically chopped, and the probe signal was measured on a pneumatic (Golay cell) detector. Huldt showed that by sweeping modulation frequency the transmitted power of the probe beam changes, and this change could be used to predict the lifetime. He measured a lifetime of 165 μs with this technique. Nilsson [31] demonstrated an improved version of Huldt's technique, where now the probe beam is also modulated to improve sensitivity. The detector used in this work was a thermocouple vacuum detector. He measured lifetimes in germanium ranging from twenty to several hundred microseconds. Nilsson also provided a general mathematical solution to the 1D continuity equation for a square-wave excitation, which is a complete description of the free-carrier recombination in the semiconductor. The minimum lifetime that could be measured by these techniques was limited by the excitation bandwidth of the setup, which is set by the speed of the mechanical chopper.

Perhaps the first modern version of the MFCA technique emerged with Sanii et. al [8], [32]. In their work the pump source is a He-Ne laser emitting at 632 nm, and the probe is a second He-Ne laser emitting at 3.39 μm. The pump is modulated using an electro-optic modulator and the probe is detected with an InAs photodiode. The use of laser sources for pump and probe, as well as semiconductor-based detectors exemplifies Sanii's work as the modern version of MFCA. In their work, Sanii et al. provide a solution to the 1D continuity equation similar to that of Nilsson [31], except Sanii's solution is for a harmonically varying pump instead of a square-wave pump. The solution for a harmonic excitation is more versatile since harmonic functions form a temporal basis

set from which all other solutions can be synthesized (i.e. the solution for an arbitrary temporal generation rate may be synthesized by a superposition of harmonic functions via a Fourier transform). The solution as presented by Sanii (and used by other authors [9], [33], [34]) is far more algebraically complicated than that of Nilsson. I demonstrate in this dissertation that the solution can be condensed significantly with the appropriate substitutions and algebraic manipulations, the final result resembling Nilsson's solution.

Sanii's solution is a general mathematical model for 1 dimensional transport and recombination in a semiconductor wafer. In principle, by fitting the MFCA signal as a function of modulation frequency to this model it is possible to extract the bulk recombination lifetime, surface recombination velocity and diffusion coefficient[5]. However, as I discuss in Chapter 3, the shape of the frequency-response curve stays roughly the same regardless of the transport and recombination properties of the wafer so it is not possible to fit the curve to determine these parameters uniquely. Zhang and Li showed how the diffusion coefficient can be extracted by varying the separation of the pump and probe beams [35]. They showed both theoretically and experimentally that when the pump and probe are sufficiently separated, the phase of the probe signal with respect to the excitation signal grows linearly with separation distance, the slope being proportional to the inverse square root of the diffusion coefficient.

Glunz et al. [9] used MFCA to measure the surface recombination velocity as a function of injected-carrier density for oxidized silicon surfaces. The surface recombination velocity is an important metric for determining the efficiency of solar cells since fast velocities lead to reduced photocurrent [36]. Since the lifetime extracted by MFCA is an effective lifetime that combines the

---

[5] The bulk lifetime is associated with recombination in the bulk of the semiconductor, whereas the surface recombination velocity is the rate at which carriers recombine at the surface. The diffusion coefficient describes the transport of the free-carriers via diffusion. These parameters will be discussed in more detail in Chapter 3. For now, it is sufficient to say that the net lifetime that is measured is a complicated function of these parameters and under particular circumstances the individual parameters can be extracted.

effects of recombination in the bulk and at the surface of the semiconductor, the bulk lifetime must be known *a priori* in order to deduce the surface recombination velocity from a single MFCA measurement. The bulk lifetime is measured in Glunz' work by submerging un-oxidized reference wafers into hydrofluoric acid and measuring the lifetime *in situ* with μ-PCD. HF reduces the surface recombination velocity to negligible levels, allowing the bulk lifetime to be measured directly [37]. In a later work, Glunz et al. used the same MFCA setup to perform high-resolution lifetime mapping on multicrystalline silicon wafers [38] with a spatial resolution of 200 μm. Multicrystalline silicon is used in commercial photovoltaic devices since it is low cost [39], however the poly-crystalline nature of the material leads to shorter recombination lifetimes and large spatial variations in the lifetime due to recombination on grain boundaries [40]. High resolution lifetime mapping is a powerful diagnostic tool for multicrystalline silicon since it can be used as feedback for optimizing the multicrystalline growth process. However, it should be noted that lifetime mapping with MFCA is slow since the frequency response of the free-carrier population must be acquired at each point on the wafer. In a later work, the authors comment that their MFCA apparatus took several hours to map a single wafer [6].

Zhang and Gao examined the effect that photoreflectance has on the MFCA signal [41]. MFCA studies collect the probe beam that transmits through the wafer under study, and it is assumed that the transmission is only affected by FCA. However, due to the Kramers-Kronig relationship a change in the absorption coefficient of a material also leads to a change in its refractive index. This change in refractive index modulates the reflection coefficient (photoreflectance), which then imposes an additional modulation on the transmission coefficient. Zhang and Gao simultaneously measure the transmitted and reflected beams, and correct the transmitted signal so that it contains only FCA effects. They measure a lifetime for both corrected and uncorrected transmitted signals, and show that they are different by about a factor of 2. This work is deficient since the magnitude of the perturbation due to photoreflectance effect should be a function of power, yet the authors do not report a value for the laser power. As far as I am aware, no other studies of MFCA have

concluded that photoreflectance has a significant effect on lifetime measurements and no other papers have cited this article, including later work by the same authors.

Ren et al. extended the 1D diffusion model that considers only diffusion and recombination along the axis of the wafer to three dimensions [42]. Their 3D model is an analytic solution to the continuity equation in three dimensions, accounting for diffusion along the axis of the wafer and parallel to the wafer surface. They use their model to fit experimentally measured data and extract the bulk lifetime, surface recombination velocity, and diffusion coefficient simultaneously. The model presented by Ren et al. is very algebraically complicated and written in terms of integrals that don't yield a closed-form solution. In this thesis I derive a superior 3D model that is general but also much more compact and usable than Ren's model.

MFCA has been used to study the interface quality of material systems outside of elemental silicon. For example, Suvanam et al. used MFCA to measure the surface recombination velocity of 4H-silicon carbide substrates with a dielectric film [43]. Measurement of the surface recombination velocity provides an indirect means of extracting the density of trap states at the interface between substrate and film [44]. Suvanam et al. show that the FCA measurements correlate with capacitance-voltage measurements of the surface trap density, indicating that MFCA can be used to directly measure the surface properties in a non-contact geometry.

A more exotic example of FCA characterization which is decidedly different from other techniques is an ultrafast pump/probe experiment that measures the FCA cross section, internal quantum efficiency, and diffusion coefficient of silicon, demonstrated by Meitzner et.al. [45]. In this work the evolution of a free-carrier population excited very close to the silicon surface ($\sim$35 nm) is monitored over a time-scale on the order of picoseconds. Since this timescale is many orders of magnitude shorter than the recombination lifetime of silicon, recombination has no effect on the measurement. The time-evolution of the carrier population as it diffuses away from the surface is measured via the fact that the FCA cross-section increases with increasing carrier density [46]. At short time-scales ($\sim$ 1 ps) the surface concentration is high and the FCA of the probe is high. At

longer times (> 100 ps) the FCA linearizes and the signal becomes constant in time. The time-evolution of the signal at short times can be used to extract the diffusivity, while the post-transient signal can be used to determine the number of injected carriers which is used to quantify the FCA cross section of the probe beam, and measure the internal quantum efficiency of silicon. Since this measurement occurs on ultrafast timescales, no information is obtained about the recombination lifetime of silicon.

One of the first time-domain FCA lifetime studies was performed by Schwartz et al. [47]. They used a Xenon flash lamp as the excitation source, but the resolvable lifetime was limited by the temporal bandwidth of the Xenon lamp. In the microsecond lifetime range a fitting procedure was required in order to extract the lifetime. One of the first studies to overcome the bandwidth limitation was performed by Warabisako et al. [48] using a Q-switched Nd:YAG laser with pulse-widths < 110 ns, operating at the fundamental wavelength of 1064 nm. Compared to the time scale of recombination in silicon the pulses of this laser provide near-instantaneous excitation of free-carriers. Using a CO_2 laser (10.6 µm wavelength) as the probe, the authors were able to demonstrate the time-resolved measurement of lifetimes in silicon shorter than 800 ns.

Johnson and Johnson used a similar experimental setup as Warabisako to study the spatial dependence of lifetimes in cast multicrystalline silicon ingots [49]. As mentioned above, the spatial dependence of lifetime is useful for process optimization when fabricating multicrystalline silicon wafers. Johnson and Johnson used a CW Nd:YAG laser operating at 1.319 µm as their probe beam, and a tunable infrared dye laser as the pump beam. The typical lifetimes they measured were in the 2-10 µs range.

Waldmeyer performed a similar study to Warabisako but with the support of a mathematical model derived from solving the 1D continuity equation [50]. Waldmeyer's model showed the conditions under which the bulk lifetime, surface recombination coefficient, and diffusion coefficient could be separated. Waldmeyer's model shows that when the wafer is sufficiently thick the bulk lifetime is measured regardless of the value of the surface recombination velocity or diffusion coefficient.

When the wafer is thin and has high surface recombination velocity, then the diffusion coefficient may be directly measured. While Waldmeyer's mathematical model is general and relevant beyond FCA-based lifetime work, it is not examined in depth in his work. In the year prior to Waldmeyer's work, Luke and Cheng published a comprehensive study on a general solution to the 1D continuity equation for free-carriers in silicon [51]. This seminal work is a highly detailed examination of the 1D continuity equation and its consequences for lifetime measurements in semiconductors. It is highly regarded and has been cited at least 273 times. Though this work focuses on silicon, it can be applied to understand the carrier dynamics in any semiconductor. The results of Luke and Cheng are cited heavily in this work, and the Luke and Cheng solution is the basis for the generalization of the 1D continuity equation into 3 dimensions that I present in later chapters.

In 1998 Linnros published two comprehensive review articles on time-domain FCA lifetime measurements [3], [7]. These articles describe in detail the standard time-domain FCA lifetime experiment, and how it may be used to characterize the transport and recombination properties of silicon. In the first article, Linnros demonstrates the measurement of the injection-level dependent lifetime using a high-power pulsed Nd:YAG laser emitting at 1064 nm as the pump beam. The energy per pulse is on the order of millijoules, which injects a very high density ($> 10^{18}$ cm^{-3}) of free-carriers into the wafer. At this level of injection in silicon, Auger-recombination is readily observable. The decay of the free-carrier density across many orders of magnitude reveals the Auger, high-level injection and low-level injection lifetimes[6]. Injection-level dependent lifetime measurements reveal information about the nature of defects causing recombination in silicon via the Shockley-Read-Hall model for recombination [1]. Linnros demonstrates that the injection-level

---

[6] "High" and "low" level injection refers to the relative concentration of injected carriers with respect to the background doping levels. High-level injection features an injected carrier density much greater than the background doping density, and vice-versa for low-level injection.

dependent lifetime that he measures is consistent with Shockley-Read-Hall theory[7]. In the second article Linnros describes the conditions required to accurately measure the bulk lifetime in the presence of low to high surface recombination velocity. He also experimentally demonstrates lifetime-mapping over a 4 inch wafer in the Auger, high-level, and low-level injection regimes. The lifetime maps in each recombination regime provide an interesting demonstration of intrinsic vs extrinsic recombination mechanisms. Auger recombination is an intrinsic mechanism that is independent of the electronic quality of the material. Lifetime maps in the Auger regime reveal a relatively constant recombination lifetime. In the high-level and low-level injection regimes, the recombination is due to Shockley-Read-Hall recombination which is an extrinsic, defect-assisted process and thus dependent on the electronic quality of the semiconductor. Lifetime maps in regimes where SRH recombination is dominant show a wide variation is lifetime due to inhomogeneities in the electronic quality of the wafer.

Linnros and Grivickas demonstrated an interesting method for measuring the diffusion coefficient in silicon using time-domain FCA [52]. In their technique, the pump beam is filtered through a grating with a sinusoidal spatial opacity before being absorbed in the silicon wafer. This leads to an injection of carriers that initially follows a sinusoidal curve. The probe beam is focused to a point along the sinusoidal profile and measures the decay of carriers, which is due to both recombination and diffusion. By sweeping the probe beam and measuring the decay at each position along the excitation profile, a two-dimensional map of position and time is built up. Fourier transformation along the spatial dimension leads to peak whose decay in time can be used to extract the diffusion coefficient. A similar study was carried out by Scajev and Jarasiuanas [53] to measure the recombination and transport parameters of CVD-grown 4H-SiC. In their work they

---

[7] Shockley-Read-Hall theory describes recombination via trap states within the bandgap. SRH recombination is typically the dominant recombination mechanism in silicon. This theory is reviewed in Chapter 2.

excite a sinusoidally varying carrier profile via optical interference of a split and then recombined pump beam.

The FCA lifetime techniques I have described so far have operated in the time or frequency domain and measure lifetime by fitting a decay curve. There are few studies that have been performed to measure lifetime under steady/quasi-steady state conditions. Perhaps the first study to ever quantify lifetime in semiconductor using FCA was performed by Harrick [54]. In this work a block of germanium material is illuminated by a tungsten lamp that is used as a pump, while the free-carrier population is monitored by the absorption of infrared radiation supplied by a globar source. Since the magnitude of absorption is proportional to the free-carrier population which is proportional to the lifetime, lifetime may be measured directly. The lifetime that is measured is on the order of milliseconds. Polla [55] describes a quasi-steady state measurement of lifetime using a chopper to modulate the pump in the quasi-steady state limit. The lifetime of various silicon wafers is examined by extracting the amplitude of the probe signal. Chang et al. describes a quasi-steady technique that characterizes the device layer and substrate of a silicon-on-insulator wafer [33], [56]. They used a Tungsten lamp as the probe and two excitation lasers (He-Ne at 632 nm, He-Cd at 442 nm) for the pump beam. By varying the pump wavelength and angle of incidence the authors are able to characterize bulk and surface recombination in the device layer and substrate of the SOI wafer. Since all steady/quasi-steady state techniques require the absolute amplitude of the signal in order to extract lifetime, these techniques require an accurate value of the free-carrier absorption cross section in order to absolutely quantify the magnitude of FCA. As is discussed later in this thesis, this cross section is not well known and it is likely the lifetimes measured in the above works have large systematic errors attached to them.

Recently, a camera-based pump/probe technique has been introduced that operates in steady or quasi-steady state [57] [6]. The first technique [57], Infrared Lifetime Mapping (ILM), is a purely steady-state technique that images the transmission of IR light through a silicon wafer onto an IR camera. The source of the infrared light is a blackbody radiator with peak emission at about 8 µm. The wafer sits between the blackbody source and the camera. A series of laser diodes emitting at

19

940 nm are used to pump the silicon wafer. The lasers are operated at a fixed power, leading to a steady-state excess carrier density in the wafer. These free-carriers attenuate the black body radiation, leading to a reduced signal on the camera. The signal from the camera is measured both when the excitation light is on and off and the signals are subtracted. This results in a contrast map, with higher contrast indicating a higher level of free-carrier absorption, and consequently higher lifetime. The drawback of ILM is that it is subject to higher noise due to it being a steady state method. Carrier Density Imaging (CDI) [6] improves upon ILM by using a modulated excitation and detection scheme. The excitation is modulated at 1.4 Hz, and the camera signal is demodulated on a lock-in amplifier. The in-phase component of the signal is due to free-carrier absorption, the magnitude of which is proportional to the lifetime. CDI is demonstrated to be capable of mapping the lifetime of a multi-crystalline silicon wafer with an area of 100 x 100 mm^2 within 10 seconds. The average lifetime of the wafer examined was about 3 μs, which proves that CDI measurements are effective for characterization of silicon wafers since they can resolve very short lifetimes.

ILM and CDI are steady/quasi-steady state measurements that require calibration in order to convert the camera signal into an absolute lifetime value. In ILM/CDI the calibration is achieved by quantifying the free-carrier absorption cross section, which then allows for an absolute value of absorption to be determined and from that the lifetime. In [6], the IR transmission through several reference wafers with known carrier concentration are used to quantify the absorption cross section, which then leads to a calibration curve. However, this calibration relationship is acquired using p-type wafers which means that only the hole absorption cross section is measured. In lifetime measurements electrons and holes are injected in equal concentrations so an accurate cross section for electrons is required as well. The authors account for this by using a correction factor that leverages the fact that the ratio between electron and holes is supposedly well known [58]. Their calibration also assumes that the absorption cross section is constant with injected carrier density, which as I demonstrate in this dissertation may not be a valid assumption.

The bulk of the work measuring lifetime in silicon using free-carrier absorption in a pump/probe geometry dates back to the 1990s. In recent years this work has tapered off, which is partly due to

the prominence of RF/microwave based approaches. The body of work surrounding RF/microwave techniques is much more extensive, as seen in Figure 2.1. For example, the paper introducing the quasi-steady photoconductance technique [5] has been cited at least 1419 times. This is in stark contrast to one of the more prominent FCA-based lifetime work in silicon [3] that has been cited at least 110 times. As well, the several commercial tools available for measuring lifetime in silicon are all based on RF/microwave photoconductivity measurements. One reason for the adoption of RF/microwave based approaches over FCA is that the former are insensitive to the optical properties of silicon's surface. Silicon wafers are typically only polished to a mirror-finish on a single side, leaving the other side optically rough. In addition to this, silicon used for solar cell applications is textured in order to improve light collection. Roughened/textured surfaces tend to scatter the probe beam used in FCA studies, so collection optics are required to study roughened samples. The primary technique developed in this work-single beam pump/probe free-carrier absorption- does not overcome this disadvantage. However, it opens a new realm of possibilities for *in situ* process monitoring that would be difficult if not impossible to implement using traditional RF/microwave-based and two-beam FCA based approaches.

2.4   Review of Single-Beam Pump Probe Studies

Up to this point, every single FCA study I have reviewed uses a dual-beam pump/probe geometry. That is the pump and probe are comprised of separate beams. There are very few studies that have implemented a pump/probe technique using a single-beam for both pump and probe. Studies that do are cited only a few times, and the work is never expanded upon. Suddendorf and Somekh published a photoreflectance study that uses a frequency-doubled Nd:YAG laser (emitting at 532 nm) laser as both the pump and probe [59]. The laser is modulated sinusoidally by an acousto-optic modulator and split into two beams after emerging from the modulator. The first beam is the sample beam which reflects from a multi-layered silicon sample and is captured by a photodetector. This beam optically induces a change in the refractive index of the sample, which leads to a change in the reflection coefficient of the beam. Frequency-mixing between the modulated beam and the modulated reflectance gives rise to a signal component at the first

21

harmonic of the modulation signal. In order to reliably extract this harmonic, stray harmonic components arising from non-linearities in the modulation transfer function must be eliminated. The second beam is used as a reference in a feedback system to suppress these stray harmonics. The reference beam is fed into a second photodetector and the signal is demodulated on a lock-in amplifier. The in-phase and quadrature components are used as feedback into the acousto-optic modulator to remove stray harmonics and purify the sample beam.

Suddendorf and Somekh's work was cited three times, once by the authors in an unrelated work and twice by another group that had published the same work in a journal and a conference proceeding. This journal article, by Ho et al. [60], employs a similar approach to Suddendorf and Somekh to study nitrogen-implanted silicon and the effect of rapid-thermal annealing on the photoreflectance signal. A 532 nm laser is modulated using a liquid-crystal modulator and the beam is split into reference and sample beams, with the reference beam providing feedback to suppress stray harmonics in the sample beam. The sample beam is collected in reflection-mode and the harmonic frequency that contains the photoreflectance signal is demodulated on a lock-in amplifier. The authors were able to show a difference in photoreflectance signal between implanted and un-implanted regions on the silicon wafer. To my knowledge this study has zero citations.

There are two studies that I have found that quantify free-carrier absorption in silicon using a single-beam [61], [62]. In the first [61], Svantesson and Nilsson use a pulsed Nd:YAG laser for the pump and measure the transmission of the laser through silicon wafers of various thicknesses. The incident power of the pump beam is varied and the transmitted power is plotted as a function of the incident power. For low powers the transmitted power is linear with incident power, which is expected when the absorption mechanism is band-to-band absorption only. However, as power is increased further the transmitted power begins to plateau due to free-carrier absorption becoming more prominent as the injected carrier density increases. By fitting the transmission curves for various sample thicknesses and powers, the authors are able to deduce values for the reflectivity, band-to-band, and free carrier absorption coefficient. A similar study was carried out by Heisel et

al. in [62]. They use a pulsed Ti-Sapphire laser and studied its transmission through a 10 µm thick silicon membrane at 800 nm at various powers. Like Svantesson and Nilsson's work, the transmitted vs incident power is initially linear when incident power is low, but begins to plateau for higher incident powers. Heisel et.al. pushed this trend even further than Svantesson and Nilsson, showing that eventually the transmitted power starts decreasing with increasing incident power, which is indicative of a saturation in absorption due to an excessively high free-carrier concentration. Both authors had follow-up studies where the single-beam technique is used, but the technique is not further expanded upon [63]–[66]. All of these studies constitute a steady-state measurement since it is the CW transmission of the laser that is measured. Since the free-carrier absorption coefficient is measured, it is possible to derive the excess carrier density from which the recombination lifetime could be determined [5]. However, these studies rely on the fitting of non-linear transmission curves with the non-linearity arising from very high carrier densities. Thus any lifetime measurement that is performed with these techniques will be measuring lifetime under very high-injection conditions, likely measuring Auger recombination. Since Auger recombination is an intrinsic recombination process, it will not reveal information about the material quality of silicon which is the desired information when performing lifetime measurements [7].

2.5   Summary of Literature Review

I have reviewed the scientific literature for free-carrier absorption-based lifetime measurements in silicon. The principles behind quasi-steady state, time-domain, and frequency-domain approaches to the technique have been discussed, along with applications primarily focused on silicon. The common feature to all FCA-based lifetime techniques that I have examined is the use of a dual-beam pump/probe geometry, *i.e.* a separate source for pump and probe. Another feature to note is that all applications that I discussed are performed on a laboratory bench top, and not for inline process control or monitoring of processes *in situ*. This is probably not a coincidence. Pump/probe FCA studies demand that the pump and probe beams overlap on the sample under study, with the beam diameters typically on the order of millimeters or less. This is straightforward enough to

implement on a bench top since the experimenter has direct access to the sample and it is easy to make the adjustments required to ensure that pump and probe are overlapped. It would be considerably more difficult to implement such a setup to monitor a process *in situ*, such as the deposition of a silicon nitride coating on a silicon wafer via chemical vapour deposition (CVD)[8], or in an annealing tube furnace. Single-beam pump/probe is a technology that is uniquely suited for monitoring of processes *in situ* since there is no consideration about beam overlap. As long as the beam strikes the sample and can be collected afterwards, single-beam pump/probe can be implemented. In Chapter 6 I will examine potential applications for single-beam pump/probe.

Another issue that has been addressed in this literature review are steady-state techniques for lifetime measurement, both FCA-based in the case of ILM/CDI and RF-based in the case of QSSPC. The common theme in all of these techniques is the requirement for the instrument to be calibrated in order to map the measured signal to the recombination lifetime. In all of the techniques examined the calibration is indirect, relying on a reference wafer of known electronic properties in order to establish the relationship between measured signal and lifetime. Verification of the veracity of the calibration requires measurement of the lifetime using a separate technique. Calibration of the QSS-FCA technique that I develop in this work is completely direct, with the relationship between quasi-steady state lifetime and the true lifetime measured unambiguously. A major advantage of QSS-FCA is that the unknown factor that is quantified is a material constant, and not a geometrical factor as is the case with the QSSPC technique. The geometrical factor restricts the QSSPC apparatus to measurements made in the same geometry[9] under which the

---

[8]CVD silicon nitride is a standard coating for silicon photovoltaic cells. It acts simultaneously as an antireflection coating and for electronic passivation of the silicon surface [67].

[9] Geometry in this context refers to the geometrical relationship between the sensing coil used by the QSSPC apparatus and the wafer under test. The coupling constant between the coil and wafer is a complicated function of position [68] which is determined during calibration. Obviously then the coil must be consistently positioned in the same place with respect to the wafer under test as it was during calibration

system is calibrated. This restriction does not apply to QSS-FCA, allowing for more flexibility in its implementation.

3 Theoretical Background

3.1   Absorption in Semiconductors: Band-to-band and Free Carrier Absorption
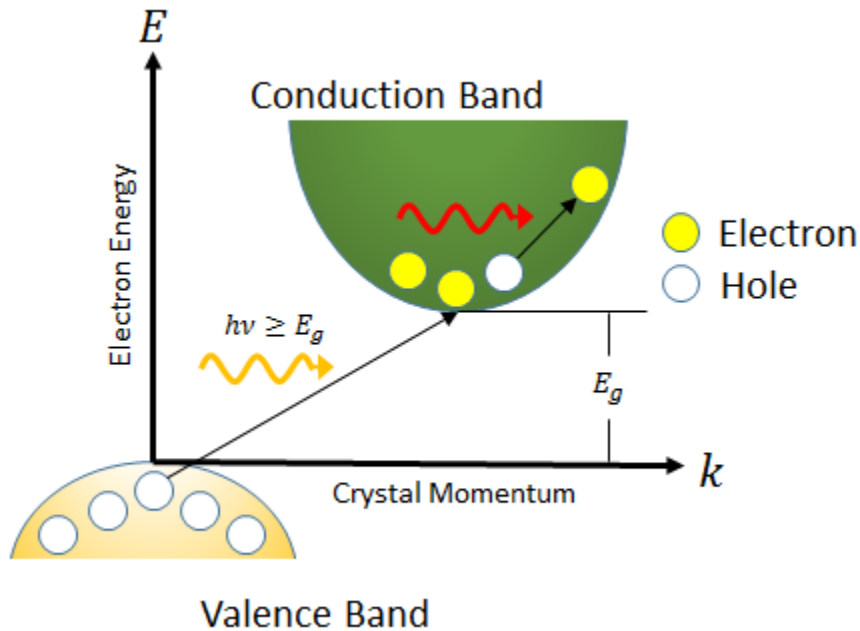
Figure 3.1: Diagram of band-to-band and free carrier absorption processes in an indirect bandgap semiconductor.

To measure lifetime in a semiconductor, electrons and holes are promoted into the conduction and valence bands, and their population over time or modulation frequency is observed. Interband absorption is used to excite electrons and holes into these bands, while intraband absorption is used to monitor their population. Intraband absorption is proportional to the density of electrons/holes in the conduction/valence bands, so its measurement gives direct access to the population density of free-carriers. Figure 3.1 shows a simplified energy band diagram for an indirect bandgap semiconductor, like silicon, illustrating interband and intraband absorption processes. Interband, or band-to-band absorption, occurs when light is absorbed to promote an electron from the valence

to the conduction band, leaving behind a hole in the valence band. For band-to-band absorption to occur, the light must usually have energy greater than the characteristic bandgap of the semiconductor. In silicon this about 1.1 eV, which corresponds to a wavelength of 1100 nm. Silicon is an indirect bandgap semiconductor, so the valence and conduction band edges are not aligned in crystal momentum (Figure 3.1). Since the momentum of light is very small[10], a momentum-conserving collision with a phonon is required in order to excite an electron to the conduction band in indirect semiconductors. This requirement of an additional quasi-particle to facilitate the transition reduces the probability of it occurring, so the absorption coefficient is much smaller in indirect bandgap than direct bandgap semiconductors such as GaAs.

Intraband absorption occurs when a free electron or hole absorbs light and is promoted to a higher energy state *within the same band*. Since intraband absorption involves free-carriers, it is also known as *free-carrier absorption* (FCA). The energy dispersion in the conduction or valence band is parabolic (or approximately so), so a transition to higher energy states requires a momentum-conserving collision. This momentum-conserving event may be lattice scattering (*i.e.* emission or absorption of a phonon), electron-hole scattering or scattering from a charged impurity [69]. The classical description of the FCA coefficient α_{FCA} is given by the Drude theory of conductivity [58]:

$$\alpha_{FCA} = \frac{q^3\lambda^2}{4\pi^2\varepsilon_0 c^3 n}\left[\frac{n}{m_n^{*2}\mu_n} + \frac{p}{m_p^{*2}\mu_p}\right] \tag{3.1}$$

where q is the fundamental electron charge, λ is the wavelength of light being absorbed, ε_0 is the permittivity of free space, c is the speed of light, n is the refractive index of the semiconductor,

---

[10] The order of phonon momentum can be estimated by $\hbar K$, where K is the reciprocal lattice vector of silicon ($K = 2\pi/a$, where a is the lattice constant of silicon). This results in a value of $1.22\text{x}10^{-24}$ kg m/s. The momentum of light is given by h/λ, which is $6.23\text{x}10^{-28}$ kg m/s. This is obviously much smaller than the phonon momentum.

m_n^* & m_p^* are the electron and hole conductivity effective masses, respectively, μ_n & μ_p are the electron and hole mobilities, respectively, and n & p are the concentrations of free electrons and holes, respectively. In this work free electrons and holes are generated in a one-to-one ratio, so $n = p$. It is helpful to write Equation (3.1) in terms of the free-carrier absorption cross section σ_{FCA}:

$$\alpha_{FCA} = \sigma_{FCA} n \qquad (3.2)$$

Equation (3.2) shows that the free-carrier absorption coefficient is proportional to a material constant and the free-carrier density. In general σ_{FCA} varies with n since the carrier mobilities are dependent on the carrier density [70]. It is well known in the literature that the Drude model underestimates the value of σ_{FCA} [71]. The Drude model is actually a simplification of a more general model derived from perturbation theory that describes FCA in terms of scattering from acoustic phonons [72]. There are also contributions due to scattering from optical phonons, scattering between electrons and holes, and scattering from ionized impurities (*i.e.* donor/acceptor atoms) in the material [46], [69], [73]. For the purposes of this work, FCA is a tool to experimentally access n. From this point of view the underlying physics of the FCA phenomenon, while interesting, is irrelevant; all that matters is that a signal can be measured that is proportional to n. For the single-beam pump/probe technique the absolute value of σ_{FCA} is unimportant since I am only interested in the relative amplitude of the FCA signal. In QSS-FCA an absolute value for σ_{FCA} will be required, which the technique provides a mechanism for measuring directly.

3.2   Recombination in Semiconductors
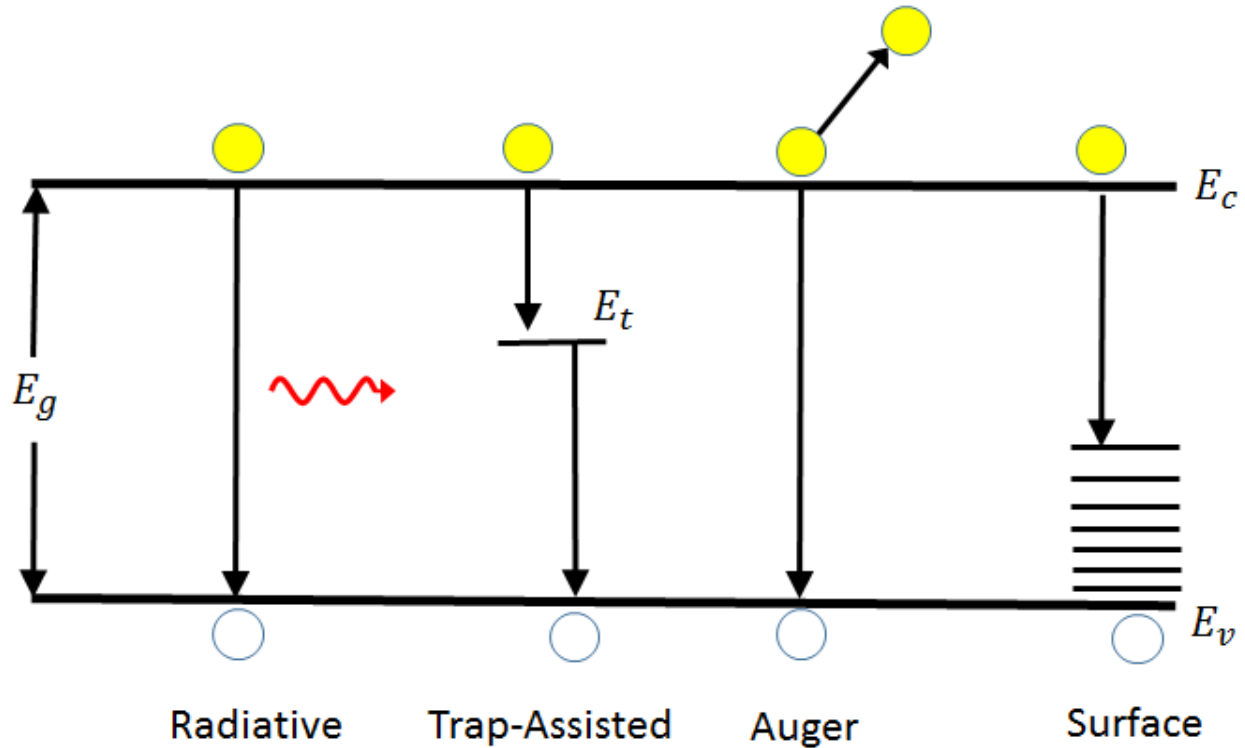
Figure 3.2: A simplified energy band diagram illustrating the fundamental recombination processes in a semiconductor. Radiative, trap-assisted (or Shockley-Read-Hall), Auger, and surface recombination processes are illustrated. Each process is a mechanism by which an electron in the conduction band falls into a hole in the valence band, annihilating both carriers.

At room temperature ($T = 300$ K) in a semiconductor, there is a finite rate at which electrons are pumped into the conduction band due to thermal excitation. For each electron pumped into the conduction band, there is a hole left behind in the valence band. In thermal equilibrium, the rate at which free-carriers are generated is equal to the rate at which they *recombine*. During *recombination*, an electron in the conduction band falls back into a hole in the valence band annihilating the two carriers. Recombination is parameterized by the *recombination lifetime*, which is the average time over which a population of carriers above the thermal equilibrium concentration recombine. The total lifetime that is measured-the *effective lifetime* τ- is the reciprocal sum of several independent recombination mechanisms:

$$\frac{1}{\tau} = \left[\frac{1}{\tau_{rad}} + \frac{1}{\tau_{Aug}} + \frac{1}{\tau_{SRH}}\right] + \frac{1}{\tau_s} \tag{3.3}$$

where $\tau_{rad}, \tau_{Aug}, \tau_{SRH}, \& \tau_s$ are the radiative, Auger, Shockley-Read-Hall, and surface lifetimes, respectively. These processes are illustrated in Figure 3.2. Equation (3.3) is a rate equation, and states that the total rate of recombination is just the sum of the rates from the contributory recombination mechanisms. Shorter lifetimes represent faster rates of recombination, and dominate the overall contribution to recombination. The squares brackets delineate the *bulk lifetime* τ_b, which is recombination that occurs within the volume of the crystal. The surface lifetime is due to recombination via trap states at the semiconductor's surface.

Radiative and Auger recombination are known as *intrinsic* recombination processes since they are fundamental processes that cannot be eliminated. Shockley-Read-Hall recombination, also known as trap-assisted recombination, is an extrinsic recombination mechanism facilitated by trap states within the semiconductor's forbidden gap. These traps are due to impurity atoms inside the crystal lattice of the semiconductor, and so Shockley-Read-Hall recombination can largely be mitigated by using hyper-pure semiconductor material. In photovoltaics, long recombination lifetimes are desirable since optically-excited charge carriers have a higher probability of reaching the pn-junction before recombination. Carriers that cross the junction are essentially "home-free" and are able to participate in electrical conduction in an external circuit. In the following section each of the recombination mechanisms listed above are described, with emphasis given to the mechanisms relevant to silicon.

3.2.1   Radiative Recombination

Radiative recombination occurs when a conduction-band electron recombines directly with a hole in the valence band, releasing energy as light. The lifetime associated with radiative recombination is given by Equation 1.32 in [1]:

$$\tau_{rad} = \frac{1}{B(n_0 + p_0) + Bn} \tag{3.4}$$

where n_0 & p_0 are the thermal equilibrium concentrations of electrons and holes, respectively, n is the density of free-carriers above the equilibrium concentration, and B is a rate constant. It is assumed that the electron and hole concentrations are equal, since free electrons and holes are generated in a one-to-one ratio by optical injection. Radiative recombination is typically the dominant mechanism for carrier recombination in *direct bandgap* semiconductors. In direct bandgap semiconductors, the edges of the valence and conductions bands are aligned in momentum-space, so an electron may transition from the conduction to valence band without a change in momentum. This results in a high rate constant, and thus a high probability of radiative recombination. Silicon has an indirect bandgap, so in order for an electron to fall from the conduction to valence band a momentum-conserving collision with the lattice (*i.e.* a phonon) must occur. The requirement of interaction with a third quasi-particle reduces the probability of radiative recombination in silicon, making it an inefficient process. Indeed the rate constant for a direct bandgap semiconductor like GaAs is $B = 2\text{x}10^{-10}$ cm^{3}s^{-1} whereas for silicon it is $B = 1\text{x}10^{-14}$ cm^{3}s^{-1}, which is a difference of four orders of magnitude [4]. This difference results in a very large span in carrier lifetimes between direct and indirect bandgap semiconductors. Choosing a background doping level of $N_d = 10^{16}$cm^{-3} and assuming carrier injection is small ($n \rightarrow 0$), the radiative lifetime in GaAs is about 500 ns, whereas for silicon it is 10 ms.

Radiative recombination is the operational mechanism behind light-emitting diodes or diode lasers. Excess electrons and holes are electrically injected and recombine radiatively to produce light. It is the indirect bandgap of silicon that makes silicon-based LEDs or lasers an elusive prospect. Still, while radiative recombination is inefficient in silicon, it still occurs and has been used for materials characterization [4], [74]. In this context, the radiative recombination in silicon is referred to as *photoluminescence*.

3.2.2   Auger Recombination

Auger recombination is similar to radiative recombination in that an electron recombines directly with a hole. In Auger recombination however, the energy of recombination is transferred to an adjacent electron or hole, instead of light. The energy transferred to the adjacent carrier excites it to a higher energy level within its respective band, after which the carrier rapidly thermalizes back to the band edge. The lifetime associated with Auger recombination in the high injection limit ($n \gg N_d$, where N_d is the doping density) is given by Equation 1.36 in [1]:

$$\tau_{Aug} = \frac{1}{C_a n^2} \tag{3.5}$$

where C_a is the *ambipolar Auger coefficient*, and n is the number of free-carriers. Equation (3.5) shows that the Auger lifetime is inversely proportional to the square of the carrier density. This non-linearity is intuitive since Auger recombination is a three-particle process, so the probability of recombination occurring will rise at higher carrier densities. In silicon, $C_a = 3.79 \times 10^{-31}$ cm^{6}s^{-1}, so for a moderate injection of carriers $n = 10^{16}$ cm^{-3} the lifetime is 26 ms, which is very high. At higher injection ($n = 10^{18}$ cm^{-3}) the lifetime drops to 2.6 μs. Auger recombination becomes the dominant recombination mechanism at high carrier densities in both direct and indirect bandgap semiconductors. In fact, Auger recombination is responsible for the droop phenomenon in LEDs, which is a reduction in the radiative efficiency at high current densities [75].

3.2.3   Shockley-Read-Hall Recombination

Shockley-Read-Hall (SRH) recombination is a trap-assisted process, whereby energy states within the forbidden bandgap of the semiconductor capture (or trap) free-carriers. Figure 3.2 illustrates a

trap-assisted recombination event, where a trap state captures an electron and then a hole to complete the recombination process. The SRH lifetime is given by the SRH equation (Equation 3.1 in [1]):

$$\tau_{SRH} = \frac{\tau_{n0}(p_0 + p_1 + n) + \tau_{p0}(n_0 + n_1 + n)}{p_0 + n_0 + n} \tag{3.6}$$

where n is the density of excess carriers, τ_{n0} & τ_{p0} are the *capture time constants* for electrons and holes, respectively, n_0 & p_0 are the equilibrium carrier densities for electrons and holes, respectively, and n_1 & p_1 are the electron and hole concentrations corresponding to a Fermi level of E_t, where E_t is the energy of the level of the trap state. The capture time constants are given by:

$$\tau_{p0} = \left(N_t \sigma_p v_{th}\right)^{-1} \tag{3.7}$$

$$\tau_{n0} = \left(N_t \sigma_n v_{th}\right)^{-1} \tag{3.8}$$

where N_t is the density of the trap state, v_{th} is the electron thermal velocity ($\sim 10^7$ cm/s at room temperature) and σ_n & σ_p are the *capture cross sections* for electrons and holes, respectively.

n_1 and p_1 are given by:

$$n_1 = N_c e^{-\frac{E_c - E_t}{kT}} \tag{3.9}$$

$$p_1 = N_V e^{\frac{E_V - E_t}{kT}} \qquad (3.10)$$

where k is Boltzmann's constant, T is temperature, E_C & E_V are the energies of the conduction and valence bands, respectively, and N_C & N_V are the effective densities of states in the conduction and valence bands, respectively.
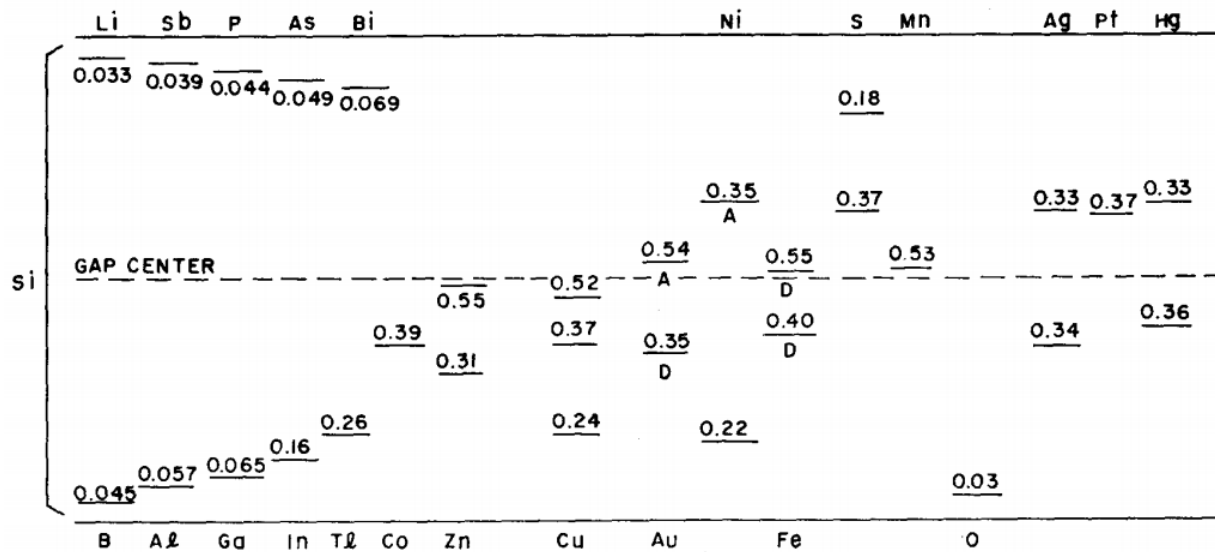
Figure 3.3: Ionization energies for various impurities in silicon. Figure printed from Sze [76].

Equation (3.6) forms the theoretical basis behind *lifetime spectroscopy*, which is the set of techniques used to probe the defects responsible for recombination in a semiconductor. Defect characterization seeks to elucidate parameters such as the energetic position E_t and density N_t of particular trap species. Figure 3.3 shows the energetic position of several impurity species in silicon. It can be seen that the impurity's position within the bandgap provides a fingerprint for the impurity's species. Measurement of the impurity content in a semiconductor is a useful diagnostic tool for identifying sources of contamination that can degrade device performance. Defect characterization is achieved experimentally by analyzing the SRH lifetime's dependence on the

injected carrier density n and temperature. Defect characterization is outside the scope of this work. In this dissertation, I am primarily focused on techniques for *measuring* the lifetime, not interpreting it. Still, it is helpful to discuss the injection-level dependence of lifetime here, since it will be encountered later on.
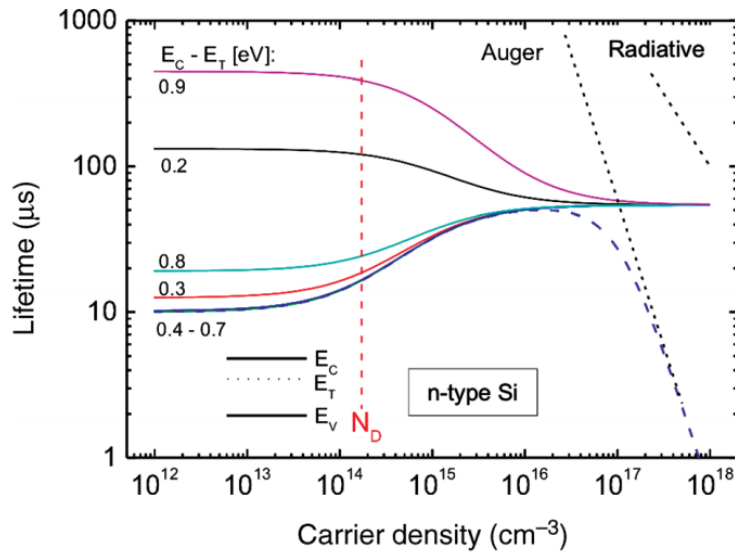
Figure 3.4: Injection level dependence of the total effective lifetime in silicon as a function of carrier injection, for various trap levels within the bandgap. Figure printed from [4].

Figure 3.4 plots the injected carrier dependence of the SRH lifetime (solid curves) and the total lifetime due to SRH and Auger recombination (long dashed curve), for n-type silicon. The family of solid curves is the SRH injection-level dependent lifetime for various trap state energies, with the trap energy level referenced to the conduction band edge. The vertical dashed line indicates the concentration of background donors, and separates the regions of low and high level injection. Clearly the SRH lifetime depends sensitively on the position of the trap state within the bandgap, in a complicated way. At low-level injection, the SRH lifetime is high for trap levels close to either band-edge. This is because carriers that fall into these trap states have a higher probability of being excited out of them by thermal agitation, delaying recombination. Deeper trap levels (traps close to the middle of the bandgap) are much more detrimental to the lifetime. Once carriers fall into these traps, it is unlikely they will be excited out by thermal agitation. In high-level injection, the

SRH lifetimes converge to a final value given by $\tau_{HLI} = \tau_{n0} + \tau_{p0}$, which is independent of the trap's position within the bandgap.

Though in high-level injection the SRH lifetime converges to a constant value, the total lifetime (long dashed curve) begins dropping before the convergence. This is due to the fact that Auger recombination starts to dominate recombination. From Figure 3.4, the pure Auger lifetime (dotted line labelled "Auger") is very long with respect to the SRH lifetime at carrier densities below $n = 10^{16}$ cm^{-3}. Beyond $n = 10^{16}$ cm^{-3} the Auger lifetime drops below the SRH lifetime and becomes the dominant recombination mechanism. For practical injection levels, the radiative lifetime (dotted line labelled "Radiative") is always much longer than the SRH and Auger lifetimes, so radiative recombination makes a negligible contribution to the total recombination lifetime.

Since silicon is an indirect bandgap semiconductor and thus has a very long radiative lifetime, the dominant recombination is Shockley-Read-Hall recombination at low levels of injection. Lifetimes in silicon are typically in the range of $1\ \mu s - 1$ ms.

3.2.4   Surface Recombination

So far all of the recombination mechanisms that have been considered are *bulk* recombination mechanisms (*i.e.* recombination that occurs within the volume of the crystal). There is also recombination that occurs at the surface. Surface recombination is closely related to Shockley-Read-Hall recombination; trap states at the surface of the semiconductor capture electrons and holes to annihilate them. The difference is that SRH recombination considers traps with discrete energy levels, whereas surface recombination considers a continuum of energy levels. The origin of trap centers at the semiconductor's surface are dangling bonds which give rise to energy states that can capture electrons and holes. The rate of surface recombination is given by a generalized form of the Shockley-Read-Hall recombination rate (Equation 1.48 in [1]):

$$U_s = (n_s p_s - n_i^2) \int_{E_v}^{E_c} \frac{v_{th} D_{it}(E_t) dE_t}{[n_s + n_1(E_t)]\sigma_p(E_t)^{-1} + [p_s + p_1(E_t)]\sigma_n(E_t)^{-1}} \tag{3.11}$$

where n_s & p_s are the electron and hole concentrations at the surface, n_i is the intrinsic concentration of carriers in silicon, E_v & E_c are the energies of the valence and conduction band edges, respectively, v_{th} is the electron thermal velocity, σ_n & σ_p are the capture cross sections of electrons and holes, respectively, E_t is the trap energy, and $D_{it}(E_t)$ is the trap density at E_t. Surface recombination is parameterized by a *surface recombination velocity*, given by:

$$S \equiv \frac{U_s}{n} \tag{3.12}$$

The surface recombination velocity (SRV) represents the flux of carriers that recombine at the surface. Higher SRVs indicate a faster rate of recombination, so it is desirable for S to be as low as possible. The upper limit on S is 10^7 cm/s [1], which is dictated by the thermal velocity for electrons (*i.e.* the SRV cannot exceed the rate at which electrons diffuse to the surface). State-of-the-art low SRVs are in the range of $S < 10$ cm/s for silicon [77], [78]. SRV is reduced by *passivating* the semiconductor's surface.

There are two mechanisms for passivation: chemical and field-effect passivation [36]. Chemical passivation involves "soaking-up" dangling bonds at the silicon surface by adding a dielectric material to the surface, deactivating the dangling bonds as trap centres. Thermally-oxidized silicon provides good passivation, and was used on the PERL (Passivated Emitted, Rear Locally-diffused) cell [79], which held the record for highest efficiency crystalline silicon solar cell until 2014 [80]. Field-effect passivation uses a built-in electric field at the semiconductor's surface to repel minority carriers [36]. Since a majority and a minority carrier are required for a recombination

event to occur, repelling minority carriers away from the surface effectively reduces recombination there. There are two origins for the electric-field at the surface. In the first, charges trapped in the dielectric film coating the semiconductor substrate induce an electric field at the surface. Silicon nitride films deposited on silicon with plasma-enhanced chemical vapor deposition (PECVD) provide good chemical and field effect passivation, achieving state-of-the-art low SRVs [78]. Silicon nitride films also act as effective anti-reflection coatings, and are standard films used in the commercial production of solar cells [67]. Another mechanism for incorporating field-effect passivation is to intentionally dope the surface with a higher concentration of carriers of the same doping type. This creates an n++,n (or p++,p) junction at the surface, where the electric field repels carriers of the opposite type. This type of field-effect passivation is referred to as front or back surface fields, depending on which side of the solar cell the additional doping is incorporated.

3.3   Measurement of Lifetime

3.3.1   Time, Frequency, and Quasi-Steady State Domains

The time rate-of-change for free electrons (or holes) in a semiconductor can be described by the following differential equation:

$$\frac{\partial n}{\partial t} = g(t) - \frac{n}{\tau} \tag{3.13}$$

where n is the concentration of electrons above the thermal equilibrium concentration, τ is the recombination lifetime and $g(t)$ is the volumetric generation rate of free carriers. This equation states that the net rate of change of carriers is the rate of generation subtracted by the rate of recombination. In lifetime experiments, $g(t)$ is due to optical excitation and n is the experimentally measured quantity. Measurements are conducted in the time, frequency, or steady-

state/quasi-steady regimes, which are distinguished by the temporal nature of $g(t)$, and how n is monitored. Time domain studies use a pulsed laser with pulse-width $\ll \tau$ to near-instantaneously excite n, and then monitor n over time as it decays back to equilibrium [3]. In this case, $g(t)$ may be approximated as a Dirac-delta function in time and Equation (3.13) becomes $\frac{\partial n}{\partial t} = -n/\tau$ with the initial condition $n(0) = n_0 = N_0$ where N_0 is the number of photons absorbed from the laser pulse. The solution to this equation is:

$$n = n_0 e^{-\frac{t}{\tau}} \tag{3.14}$$

From (3.14) it can be seen that n decays with an exponential dependence from an initial concentration n_0 back to 0 with a decay constant equal to the recombination lifetime. Therefore by monitoring n over time the lifetime can be extracted by fitting the n decay curve to an exponential function parameterized by τ. n is found by measuring a physical quantity proportional to it. In the µ-PCD technique this quantity is the power of microwaves reflected from the semiconductor, which is related to photoconductivity. In the free-carrier pump/probe technique this quantity is the absorption of an optical probe beam.

In frequency domain studies $g(t)$ describes a harmonically varying excitation of angular frequency ω, which leads to a harmonically varying n. Letting $N(\omega)$ and $G(\omega)$ be the complex amplitudes[11] of the free-carrier population and generation rate, respectively, n & $g(t)$ can be written in their harmonic form: $n = N(\omega)e^{i\omega t}$ and $g(t) = G(\omega)e^{i\omega t}$. Substituting n & $g(t)$ into (3.13) and rearranging:

---

[11] In the frequency domain the signal amplitude is a complex number. The real part is the signal component in phase with the excitation, and the imaginary part is the signal component 90° out of phase with the excitation.

$$N(\omega) = \frac{G(\omega)\tau}{1 + i\omega\tau} \tag{3.15}$$

Equation (3.15) is the frequency response of the free-carrier population under a harmonic excitation. $N(\omega)$ is a complex number, indicating an in-phase and out-of-phase component to the signal. For a generation rate that is independent of frequency, this frequency response is a Lorentzian function which describes the response of a 1st order low-pass filter, with the roll-off frequency being equal to the reciprocal of the recombination lifetime. In an experiment, the modulation frequency of the excitation is swept while the value of $N(\omega)$ is demodulated on a lock-in amplifier. The magnitude of the $N(\omega)$ curve is fit with the magnitude of (3.15) to extract τ. This is the principle behind the MFCA technique.

In steady-state or quasi-steady state lifetime measurements, n is measured following excitation with a constant or slowly varying $g(t)$. The quasi-steady state regime is distinguished by an excitation that varies slowly enough that n is always in equilibrium with it. It is a special case of Equation (3.15), where $\omega\tau \ll 1$:

$$n = G\tau \tag{3.16}$$

Equation (3.16) shows that the free-carrier population measured under a constant generation rate G is directly proportional to τ. n is measured experimentally and G is known, allowing τ to be extracted. QSSPC is the most popular commercial instrument for measuring lifetime in the quasi-steady state. In this technique, an eddy-current sensor measures the photoconductivity of the wafer, which is proportional to n. In this work I demonstrate a new QSS technique for measuring lifetime via free-carrier pump/probe.

The quasi-steady state and transient/roll-off lifetime measurement techniques have complementary advantages and disadvantages. Quasi-steady state measurements are inherently low frequency, and are not limited by finite bandwidth on the excitation or measurement side of the experiment. However, in order to use Equation (3.16) to find τ, n must be measured in absolute units. Measuring in absolute units typically requires calibration in order determine the experimental parameters that relate n to the experimentally measured quantity. Conversely, transient/roll-off techniques require bandwidth comparable to the inverse lifetime in order to resolve the time/frequency decay curves and extract τ. For a lifetime of 1 µs this corresponds to a bandwidth on the order of 100s of kHz to a MHz. However, since these techniques need only measure the relative amplitude of the signal, calibration of the measurement apparatus is not required.

In this work, measurement of lifetime is performed exclusively in the frequency or quasi-steady state regimes.

3.3.2   The Effective Lifetime

When measuring recombination lifetime the experimenter is typically interested in the bulk lifetime τ_b, particularly the Shockley-Read-Hall lifetime, since it gives access to information about the nature of defects in a semiconductor [1]. In general the actual lifetime that is measured experimentally is an *effective* lifetime that has contributions from both the bulk region of the wafer and the surface. As will be discussed in this section, the effective lifetime measured in quasi-steady and the lifetime measured in a time/frequency domain study are only equivalent in the limit of slow surface recombination velocity ($S \leq 1000$ cm/s). When surface recombination goes to zero both lifetimes are equivalent to the bulk lifetime. A distinction is made between the two, with τ_{qss} being the lifetime measured in quasi-steady state conditions, and τ being measured via the roll-off frequency of (3.15). In this section I describe the physical model from which the effective lifetime originates, and examine how it differs for the quasi-steady state and roll-off measurement approaches.

Equation (3.13) is a simplified modelled that does not take into account the 3-dimensional nature of carrier generation and diffusion. A more general equation describing the time-dependent excess electron concentration n in a semiconductor is given by:

$$\frac{\partial n(r,z,t)}{\partial t} = D\nabla^2 n(r,z,t) - \frac{n(r,z,t)}{\tau_b} + g(r,z,t) \tag{3.17}$$

where D is the diffusion coefficient, τ_b is the bulk recombination lifetime, and g is the volumetric generation rate of free-carriers. The coordinate system that is used for this equation will be illustrated in Figure 5.1. Equation (3.17) is the 3D continuity equation for electrons in cylindrical coordinates. It states that the time rate of change of the electron population in a differential volume of semiconductor material is equal to the sum of the net rates at which carriers diffuse into the volume, recombine inside the volume, and are generated due to optical-excitation. Since electrons and holes are generated and recombine in equal concentrations, charge neutrality is maintained and drift effects may be neglected. A consequence of electrons and holes being generated in equal concentrations is that the carrier diffusion becomes ambipolar [81]. In silicon, electron mobilities are higher than hole mobilities which results in a higher diffusion coefficient for electrons [69]. Since electrons and holes are generated in equal concentrations under optical excitation, electrons diffusing faster than holes would lead to a spatial charge imbalance that would tend to bring the carriers back together due to Coulombic attraction. The net result of this is that carriers tend to diffuse together with a diffusion coefficient that is intermediate between the value for electrons and holes. The consequence of ambipolar diffusion is that electron and hole transport do not need to be separately considered. The equation describing electron transport and recombination is identical to the equation describing hole transport and recombination. Therefore a complete description of charge carrier transport and recombination for lifetime experiments is given by $n(r,z,t)$ alone. Because of this, n is interpreted as the free-carrier density, not as the electron-density alone.

In typical lifetime experiments, the pump beam diameter is much larger than the diffusion length of free-carriers and the probe beam is much smaller than the pump, permitting a purely 1-dimensional treatment of the continuity equation:

$$\frac{\partial n(z)}{\partial t} = D \frac{\partial^2}{\partial x^2} n(z,t) - \frac{n(z,t)}{\tau_b} + g(z,t) \qquad (3.18)$$

where z is the dimension along the thickness axis of the wafer. For a monochromatic excitation source with absorption coefficient α passing through the wafer a single time, the axial dependence of the generation rate takes on the form $g_{ax}(z) \sim e^{-\alpha z}$, α being the absorption coefficient of the light source. The simplest case of (3.18) occurs when the generation rate is uniform along z, and recombination at the wafer surface can be neglected. In this case, n & G are independent of position and (3.18) reduces to (3.13) whose solution in the frequency domain is (3.15).

I define a generalized lifetime $\mathfrak{T}$ as the following:

$$\mathfrak{T}(\omega) \equiv \frac{N(\omega)}{G(\omega)} \qquad (3.19)$$

where $\mathfrak{T}(\omega = 0) = \tau_{qss}$. This factor is defined since it is often more convenient to discuss $N(\omega)$ normalized to the generation rate $G(\omega)$, especially when comparing different formulations of $N(\omega)$. For the simplest case involving only bulk recombination, $\mathfrak{T}$ is given by :

$$\mathfrak{T}_s = \frac{\tau}{1 + i\omega\tau} \qquad (3.20)$$
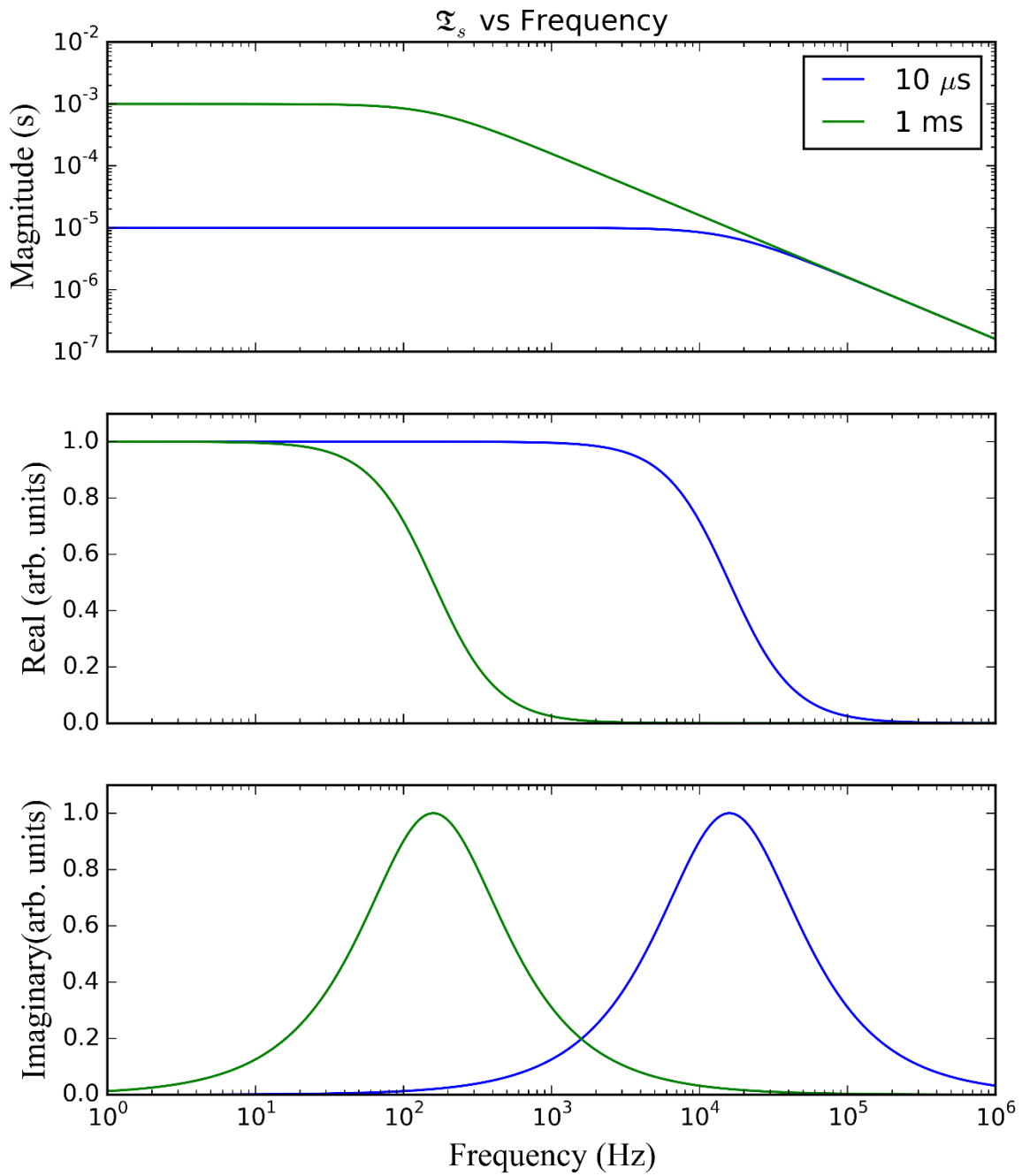
Figure 3.5: Plot of magnitude (top), real part (middle), and imaginary part (bottom) of Equation (3.20) for two different bulk recombination lifetimes τ_b

Figure 3.5 (top) plots the magnitude of $\mathfrak{T}_s$ for a $10\,\mu s$ and $1\,ms$ lifetime. There are two characteristic regions of interest: the flat region at low frequency, and the roll-off region at high frequencies. In the limit of low frequency, the amplitude is flat and equal to the bulk lifetime. At high frequencies, the frequency-response rolls-off with a characteristic decay constant equal to the bulk lifetime. The difference in frequency-response for different lifetimes is also clearly evident. Long lifetimes lead to higher amplitudes that roll-off at lower frequencies, and vice-versa for short lifetimes. It is evident from Figure 3.5 that lifetime may be extracted either from the absolute amplitude of $\mathfrak{T}_s$ or its frequency-dependence. In addition to the magnitude, the real (middle) and imaginary (bottom) components of $\mathfrak{T}_s$ are also shown. The real part is similar in shape to the magnitude. The imaginary component is more interesting since it has a characteristic peak at the angular frequency ω_p which is related to the recombination lifetime via the following relationship:

$$\tau = \frac{1}{\omega_p} \tag{3.21}$$

This shows that the peak of the imaginary component of the signal can be used to determine the lifetime. Shorter lifetimes lead to a shift of the imaginary spectrum towards higher frequencies. In general, either the real, imaginary, or magnitude of $\mathfrak{T}_s$ can be used to measure lifetime since they all contain the same lifetime information. In Chapter 6 it will be seen that the imaginary component (*i.e.* the component that is out-of-phase with respect to the pump modulation signal) is the most convenient way to extract lifetime for single-beam pump/probe studies.

Equation (3.20) is the idealized case where the wafer is perfectly passivated (*i.e.*) surface recombination is negligible. In this case the characteristic lifetime is the bulk lifetime, and is equivalent in both the quasi-steady state and transient cases. However, when the surface passivation is imperfect, there is additional recombination that lowers the excess carrier density at the surface. This in turn leads to a diffusive flux towards the surface, leading to further recombination. The situation is now further complicated by the fact that the absorption profile of the excitation source now comes into play. Surface recombination effects are more exaggerated

when the absorption coefficient is high because most of the carriers are generated close to the surface.

To account for the more general case involving surface recombination, Equation (3.18) is solved directly, applying surface-recombination boundary conditions at the front and rear surfaces of the wafer [8]:

$$D \left. \frac{\partial n}{\partial x} \right|_{x=0} = Sn(0) \tag{3.22}$$

$$-D \left. \frac{\partial n}{\partial x} \right|_{x=W} = Sn(W) \tag{3.23}$$

where W is the wafer thickness, and S is the surface recombination velocity at the surface of the wafer. It is assumed in this work that S is identical on both surfaces, which is valid since the samples that are examined have identical front and back surfaces. Luke and Cheng provide an analytic solution to this equation in the time domain [51]:

$$n(t) = \phi_0 \frac{(1-R)}{1-Re^{-\alpha\eta W}} \frac{8\alpha\eta e^{-\frac{\alpha\eta W}{2}}}{W} \sum_{n=1}^{\infty} A_n^{lc} \, e^{-\frac{t}{\tau_n}} \tag{3.24}$$

where ϕ_0 is the photon flux per unit area, α is the absorption coefficient of the pump beam, η is the ratio of pathlength through the wafer to the wafer thickness[12], R is the reflectance of the pump beam, W is the wafer thickness. The factor A_n^{lc} is known as the *Luke and Cheng coefficient* which is given by:

$$A_n^{lc} = \frac{\sin\left(\frac{\alpha_n W}{2}\right)}{((\alpha\eta)^2 + \alpha_n^2)(\alpha_n W + \sin \alpha_n W)}\left[\alpha\eta \sinh\left(\frac{\alpha\eta W}{2}\right)\cos\left(\frac{\alpha_n W}{2}\right)\right.$$
$$\left. + \alpha_n \cosh\left(\frac{\alpha\eta W}{2}\right)\sin\left(\frac{\alpha_n W}{2}\right)\right] \tag{3.25}$$

The factors α_n are related to a factor δ_n via the following relationship:

$$\frac{\alpha_n W}{2} = \delta_n \tag{3.26}$$

where δ_n are the roots of the transcendental equation:

$$\cot \delta_n = \left(\frac{2D}{SW}\right)\delta_n \tag{3.27}$$

The factors τ_n are the series effective lifetimes, given by:

---

[12] The factor η is given by $\sec \theta$, where θ is the angle of propagation inside of the wafer. Due to the high refractive index of silicon (about 3.5), the steepest angle inside the wafer will be limited to about 16.6°, which corresponds to $\eta = 1.04$. This is a small correction, but it is included here for the sake of generality.

$$\tau_n = \left(\frac{1}{\tau_b} + \alpha_n^2 D\right)^{-1} \tag{3.28}$$

It will be shown in this section that the lifetime that is measured experimentally is the first term of this series, τ_1, which will just be referred to as the *effective lifetime* in this work. The equation for the effective lifetime is:

$$\tau = \left(\frac{1}{\tau_b} + \alpha_1^2 D\right)^{-1} \tag{3.29}$$

Note that there is no dependence on z in Equation (3.24) because this dependence is averaged out by integrating over the thickness of the wafer. It is useful to do this because it is only the average carrier density that is accessible experimentally, not the spatially resolved carrier density[13]. Equation (3.24) is computed assuming that the temporal profile of the optical generation of carriers $g(z,t)$ is an impulse response function (*i.e.* it has a Dirac-Delta shape in time). The general solution for an arbitrary $g(z,t)$ is given by the convolution over the impulse response solution. The impulse-response solution given by Equation (3.24) is valid for studies where the free-carriers are excited by a pulsed laser with pulse width $\ll \tau$, since this approximates a Dirac-Delta shape. This is how lifetime is measured in time-domain free-carrier pump/probe. In this work I perform measurements in the frequency domain. In this case the generation rate is harmonically varying in time, and it is the complex amplitude of the free-carrier density $N(\omega)$ that is measured. Converting $n(t)$ to the frequency domain and writing in terms of $\mathfrak{T}$ (Appendix A) yields:

---

[13] The spatial profile of the excess carrier may be accessed experimentally with other techniques such as ellipsometry [82].

$$\mathfrak{T} = \frac{8\alpha\eta e^{-\frac{\alpha\eta W}{2}}}{1 - e^{-\alpha\eta W}} \sum_{n=1}^{\infty} \frac{\tau_n}{1 + i\omega\tau_n} A_n^{lc} \tag{3.30}$$

At first glance Equation (3.30) appears very complicated, but it is actually easy to understand in terms of the simple case stated in (3.20). Equation (3.20) shows that the frequency dependence of the free-carrier complex amplitude is of the form $\tau/(1 + i\omega\tau)$, which is a single Lorentzian roll-off curve. Equation (3.30) takes on a similar form, but now there are multiple roll-off terms instead of one. These higher order roll-offs represent the higher order decay modes of $n(t)$, which are due to diffusion of free-carriers to the surface and their recombination there. In practice, the first term is usually much larger than higher order terms and the total decay is effectively a single roll-off parameterized by τ as given by Equation (3.29). Equation (3.30) is useful because it clearly shows how the general case of both bulk and surface recombination differs from the simple case of bulk recombination only, namely that the solution is now a summation of Lorentzians instead of just a single one.

For the purposes of calculation, this formulation can be problematic because of the transcendental roots α_n. I have derived an alternative form of Equation (3.30) in Appendix B which is completely closed-form. This equation is an elegant algebraic simplification of the solution presented by Sanii [8] that reduces a very complex equation to a much simpler form. This equation, which is completely equivalent to (3.30) is given by:

$$\mathfrak{T} = \frac{L^2}{D((\alpha\eta)^2 L^2 - 1)} \left[\frac{\mu + \coth\frac{\alpha\eta W}{2}}{\nu + \coth\frac{W}{2L}} \alpha\eta L - 1 \right] \tag{3.31}$$

where L is the *effective diffusion length*, D is the diffusion coefficient, α is the absorption coefficient, and $\mu \,\&\, \nu$ are dimensionless parameters. $L, \mu \,\&\, \nu$ are given by:

$$L = \sqrt{\frac{D\tau_b}{1 + i\omega\tau_b}} \tag{3.32}$$

$$\mu = \frac{\alpha\eta D}{S} \tag{3.33}$$

$$\nu = \frac{D}{LS} \tag{3.34}$$

where S is the surface recombination velocity of the front and rear surface, and ω is the angular modulation frequency.
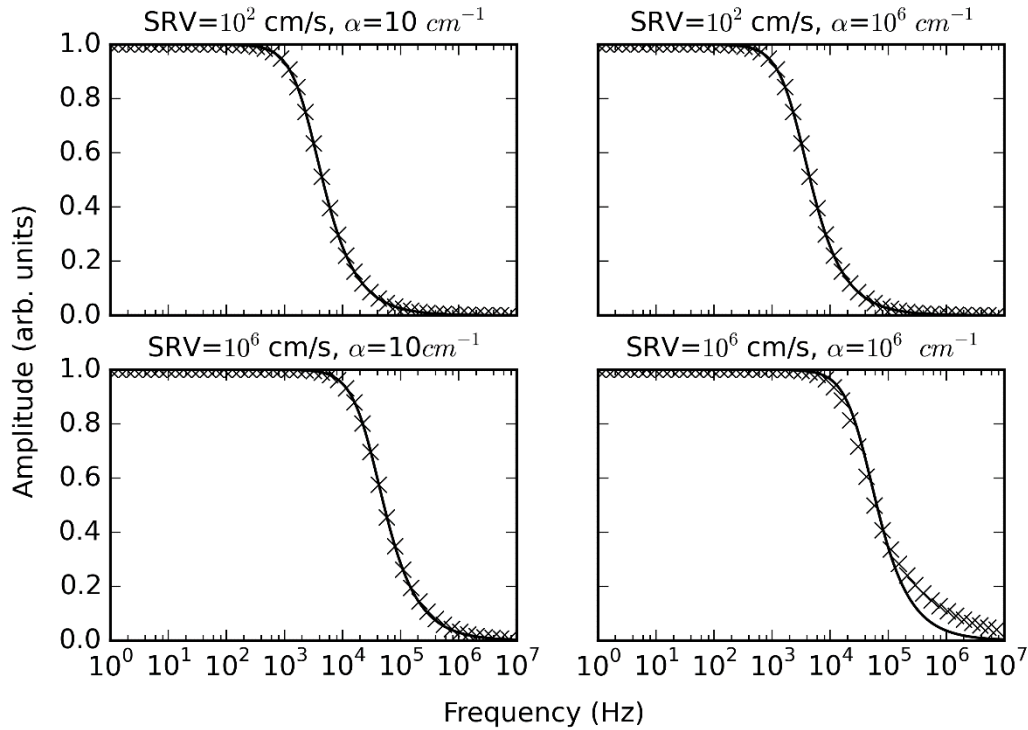
Figure 3.6: Plot of Equation (3.31) vs frequency ('x' markers) and a fit to Equation (3.20) (solid-line) for various combinations of surface recombination velocity and absorption coefficient

To demonstrate how the exact solution for the frequency-domain free-carrier concentration (Equation (3.30) or (3.31)) differs from simplified solution in (3.20), I compare the two for various surface recombination velocities and absorption coefficients in Figure 3.6. For this comparison I have chosen $\tau_b = 100$ µs, $W = 300$ µm, and $D = 16$ cm^2/s, which are reasonable values for a silicon wafer. The absorption coefficient α and the SRV are varied between low and high values[14] to demonstrate how surface recombination affects the shape of the curve. The exact solution is plotted for a particular set of parameters, and then fitted to the simplified model given by Equation (3.20) to determine the effective lifetime. In all but one case the exact solution is fitted well to the

---

[14] "Low" values for α are values such that $\alpha W \sim 1$, and "high" values are $\alpha W \gg 1$. "Low" values for SRV are values where $S \sim 10^2$ cm/s which is reasonable for a passivated silicon surface. "High" values for SRV are values where $S \sim 10^6$ cm/s which is reasonable for an unpassivated silicon surface [36].

simplified model, and the fitted lifetime is consistent with the effective lifetime given by Equation (3.29). The one case where the fit does break down is when both the surface recombination velocity and absorption coefficient are high (bottom right of Figure 3.6). This behavior can be explained with reference to Equation (3.30). In the case when the absorption coefficient is small, only the first term in the series is dominant and so the frequency-dependence of the free-carrier population takes on the same form as the simplified model in (3.20). In the case where both SRV and the absorption coefficient are high, the frequency-response is perturbed from its Lorentzian shape at high frequencies. This is because higher order terms in Equation (3.30) are coming into play. The lifetime corresponding to the first term (i.e the effective lifetime) is $\tau_1 = 5.40$ μs, but the lifetime fit by the Lorentzian is $\tau = 4.34$ μs. In this case, a single Lorentzian curve does not adequately fit the exact solution. However, it should be noted that higher order terms in (3.30) only contribute to the high-frequency regions of the roll-off curve. If the fit range is restricted, better agreement between the fit and the actual effective lifetime is found. In this case, fitting from 10 Hz to 100 kHz results in $\tau = 4.86$ μs, which is closer to the true value.
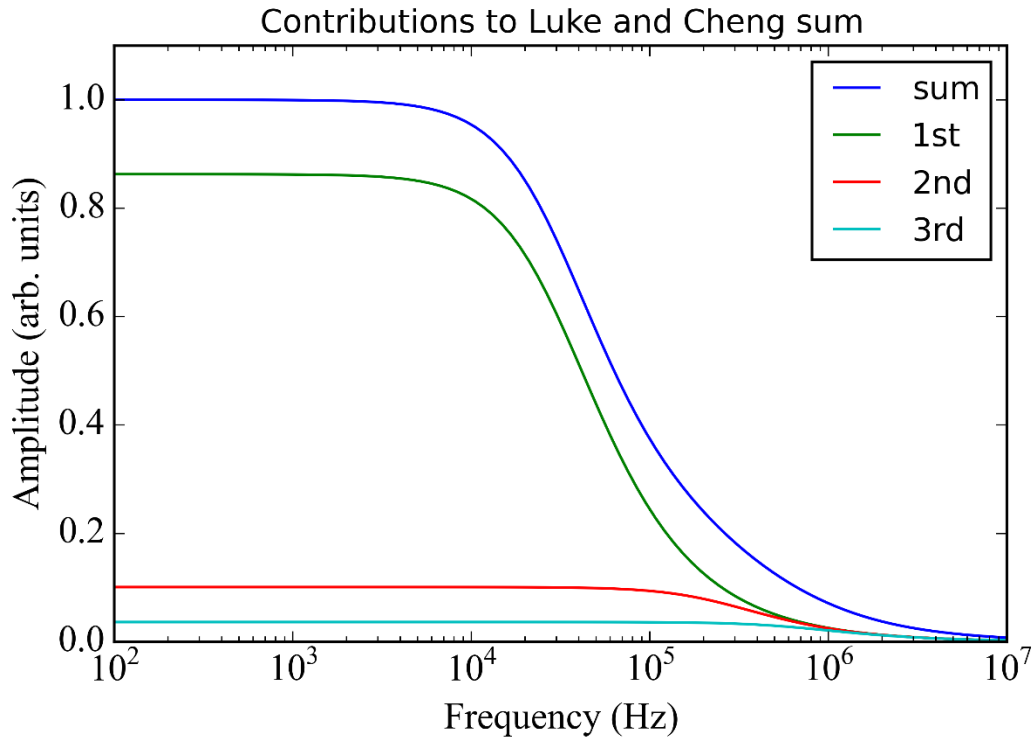
Figure 3.7: Individual Lorentzian curves that contribute to sum in Equation (3.30). The first three terms of the sum are included, as well as the total sum. The surface recombination velocity is set to $S = 10^6 \; cm/s$ and the absorption coefficient is $\alpha = 10^5 \; cm^{-1}$.

To illustrate the origin of the high frequency deviation, it is helpful to consider the contributions of the individual Lorentzians from Equation (3.30) to the overall sum. This is shown in Figure 3.7 where the first three terms and the total sum are plotted together. The first term is clearly dominant over the higher order terms. Since the higher order terms roll-off at higher frequencies, they don't contribute to the overall shape of total sum at low frequencies. This is why a fit to the exact solution in the bottom-right of Figure 3.6 yields a lifetime close to that of the first term, when the fit is restricted to low frequencies. At higher frequencies, the higher order terms contribute to the overall shape of the curve since the first order term has rolled-off, which leads to the deviation from the purely Lorentzian decay. The point of this discussion is to show that **only in the case when both the surface recombination velocity and the absorption coefficient are high** that higher order terms in (3.30) need to be considered. In all other cases, the higher order terms can be safely omitted. This is important for this work since often I will use only the first term of the series in

Equation (3.30) when performing analyses. The condition of a low absorption coefficient is met experimentally by choosing a pump source that has a relatively weak absorption coefficient. In this work I use a 1064 nm laser. This is close to the band-edge of silicon, and so the absorption coefficient is small ($\alpha = 9.85 \text{ cm}^{-1}$).
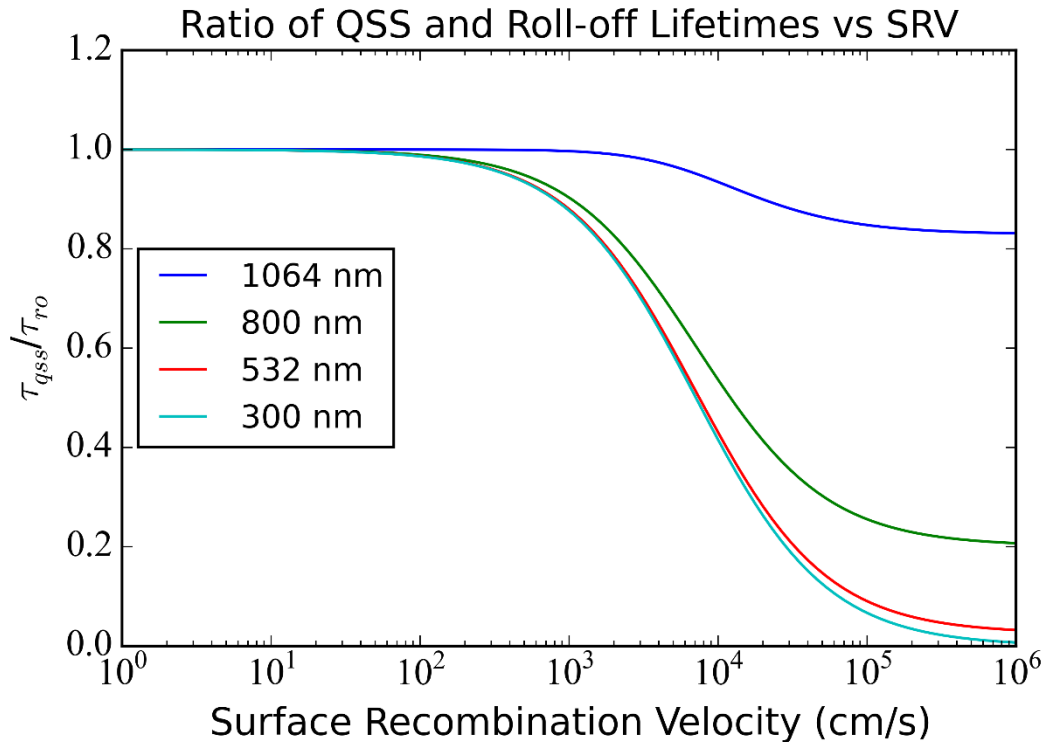
Figure 3.8: Ratio of Quasi-Steady State Lifetime to Roll-off lifetime for various absorption coefficients.

In general, the *roll-off lifetime* found by fitting $\mathfrak{T}$ to the frequency-dependence in Equation (3.20) does not correspond to the quasi-steady state lifetime when $\omega \to 0$. This can be seen in Figure 3.7 where higher order terms from Equation (3.30) don't contribute to the shape of the curve at low-frequencies, but do affect the amplitude. Figure 3.8 plots the ratio of the quasi-steady state lifetime to the lifetime found by fitting $\mathfrak{T}$ to Equation (3.20) as a function of surface recombination velocity, for various absorption coefficients. The absorption coefficients correspond to wavelengths that

range from the NIR to UV. As in Figure 3.6, $\tau_b = 100$ µs, $W = 300$ µm, $D = 16$ cm^2/s. Figure 3.8 demonstrates how the equivalence between τ_{qss} and τ depends on the surface recombination velocity and absorption coefficient. The reason for the discrepancy is in how the quantities τ_{qss} & τ emerge. τ_{qss} is proportional to the amplitude of the carrier density n (see Equation (3.16)). When the SRV is high, carriers are consumed by the surface and τ_{qss} is reduced. This effect is small when the absorption coefficient is low since carriers are generated uniformly throughout the wafer, and only carriers close to the surface are lost to surface recombination. When the absorption coefficient is high, most of the carriers are generated close to the front surface and so a significant fraction of them recombine, lowering τ_{qss}. The important takeaway from Figure 3.8 is that when the pump is weakly absorbed (the curve corresponding to 1064 nm illumination), the quasi-steady state lifetime is close to the true lifetime even when the surface recombination velocity is high. Since 1064 nm radiation is used as the pump in this work, the discrepancy between τ_{qss} and τ can be ignored.

3.3.3   Summary

This section may be summarized with the following points:

1. The lifetime that is of interest to experimenters is the bulk lifetime τ_b since it provides direct access to the material quality of the semiconductor wafer.
2. The lifetime that is measured experimentally is an effective lifetime that depends on both bulk and surface recombination.
3. Even in the presence of high surface recombination, the frequency-dependence of the free-carrier population takes on the same form as the simplified solution in Equation (3.20), so long as the absorption coefficient is low. In this work the absorption coefficient is sufficiently low that this assumption is valid.
4. The lifetime measured in quasi-steady state and that measured with the roll-off technique are only equivalent in the case of low surface recombination velocity. However, the discrepancy between the two is small when the absorption coefficient is small.

The purpose of this section is to detail that what is measured experimentally is an effective lifetime and not the true bulk lifetime. The most important result of this section is that even in the presence of surface recombination, the functional form of the frequency-response is nearly identical to the simplified case where only bulk recombination occurs. This means that the simplified model of (3.20) is sufficient for extracting the effective lifetime experimentally. The separation of the effective lifetime into its bulk and surface components is outside the scope of this work. The scope of this work is to demonstrate novel techniques for measuring the effective lifetime, and showing that it matches with the effective lifetime measured using traditional approaches.

4 Experimental Apparatus

4.1 Overview
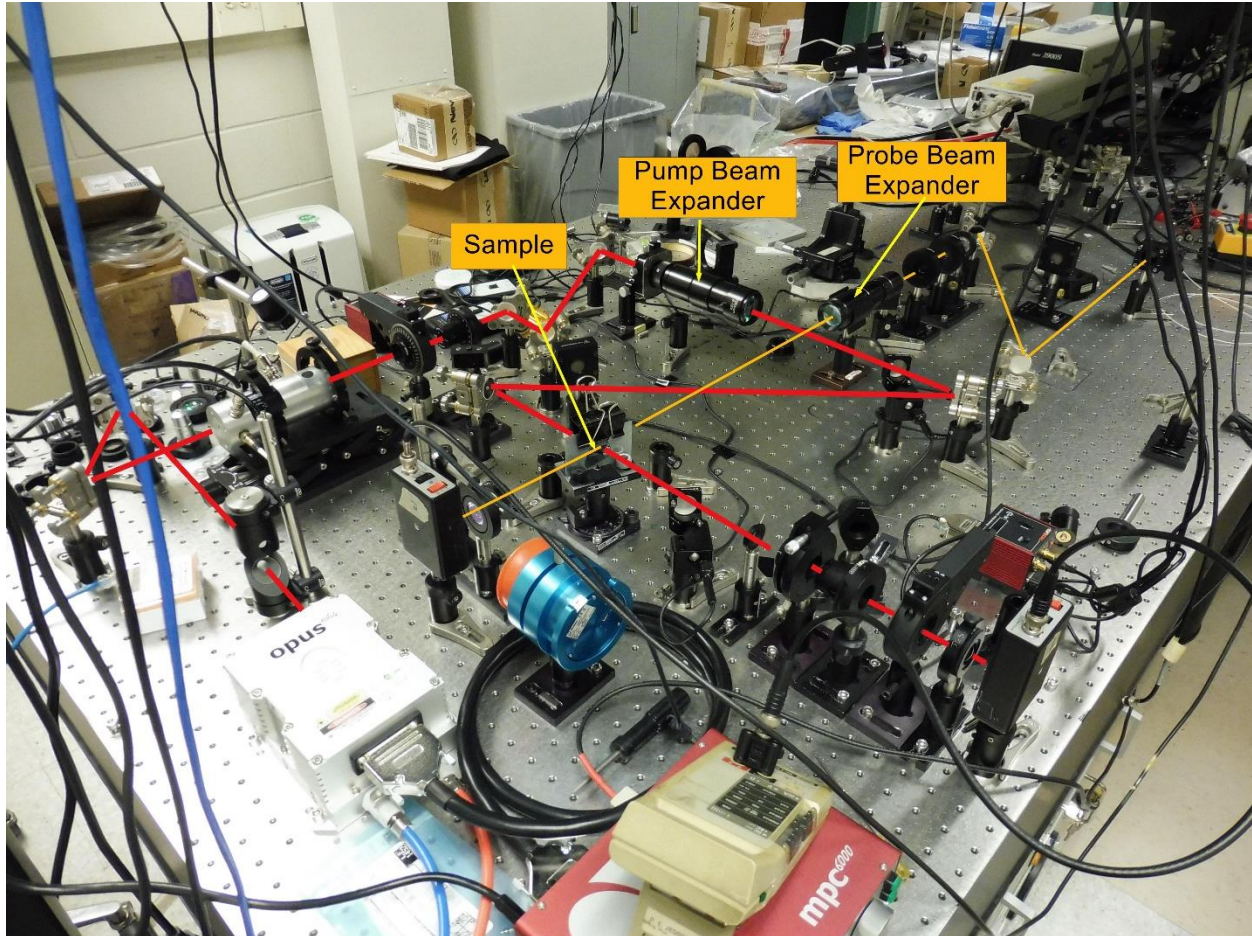
Figure 4.1: Photograph of experimental apparatus. The path of the pump beam and probe beams from source to detector is shown by red and green lines, respectively.

This work uses a generic pump/probe configuration for performing lifetime measurements. The pump laser emits 1064 nm radiation which has energy above the bandgap of silicon and thus can be used to generate free electron-hole pairs. The probe laser emits 1550 nm radiation which has energy below the bandgap of silicon, and is absorbed primarily by intraband free-carrier absorption. In both single-beam and QSS-FCA techniques, the pump and probe beam are both

utilized. The role of the probe beam in the single-beam experiment is to validate the results acquired with the single-beam technique. The experimental apparatus is shown in Figure 4.1. The red and green lines show the path of the pump and probe lasers, respectively, from source to detector. The apparatus can be broken down into three branches: Pump, Probe, and Measurement branches. The individual branches will be described in this Chapter.

4.2   Pump Branch
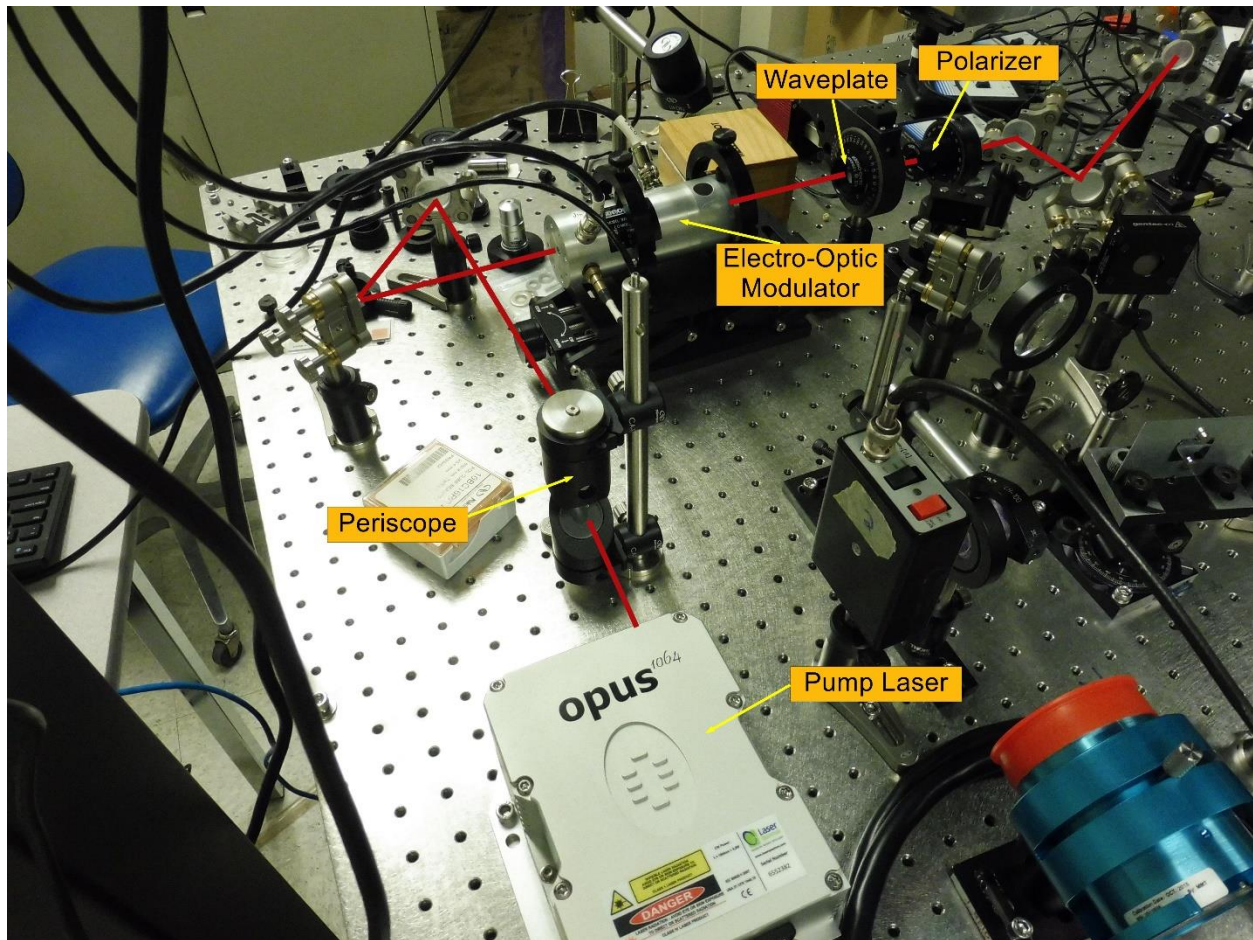
Figure 4.2: Annotated photograph of the Pump branch of the experimental apparatus. The laser beam path is shown by the red line.

The pump branch consists of the pump laser source, as well as components that modulate the laser beam, and control its size and power. Figure 4.2 shows an annotated photograph of the components

of the pump branch, with a red line denoting the path of the laser. The pump source is a Laser Quantum Opus laser emitting horizontally polarized 1064 nm radiation and capable of producing 10 W of optical power. The laser is operated at an output power of 2 W in this work. The laser is mounted to a heatsink which is maintained at 22℃ via water-cooling. The beam emitted from the pump laser is raised to a height of about 3 inches using a periscope, and is then guided through a Conoptics electro-optic modulator (EOM) using two mirrors. The EOM is a Lithium Tantalate (LTA) Pockel's cell, custom-built for 1064 nm and capable of sustaining the full 10 W of the laser. The modulator is driven by a Conoptics Model 25 A driver (not shown), which is capable of impressing an arbitrary analog signal on the laser beam in the frequency range of 0 to 25 MHz. The EOM provides pump modulation for the frequency-dependent studies of this work. The modulation signal is sinusoidal and originates from a Zurich Multi-Frequency Lock-in amplifier (MFLI). After passing through the EOM, the laser beam passes through a half-waveplate/polarizer pair. The beam is linearly polarized, and its polarization direction can be changed by rotation of the half-waveplate. The polarizer is a glan-laser calcite polarizer which is oriented to pass p-polarized light and reject s-polarized light. Rotation of the half-waveplate changes the degree of p and s polarization of the laser beam, which in conjunction with the polarizer provides the experimenter with a means of controlling the laser power. The waveplate is mounted to a motorized rotational stage which can be interfaced with a computer so that power can be controlled remotely. After emerging from the polarizer, the laser beam is guided through a Standa beam expander (shown in Figure 4.1) which can increase the diameter of the beam from 2-12x its native diameter (~1.77 mm at the sample stage). After emerging from the beam expander, the laser is guided to the sample.

4.3   Probe Branch
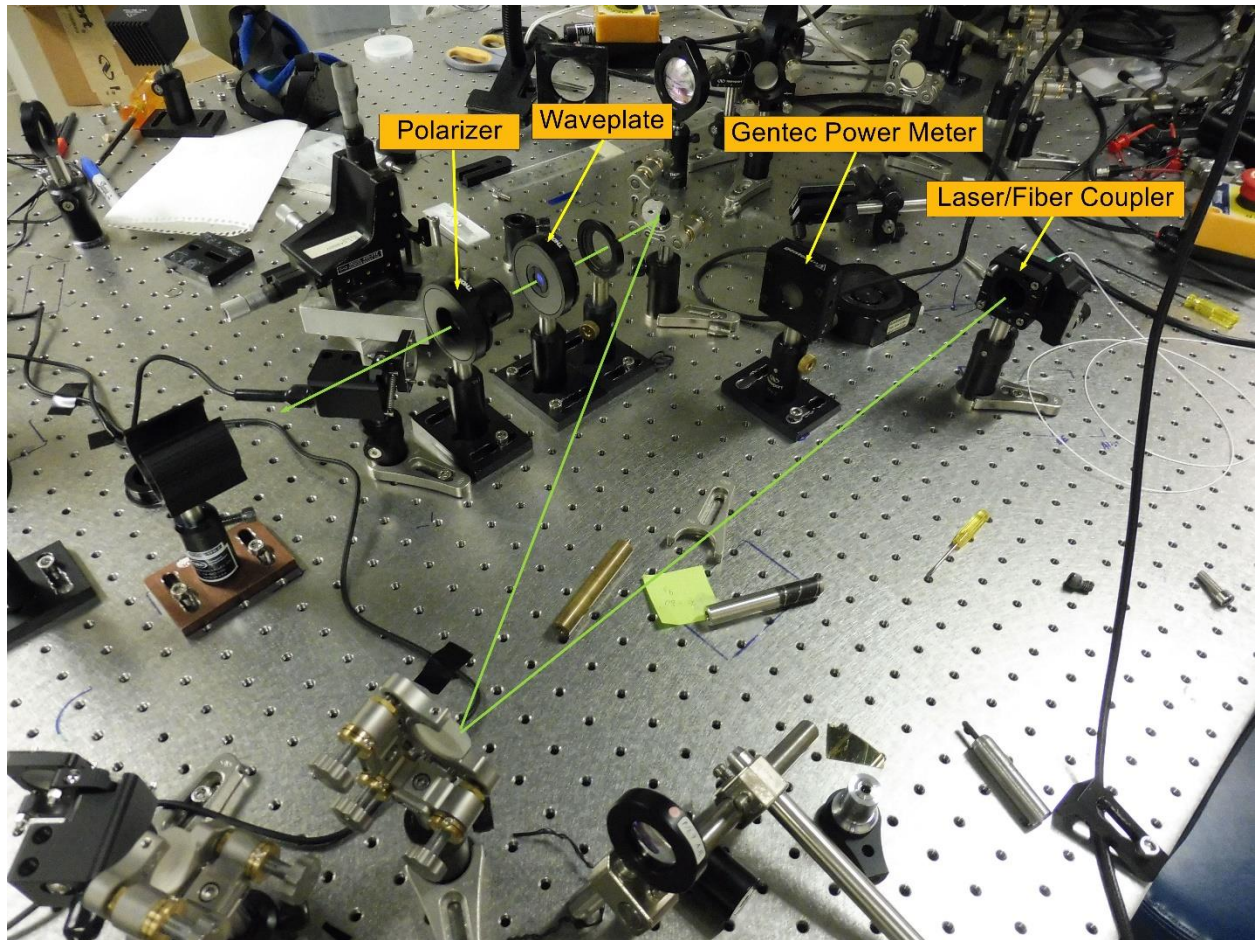
Figure 4.3: Annotated photograph showing the Probe branch of the experimental apparatus. The laser beam path is shown by the green line.

The components that comprise the probe branch are shown in Figure 4.3 with the beam path denoted by the green line. The probe laser is a Thorlabs fiber optic laser emitting at 1550 nm, driven by a constant current source. The laser is capable of producing 100 mW of optical power, though it is usually operated at about a quarter of the full output. Since the laser is not equipped with a power feedback diode, it is operated in constant current mode. The end of the fiber is attached to fiber-coupling optics which collimate the beam. The laser is then guided through a half-waveplate/polarizer pair for power control. The half-waveplate is a superachromatic

waveplate which is designed to operate over a broad range of wavelengths, including 1550 nm. The polarizer is a glan-laser calcite polarizer, oriented to reject s-polarized light and pass p-polarized light. After the half-waveplate/polarizer, the laser is either expanded to a large diameter with a beam-expander (shown in Figure 4.1) or focused to a small diameter with a lens. The size of the pump and probe beams with respect to one another is set by the experimental study being carried out.

4.4   Measurement Branch
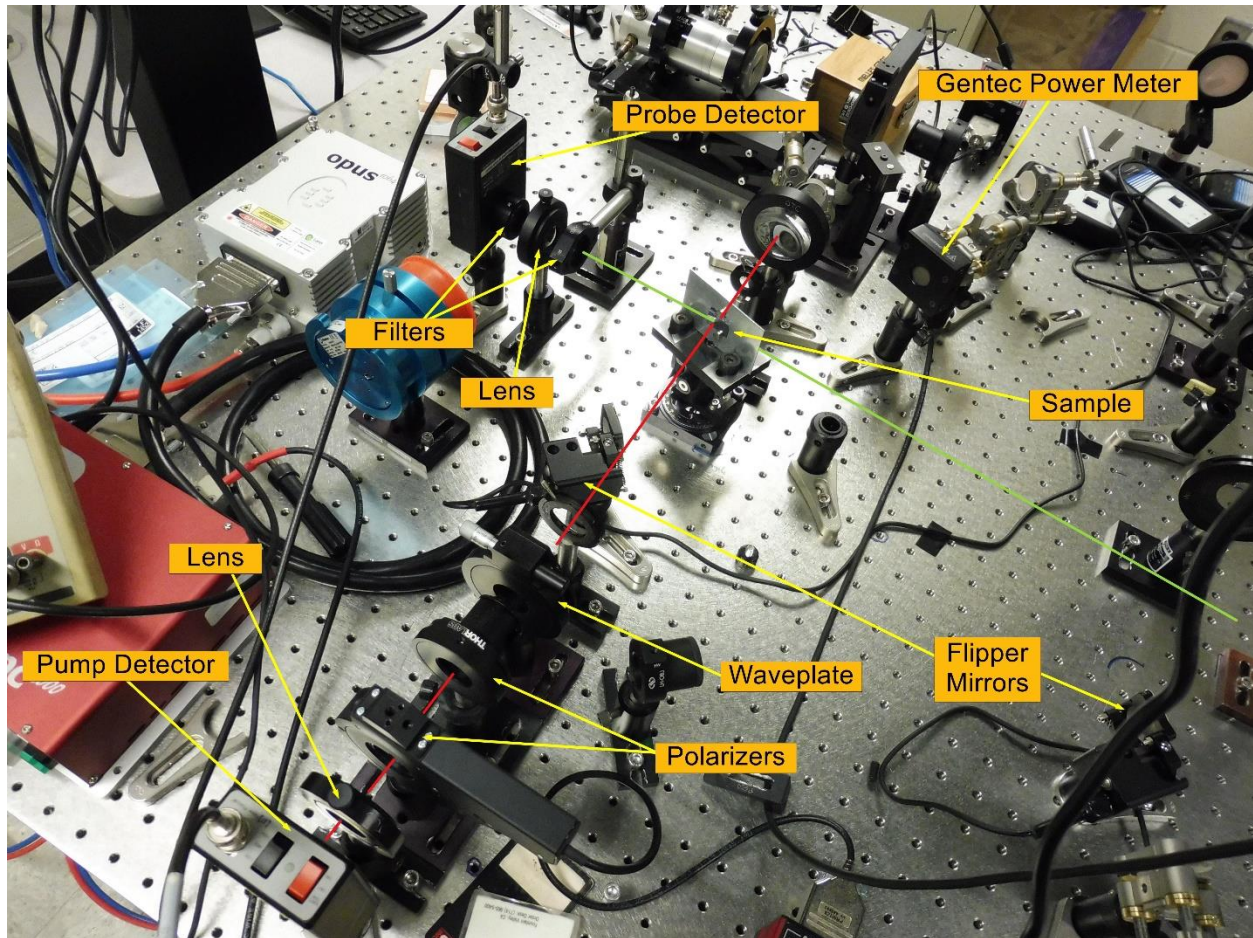
Figure 4.4: Annotated photograph showing the Measurement branch of the experimental apparatus. The beam paths of the pump and probe lasers are denoted by red and green lines, respectively.

The Measurement branch is shown in Figure 4.4. The detection branch consists of the sample stage, separate photodetectors for measuring the pump and probe beam signals, calibrated power meters for quantifying the absolute power of the pump laser and a lock-in amplifier (not shown) for demodulation of the pump and probe signals. The silicon wafer that is under examination is mounted to the sample holder with its surface normal parallel to the table. The pump and probe beams illuminate the sample on the same side, and propagate orthogonal to one another. The sample holder is rotated so that the angle of incidence for the pump and probe beams is 15° & 75°, respectively. The 75° angle of incidence is approximately Brewster's angle for the probe laser. Since the probe laser is p-polarized, illuminating the sample at Brewster's angle ensures negligible reflection of the probe laser from the silicon wafer. The pump and probe beams transmit through the silicon wafer and are collected by their respective photodetectors. Both photodetectors are Newport Model 2033 Germanium photodiodes with built-in transimpedance amplifiers. The amplifiers have variable gain, which are set to 2000x in this experiment. At this setting the detectors have a bandwidth of 200 kHz which is sufficient for all experiments in this work. For each detector, a lens is used to focus the beam into the photodiode. The probe detector is outfitted with a 1550 nm bandpass filter to reject stray 1064 nm pump light from entering and corrupting the probe signal. The filter does pass some 1064 nm light so a second long pass filter is installed before the lens to further suppress stray pump light. The pump detector is preceded by a half-waveplate/polarizer pair[15] to control the power into the detector. This is necessary because the detector saturates at about 10 mW of optical power, and the pump power often exceeds 100 mW in these experiments. The power into the probe detector is set by the waveplate/polarizer pair in the Probe Branch. The signal from the pump or probe detector is fed into a lock-in amplifier using a BNC cable.

---

[15] There is a second polarizer after the half-waveplate/polarizer, which is configured to pass the pump light. It does not have a functional purpose for the studies in this work.

The incident, reflected, and transmitted power of the pump beam are measured by Gentec calibrated power meters. The power meter shown in Figure 4.4 collects the beam that reflects from the silicon sample. To collect the incident power and the power transmitted through the silicon wafer, the laser beam has to be disrupted. Two flipper mirrors placed into the path of the incident and transmitted beams can be toggled to guide the laser into a power meter. The power meter that measures the incident and transmitted beams is shown in Figure 4.3.

4.5   Experimental Methodology

Both of the techniques that I have developed in this work have a similar experimental methodology, which is discussed here. The main practical difference between the two is that in single-beam pump/probe experiments both the signal from the 1064 nm pump laser and the signal from the 1550 nm probe laser are collected. The former signal contains single-beam pump/probe data, while the latter signal contains dual-beam pump/probe data used to verify the single-beam results. In QSS-FCA experiments, only the probe signal is required so the pump is ignored. In both techniques the experimentally measured quantity is the amplitude and phase of the pump or probe beam collected by the photodetector. This information is acquired on a lock-in amplifier.

The first step after turning on the equipment is to modulate the pump beam. A DC-coupled sine wave is outputted from a Zurich Multi-Frequency Lock-in amplifier (MFLI) and inputted into a Conoptics Model 25A Driver. The Model 25A amplifies the signal and drives the Pockel's cell of the EOM which modulates the pump laser. The average power that is output from the EOM is set by the DC bias on the Model 25A driver. The signal from the pump detector is fed into the Zurich MFLI input channel. The input channel is AC-coupled since the DC component of the signal is not required. The power into the pump detector is controlled so that the amplitude of the pump signal demodulated by the lock-in amplifier is about 0.400 Vrms. For both single-beam pump/probe and QSS-FCA experiments, the amplitude and phase of the signal is collected as a function of pump modulation frequency. The frequency is swept from about 100 Hz-100 kHz in logarithmically spaced steps. The Sweeper module on the Zurich MFLI provides a fast and efficient way of collecting the signal amplitude and phase as a function of modulation frequency.

When collecting the 1550 nm probe signal, the time constant is set to a long time (100-1000 ms) to suppress random noise, and a single frequency spectrum is acquired. When collecting single-beam data, the demodulation time constant on the lock-in is set to a short time (1-10 ms) and several frequency spectra are collected rapidly and then averaged. The reasoning behind this unconventional method of data collection will be discussed later in Chapter 6.4. Prior to collecting frequency spectra from the pump or the probe, the pump power that is incident upon the sample and reflected and transmitted through it is measured. The reflected power is measured *in situ*, whereas the incident and transmitted powers are measured by disrupting the path of the pump laser and guiding it into a power meter using flipper mirrors.

The experimental setup is almost entirely automated, and controlled via a custom instrument control Application Programming Interface (API) I wrote in the Python programming language. This API gives an experimenter complete control over laboratory instruments that interface with GPIB and USB connections. Control of laser power, modulation amplitude and frequency, positioning of flipper mirrors, and data acquisition all occur remotely and automatically. Switching in new samples, and changing and measuring the area of the pump and probe beams is the only part of the experiment that requires human intervention. Beam profiles for the pump and probe are measured on the Nanoscan beam profiler. These profiles, shown in Appendix K, confirm a Gaussian distribution of laser power and allow for the extraction of the beam radius for quantitative calculations.

4.6   Sample Specifications

Table I: Specifications of Silicon Wafers Used in This Study

Wafer ID	Thickness (μm)	Resistivity (Ω cm)	Doping Density (cm^{-3})	Surface
El-Cat 2_9	325 ± 2	$1 - 10$	3.2×10^{15}	Thermal Oxide (100 nm)
Thick Wafer	1470 ± 2	$1 - 5$	4.51×10^{14}	Native Oxide

Two n-type (phosphorus-doped) monocrystalline silicon wafers are examined in this study. The wafer specifications are shown in Table I. The thinner wafer is FZ grown while the thicker wafer is CZ silicon. Both wafers are double-side polished.

5 Generalized Semiconductor Pump/Probe Equation

5.1 Overview

In this chapter I will develop a generalized pump/probe equation to describe the signal measured in a generic pump/probe experiment on a semiconductor wafer. This general model will be used to derive the models describing the single-beam pump/probe and QSS-FCA techniques, which are special cases of the general model. The general model is derived from an equation that describes the free-carrier density $n(r, z, t)$ as a function of radial (r) and axial (z) position, and time (t). The equation for $n(r, z, t)$ provides a general description of free-carrier transport and recombination in a semiconductor for an arbitrary set of wafer parameters.

5.2 Mathematical Model of 3D Diffusion and Recombination

In Chapter 3, I reviewed the 1D solution to the free-carrier continuity equation in both the time (Equation (3.24)) and frequency (Equation (3.30)) domain. These relationships account for the optical generation, 1-D transport and recombination of excess electrons in a semiconductor. Being a 1-dimensional solution, the equations only account for movement of electrons along the axial-axis of the wafer; lateral diffusion in the plane of the wafer is neglected. This analysis is valid for pump/probe studies where the pump beam is much larger than the probe, or the probe beam is much larger than the pump. In the case where the probe illuminates the centre of a much larger pump, the area being probed is under a uniform excitation where concentration gradients (and thus diffusion effects) are negligible. When the probe beam is much larger than the pump, diffusion of carriers does not affect the signal since carries cannot escape the volume of the probe beam. When the pump and probe are comparable in size and that size is comparable to the free-carrier diffusion length $\sqrt{D\tau}$ of the semiconductor, then diffusion must be accounted for. This consideration is especially important for single-beam pump/probe studies since the pump and probe beam sizes cannot be varied independently of one another. The derivation of $n(r, z, t)$ is lengthy so I have relegated it to Appendix C. The derivation results in the following equation:

$$n(r,z,t) = e^{-\frac{t}{\tau_b}} \frac{1}{\frac{t}{\tau_D}+1} e^{\frac{-2r^2}{w^2\left(\frac{t}{\tau_D}+1\right)}} \sum_n \left[A_n^{ax} e^{-\alpha_n^2 Dt} \cos\alpha_n z + B_n^{ax} e^{-\beta_n^2 Dt} \sin\beta_n z\right] \tag{5.1}$$

Equation (5.1) is a general description of free-carrier transport in a semiconductor under a Gaussian-shaped excitation beam. The solution is derived by assuming an optical generation rate that is a Dirac-Delta function in time. To compute the solution for an arbitrary temporal profile, (5.1) must be convolved over the profile. For a harmonic excitation of angular frequency ω, this convolution takes the form:

$$n_\omega(r,z,t) = \int_0^t n(r,z,t-\tau)\left(1+me^{i\omega\tau}\right)d\tau \tag{5.2}$$

where n_ω is the excess carrier density for a harmonically varying optical generation rate. The term $\left(1+me^{i\omega\tau}\right)$ describes this optical generation. Here m is the *modulation depth* of the pump which is real number between 0 and 1 that describes the magnitude of the excitation's AC component relative to the DC component. Since $0 \le m \le 1$, the magnitude of $\left(1+me^{i\omega\tau}\right)$ is always greater than 0. This condition is necessary since optical generation can only add free-carriers, it cannot remove them[16]. The integral starts at 0 since $n(r,z,t) = 0$ for $t < 0$. In the limit of long t, the time-dependence of n_ω will be purely harmonic and the convolution ranges from 0 to infinity. A convolution in the time domain is just a multiplication in the frequency domain, so:

---

[16] Technically optical excitation can remove free-carriers via simulated emission, but this effect isn't present in this work.

$$N_\omega(r, z, \omega') = N(r, z, \omega')\big(\delta(\omega') + m\delta(\omega' - \omega)\big) \tag{5.3}$$

where δ are Dirac-Delta functions, $N_\omega(r, z, \omega')$ is the Fourier transform of n_ω, and $N(r, z, \omega')$ is the Fourier transform of n (Equation (5.1)). According to Equation (5.3) the frequency domain representation of n_ω consists of a DC component (*i.e.* $\omega' = 0$) and an AC component (*i.e.* $\omega' = \omega$) at ω. This makes sense since the optical generation rate consists of a DC light level with a harmonically varying ripple superimposed on top of it. Using this information, n_ω can be written in terms $N(r, z, \omega)$:

$$n_\omega(r, z, t) = N(r, z, 0) + mN(r, z, \omega)e^{i\omega t} \tag{5.4}$$

5.3   Generalized Theory of Semiconductor Pump/Probe Experiments
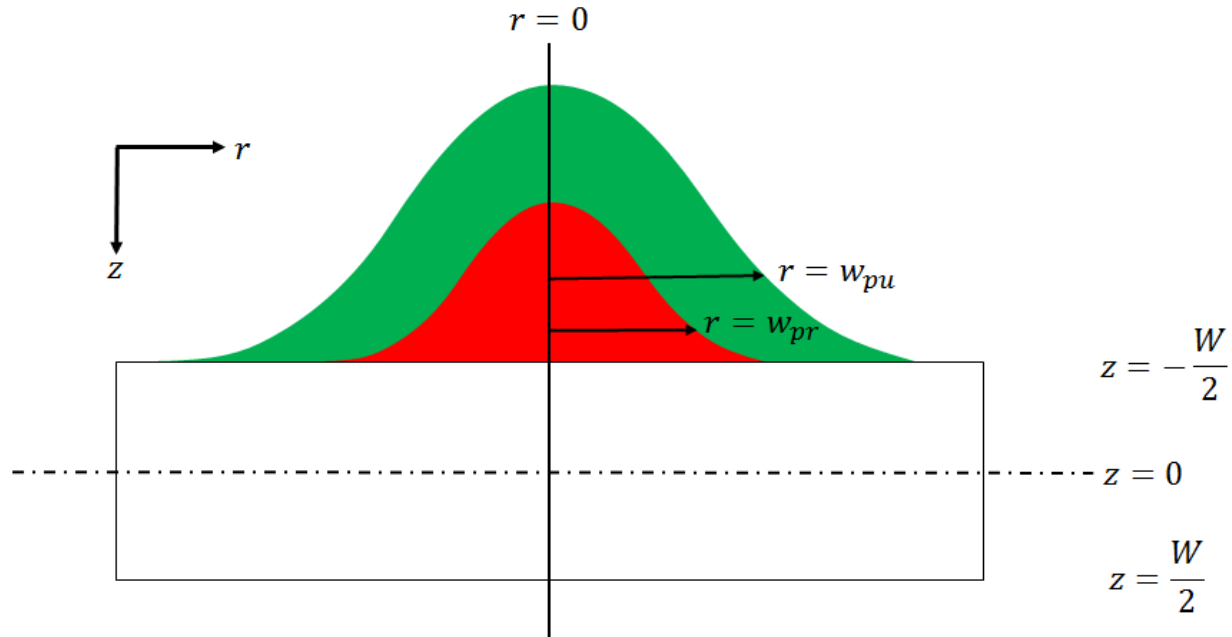
Figure 5.1: Cylindrical Coordinate System for Pump/Probe Experiment. Green and red Gaussian curves correspond to pump and probe beams, respectively. The coordinate system is centered at the center of a wafer of thickness W. The r coordinate describes the plane of the wafer and the z coordinate describes the axis.

In this section I will derive a generalized equation to describe pump/probe experiments in a semiconductor. This analysis is very general, making no assumptions about the semiconductor's thickness, bulk lifetime, surface recombination velocity, or diffusion coefficient, except that they remain constant. In addition to this, the angle of incidence, incident power, wavelength, and beam radius for both pump and probe are kept general. Perhaps the biggest assumption that is made is that the reflection and transmission from the front and back side of the semiconductor is specular, instead of diffuse. Physically this means that the semiconductor under study is double-side polished, which is the case for the wafers examined in this work. Diffusely reflecting surfaces will scatter the incident light over a range of angles. The angle of propagation inside the wafer sets the pathlength the light travels through, with longer paths experiencing a greater amount of FCA. Modelling the signal that is expected in this case requires a more general mathematical treatment, which is beyond the scope of this work. Figure 5.1 shows the cylindrical coordinate system that is

used to develop the general equation. Two Gaussian laser beams are overlapped on the same side of a silicon wafer of thickness W, with their peaks positioned at $r = 0$. Green and red Gaussian curves correspond to the pump and probe beams, respectively. Beam radii w_{pu} & w_{pr} are defined by the point where the laser power drops to $1/e^2$ of the peak power. The radial coordinate r describes the plane of the wafer, while the axial coordinate z corresponds to the thickness-axis of the wafer. The coordinate system is centred at the centre of the wafer.

In the first stage of this derivation, I derive the general expression for the transmission of the probe beam through the semiconductor wafer in the presence of an arbitrary absorption factor and non-zero surface reflectance. Consider a monochromatic laser beam of power P_{pr} hitting a semiconductor surface with an interfacial reflectance coefficient of R_{pr}. The subscript pr indicates that this beam is the *probe* beam. In general, P_{pr} may depend on time. If the absorption factor for a single pass through the laser is given by $e^{-\eta\beta}$, then the total power that transmits through the wafer is given by (Appendix I):

$$P_{tr} = \frac{T_{pr}^2}{1 - R_{pr}^2 e^{-2\eta_{pr}\beta}} P_{pr}\, e^{-\eta_{pr}\beta} \tag{5.5}$$

where $T = 1 - R$ is the interfacial transmission coefficient. η is a factor equal to the single-pass pathlength of the laser through the wafer divided by the wafer thickness. The factor η is the relative increase in pathlength due to an oblique angle of propagation through the wafer. η is given by:

$$\eta_{pr} = \sec\theta_{pr} \tag{5.6}$$

where θ_{pr} is the angle of propagation inside of the wafer. β is a factor describing the attenuation of the laser beam through the wafer. The origin of absorption is either band-to-band or free-carrier

70

absorption. Writing $\beta = \beta_{bb} + \beta_{FCA}$, where β_{bb} & β_{FCA} are the band-to-band and FCA components, respectively. Equation (5.5) becomes:

$$P_{tr} = \frac{T_{pr}^2}{1 - R_{pr}^2 e^{-2\eta_{pr}\beta_{bb}} e^{-2\eta_{pr}\beta_{FCA}}} P_{pr} e^{-\eta_{pr}\beta_{bb}} e^{-\eta_{pr}\beta_{FCA}} \tag{5.7}$$

The band-to-band absorption factor is given by the product of the band-to-band absorption coefficient α and the wafer thickness W:

$$\beta_{bb} = \alpha_{pr} W \tag{5.8}$$

The first assumption that is made is that β_{FCA} is sufficiently small that $e^{-\beta_{FCA}}$ may be approximated as a first order Taylor expansion[17]. Doing this, it can be shown (Appendix J) that (5.7) becomes:

$$P_{tr} = \frac{T_{pr}^2}{1 - R_{pr}'^2} P_{pr}'\left(1 - \Re_{pr}\eta_{pr}\beta_{FCA}\right) \tag{5.9}$$

where P' and R' are the effective incident powers and reflectance coefficients, respectively, and $\Re$ is the multiple-reflection correction factor. These are given by:

---

[17] In this work $\beta_{FCA} \sim 10^{-3}$ so a first-order Taylor approximate of $e^{-\beta_{FCA}}$ is valid.

$$P' = Pe^{-\eta\beta_{bb}} \tag{5.10}$$

$$R' = Re^{-\eta\beta_{bb}} \tag{5.11}$$

$$\mathfrak{R} = \frac{1 + R'^2}{1 - R'^2} \tag{5.12}$$

Equation (5.9) can be generalized to include the variation of the power as a function of radial position from the center of illumination. If the laser beam is Gaussian in shape with a radius of w_{pr} and incident power P_0, then the differential power in an area element $2\pi r dr$ is given by $\frac{2P_0}{\pi w_{pr}^2} e^{-\frac{2r^2}{w_{pr}^2}} 2\pi r dr$. Therefore the total probe power that transmits through the wafer is given by

$$P_{tr} = \int_0^\infty \frac{T_{pr}^2}{1 - R_{pr}'^2} \frac{2P_{pr}'}{\pi w_{pr}^2} e^{-\frac{2r^2}{w_{pr}^2}} \left(1 - \mathfrak{R}_{pr}\eta_{pr}\beta_{FCA}\right)(2\pi r dr) \tag{5.13}$$

Equation (5.13) is a general description of a Gaussian probe beam passing through a wafer, which accounts for the surface reflection of the beam, and its attenuation due to both band-to-band and free-carrier absorption. The origin of free-carriers is due to both the background doping of the wafer, and due to the free-carriers excited by the pump beam.

The factor β_{FCA} is given by:

$$\beta_{FCA} = (\sigma_{FCA,e} N_e + \sigma_{FCA,p} N_h)W + \sigma_{FCA,e} \int_{-\frac{W}{2}}^{\frac{W}{2}} n_\omega(r,z,t)dz \tag{5.14}$$

$$+ \sigma_{FCA,h} \int_{-\frac{W}{2}}^{\frac{W}{2}} p_\omega(r,z,t)dz$$

where $\sigma_{FCA,e}$ & $\sigma_{FCA,h}$ are the individual FCA cross sections for electrons and holes, respectively, and N_e & N_h are the thermal equilibrium concentrations of electrons and holes in the semiconductor, respectively. W is the wafer thickness, and $n_\omega(r,z,t)$ & $p_\omega(r,z,t)$ are the electron and hole concentrations in excess of the thermal equilibrium values, respectively. The excess carrier densities are assumed to vary harmonically in time. The first bracketed term is the FCA component due to intrinsic free-carriers and free-carriers that originate from donors and acceptors. The remaining terms are due to excess carriers generated by optical excitation. Since these carriers are generated in a one-to-one ratio, $n_\omega(r,z,t) = p_\omega(r,z,t)$ and thus (5.14) can be written in terms of just $n_\omega(r,z,t)$:

$$\beta_{FCA} = \beta_{FCA,0} + \sigma_{FCA} \int_{-\frac{W}{2}}^{\frac{W}{2}} n_\omega(r,z,t)dz \tag{5.15}$$

where σ_{FCA} is the total FCA cross section due to electrons and holes, $\beta_{FCA,0}$ is just the FCA factor due to the equilibrium concentration of carriers. Substituting in the expression for n_ω (Equation (5.4)):

$$\beta_{FCA} = \beta_{FCA,0} + \sigma_{FCA} \int_{-\frac{W}{2}}^{\frac{W}{2}} [N(r,z,0) + m_{pu} N(r,z,\omega)e^{i\omega t}]dz \tag{5.16}$$

$$\beta_{FCA} = \left[\beta_{FCA,0} + \sigma_{FCA}\int_{-\frac{W}{2}}^{\frac{W}{2}} N(r,z,0)dz\right] + \sigma_{FCA}m_{pu}e^{i\omega_{pu}t}\int_{-\frac{W}{2}}^{\frac{W}{2}} N(r,z,\omega)dz \qquad (5.17)$$

where m_{pu} is the modulation depth of the pump beam and ω_{pu} is the angular frequency of the pump excitation. Equation (5.17) can be simplified by noting that the term in square brackets is a DC term which will not be demodulated by the lock-in amplifier that is used to extract the signal. Therefore it can be dropped. Substituting (5.17) into (5.13) and dropping the DC term:

$$\tilde{P}_{tr} = \int_{0}^{\infty} \frac{T_{pr}^2}{1-R_{pr}'^2}\frac{2P_{pr}'}{\pi w_{pr}^2}e^{-\frac{2r^2}{w_{pr}^2}}\left(1\right. \qquad (5.18)$$

$$\left. - \mathfrak{R}_{pr}\eta_{pr}\sigma_{FCA}m_{pu}e^{i\omega_{pu}t}\int_{-\frac{W}{2}}^{\frac{W}{2}} N(r,z,\omega)dz\right)(2\pi rdr)$$

In Equation (5.18) I have used the symbol $\tilde{P}_{tr}$ to denote that the transmitted power is now a complex number due to the complex exponential $e^{i\omega_{pu}t}$ and $N(r,z,\omega)$ terms. All other factors in (5.18) are real numbers. The actual power that is transmitted through the wafer is obtained by taking the real part of $\tilde{P}_{tr}$ (i.e. $P_{tr} = \text{Re}[\tilde{P}_{tr}]$).

Multiply the terms with the radial dependence into the brackets:

$$\tilde{P}_{tr} = \frac{T_{pr}^2}{1 - R_{pr}'^2} \frac{2P_{pr}'}{\pi w_{pr}^2} \left(2\pi \int_0^\infty r e^{-\frac{2r^2}{w_{pr}^2}} dr \right.$$ (5.19)

$$\left. - 2\pi \Re_{pr} \eta_{pr} \sigma_{FCA} m_{pu} e^{i\omega_{pu}t} \int_{r=0}^{r=\infty} \int_{z=-\frac{W}{2}}^{z=\frac{W}{2}} r e^{-\frac{2r^2}{w_{pr}^2}} N(r,z,\omega) dz dr \right)$$

$$\tilde{P}_{tr} = \frac{T_{pr}^2}{1 - R_{pr}'^2} \frac{2P_{pr}'}{\pi w_{pr}^2} \left(\frac{\pi w_{pr}^2}{2} \right.$$ (5.20)

$$\left. - 2\pi \Re_{pr} \eta_{pr} \sigma_{FCA} m_{pu} e^{i\omega_{pu}t} \int_{r=0}^{r=\infty} \int_{z=-\frac{W}{2}}^{z=\frac{W}{2}} r e^{-\frac{2r^2}{w_{pr}^2}} N(r,z,\omega) dz dr \right)$$

By definition, $N(r,z,\omega)$ is the Fourier transform of $n(r,z,t)$:

$$\tilde{P}_{tr}$$ (5.21)

$$= \frac{T_{pr}^2}{1 - R_{pr}'^2} \frac{2P_{pr}'}{\pi w_{pr}^2} \left(\frac{\pi w_{pr}^2}{2} \right.$$

$$\left. - 2\pi \Re_{pr} \eta_{pr} \sigma_{FCA} m_{pu} e^{i\omega_{pu}t} \int_{r=0}^{r=\infty} \int_{z=-\frac{W}{2}}^{z=\frac{W}{2}} \int_{t=0}^{\infty} r e^{-\frac{2r^2}{w_{pr}^2}} n(r,z,t) e^{-i\omega t} dt \, dz dr \right)$$

Note that the Fourier transform is computed from 0 to infinity and not from negative to positive infinity. This is because $n(r,z,t) = 0$ for $t < 0$. The triple integral in (5.21) is computed in Appendix D. Substituting the result into (5.21):

$$\tilde{P}_{tr} \tag{5.22}$$

$$= \frac{T_{pr}^2}{1 - R_{pr}'^2} \frac{2P_{pr}'}{\pi w_{pr}^2} \left(\frac{\pi w_{pr}^2}{2} \right.$$

$$\left. - 2\pi \Re_{pr} \eta_{pr} \sigma_{FCA} m_{pu} e^{i\omega_{pu}t} \left[2w_{pr}^2 \tau_D g_0 \alpha \eta_{pu} e^{-\frac{\alpha \eta_{pu} W}{2}} \sum_n e^{\frac{\tau_D^{pu} + \tau_D^{pr}}{\tau_n'}} \Gamma\left(0, \frac{\tau_D^{pu} + \tau_D^{pr}}{\tau_n'} \right) A_n^{lc} \right] \right)$$

$$\tilde{P}_{tr} \tag{5.23}$$

$$= \frac{T_{pr}^2}{1 - R_{pr}'^2} \frac{2P_{pr}'}{\pi w_{pr}^2} \frac{\pi w_{pr}^2}{2} \left(1 \right.$$

$$\left. - 8\Re_{pr} \eta_{pr} \sigma_{FCA} m_{pu} e^{i\omega_{pu}t} \tau_D g_0 \alpha \eta_{pu} e^{-\frac{\alpha \eta_{pu} W}{2}} \sum_n e^{\frac{\tau_D^{pu} + \tau_D^{pr}}{\tau_n'}} \Gamma\left(0, \frac{\tau_D^{pu} + \tau_D^{pr}}{\tau_n'} \right) A_n^{lc} \right)$$

$$\tilde{P}_{tr} \tag{5.24}$$

$$= \frac{T_{pr}^2}{1 - R_{pr}'^2} P_{pr}' \left(1 \right.$$

$$\left. - 8\Re_{pr} \eta_{pr} \sigma_{FCA} m_{pu} e^{i\omega_{pu}t} \tau_D g_0 \alpha \eta_{pu} e^{-\frac{\alpha \eta_{pu} W}{2}} \sum_n e^{\frac{\tau_D^{pu} + \tau_D^{pr}}{\tau_n'}} \Gamma \left(0, \frac{\tau_D^{pu} + \tau_D^{pr}}{\tau_n'} \right) A_n^{lc} \right)$$

where τ_n' is the frequency-dependent effective lifetime factor, given by:

$$\tau_n' = \frac{\tau_n}{1 + i\omega_{pu}\tau_n} \tag{5.25}$$

And τ_D^{pu} and τ_D^{pr} are the pump and probe *diffusion time constants*, given by:

$$\tau_D^{pu(pr)} = \frac{w_{pu(pr)}^2}{8D} \tag{5.26}$$

The function Γ is the *upper incomplete gamma function*. Equation (5.24) can be reduced by bundling several terms into the 3D frequency-dependent factor ξ:

$$\tilde{P}_{tr} = \frac{T_{pr}^2}{1 - R_{pr}'^2} P_{pr}'\left(1 - 8\Re_{pr}\eta_{pr}m_{pu}\xi(\omega_{pu})e^{i\omega_{pu}t}\right) \tag{5.27}$$

where $\xi(\omega)$ is given by:

$$\xi(\omega_{pu}) = \sigma_{FCA}\tau_D^{pu}g_0\alpha\eta_{pu}e^{-\frac{\alpha_{pu}W}{2}}\sum_n e^{\frac{\tau_D^{pu}+\tau_D^{pr}}{\tau_n'}}\Gamma\left(0, \frac{\tau_D^{pu}+\tau_D^{pr}}{\tau_n'}\right)A_n^{lc} \tag{5.28}$$

To further generalize the expression for the transmitted probe power $\tilde{P}_{tr}$, I incorporate a harmonic time dependence into the probe beam. Replace P_{pr}' with $P_{pr}'(1 + m_{pr}\cos(\omega_{pr}t + \phi_{pr}))$, where ω_{pr} is the modulation frequency of the probe, m_{pr} is the modulation depth, and ϕ_{pr} is a phase term:

$$\tilde{P}_{tr} = \frac{T_{pr}^2}{1 - R_{pr}'^2} P_{pr}'(1 + m_{pr}\cos(\omega_{pr}t + \phi_{pr}))(1 \\ - 8\Re_{pr}\eta_{pr}m_{pu}\xi(\omega_{pu})e^{i\omega_{pu}t}) \tag{5.29}$$

Equation (5.29) is a general equation for pump/probe lifetime experiments in semiconductors. It can be used to predict the signal expected when the pump and probe beams have an arbitrary radius, incident power, wavelength and modulation frequency for a semiconductor sample with arbitrary surface reflectance, thickness, bulk recombination lifetime, and surface recombination velocity. The main assumptions are that the pump and probe beams are Gaussian in shape, are

centered on the same point, and that the magnitude of free-carrier absorption is small. The assumption that the pump and probe lasers are centred on the same point is necessary in order to take advantage of the radial symmetry between the profiles of the probe laser power and free-carrier distribution (see the integration over r in Appendix D, Equations (D.11) and (D.12)). The Gaussian shape is the characteristic shape of single-mode lasers, so this requirement is usually satisfied by the experimental apparatus. However, the angle of incidence on the semiconductor wafer must be shallow otherwise the projection of the beam over the surface takes on an elliptical shape and the Gaussian approximation is invalidated. The long axis of the ellipse is 10% larger than the short axis for an angle of incidence of 25 degrees. This condition is met by the 1064 nm pump laser, which illuminates the sample at 15°. The condition is violated by the 1550 nm probe laser since its angle of incidence is 75°. This is not a concern for this work since the probe laser is either expanded to a diameter much larger than the pump, or focused to a diameter much smaller than the pump. In the former case the probe laser is uniform over the free-carrier profile and so it has no radial dependence. In the latter case the probe laser illuminates a region where the free-carrier profile is uniform, so the specific distribution of the probe power is irrelevant; all that matters is the total power illuminating the region.

5.4   Special Cases of ξ factor

Appendix H derives several special cases of ξ which will be useful later on. They are summarized here. Single beam and dual beam cases are identified by subscripts 'SB' and 'DB', respectively.

Case 1: Surface Recombination Velocity equal to 0

$$\xi_{SB} = \frac{1}{8}\sigma_{FCA}\tau_D g_0 (1 - e^{-\alpha\eta W})e^{\frac{2\tau_D}{\tau'}}\Gamma\left(0, \frac{2\tau_D}{\tau'}\right) \tag{5.30}$$

$$\xi_{DB} = \frac{1}{8}\sigma_{FCA}\tau_D^{pu}g_0(1 - e^{-\alpha\eta_{pu}W})e^{\frac{\tau_D^{pu}+\tau_D^{pr}}{\tau'}}\Gamma\left(0,\frac{\tau_D^{pu}+\tau_D^{pr}}{\tau'}\right) \tag{5.31}$$

In Case 1 the summation over n is reduced to a single term. The frequency dependence of ξ is due to bulk recombination and radial diffusion only.

Case 2: Pump and Probe Beam Diameters large enough to neglect radial diffusion $\left((\tau_D^{pu} + \tau_D^{pr}) \gg \tau_n'\right)$

$$\xi_{SB} = \frac{1}{2}\sigma_{FCA}g_0\alpha\eta e^{-\frac{\alpha\eta W}{2}}\sum_n \frac{\tau_n}{1 + i\omega\tau_n}A_n^{lc} \tag{5.32}$$

$$\xi_{DB} = \begin{cases} \frac{\tau_D^{pu}}{\tau_D^{pr}}\sigma_{FCA}g_0\alpha\eta_{pu}e^{-\frac{\alpha\eta_{pu}W}{2}}\sum_n \frac{\tau_n}{1 + i\omega\tau_n}A_n^{lc}, & \tau_D^{pr} \gg \tau_D^{pu} \\[2em] \sigma_{FCA}g_0\alpha\eta_{pu}e^{-\frac{\alpha\eta_{pu}W}{2}}\sum_n \frac{\tau_n}{1 + i\omega\tau_n}A_n^{lc}, & \tau_D^{pu} \gg \tau_D^{pr} \end{cases} \tag{5.33}$$

In Case 2, the terms that carry the radial diffusion effect are removed and the frequency dependence of ξ takes on the same form as the simple 1D continuity equation (Equation (3.30)). To understand this it is helpful to reformulate the $\left(\tau_D^{pu} + \tau_D^{pr}\right)/\tau_n'$ term in terms of the free-carrier diffusion length L_n. Substituting in the values for $\tau^{pu} \& \tau^{pr}$ (Equation (5.26)) and setting the modulation frequency ω to 0 ($\tau_n' \to \tau_n$):

$$\frac{\tau^{pu} + \tau^{pr}}{\tau_n} = \frac{w_{pu}^2 + w_{pr}^2}{8L_n^2} \tag{5.34}$$

The free-carrier diffusion length is the average distance free-carriers travel before recombining. From Equation (5.34) it can be seen that when $\left(\tau_D^{pu} + \tau_D^{pr}\right) \gg \tau_n'$, the pump and probe beam diameters are much larger than the diffusion length of free-carriers. If the pump beam is much larger than the diffusion length, then the free-carrier profile generated by the pump is unperturbed by diffusion effects over time (or frequency). When the probe beam is much larger than the diffusion length, its power is changing slowly with respect to diffusion along the radial axis of the beam. In this case, the carriers cannot diffuse out of the area covered by the probe beam and escape detection. In this work the dual-beam pump/probe is configured either so $\tau^{pu} \gg \tau^{pr}$ or $\tau^{pr} \gg \tau^{pu}$. The frequency-dependence is the same regardless, but there is a difference in prefactor. Both cases are listed in Equation (5.33).

Case 3: Surface recombination velocity goes to 0 and pump or probe beam large enough to neglect radial diffusion $\left(\left(\tau_D^{pu} + \tau_D^{pr}\right) \gg \tau_n'\right)$

$$\xi_{SB} = \frac{1}{16} \sigma_{FCA} g_0 (1 - e^{-\alpha \eta W}) \frac{\tau}{1 + i\omega\tau} \tag{5.35}$$

$$\xi_{DB} = \begin{cases} \dfrac{1}{8}\dfrac{\tau_D^{pu}}{\tau_D^{pr}}\sigma_{FCA}g_0(1 - e^{-\alpha\eta_{pu}W})\dfrac{\tau}{1 + i\omega\tau}, \tau_D^{pr} \gg \tau_D^{pu} \\[2ex] \dfrac{1}{8}\sigma_{FCA}g_0(1 - e^{-\alpha\eta_{pu}W})\dfrac{\tau}{1 + i\omega\tau}, \tau_D^{pu} \gg \tau_D^{pr} \end{cases} \qquad (5.36)$$

Case 3 is a combination of Case 1 and Case 2. In this case the behavior as a function of frequency ω is identical to the simplified model in Equation (3.20). This is expected since zero surface recombination velocity and negligible radial diffusion reduces the problem to the simple case of measuring the bulk lifetime τ.

6 Single Beam Pump/Probe

6.1 Overview

Pump/probe spectroscopy is an indispensable tool that has a diverse range of applications amongst the physical sciences. Pump/probe studies with ultrafast lasers have been used to probe the fundamental dynamics of chemical and atomic systems from picosecond to femtosecond to even attosecond resolution [83], [84]. In the biological sciences, pump/probe techniques have been developed to measure the temperature of cancer cells, or perform time-resolved crystallography on biological macromolecules [85], [86]. In semiconductor physics, pump/probe studies have been used to measure the fundamental thermalization dynamics of electrons [87]. The common feature among all of these techniques is the use of separate beams for pump and probe. This is necessary in applications where the pump beam is not sensitive to the quantity being pumped. For example in Refs [86] Schmidt et al. study photo-excited stages of complex proteins with x-ray diffraction. An optical pump laser excites the proteins and a pulse of x-rays probes their crystal structure. Clearly an optical pump cannot interact with the protein in a way that elucidates crystallographic information, so in this application it is necessary to have separate beams for pump and probe. However, in semiconductor pump/probe studies, the pump beam that excites free-carriers is also attenuated by them via free-carrier absorption. Therefore it should be possible to perform pump/probe experiments in semiconductors using a single laser beam as both the pump and the probe. A single-beam pump/probe technique would have a tremendous advantage over its dual-beam counterpart in terms of cost, complexity, and implementation challenges. By removing the second beam, the supporting optics for that beam are eliminated and physical space is freed up. The problem of overlapping the pump and probe on the sample under study is also eliminated.

In this chapter I develop a single-beam pump/probe method for measuring effective lifetime in silicon. I use an Nd:YAG laser emitting at 1064 nm as the combined pump and probe. 1064 nm is very close to the absorption edge of silicon (~1100 nm), and since silicon is an indirect bandgap

semiconductor, the laser is weakly absorbed. In this work, about 25-65% of the laser is absorbed in the wafer. Low absorption is necessary so that a fraction of the beam can transmit through the wafer and be collected and analyzed. The single-beam signal is modelled using the generalized pump/probe equation from Chapter 5.3, which provides a general description of the signal accounting for bulk and surface recombination, as well as 3D carrier transport within the semiconductor. In the limit where the beam radius is large with respect to the free-carrier diffusion length, the model predicts that the lifetime measured by the single-beam technique is the 1D effective lifetime containing bulk and surface recombination. This is the lifetime that is usually measured in dual-beam studies, and the one that is of interest for defect spectroscopy in silicon [1]. I have experimentally verified that the lifetimes measured by the single and dual-beam experiments agree when the pump beam radius is large. When the beam radius is small with respect to the diffusion length, free-carriers generated by the pump escape the volume of the laser spot. This additional loss mechanism shortens the lifetime, and complicates the extraction of the effective recombination lifetime. Experimentally, this manifests as a shifting of the imaginary component of the signal to high frequencies, and a broadening of the peak. I have confirmed this experimentally, and showed that when the curve is fit to the general 3D model the effective 1D lifetime is determined, along with information containing the diffusion coefficient of the semiconductor. This demonstrates that even in the more complex case when bulk and surface recombination, as well as radial diffusion losses affect the signal, the effective recombination lifetime can still be determined unambiguously. I have also verified that the amplitude of the signal predicted by the 3D model is consistent with experimentally measured values.

The content of this chapter is as follows. In 6.2 I derive the mathematical model governing single beam pump probe and explore how the pump/probe beam radius affects the measurement of the effective recombination lifetime. In 6.3 I provide experimental validation of single-beam pump/probe in the limit where the beam radius is much larger than the diffusion length of free-carriers. In this limit the general pump/probe model predicts that the frequency dependence of the single-beam signal should be identical to that of the 1D model described in 3.3.2. This is confirmed experimentally, and is consistent with the lifetime measured by the dual-beam technique. In 6.4 I

describe the specifics of single-beam pump/probe data acquisition, and develop a strategy for separating out the probe contribution to the measured signal. It is demonstrated that drift effects, and not random noise, are what limits single-beam measurements. In 6.5 I compare the measured signal amplitude to what is predicted by the model and show quantitative agreement between the two. In 6.6 I show that in the limit where the beam radius is much smaller than the diffusion length of free-carriers, the lifetime that is measured by the single-beam technique is dominated by radial diffusion effects as is expected from the model. By fitting the frequency-dependence of the measured signal, the true effective recombination lifetime is extracted. In 6.7 I discuss some additional considerations for the single-beam technique, and in 6.8 I summarize the results of this section.

6.2   Theoretical Description of Single Beam Pump/Probe Technique

6.2.1   Derivation of Model for Single-Beam Pump/Probe

Experimentally I measure the transmission of a probe beam through a silicon wafer, and use the detected signal to measure the lifetime of the wafer. The signal measured in single-beam pump/probe experiments can be derived using the generalized pump/probe equation (Equation (5.29)). In single-beam pump/probe studies, the pump and probe beams are identical. Dropping the subscripts 'pu' and 'pr', the power transmitted through a wafer in the single-beam pump/probe technique is given by:

$$\tilde{P}_{tr} = \frac{T^2}{1 - R'^2} P_0'(1 + m \cos \omega t)\big(1 - 8\Re \eta m \xi(\omega)e^{i\omega t}\big) \tag{6.1}$$

where $\xi(\omega)$ is given by:

$$\xi(\omega) = \sigma_{FCA}\tau_D g_0 \alpha \eta e^{-\frac{\alpha \eta W}{2}} \sum_n e^{\frac{2\tau_D}{\tau_n'}} \Gamma\left(0, \frac{2\tau_D}{\tau_n'}\right) A_n^{lc} \tag{6.2}$$

In (6.1) I have converted the symbol P'_{pr} to P'_0, and set the phase factor ϕ_{pr} to zero since the pump and probe modulations are initially in phase with each other. Multiplying through (6.1):

$$\tilde{P}_{tr} = \frac{T^2}{1 - R'^2} P'_0 + \frac{T^2}{1 - R'^2} P'_0 m \left[\cos \omega t - 8\Re\eta\xi(\omega)e^{i\omega t}\right] \qquad (6.3)$$

$$- \frac{T^2}{1 - R'^2} P'_0 m^2 8\Re\eta\xi(\omega)e^{i\omega t} \cos \omega t$$

The real part of Equation (6.3) is the power that is measured experimentally, P_{tr}:

$$P_{tr} \equiv \text{Re}[\tilde{P}_{tr}] = \frac{T^2}{1 - R'^2} P'_0 \qquad (6.4)$$

$$+ \frac{T^2}{1 - R'^2} P'_0 m [\cos \omega t - 8\Re\eta\xi_{re} \cos \omega t + 8\Re\eta\xi_{im} \sin \omega t]$$

$$- \frac{T^2}{1 - R'^2} P'_0 m^2 8\Re\eta(\xi_{re} \cos \omega t - \xi_{im} \sin \omega t) \cos \omega t$$

where $\xi_{re} = \text{Re}[\xi(\omega)]$ and $\xi_{im} = \text{Im}[\xi(\omega)]$ (i.e. $\xi = \xi_{re} + i\xi_{im}$). Factoring Equation (6.4) and using the identities $\cos^2 \omega t = \frac{1}{2}(1 + \cos 2\omega t)$ and $\sin \omega t \cos \omega t = \frac{1}{2} \sin 2\omega t$:

$$P_{tr} = \frac{T^2}{1 - R'^2} P'_0 (1 - 4\Re\eta m^2 \xi_{re}) \qquad (6.5)$$

$$+ \frac{T^2}{1 - R'^2} P'_0 m [(1 - 8\Re\eta\xi_{re}) \cos \omega t + 8\Re\eta\xi_{im} \sin \omega t]$$

$$- \frac{T^2}{1 - R'^2} P'_0 m^2 4\Re\eta(\xi_{re} \cos 2\omega t - \xi_{im} \sin 2\omega t)$$

Equation (6.5) describes the exact time-resolved power that is seen on a detector for single-beam pump/probe. There is a DC term, and terms at the fundamental frequency and its 1st harmonic. The DC term is just the signal seen after attenuation of the beam due to band-to-band absorption, subtracted by a small contribution due to the rectification of the FCA term that goes as $\cos^2 \omega t$. The fundamental term is the power seen after attenuation of the beam due to band-to-band absorption, reduced further by free-carrier absorption. The second harmonic term is due entirely to free-carrier absorption. This term arises due to frequency mixing between the modulation of the laser at ω and the FCA term at ω. Each of the harmonic terms can be individually isolated with a lock-in amplifier. In order to extract lifetime information from the single beam experiment the ξ_{re} or ξ_{im} terms must be isolated. The obvious way of doing this would be to measure the component of the power at 2ω since it is arises purely due to FCA; in the absence of FCA there should be no contribution to the signal at 2ω. However, this is not straightforward to do experimentally. Due to non-linearities in the experimental setup, there are spurious signals that exist at 2ω that are larger than the free-carrier signal[18]. These non-linearities are likely due to distortion in the electro-optic modulator but can also arise in the photodiode detector and its transimpedance amplifier. The non-linearity at 2ω can be suppressed by splitting the laser beam prior to hitting the sample, and using one component as a reference beam in a feedback loop. This is the approach that has been used in the few single-beam pump/probe studies in the literature [59], [60]. There are several drawbacks to this approach. Firstly, it complicates the implementation of the technique since now a second detector is required as well as an amplifier with very high gain over a sufficient bandwidth for mapping out the frequency-response of ξ_{re} or ξ_{im}. Secondly, it is required that both the sample detector and feedback detector have very similar characteristics so that performing a feedback loop with one detector will effectively suppress distortion in the second. In the development of this technique I have attempted to extract the FCA component from the 2ω term, but was never able

---

[18] Empirically, stray harmonic components are about 10^{-2} of the direct pump signal. The FCA signal is typically less than 10^{-3}.

to acquire consistent results. In the case when no feedback scheme was implemented, the 2ω signal was dominated by a background signal that originates due to distortion of the ω term. When feedback was implemented there was still a non-zero signal at 2ω when a sample was absent. I attribute this to the fact that the sample and feedback detectors were not identical, so suppressing the 2ω in one detector does not translate into a reduced 2ω in another.

I have found that the most reliable method of isolating the FCA contribution is to extract it from the fundamental term in (6.5). The entire fundamental term is measured by demodulating the detector signal on a lock-in amplifier at a frequency of ω. In general, the signal consists of an in-phase component and out-of-phase component, which are given by the coefficients of the $\cos \omega t$ and $\sin \omega t$ terms in (6.5), respectively. The demodulated signal can be represented as a complex number S_ω, given by:

$$S_\omega(\omega) = \zeta(\omega) \frac{T^2}{1 - R'^2} P_0' m [1 - 8\Re \eta \xi(\omega)] \tag{6.6}$$

where $\zeta(\omega)$ is the transimpedance transfer function[19] of the detector. The physical interpretation of (6.6) is quite straightforward. It is the signal due to the total laser power that transmits through the wafer, accounting for the reflection and absorption losses. In the absence of FCA the signal is $\zeta(\omega) \frac{T^2}{1-R'^2} P_0'$ which is the signal when the only absorption loss is band-to-band absorption. In the presence of FCA there is additional attenuation of the beam which reduces the intensity beyond what is expected from band-to-band absorption alone. This additional absorption is frequency dependent, since the amplitude of the free-carrier population depends on frequency.

---

[19] In general the transimpedance transfer function is a complex number since the detector can change the magnitude and phase of the transduced signal.

When no sample is present the background signal $S_b'(\omega)$ is given by:

$$S_b'(\omega) = \zeta(\omega)P_0 \tag{6.7}$$

Here the signal is just due to the incident power and the detector's transimpedance response. In practice, I control the power into the pump detector with a half-waveplate/polarizer pair, and always maintain the same amount of power throughput into the detector regardless of whether or not a sample is in place. This is to ensure that the experimental conditions between measuring the sample spectrum and the background spectrum are as close as possible. Large power differences between measurements of these spectra could reveal non-linearities in the detector's transimpedance response. Even though any deviations from linearity are probably small, the free-carrier signal itself is also quite small (typically $|8\Re\eta\xi(\omega)| < 10^{-3}$), so it is proactive to avoid introducing non-linearities when possible. Let S_b be this new background spectrum, where the power into the detector is adjusted to match the power that was incident upon the detector when S_ω was collected. Since $|8\Re\eta\xi(\omega)| \ll 1$, $S_\omega \sim S_b$ and the prefactor in front of S_b is the same as S_ω. Thus S_b can be written as:

$$S_b = \zeta(\omega)\frac{T^2}{1 - R'^2}P_0'm \tag{6.8}$$

Dividing S_ω by S_b yields the signal that is analyzed for single-beam pump/probe measurements:

$$\mathcal{S} \equiv \frac{S_\omega}{S_b} = 1 - 8\Re\eta\xi(\omega) \tag{6.9}$$

Note that all terms related to power and the transimpedance response of the detector have been removed. Equations (6.6) and (6.9) reveal a unique characteristic of single-beam pump/probe that differentiates it from traditional dual-beam measurements. The measured signal is proportional to a factor of unity subtracted by the FCA component. The factor of unity corresponds to the pump signal whereas the other term corresponds to probe signal. In other words, the measured signal is a superposition of the pump and probe signals. In almost every other pump/probe experiment the probe signal is entirely decoupled from the pump since the probe is a separate beam. So long as the pump source is rejected by the probe detector it is not measured. This makes it easy to discriminate between the two. In the single-beam technique they are necessarily coupled. Since the induced FCA is quite small, the drive signal is significantly larger than the desired probe. During early trials in the development of the single-beam technique I tried many strategies for isolating the free-carrier signal using Equation (6.6) before finally settling on the formulation of Equation (6.9). Some of the unsuccessful schemes are discussed in Appendix G. Formulating Equation (6.9) is a useful way to isolate the FCA component since it eliminates the instrumentation response of the detector and reduces the measureable quantity to a simple relationship. The imaginary part of this relationship is due entirely due to FCA. In general $\xi(\omega)$ is a complex quantity. Since $\xi(\omega) = \xi_{re}(\omega) + i\xi_{im}(\omega)$, the real and imaginary components X & Y of (6.9) are:

$$X = 1 - 8\Re\eta\xi_{re}(\omega) \tag{6.10}$$

$$Y = -8\Re\eta\xi_{im}(\omega) \tag{6.11}$$

Equation (6.11) shows that the imaginary component of $\mathcal{S}$ is directly proportional to the imaginary component of the FCA spectrum. In other words, by taking the imaginary component of the signal the probe beam contribution is isolated, decoupling it from the pump contribution. It is this component of the signal that is used to determine the effective recombination lifetime of the wafer.

6.2.2   The Effect of Beam Radius on Lifetime Measurements

The signal in FCA pump/probe studies is sensitive to the free-carrier density that falls within the volume of probe beam. Along the axis of the wafer (the z axis in Figure 5.1), the only way for carriers to escape the probe beam is to recombine in the bulk, or diffuse to the surfaces of the wafer and recombine there. This is because the probe beam propagates along the axis of the wafer, so it "sees" the free-carriers no matter where they are along that axis. The rate at which carriers escape along the axis of the wafer is $1/\tau$, where τ is the *effective recombination lifetime* which is a function of recombination rates in the bulk and at the surface of the semiconductor (see Equation (3.29)). Since the probe beam has a finite radius, carriers diffusing in the plane of the wafer (r-axis in Figure 5.1) can escape the probe beam without recombining. The rate at which carriers diffuse out of the probe volume is given by $1/\tau_r$ where τ_r is the *radial diffusion lifetime*. The total rate at which carriers escape the probe beam $1/\tau_{3D}$ is the sum of the rates at which carriers recombine and diffuse out of the beam:

$$\frac{1}{\tau_{3D}} = \frac{1}{\tau} + \frac{1}{\tau_r} \tag{6.12}$$

where τ_{3D} is the *3D effective lifetime*. As discussed in 3.3.1, the imaginary component of the 1D FCA signal has a characteristic peak ω_p in the imaginary spectrum that corresponds to the effective lifetime τ (see Figure 3.5). In the 3D case, this peak corresponds to the 3D effective lifetime, which is given by:

$$\tau_{3D} = \frac{1}{\omega_p} \tag{6.13}$$

The 3D effective lifetime is what is measured experimentally in single-beam pump/probe. The effective lifetime τ is set by the properties of the sample under investigation and generally remains fixed in a single measurement. The radial diffusion lifetime τ_r also depends on the properties of the sample, but it is also dependent on the beam radius which can be controlled by the experimenter. If the probe radius is large with respect to the free-carrier diffusion length, then the rate at which carriers escape by diffusion will be very low and $\tau_{3D} \sim \tau$. When the beam radius is very small with respect to the diffusion length, the rate of escape due to diffusion is very high and $\tau_{3D} \sim \tau_r$. From Equation (6.12) it is clear that $\tau_{3D} \leq \tau$. Note that τ_r is not the same as the diffusion time constant τ_D. τ_r is a lifetime that is defined through Equation (6.12), and is used to describe the rate at which carriers leave the probe volume without recombining.

To get an understanding how the relationship between beam radius and carrier diffusion length affect τ_{3D}, I examine the frequency-dependent terms of the FCA signal. These terms are inside the summation in the factor ξ (Equation (6.2)). Since the first term of the series is dominant (Figure 3.7), the frequency-dependence can be approximated by the factor $\mathcal{F}$:

$$\mathcal{F} = \tau_D e^{\frac{2\tau_D}{\tau}(1+i\omega\tau)} \Gamma\left(0, \frac{2\tau_D}{\tau}(1 + i\omega\tau)\right) \tag{6.14}$$

In Equation (6.14) I have substituted $\tau' = \frac{\tau}{1+i\omega\tau}$ (Equation (5.25)). The frequency dependent term of the argument $(1 + i\omega\tau)$ is weighted by the factor $2\tau_D/\tau$. The magnitude of this factor controls the relative contribution of τ_r to τ_{3D}. It is shown in Appendix H that when $\frac{2\tau_D}{\tau} \gg 1$, the frequency dependence of $\mathcal{F}$ reduces to the simple case of 1D diffusion. This is Case 2 of the ξ factor in Chapter 5.4. An intuitive interpretation of the factor $2\tau_D/\tau$ is revealed by substituting in $\tau_D = w^2/8D$ and using the fact that the free-carrier diffusion length is $L = \sqrt{D\tau}$. The factor $2\tau_D/\tau$ becomes:

$$\frac{2\tau_D}{\tau} = \frac{1}{4}\frac{w^2}{L^2} \tag{6.15}$$

From Equation (6.15) it is clear that the factor $2\tau_D/\tau$ is related to the ratio of the beam radius to diffusion length. Obviously if the beam radius is large with respect to diffusion length, diffusion effects are negligible.
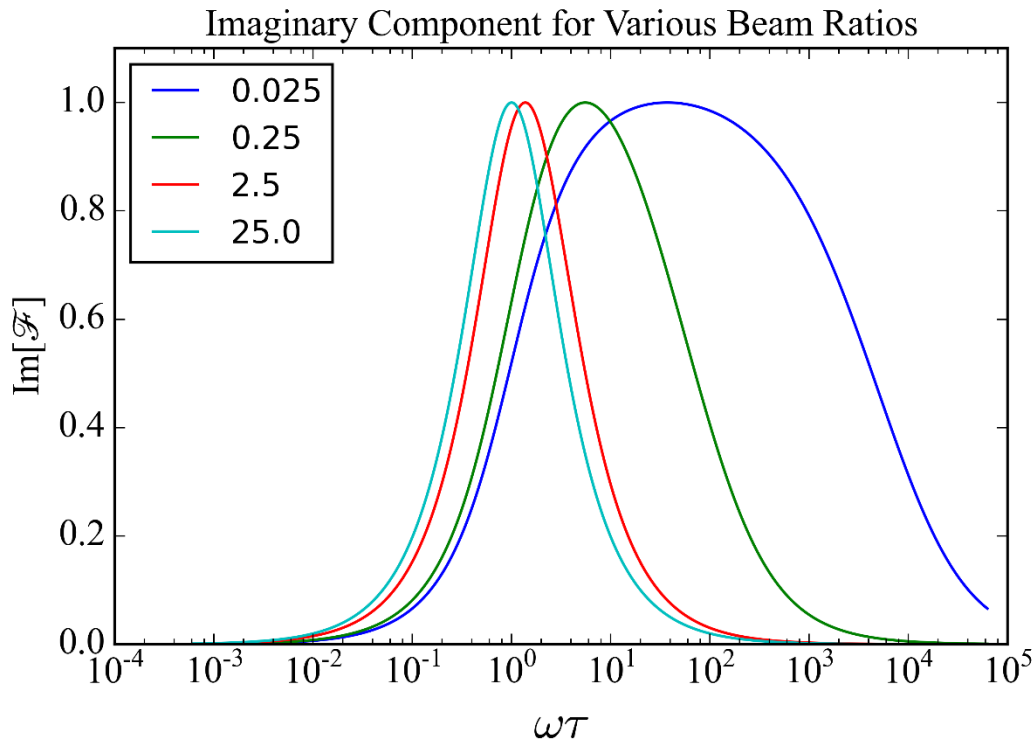
Figure 6.1: Plot of imaginary component of FCA signal vs ωτ for various probe beam ratios. The probe beam ratio is defined as the probe radius divided by the effective diffusion length of free-carriers. Beam ratios are labelled in the legend.

Figure 6.1 plots the imaginary component of Equation (6.14) vs $\omega\tau$ for various beam ratios, with the peak amplitude normalized to unity for each curve. The *probe beam ratio* is defined as the ratio of the beam radius to the diffusion length. Note that τ here is the effective recombination lifetime, not the 3D effective lifetime. When the beam radius is 25 times larger than the diffusion length,

the imaginary component peaks at $\omega\tau = 1$. This means that $\tau = 1/\omega_p$ which follows from Equations (6.12) & (6.13) if $\tau_r \to \infty$. As the beam ratio is reduced with respect to diffusion length, the peak of the imaginary component shifts towards higher frequencies and the curve broadens. In this case, $1/\omega_p$ no longer corresponds to the effective recombination lifetime and diffusion effects have to be explicitly accounted for in order to extract τ. The effective recombination lifetime τ is the quantity that experimenters are typically interested in since it is a direct measure of the electronic quality of a semiconductor wafer [1]. From this perspective, radial diffusion effects are parasitic and obfuscate the quantity of interest. The simple solution to this is to configure the pump/probe radius beam such that diffusion is negligible. However, single-beam pump/probe would be considerably more flexible if it was possible to deduce τ regardless of the beam radius. The most obvious way to unambiguously resolve τ is to fit the imaginary component of the signal to (6.14). Fitting is performed in Chapter 6.6 to extract τ & τ_D simultaneously.

Alternatively, it would be useful to be able to extract τ directly from the peak position ω_p. To do this I introduce a modified version of Equation (6.13):

$$\tau = \frac{\mathcal{D}}{\omega_p} \tag{6.16}$$

where $\mathcal{D}$ is the *diffusive factor*, which is a dimensionless number greater than or equal to unity. When the beam radius is large $\mathcal{D} \to 1$ and the effective lifetime is just the inverse of the peak angular frequency ω_p. As the beam radius becomes smaller, for a fixed effective lifetime τ, ω_p shifts to higher frequencies which means that the diffusive factor must increase to compensate. Alternatively, the effective lifetime can be related directly to τ_{3D} by substituting Equation (6.13) into (6.16):

$$\tau = \mathcal{D}\tau_{3D} \tag{6.17}$$
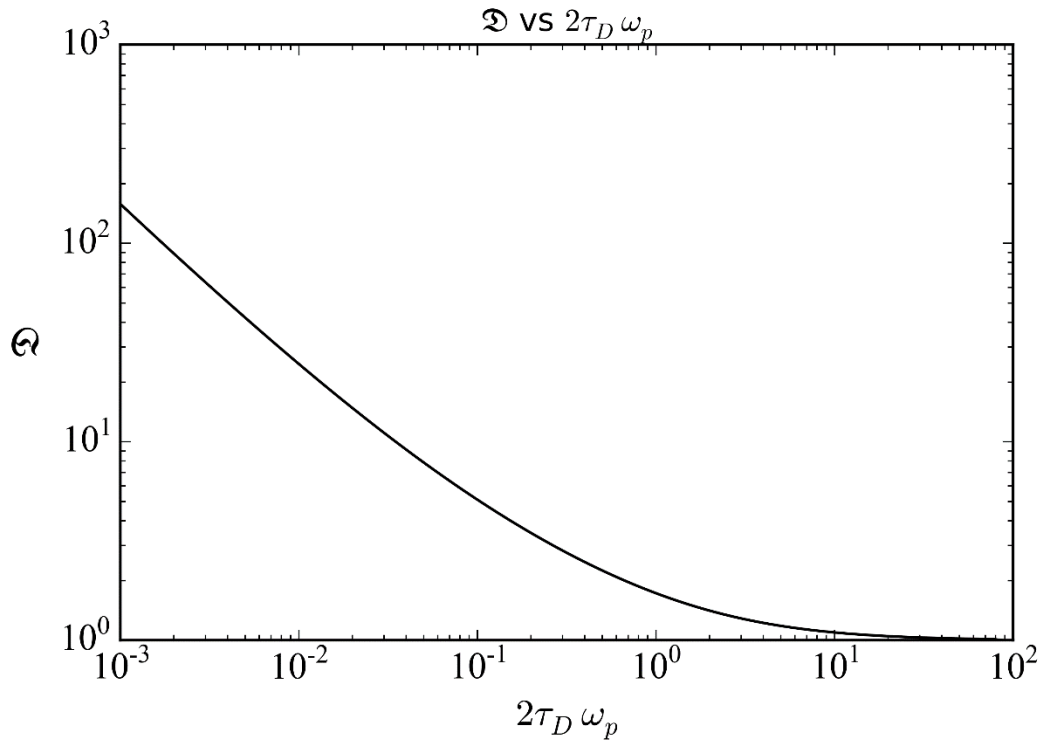
Figure 6.2: Plot of Diffusive factor vs $2\tau_D\omega_p$

The diffusive factor is determined in Appendix E. I derive an equation that implicitly relates $\mathcal{D}$ to the factor $2\tau_D\omega_p$. This factor is not arbitrary, and emerges naturally from the mathematical analysis of the peak position of $\text{Im}[\mathcal{F}]$. For each value of $2\tau_D\omega_p$ there is a unique diffusive factor $\mathcal{D}$. The diffusive factor is plotted vs $2\tau_D\omega_p$ in Figure 6.2. As the beam radius is increased the diffusion is mitigated and $\mathcal{D} \to 1$. When the beam radius is small, $\mathcal{D} > 1$. As long as $2\tau_D$ can be

determined[20], the effective lifetime can be always be isolated by a measurement of ω_p and extraction of the appropriate $\mathcal{D}$ from Figure 6.2.

As an example, consider the case where the effective lifetime is $\tau = 100$ μs, the diffusion coefficient is $D = 16$ cm^2/s, and the beam radius is $w = 10$ μm. The diffusion length is $\sqrt{D\tau} = 400$ μm, and so the beam ratio is 0.025. Using these parameters, the imaginary component of $\mathcal{F}$ peaks at $\omega_p = 3.74 \times 10^5$ rad/s. This corresponds to $\tau_{3D} = 2.67$ μs, which is clearly much shorter than the effective recombination lifetime that is being measured. Of course this is expected since the beam radius is much smaller than the diffusion length and the lifetime is dominated by the radial diffusion lifetime. Since w & D are known τ_D can be computed and so can the factor $2\tau_D\omega_p$, which is this case is 5.84×10^{-3}. From Figure 6.2 this corresponds to a diffusive factor of $\mathcal{D} = 37.39$. Using the values of $\mathcal{D}$ & ω_p I arrive at an effective lifetime of $\tau = 99.7$ μs using Equation (6.16) which is within 0.7% of the true effective lifetime. Thus even in the case when the radial diffusion affects the single-beam pump/probe lifetime, the desired effective lifetime can still be determined from the peak position ω_p, if τ_D is known.

6.3   Experimental Validation of Single-Beam Pump/Probe in 1D limit

In this section I provide experimental validation of the single-beam pump/probe experiment for the case where the beam is sufficiently large to neglect radial diffusion effects in the measured lifetime. In this case, the lifetime measured by the single-beam technique should correspond to the true effective recombination lifetime τ. The effective lifetime is measured independently using MFCA in dual-beam pump probe configuration, where the probe beam is a 1550 nm laser. Details about the experimental configuration of the single and dual beam experiments are provided in Chapter 4. Summarizing here, the probe beam is a p-polarized 1550 nm laser which is expanded

---

[20] τ_D contains the beam radius w and diffusion coefficient D. The beam radius is defined by the experimenter and is always measureable. The diffusion coefficient is a material constant whose behavior in silicon is well-behaved so it may always be estimated [81].

to a large diameter[21] via a beam-expander, and then illuminates the silicon sample at Brewster's angle to reduce reflectance to 0. The probe beam is held at a fixed power and is not directly modulated. The probe beam diameter is much larger than the pump diameter so that the all free-carriers generated by the pump are probed, and none can escape via radial diffusion. This means that the dual-beam method will be sensitive to only recombination, and not diffusion. The pump beam is expanded to a radius of 3.84 mm, which is about 9.6 times larger than the free-carrier diffusion length of the sample under study in this section.

6.3.1   Mathematical Derivation of Single and Dual-Beam Signals

The signal that is extracted in single-beam pump/probe is given by (6.9), which is derived in 6.2.1. Substituting in the ξ factor from Case 2 in 5.4, the single-beam signal is given by:

$$\mathcal{S} = 1 - 4\Re\eta\sigma_{FCA}g_0\alpha\eta e^{-\frac{\alpha\eta W}{2}} \sum_n \frac{\tau_n}{1 + i\omega\tau_n} A_n^{lc} \tag{6.18}$$

Taking the imaginary component of the signal:

$$Y_{SB} = 4\Re\eta\sigma_{FCA}g_0\alpha\eta e^{-\frac{\alpha\eta W}{2}} \sum_n \frac{\omega\tau_n^2}{1 + \omega^2\tau_n^2} A_n^{lc} \tag{6.19}$$

For the dual beam technique, the signal can be derived from the generalized pump/probe equation in 5.3 (Equation (5.29)). The probe beam does not experience band-to-band absorption, so $P'_{pr} = P_{pr}$. The probe reflectance at the surface is 0 so $R'_{pr} = R_{pr} = 0$, $T_{pr} = 1$ & $\Re = 1$. The probe

---

[21] The probe beam is expanded to completely fill the aperture of the sample holder, which is about 1 cm in diameter.

beam is not modulated so $m_{pr} = 0$. Substituting these into Equation (5.29) and taking the real part:

$$P_{tr} = P_{pr}\big(1 - 8\eta_{pr}m(\xi_{re}\cos\omega t - \xi_{im}\sin\omega t)\big) \tag{6.20}$$

Equation (6.20) is the probe power transmitted through the silicon wafer for the dual-beam pump/probe technique. Note that the time-dependent component is due to FCA induced by the pump modulation of the free-carrier density. Experimentally this power is transduced by a photodiode/transimpedance amplifier, and the resultant signal is fed into a lock-in amplifier. The time-dependent term is then demodulated. The resultant signal is:

$$S_{DB} = -8\zeta(\omega)P_{pr}\eta_{pr}m\xi(\omega) \tag{6.21}$$

where $\zeta(\omega)$ is the transimpedance response (*i.e.* the conversion between power and voltage) of the photodetector. A negative sign on Equation (6.21) ensures that the imaginary component is positive, which is consistent with the sign of the imaginary component of the single-beam signal. When the probe beam is much larger than the pump, and greater than the diffusion length of free-carriers, the ξ factor is given by Equation (5.33) (Case 2 in 5.4). Substituting this in:

$$S_{DB} = -8\zeta(\omega)P_{pr}\eta_{pr}m\frac{\tau_D^{pu}}{\tau_D^{pr}}\sigma_{FCA}g_0\alpha\eta_{pu}e^{-\frac{\alpha\eta_{pu}W}{2}}\sum_n\frac{\tau_n}{1+i\omega\tau_n}A_n^{lc} \tag{6.22}$$

Taking the imaginary component of this signal:

$$Y_{DB} = 8\zeta(\omega)P_{pr}\eta_{pr}m\frac{\tau_D^{pu}}{\tau_D^{pr}}\sigma_{FCA}g_0\alpha\eta_{pu}e^{-\frac{\alpha\eta_{pu}W}{2}}\sum_n\frac{\omega\tau_n^2}{1+\omega^2\tau_n^2}A_n^{lc} \tag{6.23}$$

Bundling together the prefactors that precede the series terms in Equations (6.19) & (6.23) the final equations for the single and dual beam signals are given by:

$$Y_{SB} = K_{SB}\sum_n\frac{\omega\tau_n^2}{1+\omega^2\tau_n^2}A_n^{lc} \tag{6.24}$$

$$Y_{DB} = K_{DB}\sum_n\frac{\omega\tau_n^2}{1+\omega^2\tau_n^2}A_n^{lc} \tag{6.25}$$

Equations (6.24) & (6.25) prove that when radial diffusion is negligible, the frequency-dependence of the single and dual beam signals are identical, except for a prefactor. This frequency dependence is identical to that of the 1D model discussed in 3.3.2 (Equation (3.30)), which is expected since the beam radius is larger than the free-carrier diffusion length.

6.3.2   Experimental Validation
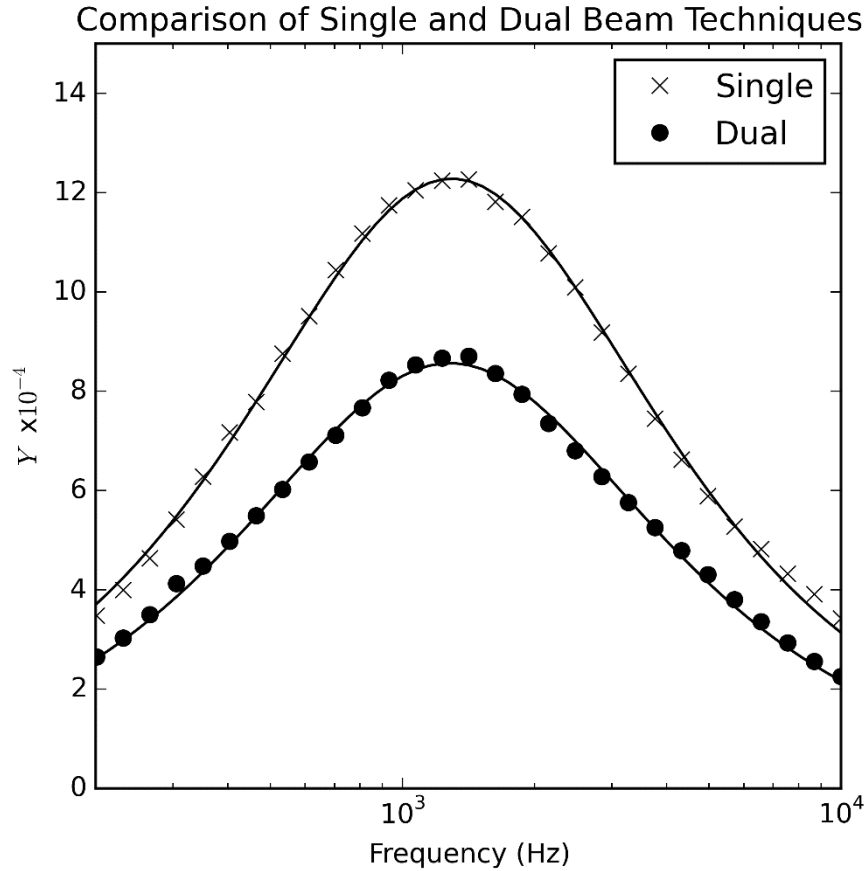
Figure 6.3: Comparison of single and dual beam pump/probe techniques for thick silicon wafer. Datapoints are denoted by discrete symbols. Continuous lines represent fits to data. Curves are fitted with the frequency dependence of the 1D recombination model (Equation (3.30)). The amplitude of the single beam data is given in absolute units while the amplitude of the probe beam data is scaled arbitrarily for comparison. The data in this figure is collected using a pump power of 654 mW. Given the beam radius of 3.84 mm, this corresponds to an intensity of 1412 mW/cm^2.

Equations (6.24) & (6.25) are validated experimentally on the thick wafer (see Table I for sample specifications). The pump beam radius is set to $w = 3.84$ mm, and the probe beam radius is adjusted to uniformly illuminate the aperture of the sample holder (diameter ~ 10 mm). The average power of the pump beam is 654 mW. Figure 6.3 shows a plot of the imaginary component of the single and dual beam signals over a frequency range of 200 Hz to 10 kHz. Both data sets

are fitted[22] to the frequency-dependence of the 1D recombination model (Equation (3.30)). The experimental data is represented by discrete symbols and the fits are represented by the solid curves. The amplitude of the single-beam data is given in absolute units, whereas the amplitude of the dual-beam data is scaled arbitrarily so that both datasets may be compared on a single axis.

It can be seen that both the single and dual beam pump/probe signals exhibit nearly-identical frequency dependences, which are well described by theory. The effective lifetime is extracted from the peak of the fits, with the single and dual beam techniques yielding $\tau_{SB} = 123.7 \pm 0.5$ µs and $\tau_{DB} = 124.0 \pm 0.7$. These lifetimes are identical to within experimental precision, the precision being quoted in a one-sigma confidence interval. Clearly the beam radius is large enough that radial diffusion effects are negligible in the single-beam data. The question now is whether or not this is expected from the theory? Experimentally I have determined that $\tau_{3D} = \tau$, which implies that the diffusive factor (Equation (6.17)) is equal to unity. Using $D = 16$ cm^2/s, and using the peak of the single-beam data for ω_p, I calculate $2\tau_D\omega_p = 18.6$. This corresponds to a diffusive factor of $\mathcal{D} = 1.05$ (Equation (E.13)). This diffusive factor implies that the effective lifetime should be $\tau = 129.9$ µs, but instead I measure a value of 124 µs from the dual-beam technique. I am not sure what the reason is for this discrepancy. One potential issue is that the pump beam radius is incorrect. Figure K.1 shows a screenshot of the pump beam profile characteristics measured by the Nanoscan Beam Profiler. The profile fits well to a Gaussian curve, and has $< 2\%$ eccentricity between the x and y components of the beam. The standard deviation of the measured beam diameters is $< 1\%$ of the mean. Using the beam radius of the y component ($w = 3.87$ mm), the diffusive factor is still $\mathcal{D} = 1.05$. Since the beam is incident upon the sample at 15° to the normal, the projected radius will actually be a factor of 1.03 ($\sec 15°$) longer in one direction. This is not enough to appreciably change the value of $\mathcal{D}$. Regardless of the source of the discrepancy, the single-beam has outperformed here and it recovers the same value of effective lifetime as the

---

[22] The fitting routine uses non-linear least squares fitting. The uncertainty of the τ extracted from the fit as the square root of the parameter's covariance.

dual-beam technique! This is proof of concept that single-beam pump/probe technique can be used for lifetime metrology, and can supersede dual beam pump/probe.
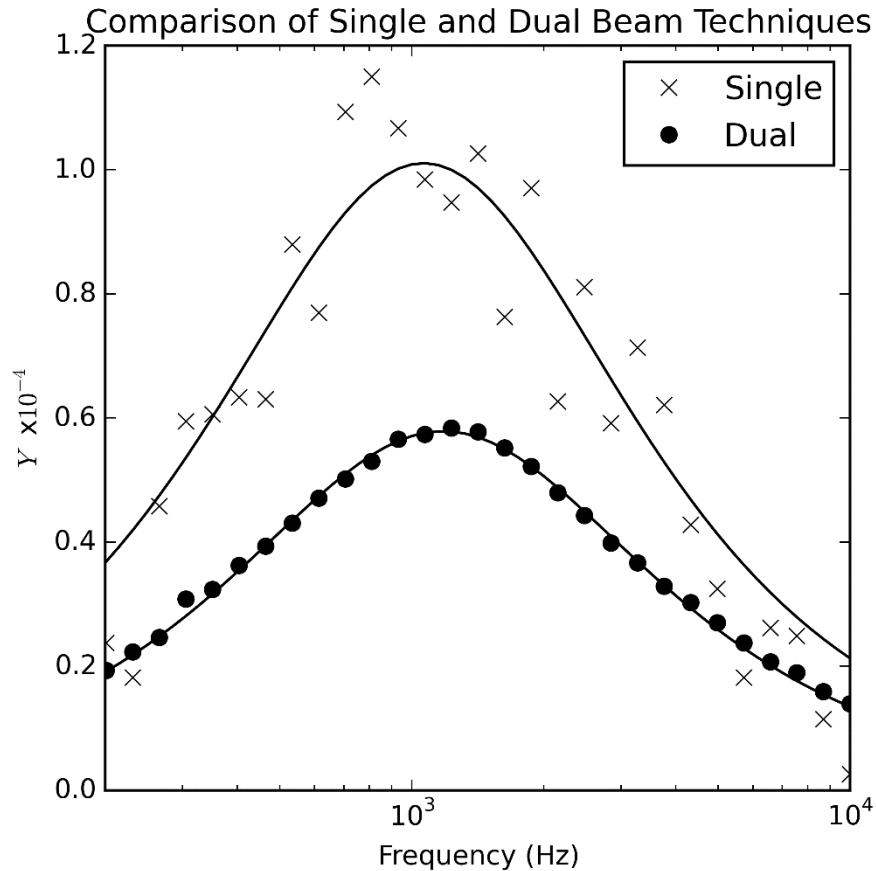
Figure 6.4: Comparison of single and dual beam pump/probe techniques for thick silicon wafer. Datapoints are denoted by discrete symbols. Continuous lines represent fits to data. Single beam data amplitude is given in absolute units while the probe beam data is scaled arbitrarily for comparison. This data is collected using a pump power of 70 mW. Given the beam radius of 3.84 mm, this corresponds to an intensity of 151 mW/cm^2.

The data in Figure 6.3 is collected at a power of 654 mW. Given the beam diameter, this corresponds to an intensity of 1412 mW/cm^2. Clearly the signal-to-noise ratio of the measurement is high since the data is well-fit to the theoretical model. In Figure 6.4 I have plotted data taken at a pump power of 70 mW (intensity of 151 mW/cm^2). The spread in the single-beam data points indicates a much lower signal-to-noise ratio than the data in Figure 6.3. The lifetimes extracted from the peak of the fits for the single and dual-beam techniques are $\tau_{SB} = 150 \pm 5$ μs and $\tau_{DB} =$

135.0 ± 0.7 µs. In this case the discrepancy between the two techniques is greater. From a theoretical point of view, there are no circumstances where the lifetime measured by the single-beam experiment should exceed the effective lifetime measured by the dual-beam configuration. The reason why this happens here is that the single-beam data is noisy and the peak location is not obvious from the spread of datapoints. Interestingly though, the lifetime that is fit is within 10% of the dual-beam technique. Later on I will explore the detection limits of the single-beam technique.

6.4   Specifics of single-beam data acquisition and detection limits

In experiments that use a lock-in amplifier to extract signals, the signal-to-noise ratio is controlled by setting the time-constant on the lock-in's low-pass filter. Longer time constants correspond to narrower bandwidths and thus greater rejection of signal noise. However, since the low-pass filter has a settling time lasting several time constants, long time constants lead to long acquisition times. In this work, the dual-beam pump/probe data is typically collected with a time constant of 100 ms over a frequency range spanning 100 Hz to 100 kHz. Depending on how many discrete frequencies are collected, it can take several minutes to acquire a single spectrum. This is not a problem for dual-beam data collection. For single-beam data, long acquisition times degrade the signal due to drift effects.

From the definition of the single-beam signal $\mathcal{S}$ in 6.2.1 (Equation (6.9)) it can be seen that the relationship between the sample and background spectra $\mathcal{S}_\omega$ & $\mathcal{S}_b$ is:

$$\mathcal{S}_\omega(\omega) = \mathcal{S}_b(\omega)\big(1 - 8\Re\eta\xi(\omega)\big) \tag{6.26}$$

$\mathcal{S}_\omega$ is the raw signal collected from the pump/probe beam that transmits through the silicon wafer, and $\mathcal{S}_b$ is the signal collected when the wafer is removed. In order to form the single-beam pump/probe signal $\mathcal{S}$, $\mathcal{S}_b(\omega)$ is measured separately from $\mathcal{S}_\omega(\omega)$. The main concern here is

whether or not the background spectrum measured separately corresponds to the background spectrum inside (6.26) when $\mathcal{S}_\omega$ is collected. Frequency-spectra are susceptible to drift errors when collected over a long time. For example, say that one spectrum $\mathcal{S}_b$ is measured over several minutes and the laser power is slowly drifting upwards over that time. Then the spectrum is collected again, but now the laser power is drifting downwards. Obviously these spectra are not identical. Normally drift is a small effect. Experimentally, I have observed that the signal demodulated from the detector drifts only a few percent over time. In the dual-beam pump/probe technique, this is acceptable because the signal is only composed of the probe signal. In the single-beam technique the signal is a superposition of both the pump and the probe (see 6.2.1). The probe component has to be separated from the pump, which is very challenging since the probe signal is on the order of $10^{-4} - 10^{-3}$ of the pump signal. For single-beam pump/probe, drift must be mitigated as much as possible. The strategy I have adopted is instead of collecting a single spectrum with a long time-constant, I collect several spectra with a short time constant and then average them. If the time constant is short, the entire spectrum is collected on a timescale shorter than drift effects so the relative spectrum remains unaffected by drift. The trade-off is that since the time-constant is short, each spectrum is more susceptible to random noise. The more spectra that are collected, the more this noise can be suppressed by averaging.

Background Comparison for Short and Long Time-Constants
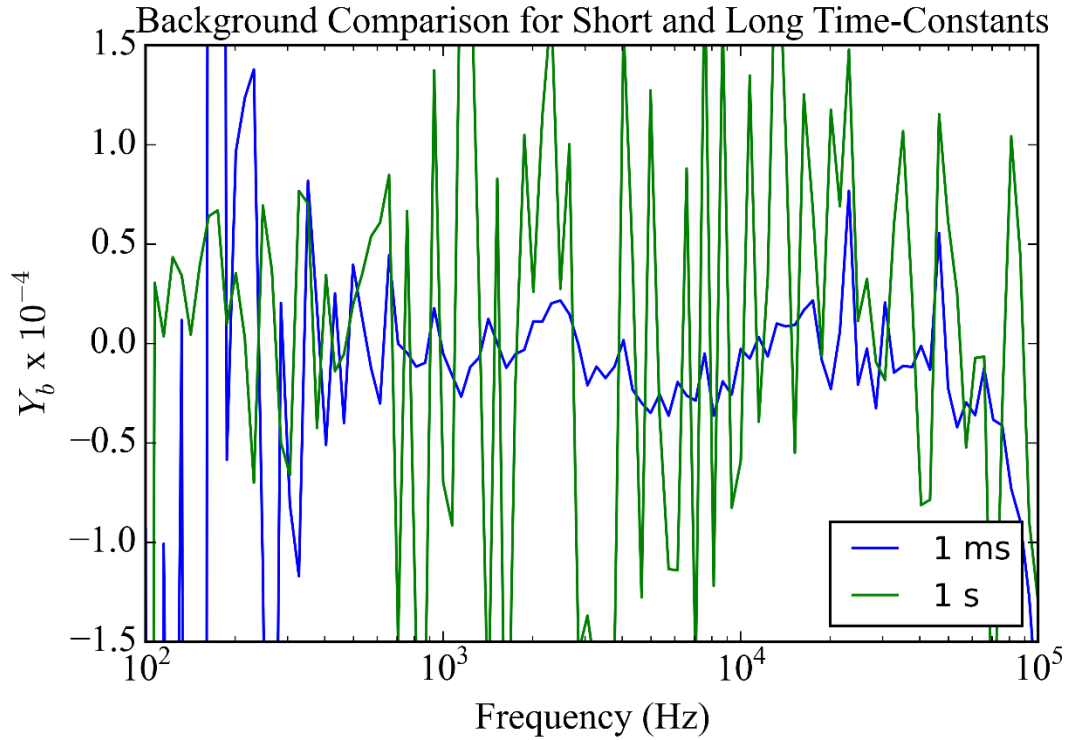
Figure 6.5: Imaginary component background for 1 ms and 1 s time constants. The '1 ms' data is averaged over 10 spectra, while the '1 s' data is composed of a single spectrum. The total measurement time for the '1 ms' and '1 s' data are 1 minute, and 25 minutes, respectively.

The detection floor of single-beam pump/probe can be estimated by dividing two separate spectra taken without a sample in place. If the spectra are identical, the real part should be unity across all frequencies, and the imaginary part should be 0. Any deviation from 0 in the imaginary component reveals the practical detection limits of the single-beam technique as has been presented here. The imaginary background is defined by the following equation:

$$Y_b = \text{Im} \left[\frac{\mathcal{S}_{b1} + \mathcal{S}_{b2} + \cdots \mathcal{S}_{bk}}{\mathcal{S}'_{b1} + \mathcal{S}'_{b2} + \cdots \mathcal{S}'_{bk}} \right] \tag{6.27}$$

where $\mathcal{S}_{bi}$ are elements of the first set of background spectra taken, and S'_{bi} are elements of the second set. There are k-number of spectra collected at each time constant. Figure 6.5 shows Y_b for spectra collected with a 1 ms and 1 s time constant. For the 1 ms time constant, there are 10 spectra in each background set, and for the 1 s time constant there is only 1. It is clear that background suppression is superior with the 1 ms time-constant. This provides justification for the measurement methodology that I have outlined in this section. That is, better background suppression is achieved by averaging several spectra taken with a short time constant, as opposed to taking data with long time constants. What is interesting is that it takes only 1 minute to collect all of the 1 ms data, and 25 minutes for the 1 s data. This is evidence that the signal in single-beam pump/probe experiments is affected more by drift than random noise. If random noise was the limiting factor then it is expected that the 1 s data would yield a lower measurement background than 1 ms data. The fact the 1 ms data is superior indicates that slow drift in the measurement apparatus is what limits measurements collected over a long time. In this experiment there may be several sources of drift. The first is drift in the output power of the laser. Perhaps the largest source is operating point of the electro-optic modulator that modulates the pump beam. The EOM uses a DC bias to control the ratio of AC to DC components of the pump power modulation. I have observed that this ratio can change by several percent throughout the day.
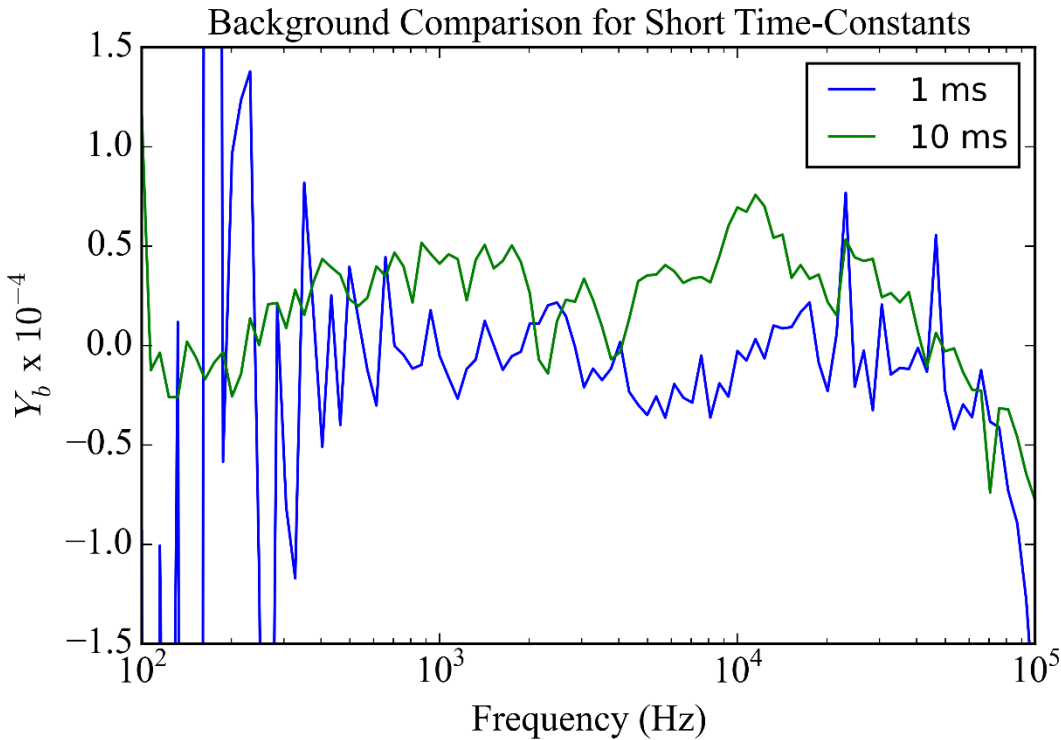
Figure 6.6: Imaginary component background for 1 ms and 10 ms time constants. Both data sets include 10 spectra. The total measurement time for the '1 ms' and '1 s' data are 1 minute, and 3 minutes, respectively.

Figure 6.5 shows that the 1 ms time constant is clearly superior to 1 s. However, at low frequencies there is a significant amount of variation in the 1 ms background data, which exceeds that of the 1 s data. This can be explained by the fact that noise tends to increase towards low frequencies due to 1/f noise. Figure 6.6 compares 1 ms and 10 ms time constants. In this case both datasets include 10 spectra each. The 10 ms data takes about 3 minutes to collect. It is clear that a 10 ms time constant provides superior background suppression at low frequencies than 1 ms. Though the 10 ms data takes a longer time to collect, it takes about the same amount of time to collect as the dual-beam data used in this work.

Since the single-beam technique measures both the pump and probe contributions simultaneously, the measurement apparatus requires a wide dynamic range. For signals digitized by an analog-to-digital converter (ADC), the ADC must be able to simultaneously digitize the small FCA

107

component of the signal as well as the pump, while not being saturated. The lock-in amplifier used in this experiment has a 14 bit resolution which limits the resolvable free-carrier signal to 1 part in 2^{14} of the pump beam (*i.e.* the minimum FCA signal is $6.1 \, x \, 10^{-5}$ of the pump). The practical detection limit is expected to be somewhat higher due to random noise in the measurement. The data shown in Figure 6.5 and Figure 6.6 demonstrate that the detection floor of the single-beam technique approaches the limit set by the ADC. For example, the amplitude of the 10 ms background spectrum is $< 10^{-4}$, which shows that single-beam pump/probe measurements are able to approach the detection floor.

The detection floor can be written in terms of the lifetime and the pump intensity. This will allow one to estimate the range of practical lifetimes that may be measured. Let f_{fca} be the fractional FCA signal, which from Equation (6.9) is given by:

$$f_{fca} = 8\Re\eta\xi(\omega) \tag{6.28}$$

For simplicity I will assume that the beam radius is sufficiently large that radial diffusion can be neglected, and that the surface recombination is 0. In this case ξ is given by Equation (5.35):

$$f_{fca} = \frac{1}{4}\Re\eta\sigma_{FCA}g_0(1 - e^{-\alpha\eta W})\frac{\tau}{1 + i\omega\tau} \tag{6.29}$$

Substituting in the value for g_0 (Equation (D.10)):

$$f_{fca} = \frac{1}{4} \Re \eta \sigma_{FCA} \frac{2P_0 \lambda}{\pi w^2 hc} \frac{1-R}{1-Re^{-\alpha \eta W}} (1 - e^{-\alpha \eta W}) \frac{\tau}{1 + i\omega\tau} \tag{6.30}$$

Note that the factor $\frac{1-R}{1-Re^{-\alpha\eta W}}(1 - e^{-\alpha\eta W})$ is the fraction of power absorbed in wafer f_a (Equation (I.19)):

$$f_{fca} = \frac{1}{2} \Re \eta \sigma_{FCA} \frac{P_0 \lambda}{\pi w^2 hc} f_a \frac{\tau}{1 + i\omega\tau} \tag{6.31}$$

For simplicity it can be assumed that $\eta = 1$ (normally incident light). The reflectance of bare silicon at 1064 nm is about $R = 0.3$. Using the band-to-band absorption coefficient $\alpha = 9.85$ cm^{-1} and assuming the wafer has a thickness of 300 microns, $\Re \approx 1.1$. For simplicity I will just assume that $\Re = 1$. The fractional signal is then given by:

$$f_{fca} = \frac{1}{2} \sigma_{FCA} \frac{P_0 \lambda}{\pi w^2 hc} f_a \frac{\tau}{1 + i\omega\tau} \tag{6.32}$$

Letting the modulation frequency go to 0, and collecting $P_0/\pi w^2$ into the pump intensity I_{pu}:

$$f_{fca} = \frac{1}{2} \sigma_{FCA} I_{pu} \frac{\lambda}{hc} f_a \tau \tag{6.33}$$

Rearranging, the lifetime-intensity product can be written in terms of f_{fca}:

$$I_{pu}\tau = \frac{2hc}{\lambda}\frac{1}{\sigma_{FCA}f_a}f_{fca} \tag{6.34}$$

With the intensity-lifetime product known, one can set the intensity required to achieve a particular lifetime measurement sensitivity. Using the pump wavelength $\lambda = 1064$ nm, FCA cross section[23] $\sigma_{FCA} = 8\mathrm{x}10^{-10}$ μm^2, $f_a = 1$, and $f_{fca} = 6.10\mathrm{x}10^{-5}$ the intensity-lifetime product is $2.85 \times 10^{-2}\frac{W \cdot s}{m^2}$. The intensity used for the study in Figure 6.3 is $14{,}120$ W/m^2, so the minimum measureable lifetime is estimated to be $\tau = 2$ μs. Lifetimes on the order of microseconds represent the lower limit of recombination lifetimes in silicon [6], so if the single-beam pump/probe technique is sensitive to lifetimes this low, it is practical for general silicon lifetime metrology. The minimum detectable lifetime decreases with increasing intensity since higher intensity light results in a greater amount of FCA of the laser, leading to a higher signal.

6.5   Power Dependence of Single Beam Signal and measurement of σ_{FCA}

One way to further validate the single-beam pump/probe technique is to verify that the signal amplitude given by Equation (6.11) exhibits a linear dependence with incident power. The raw FCA signal as given by Equation (6.6) is quadratic with incident power because both the free-carrier population and the beam that probes it grow linearly with power. One of these power dependences is removed during the normalization procedure, hence why the final signal is linear with power. In this section I explore that dependence and show how the free-carrier absorption cross section σ_{FCA} can be measured. The cross section is in the range of values found in the

---

[23] This is approximately the value for σ_{FCA} experimentally measured in 6.5.

literature, which shows quantitative agreement between the signal-beam pump/probe model and experimental results.

I have examined the power dependence experimentally on the thick wafer. The pump beam diameter is set to 7.5 mm to ensure that radial diffusion effects are negligible, and for simplicity it will be assumed that the surface recombination in the wafer is negligible. In this configuration ξ is given by Equation (5.35). Substituting this into Equation (6.9):

$$S = 1 - 8\Re\eta \frac{1}{16}\sigma_{FCA}g_0(1 - e^{-\alpha\eta W})\frac{\tau}{1 + i\omega\tau} \tag{6.35}$$

The imaginary component of S contains exclusively the FCA signal:

$$Y = \text{Im}[S] = \Re\eta\frac{1}{2}\sigma_{FCA}g_0(1 - e^{-\alpha\eta W})\tau^2\frac{\omega}{1 + \omega^2\tau^2} \tag{6.36}$$

Substituting the value for g_0 (Equation (D.10)):

$$Y = \Re\eta\frac{1}{2}\sigma_{FCA}\left[\frac{2P_0\lambda}{\pi w^2 hc}\frac{1 - R}{1 - Re^{-\alpha\eta W}}\right](1 - e^{-\alpha\eta W})\tau^2\frac{\omega}{1 + \omega^2\tau^2} \tag{6.37}$$

$$Y = Y_a\frac{\omega}{1 + \omega^2\tau^2} \tag{6.38}$$

where Y_a is the imaginary amplitude, given by:

$$Y_a = \Re \eta \sigma_{FCA} \frac{P_0 \lambda}{\pi w^2 hc} f_a \tau^2 \tag{6.39}$$

where I have used the fact that the fraction of power absorbed in the wafer f_a is given by $f_a = \frac{1-R}{1-Re^{-\alpha\eta W}}(1-e^{-\alpha\eta W})$ (Equation (I.19)). Substituting in the value for $\Re$ (equations (5.8), (5.11) & (5.12)):

$$Y_a = \left[\frac{1 + R^2 e^{-2\eta\alpha W}}{1 - R^2 e^{-2\eta\alpha W}} \right] \eta \sigma_{FCA} \frac{P_0 \lambda}{\pi w^2 hc} f_a \tau^2 \tag{6.40}$$

$$Y_a = K\tau^2 \sigma_{FCA} P_0 \tag{6.41}$$

where K is a proportionality constant given by:

$$K = \left[\frac{1 + R^2 e^{-2\eta\alpha W}}{1 - R^2 e^{-2\eta\alpha W}} \right] \eta \frac{\lambda}{\pi w^2 hc} f_a \tag{6.42}$$
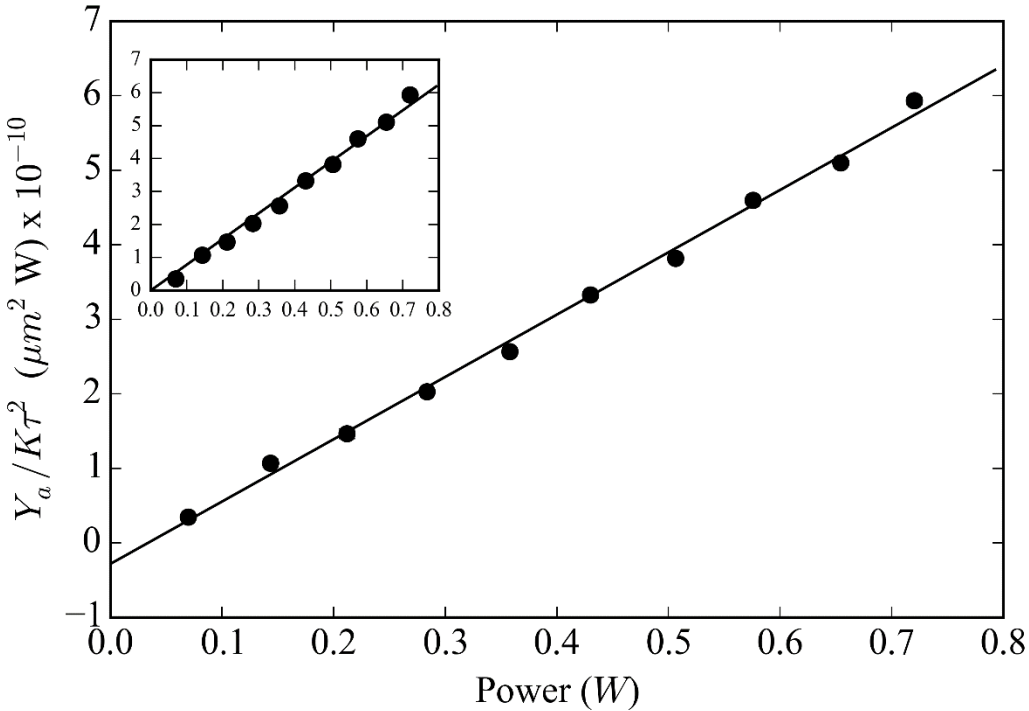
Figure 6.7: Plot of $Y_a/K\tau^2$ vs average incident power on Thick Sample. The trend is linear as predicted by Equation (6.41). Inset: Same plot but with the line of best-fit forced through 0.

According to (6.41) a plot of $Y_a/K\tau^2$ vs incident power P_0 should yield a straight line whose slope is σ_{FCA}. An experiment was performed on the thick wafer to validate this relationship. The beam radius was set to 7.5 mm to eliminate the effect of radial diffusion. At each power the frequency spectrum is swept out and the imaginary component is fitted to Equation (6.38) to extract Y_a & τ. The value of K is computed using (6.42) and then the values of $Y_a/K\tau^2$ are plotted vs the average incident power in Figure 6.7. The vertical error bars on the datapoints are too small to see, with most being below 1%. It is clear that the dependence is indeed linear with most of the datapoints falling on to the line of best-fit. There is a slight offset from 0. The spread of datapoints in Figure 6.7 is indicative of an underlying uncertainty that has not been accounted for. One possible origin of the uncertainty is from the normalization procedure that divides the sample spectrum by the background spectrum (Equation (6.9)). The normalization procedure assumes that the power into the detector is identical when the sample and background spectra are taken. Deviations from this

assumption would result in an incomplete removal of the prefactor during normalization, changing the value of the amplitude. The FCA cross section, as measured by the slope of the line, is $\sigma_{FCA} = (4.2 \pm 0.1)$ x 10^{-10} μm^2. The error[24] in σ_{FCA} arises from the spread of the datapoints about the straight line in Figure 6.7, as well as the uncertainty in the factor K. As will be discussed further in 7.4 there is a wide spread in σ_{FCA} values across the literature, with the values varying by about a factor of 5. Svantesson [64] measured a cross section of $\sigma_{FCA} = 5.1$ x 10^{-10} μm^2 at 1064 nm. Meitzner et al. [45] measured a cross section of $\sigma_{FCA} = 16.9$ x 10^{-10} μm^2 at 1510 nm, which becomes $\sigma_{FCA} = 8.39$ x 10^{-10} μm^2 when corrected to a value at 1064 nm using the λ^2 scaling of the FCA cross section [58]. The FCA cross section will be discussed further in 7.4.

In Figure 6.7 the y-intercept of the line of best-fit was left as a fit parameter. This results in a non-zero intercept in the main figure, which is unphysical since the signal amplitude must go to 0 when the power is 0. This implies some sort of systematic offset or that a straight line is not an appropriate fit to the data. As will be discussed in 7.5 the value of σ_{FCA} is not constant and actually increases with increasing injected carrier density. This would imply that σ_{FCA} is increasing with power in Figure 6.7. The inset of the figure shows the same plot with the line of best-fit forced through 0. For low powers the datapoints are below the line and at higher powers they are above, which is consistent with σ_{FCA} increasing as the power increases. Although σ_{FCA} changes with carrier density, Figure 6.7 provides evidence that this change is not significant. In any case the variation of σ_{FCA} only has consequences for the amplitude of the signal. The frequency-dependence will not be affected by this variation unless the carrier density changes significantly

---

[24] The values of Y_a & τ are measured at each power, while the factor K is unchanged measurement-to-measurement. The uncertainty in slope arises from the statistical spread of Y_a/τ, and from the uncertainty in the factor K. To compute the uncertainty of σ_{FCA}, Y_a/τ is plotted vs power and the slope uncertainty is extracted from the square root of the covariance. σ_{FCA} is then computed by dividing Y_a/τ by K, and the uncertainty is computed by propagating the uncertainty.

in a measurement. Since this is an AC measurement, the change in carrier density can be kept small by tuning the modulation depth m.

6.6   Validation of Radial Diffusion

In 6.3 I demonstrated that the single beam pump/probe technique extracts the same lifetime value as dual-beam pump/probe in the limit where the beam radius is large enough to mitigate radial diffusion effects. In this section I will examine the more general case where both recombination and carriers escaping the beam via radial diffusion affect the frequency-response of the FCA signal. As discussed above, it is the imaginary component of the signal that is extracted experimentally. This signal is given by substituting the ξ factor from Equation (6.2) into Equation (6.11):

$$Y = -8\Re\eta\sigma_{FCA}\tau_D g_0 \alpha\eta e^{-\frac{\alpha\eta W}{2}} A_1^{lc} \, \text{Im}\left[e^{\frac{2\tau_D}{\tau_1'}}\Gamma\left(0, \frac{2\tau_D}{\tau_1'}\right)\right] \tag{6.43}$$

To simplify the discussion, I have used only the first term of the series over n in (6.43), which is justified when the absorption coefficient is low ($\alpha W \sim 1$) as discussed in 3.3.2. Next, the expression for τ_1' is substituted, which contains the frequency dependent terms (Equation (5.25)):

$$Y = Y_0 \, \text{Im}\left[e^{\frac{2\tau_D}{\tau}(1+i\omega\tau)}\Gamma\left(0, \frac{2\tau_D}{\tau}(1+i\omega\tau)\right)\right] \tag{6.44}$$

Here I have bundled together the prefactor into a constant Y_0. All of the frequency dependent terms are contained within the imaginary component of the exponential and incomplete Gamma function terms.

I will validate (6.44) experimentally by comparing the lifetime measured by the single and dual-beam methods when the pump beam is smaller than the diffusion length of free-carriers. I have performed this experiment on the thick wafer (see Table I for specifications). The beam radius is set with a lens by moving the position of the lens with respect to the sample holder. The lens has a long focal length (~5 cm) so the beam radius changes slowly as it the beam propagates. The wafer under study has a thickness of 1.5 mm, so the beam radius will not change appreciably when propagating through the wafer. This condition is necessary since the model assumes that w is constant along the z axis of the wafer. The beam radius is measured by the Nanoscan beam-profiler, which measures an average radius of 46 μm (see Figure K.2).

Figure 6.8: Comparison of Y for single and dual-beam techniques at a pump-beam radius of 46 μm. Markers represent experimental datapoints and solid lines represent fits. Single and dual-beam data are fit to the frequency dependence in Equations (6.44) and (3.30), respectively. Single-beam data is given in absolute units, whereas dual-beam data is arbitrarily scaled for comparison.

Figure 6.8 plots the single and dual-beam frequency spectra for a pump radius of 46 μm. The single-beam data is given in absolute units, and the dual-beam data is arbitrarily scaled for

comparison. The effective lifetime measured by the peak of the dual-beam data is 111 μs, which corresponds to a diffusion length of $\sqrt{D\tau} = 421$ μm if $D = 16$ cm^2/s. Therefore the beam radius is about nine times smaller than the diffusion length. As discussed in 6.2.2 (Figure 6.1 in particular) when the beam radius is small with respect to the diffusion length the measured lifetime is shorter than the effective recombination lifetime since there is a competing radial diffusion process by which carriers escape the probe beam. Experimentally this manifests as a shift towards high frequencies, as well as a broadening of the peak from the imaginary component of the measured signal. This behavior can be seen in Figure 6.8 in the single-beam frequency-spectrum. The peak frequency has shifted from 1.43 kHz to 20.7 kHz and the peak is significantly broader. The lifetime measured by the peak of the single-beam spectrum is 7.68 μs, which is about 7% of the effective recombination lifetime. According to Equation (6.12), this corresponds to a radial lifetime of $\tau_r = 8.25$ μs. Clearly the lifetime is now dominated by radial diffusion effects, and not the recombination lifetime.

From Figure 6.8 it can be seen that the single-beam data is fitted well to Equation (6.44). Quantitatively, the single-beam fit yields an effective recombination lifetime of $\tau_{SB} = 112.7 \pm 1.4$ μs and the dual-beam data yields $\tau_{DB} = 111.4 \pm 0.5$ μs. Thus the single-beam technique measures lifetimes that are consistent with the dual-beam method, even when radial diffusion effects are dominant. Since radial diffusion effects are now in play, information about the diffusion coefficient D can be directly inferred from the fit parameter τ_D, which is given by $w^2/8D$. The fitted value is $\tau_D = 54 \pm 3$ ns. The average beam radius was measured[25] to be $w = 46 \pm 6$ μm. From this average radius and the fitted diffusion time constant τ_D, I calculate that the diffusion coefficient should be $D = 49 \pm 14$ cm^2/s. This is too high for crystalline silicon, where the

---

[25] The beam radius is measured by the Nanoscan beam profiler (see Figure K.2 for the beam profile). The profiler showed an eccentricity of 1.32 between the x and y components of the beam. For calculations, the beam radius is taken as the average of the radius of the x and y components, and the uncertainty is taken as the standard deviation of the values.

maximum ambipolar diffusion coefficient is about $D = 16 \text{ cm}^2/\text{s}$ [81]. The beam radius that has been experimentally measured clearly does not yield a consistent diffusion coefficient from the fitted τ_D. One hypothesis for this is that the fit of τ_D & τ is not unique, and the least-squares fitting method converged on a local minimum instead of the global minimum around the true values of τ_D & τ. Since Equation (6.44) has a different functional dependence on τ than τ_D it appears unlikely that different pairs of τ_D & τ would properly fit the experimental dataset.
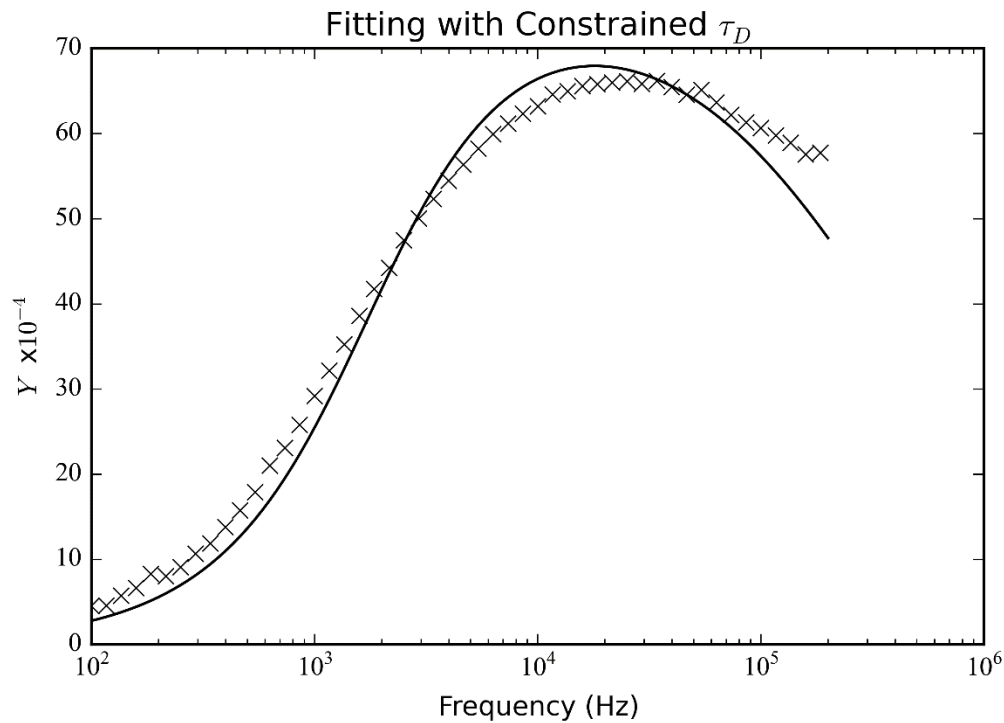
Figure 6.9: Fitting single-beam data with constrained τ_D. τ_D is constrained to be within +- 10% of the value that it should be based on the measured beam radius and estimated diffusion coefficient.

One way to demonstrate the uniqueness of the fit in Figure 6.8 is to constrain τ_D to be close to its true value, and then fit for τ. If the fit in Figure 6.8 is not unique, then it is expected that the fitting algorithm will find a curve that matches experimental data well, but gives a spurious value for τ. Figure 6.9 shows this fit, with τ_D constrained to be within 10% of the calculated value ($\tau_D = 165$ ns). The fitted lifetime is now $\tau = 90 \pm 4$ µs, which is inconsistent with the dual-beam lifetime $\tau_{DB} = 111.4 \pm 0.5$ µs. Clearly the quality of the fit has degraded dramatically when τ_D is

constrained, which shows that the fit in Figure 6.8 is indeed unique. Since the fit to the single-beam data in Figure 6.8 extracts the correct effective recombination lifetime, it is likely that the τ_D value I have calculated is incorrect. It is possible that the beam radius that was measured is erroneous. Using a diffusion coefficient of $D = 16 \text{ cm}^2/\text{s}$ and the fitted value for τ_D, I calculate that the beam radius should be $w = 26 \text{ µm}$. This is about a factor of $\sqrt{3}$ smaller than the radius that I measured. Assuming the beam waist is equal to 26 µm, the beam radius will expand[26] to 46 µm over a distance of 4.2 mm from the beam waist. The positioning of the beam profiler was performed by eye, and it is quite possible that there is at least a 4 mm discrepancy between the plane of the profiler and the plane of the sample holder. This could easily explain the discrepancy in the τ_D I determine from fitting, and the one I calculate from beam radius measurements. Further investigation is required in order to conclusively determine whether or not the fitted τ_D is accurate.

---

[26] The beam radius as a function of propagation distance for a Gaussian beam is given by $w = w_0\sqrt{1 + \left(\frac{z}{z_R}\right)^2}$, where w_0 is the beam waist, and $z_R = \pi w_0^2/\lambda$ is the Rayleigh length.

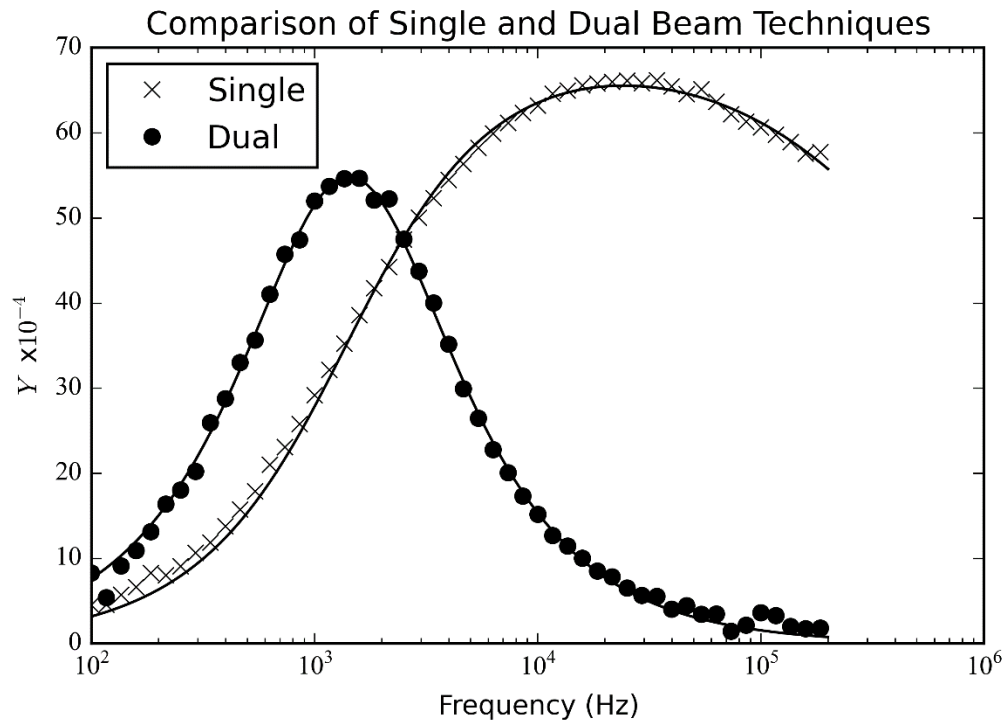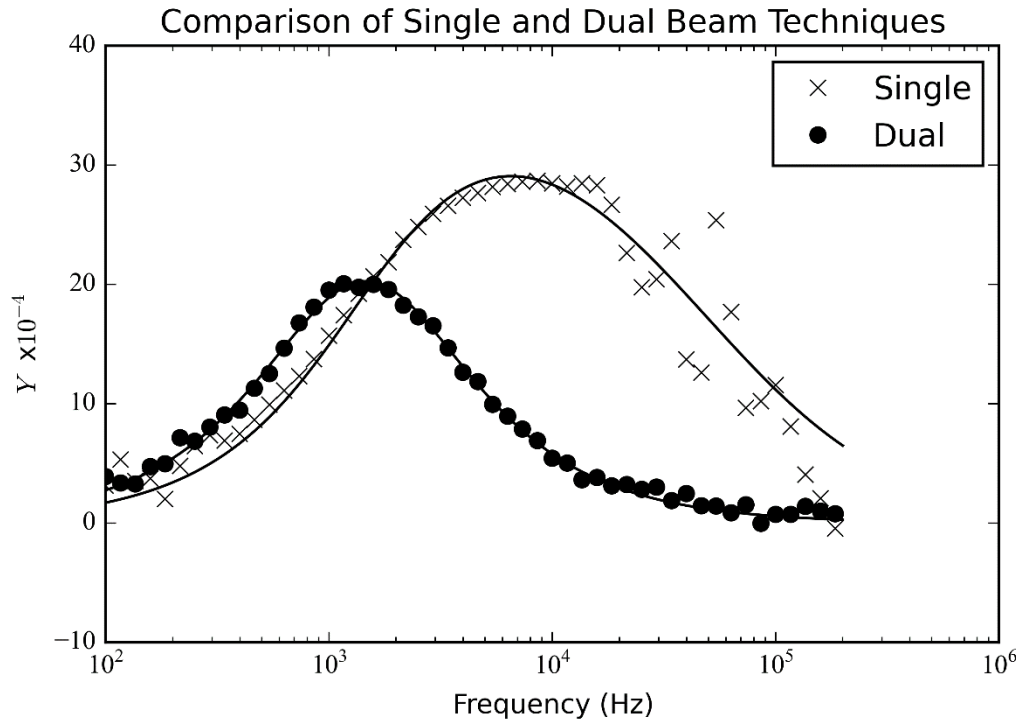Figure 6.10: Comparison of Y for single and dual-beam techniques at a pump-beam radius of 72 μm. Markers represent experimental datapoints and solid lines represent fits. Single and dual-beam data are fit to the frequency dependence in Equations (6.44) and (6.25), respectively. Single-beam data is given in absolute units, whereas dual-beam data is arbitrarily scaled for comparison.

To show that the results of Figure 6.8 were not just a coincidence I performed the same measurement at a beam radius of 72 μm. The comparison of the single and dual-beam techniques for this pump radius is shown in Figure 6.10. There is a greater spread in high frequency datapoints, which suggests some sort of noise effect. I am not sure what the origin of this is since the same effect is not seen at low-frequency datapoints, which would be more susceptible to noise anyways. In any case, the lifetimes fitted by the single and dual beam techniques are $\tau_{SB} = 109 \pm 19$ μs and $\tau_{DB} = 108.8 \pm 0.9$ μs, respectively. Again the effective recombination lifetime measured by the single and dual beam techniques is the same to within the measurement precision. This time the fitted value of the diffusion time constant is $\tau_D = 1.53 \pm 0.38$ μs. The longer diffusion time constant than the previous dataset is consistent with the larger beam radius. Using the measured beam radius of $w = 72 \pm 5$ μm and the fitted value for τ_D leads to a diffusion coefficient of $D =$

$4.2 \pm 1.2 \text{ cm}^2/\text{s}$. This value is within the realm of possibility for silicon and suggests a high level of carrier injection. The injected carrier density can be calculated via Equation (3.16). In this case the generation rate can be estimated by dividing the total photon flux absorbed in the wafer $(P_0 \lambda f_a / hc)$ by the cylindrical volume the carriers occupy after diffusion. This is just the total number of photons absorbed in the wafer, divided by a cylinder of volume $\pi L^2 W$, where $L = \sqrt{D\tau}$ is the diffusion length and W is the wafer thickness. The estimate for the carrier density is then given by:

$$ n = \frac{P_0 \lambda f_a / hc}{\pi L^2 W} \tau = \frac{P_0 \lambda f_a}{hc\pi DW} \tag{6.45} $$

For the data displayed in Figure 6.10, the average power is $P_0 = 32$ mW and the fraction of power absorbed in the wafer is about $f_a = 0.65$. Using the diffusion coefficient of $D = 4.2 \text{ cm}^2/s$ and the wafer thickness $W = 1470$ μm, the injected carrier density is estimated to be $n = 5.74\text{x}10^{16} \text{ cm}^{-3}$. According to Refs [81] the diffusion coefficient should be greater[27] than $10 \text{ cm}^2/\text{s}$. Again, one possibility for this is that the beam radius used for the calculations is incorrect. Further experimental work is required in order to answer this question.

Regardless of the discrepancies between the calculated and fitted τ_D factors in Figure 6.8 and Figure 6.10, the effective lifetime measured by single-beam pump/probe is the same as dual-beam pump/probe to within experimental precision for both of these datasets. This is an important result because it shows that even when the beam radius is very small with respect to the diffusion length, the true effective recombination lifetime can still be measured. In fact, it is quite remarkable that this is the case. As shown in the discussion of the dataset in Figure 6.8, the lifetime measured by the peak of the single-beam spectrum is $\tau_{3D} = 7.68$ μs whereas the radial lifetime is determined

---

[27] It is self-referential to use the diffusion coefficient to estimate the carrier density, which is then used to estimate the diffusion coefficient. This is valid here since the diffusion coefficient varies slowly (by a factor <10) while n varies over orders of magnitude.

to be $\tau_r = 8.25$ μs. Since the effective recombination lifetime is about $\tau = 109$ μs, the dataset in Figure 6.8 is clearly diffusion-limited. However, the true effective lifetime can still be determined by fitting of the curve. This section has demonstrated that the beam radius isn't required for measuring the effective recombination lifetime, and even in the case when the radius is small and the lifetime is diffusion limited, the recombination lifetime can be determined.

6.7   Additional Considerations

In this section I discuss some additional considerations about the single-beam technique. The first is the range of viable sample thicknesses that can be studied. In order to measure the transmitted pump beam, a non-negligible fraction of the laser beam must be transmitted through the wafer. For 1064 nm radiation whose absorption coefficient in silicon is 9.85 cm^{-1}, the maximum wafer thickness such that 1% of the pump beam transmits through the wafer is about 4.7 mm ($e^{-\alpha W} = 0.01$). This is sufficient for most applications since silicon wafers are usually on the order of hundreds of microns in thickness. For example, photovoltaic applications typically use wafer thicknesses on the order of 200 μm. For thinner wafers the fraction of power absorbed at 1064 nm becomes smaller due to the poor absorption of this wavelength. At $W = 100$ μm, only 10% of the beam will be absorbed. For thinner samples then, it might be useful to use shorter wavelength radiation where the absorption coefficient is higher.

Another consideration is the interplay between band-to-band absorption and free-carrier absorption. It has been assumed that the band-to-band absorption which generates the free-carriers and the FCA which probes them are independent of each other. This is valid when the FCA is much smaller than band-to-band absorption. However, when the carrier density is high enough that FCA and band-to-band absorption are comparable, the FCA will lead to a saturation of band-to-band absorption. The rate of band-to-band absorption will be limited by FCA. I have neglected this effect in this work, which I will justify with the following analysis. In general, the interplay between band-to-band and FCA can be accounted for by modifying the generation term of the continuity equation. The 1D continuity equation accounting for free-carrier absorption is given by:

$$\frac{\partial n}{\partial t} = D \frac{\partial^2 n}{\partial z^2} - \frac{n}{\tau} + G_0(t)e^{-\left(\alpha z + \int_0^z \alpha_{FCA}(t)dz\right)} \tag{6.46}$$

where $\alpha_{FCA}(t)$ is the FCA coefficient, given by:

$$\alpha_{FCA} = \sigma_{FCA}n(z,t) \tag{6.47}$$

Using a first order Taylor expansion on the FCA exponential and substituting in α_{FCA}:

$$\frac{\partial n}{\partial t} = D \frac{\partial^2 n}{\partial z^2} - \frac{n}{\tau} + G_0(t)e^{-\alpha z}\left(1 - \int_0^z \sigma_{FCA}n(z',t)dz'\right) \tag{6.48}$$

The last term in Equation (6.48) is the volumetric rate of free-carrier generation. It can be seen that the effect of FCA is to reduce the magnitude of the generation rate. This is intuitive of course, since FCA results in intraband transitions that do not contribute to the number of free-carriers. Equation (6.48) is an integro-differential equation. I have not been able to find an analytic solution to this equation. However, it can be easily shown that the FCA correction is negligible for the carrier densities reached in this work. First, assume that the equation is in steady state so that the time dependences drop out. Next, assume that $n(z)$ is uniform in z. Then the generation rate at the back side of the wafer is given by:

$$G = G_0 e^{-\alpha z}(1 - \sigma_{FCA}nW) \tag{6.49}$$

The fraction of the generation rate that is band-to-band absorption is simply:

$$f = \frac{G}{G_0 e^{-\alpha z}} = 1 - \sigma_{FCA} n W \qquad (6.50)$$

In this thesis I measure a value of $\sigma_{FCA} = 8 \times 10^{-10} \ \mu m^2$. If the wafer thickness is 300 μm, then:

$$f = 1 - 2.4 \times 10^{-19} n \qquad (6.51)$$

where n has units of cm^{-3}. In this work the injected carrier densities do not exceed $10^{17} \ cm^{-3}$ so the band-to-band absorption is at least 97.6% of the total absorption.

6.8 Summary

In this chapter I have developed single-beam pump/probe, which is a technique for measuring the recombination lifetime of semiconductors in which the pump and probe are the same beam. In 6.2.1 I use the generalized pump/probe equation (Equation (5.29)) to derive the model behind this technique. Since the pump and probe beam are the same, this is as straightforward as dropping all of the subscripts specific to pump and probe beams. In 6.2.2 I use this model to explore the consequences that beam diameter has on the measurement of lifetime, from a theoretical point of view. In the limit when the beam diameter is large with respect to the diffusion length, the model reduces to the solution of the 1D continuity equation. In this case the lifetime measured is the effective recombination lifetime that contains information about the bulk and surface recombination. When the beam diameter is small with respect to the diffusion length, the full 3D model is required to describe the measured lifetime. In this case, the lifetime contains bulk and surface recombination effects, as well as effects due to radial diffusion out of the probed volume. I discuss a numerical method for extracting the 1D effective lifetime for an arbitrary beam diameter from the peak of the imaginary component of the signal. In 6.3 I provide experimental demonstration of the single-beam technique in the case where the beam diameter is large with

respect to diffusion length. The results are compared with the dual-beam technique, and are consistent. In 6.4 I discuss the specifics of how single-beam pump/probe data is actually acquired and how experimental drift, and not random noise, degrades single-beam data. I implement a strategy for eliminating the drift effects and show that the detection floor is comparable to the bit-resolution on the instrument that digitizes the signal. In 6.5 I show that the amplitude of the signal is quantitatively consistent with the model I have derived. Using the power dependence of the signal I am able to extract the free-carrier absorption cross section σ_{FCA} of silicon, which is consistent with values from the literature. In 6.6 I demonstrate a more general application of single-beam pump/probe where the radius is small enough for radial diffusion, as well as bulk and surface recombination, to affect the measured lifetime. In the case where beam radius is very small with respect to the diffusion length, I show that the single-beam frequency spectrum is shifted towards higher frequencies and significantly broadened, as is expected from theory. The mathematical model fits the experimental data well, and the effective recombination lifetime that is measured is identical to that of the dual-beam technique, to within experimental precision. The diffusion time constants τ_D that are measured are not consistent with calculated values, which I attribute to erroneous measurements of the beam radius; further experimental work is required in order to verify this. Based on the results of this chapter, I have demonstrated for the first time a single-beam pump/probe technique that is capable of extracting the same recombination lifetime as the traditional dual-beam technique. This cements single-beam pump/probe as a viable alternative to the state-of-the-art pump/probe technique.

7 Quasi-Steady State Free-Carrier Absorption

7.1 Overview

In this section I introduce Quasi-Steady State Free Carrier Absorption (QSS-FCA), a new QSS technique for measuring lifetime based on free-carrier absorption. This technique employs the same dual-beam pump/probe geometry used in time or frequency-resolved FCA lifetime techniques, but improves upon these techniques by reducing the measurement of lifetime to a single data point acquired at low frequency. As was detailed in Chapter 3, the advantage of steady-state/quasi-steady state over transient/roll-off techniques is that the measurement is performed at low frequencies, so the experimental apparatus only requires a modest bandwidth. The disadvantage is that signal must be resolved in absolute units, which often requires calibration of the measurement apparatus. The industry standard QSS technique, QSSPC, was reviewed in Chapter 2 along with other QSS techniques such as ILM and CDI. Both QSSPC and CDI use reference wafers of known conductivity for their calibration. The reference wafer establishes the relationship between the signal measured from the apparatus and the free-carrier density in the wafer. With this calibration, the excess free-carrier density of an arbitrary wafer can be measured, and converted to a lifetime using Equation (3.16). There are several issues with this calibration procedure that are overcome with the QSS technique that I develop here. In QSS-FCA, the relationship between the signal measured by the apparatus and the recombination lifetime is established directly, without using a reference sample with specified electronic properties. The calibration constant is the free-carrier cross section σ_{FCA}, which is a material constant. This is in contrast to QSSPC where the calibration constant contains geometrical factors related to the position of the sample with respect to the photoconductivity sensor. Since the calibration constant for QSS-FCA is a material constant, once it is established it needn't ever be measured again and is valid for any experimental configuration. This provides an experimenter with much greater flexibility in building a QSS-FCA apparatus as opposed to a QSSPC system.

In 7.2 I use the generalized pump/probe theory I developed in 5.3 to derive a mathematical model describing QSS-FCA. This theory is validated experimentally in 7.3 on two n-type silicon wafers and a value for the free-carrier absorption cross section σ_{FCA} is measured. In 7.4 I compare my value of σ_{FCA} with values from the literature, which reveals a discrepancy. Reasons for the discrepancy are proposed as well as how to reconcile them. The underlying physics of σ_{FCA} and how it relates to my work and other work are also discussed. In 7.5 I discuss the dependence of σ_{FCA} on the free-carrier density, having previously treated σ_{FCA} as a constant in 7.3. I find that this dependence is described reasonably well by the classical Drude model, which has not been demonstrated elsewhere as far as I am aware. In 7.6 I discuss how to account for the dependence of σ_{FCA} on free-carrier density so that lifetime may still be measured unambiguously under QSS conditions.

7.2   Quasi-Steady State Free-Carrier Absorption-Theoretical Description

The recommended geometry for two-beam pump/probe studies in silicon is to use a pump beam with diameter much larger than that of the probe beam, and large enough that radial diffusion effects can be neglected ($\tau_D^{pu} \gg \tau_n'$) [38]. This is Case 2 of ξ given in 5.4. This ensures that the 1-dimensional continuity equation holds[28], and that the probe beam examines an area of uniform illumination, mitigating effects of radial diffusion. Experimentally it is the change in transmitted probe power due to FCA that is measured, and this is related to the recombination lifetime. The equation describing the probe transmission as a function of time can be derived from Equation (5.29), which is the generalized pump/probe equation. In QSS-FCA the pump beam is modulated harmonically at angular frequency ω, (*i.e.* $\omega_{pu} = \omega$), while the probe beam is unmodulated ($m_{pr} = 0$). Using the generalized pump/probe equation (5.29), the transmitted probe power is:

---

[28] Reference [38] states that "Only if the illuminating spot has a diameter more than five times the sample thickness is the simplification valid". This is given without any justification. According to my model, the only condition required for the 1D continuity equation to be valid is for $(\tau^{pu} + \tau^{pr}) \gg \tau_n'$.

$$\tilde{P}_{tr} = \frac{T_{pr}^2}{1 - R_{pr}^2} P_{pr}\left(1 - 8\Re_{pr}\eta_{pr}m_{pu}\xi(\omega)e^{i\omega t}\right)$$
(7.1)

Note that the primes in the P_{pr} and R_{pr} terms have been dropped. This is because the probe beam has energy below the bandgap of the semiconductor and so the band-to-band absorption factor β_{bb} in Equations (5.10) & (5.11) is 0. Since the probe radius is very small compared to the pump, and the pump beam is sufficiently large, ξ simplifies. This case is given by Equation (5.33) ($\tau_D^{pu} \gg \tau_D^{pr}$):

$$\xi = \sigma_{FCA}g_0\alpha\eta e^{-\frac{\alpha\eta W}{2}}\sum_n \frac{\tau}{1 + i\omega\tau}A_n^{lc}$$
(7.2)

Substituting in the value for g_0 (Equation (D.10)):

$$\xi = \sigma_{FCA}\left[\frac{2P_{pu}\lambda_{pu}}{\pi w_{pu}^2 hc}\frac{1 - R_{pu}}{1 - R_{pu}e^{-\alpha\eta W}}\right]\alpha\eta e^{-\frac{\alpha\eta W}{2}}\sum_n \frac{\tau}{1 + i\omega\tau}A_n^{lc}$$
(7.3)

Multiply the top and bottom of (7.3) by $8(1 - e^{-\alpha\eta W})$ and use the fact that the fraction of pump power absorbed in the wafer is given by $f_a = \frac{(1-R)(1-e^{-\alpha\eta W})}{1-Re^{-\alpha\eta W}}$ (Equation (I.19)):

$$\xi = \sigma_{FCA} \frac{2P_{pu}\lambda_{pu}}{\pi w_{pu}^2 hc} \frac{f_a}{8} \left[\frac{8\alpha\eta e^{-\frac{\alpha\eta W}{2}}}{1 - e^{-\alpha\eta W}} \sum_n \frac{\tau_n}{1 + i\omega\tau_n} A_n^{lc} \right] \tag{7.4}$$

The factor in the square brackets is $\mathfrak{T}$ from Chapter 3 (Equation (3.30)), where $\mathfrak{T} \equiv N(\omega)/G(\omega)$. Recall that Equation (3.30) is the general solution to the 1D diffusion equation in the frequency domain, neglecting the radial diffusion. This is expected of course since the pump beam diameter is large enough to neglect radial diffusion effects. The expression for $\mathfrak{T}$ is relatively complicated and includes the bulk lifetime, surface recombination velocity and diffusion coefficient, among other parameters. However, as described in Chapter 3, regardless of the values of the bulk lifetime and surface recombination velocity, the shape of $\mathfrak{T}$ is still Lorentzian unless both the absorption coefficient and surface recombination velocity is very high. Since this experiment uses a pump laser with wavelength very close to the band edge of silicon, the absorption coefficient is small and it is expected that $\mathfrak{T}$ is Lorentzian in shape. Another way of saying this is that only the first term in the series in Equation (7.4) is dominant (see discussion of Figure 3.7). Rewriting with only the first term:

$$\xi = \sigma_{FCA} \frac{2P_{pu}\lambda_{pu}}{\pi w_{pu}^2 hc} \frac{f_a}{8} \left[\frac{8\alpha\eta e^{-\frac{\alpha\eta W}{2}}}{1 - e^{-\alpha\eta W}} \frac{\tau}{1 + i\omega\tau} A_1^{lc} \right] \tag{7.5}$$

Recall that by definition, $\mathfrak{T}(0) = \tau_{qss}$, where τ_{qss} is the quasi-steady state lifetime. Since the term in square brackets in Equation (7.5) is $\mathfrak{T}$ then τ_{qss} is given by:

$$\tau_{qss} = \frac{8\alpha\eta e^{-\frac{\alpha\eta W}{2}}}{1 - e^{-\alpha\eta W}} A_1^{lc}\tau \tag{7.6}$$

In the limit where the pump absorption coefficient is low $(\alpha W \sim 1)$, $\tau_{qss} \sim \tau$, as discussed in Chapter 3 (Figure 3.8). For the sake of generality I will keep the symbol τ_{qss} and not substitute τ. However, unless otherwise specified, they can be treated as equivalent for the remaining discussion.

Substituting τ_{qss} into (7.5):

$$\xi = \sigma_{FCA}\frac{2P_{pu}\lambda_{pu}}{\pi w_{pu}^2 hc}\frac{f_a}{8}\frac{\tau_{qss}}{1 + i\omega\tau} \tag{7.7}$$

Substituting ξ back into (7.1):

$$\tilde{P}_{tr} = \frac{T_{pr}^2}{1 - R_{pr}^2}P_{pr}\left(1 - \Re_{pr}\eta_{pr}m_{pu}\sigma_{FCA}\frac{2P_{pu}\lambda_{pu}}{\pi w_{pu}^2 hc}f_a\frac{\tau_{qss}}{1 + i\omega\tau}e^{i\omega t}\right) \tag{7.8}$$

To simplify the interpretation of the experiment, the probe is p-polarized and brought into the sample at Brewster's angle. This results in zero reflectance from the front and back surfaces (*i.e.* $T_{pr} = 1$, $R_{pr} = 0$, and $\Re = 1$):

$$\tilde{P}_{tr} = P_{pr}\left(1 - \eta_{pr}m_{pu}\sigma_{FCA}\frac{2P_{pu}\lambda_{pu}}{\pi w_{pu}^2 hc}f_a\frac{\tau_{qss}}{1 + i\omega\tau}e^{i\omega t}\right) \tag{7.9}$$

Taking the real part of (7.9) yields the transmitted probe power that is measured experimentally:

$$P_{pr} = P_{pr}\left(1 - \eta_{pr}m_{pu}\sigma_{FCA}\frac{2P_{pu}\lambda_{pu}}{\pi w_{pu}^2 hc}f_a\frac{\tau_{qss}}{1+\omega^2\tau^2}(\cos\omega t + \omega\tau\sin\omega t)\right) \tag{7.10}$$

Experimentally, the power is transduced onto a detector and the resultant signal is demodulated on a lock-in amplifier at the frequency ω. From Equation (7.10) it can be seen that the signal consists of in-phase and out-of-phase components, given by the coefficients of the $\cos\omega t$ and $\sin\omega t$ terms, respectively. The signal can be written in terms of a complex number $\mathcal{S}(\omega)$ where the real and imaginary components correspond to the in-phase and out-of-phase components of the signal:

$$\mathcal{S}(\omega) = \zeta(\omega)\eta_{pr}m_{pu}\sigma_{FCA}\frac{2P_{pu}\lambda_{pu}}{\pi w_{pu}^2 hc}f_a\frac{\tau_{qss}}{1+i\omega\tau} \tag{7.11}$$

where $\zeta(\omega)$ is the transimpedance transfer function of the detector. The signal is represented as a complex number since it is has a component that is in-phase and a component that is out-of-phase with the detector. The real and imaginary parts of the term after $\zeta(\omega)$ are the prefactors of the $\cos\omega t$ and $\sin\omega t$ terms in Equation (7.11). Equation (7.11) states that the signal measured as a function of frequency follows a Lorentzian frequency dependence like the one shown in Figure 3.5. The QSS region is defined by the flat region of the roll-off curve when the modulation frequency is small compared to the inverse effective lifetime. From the measurement of this amplitude, the lifetime τ_{qss} may be measured.

In the quasi-steady state limit ($\omega\tau \ll 1$) Equation (7.11) reduces to:

$$S_{qss} = \zeta(0)\eta_{pr}m_{pu}\sigma_{FCA}\frac{2P_{pu}\lambda_{pu}}{\pi w_{pu}^2 hc}f_a\tau_{qss} \tag{7.12}$$

From Equation (7.11) it is clear that the lifetime may be extracted in two ways. By sweeping the modulation frequency ω from low to high values the Lorentzian decay is swept out (see Figure 3.5) and may be fitted to find τ. This of course is how lifetime is measured using the MFCA technique. Alternatively, in the quasi-steady state limit $(\omega\tau \ll 1)$ $S(\omega)$ becomes linearly proportional to τ_{qss}. If the proportionality constant is known, then a direct measurement of S_{qss} yields the lifetime. This is the basis of the Quasi-Steady State Free-Carrier Absorption technique.

The signal from the probe detector has an AC and DC component. The AC component is due to the modulation of excess free-carriers by the pump beam. The DC component is due to unmodulated transmission of the CW probe laser, which is given by $S_{DC} = \zeta(0)P_{pr}$. Dividing the QSS signal by the DC signal yields the *reduced signal s*:

$$s \equiv \frac{S_{qss}}{S_{DC}} = \eta_{pr}m_{pu}\sigma_{FCA}\frac{2P_{pu}\lambda_{pu}}{\pi w_{pu}^2 hc}f_a\tau_{qss} \tag{7.13}$$

Bundling experimental factors into a proportional constant K:

$$s = K\sigma_{FCA}\tau_{qss} \tag{7.14}$$

where K is given by:

$$K = \eta_{pr} m_{pu} \frac{2P_{pu}\lambda_{pu}}{\pi w_{pu}^2 hc} f_a \tag{7.15}$$

The reduced signal s can also be written in terms of the excess carrier density n. This formulation will be useful later on. In steady-state, the excess carrier density n is given by Equation (3.16). The generation rate G is just the average photon-flux density absorbed inside the wafer divided by the wafer thickness. The average photon flux density for a Gaussian beam is $2P_{pu}/\pi w^2 hc$. Thus the average generation rate is given by:

$$G = \frac{1}{W} \frac{2P_{pu}\lambda_{pu}}{\pi w_{pu}^2 hc} f_a \tag{7.16}$$

Using Equation (3.16) and (7.16) the AC excess carrier density n_{AC}[29] is given by:

$$n_{AC} = \frac{1}{W} \frac{2P_{pu} m_{pu} \lambda_{pu}}{\pi w_{pu}^2 hc} f_a \tau_{qss} \tag{7.17}$$

---

[29] The subscript 'AC' is used here to differentiate the excess carrier density extracted via an AC measurement to the average excess carrier density. The DC excess carrier density is given by n_{AC}/m_{pu} where m_{pu} is the modulation depth of the laser.

Note that the power term P_{pu} is multiplied by the pump modulation depth m_{pu}. This is because Equation (7.17) describes the AC free-carrier density, which is due to the AC power $P_{pu}m_{pu}$. Using just the DC pump power P_{pu}, the average excess carrier density is given by:

$$n = \frac{1}{W} \frac{2P_{pu}\lambda_{pu}}{\pi w_{pu}^2 hc} f_a \tau_{qss} \tag{7.18}$$

$\mathcal{S}_{qss}$ can now be written in terms of the excess carrier density:

$$\mathcal{S}_{qss} = \zeta(0)\sigma_{FCA}n_{AC}W \tag{7.19}$$

Dividing $\mathcal{S}_{qss}$ by the DC probe signal $\mathcal{S}_{DC} = \zeta(0)P_{pr}$ and substituting $n_{AC} = m_{pu}n$ the reduced signal written in terms of n is given by:

$$\mathcal{s} = m_{pu}\sigma_{FCA}nW \tag{7.20}$$

Equation (7.14) demonstrates that the ratio of the AC to DC component of the probe signal in the QSS limit is linearly proportional to lifetime. If the proportionality constant is known, then the lifetime can be determined simply via a measurement of the AC and DC components of the probe signal. This is a significant simplification of the traditional MFCA technique since only a single low-frequency measurement of the probe signal is required to extract the lifetime. This eliminates the requirement of sweeping the modulation frequency and extracting lifetime from the frequency-response of the free-carrier population. The factor K contains only experimental constants and easily measured quantities, so its determination is straightforward. The factor σ_{FCA} is a material constant for silicon, which in principle means that it is well known and can simply be looked up.

In practice however, the value for σ_{FCA} varies widely across the literature, and has a high uncertainty [71]. Therefore it is advisable to first determine a value for σ_{FCA} so that it can be used in subsequent measurements. σ_{FCA} can be measured directly using Equation (7.14) if τ_{qss} is known *a priori*. Of course τ_{qss} can be measured independently using the MFCA!

7.3   Experimental Validation of Quasi-Steady State Free-Carrier Absorption
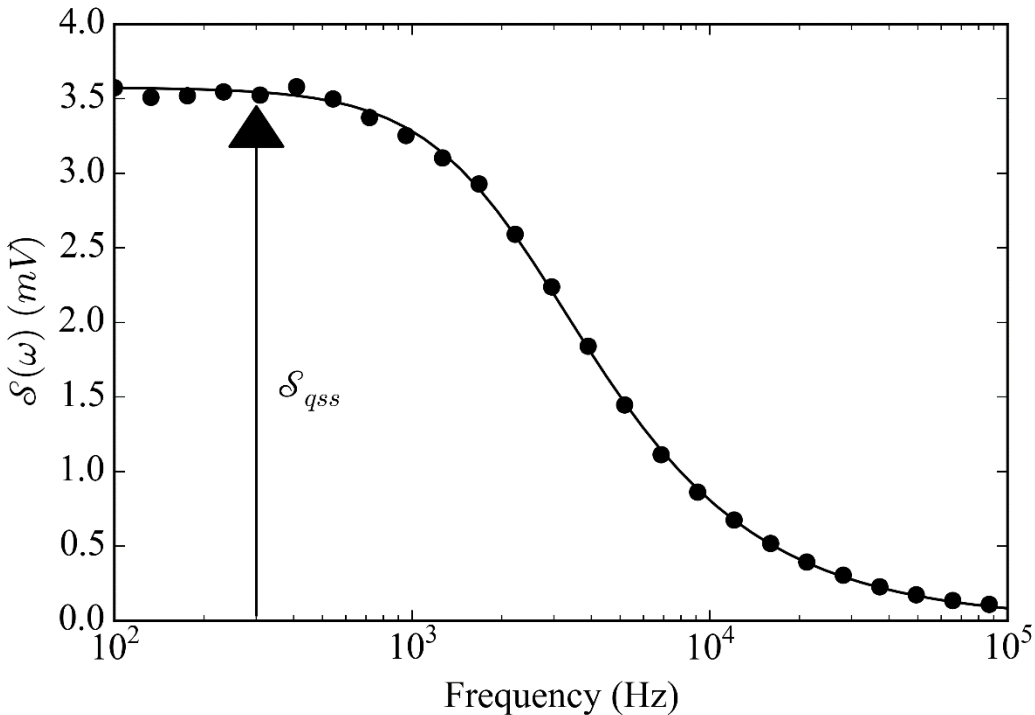
Figure 7.1: Plot of experimentally signal $\mathcal{S}(\omega)$ as a function of modulation frequency (dots). The data is fitted to the frequency dependence in Equation (7.11) (solid line). Data is from El-Cat 2_9 sample at 650 mW of incident power. An arrow shows the quasi-steady state amplitude $\mathcal{S}_{qss}$. The fitted lifetime is 69 µs.

In this section I will provide experimental validation of Equation (7.14) by examining the dependence of $\mathcal{S}_{qss}$ on τ. This requires several datapoints with a variety of lifetime values. This is accomplished here by examining two different samples, and measuring the lifetime at a variety of power levels, ranging from 10 to 650 mW. Due to the injection-level dependence of lifetime (see 3.2.3), the lifetime for each sample will be different at different powers. These measurements

provide a wide enough spread of lifetimes to convincingly validate Equation (7.14). A dual-beam configuration is used as described in Chapter 4, with the pump and probe diameters set to 6 mm, and 50 microns, respectively. As described in 7.2, this pump/probe configuration ensures that radial diffusion effects are negligible and the experiment is adequately described by the 1D recombination model. For each sample at each power level, the true lifetime is determined by measuring the amplitude of the free-carrier population as a function of frequency, then fitting to the frequency dependence of Equation (7.11). The amplitude of the fit yields $\mathcal{S}_{qss}$. An example of this measurement is shown in Figure 7.1.
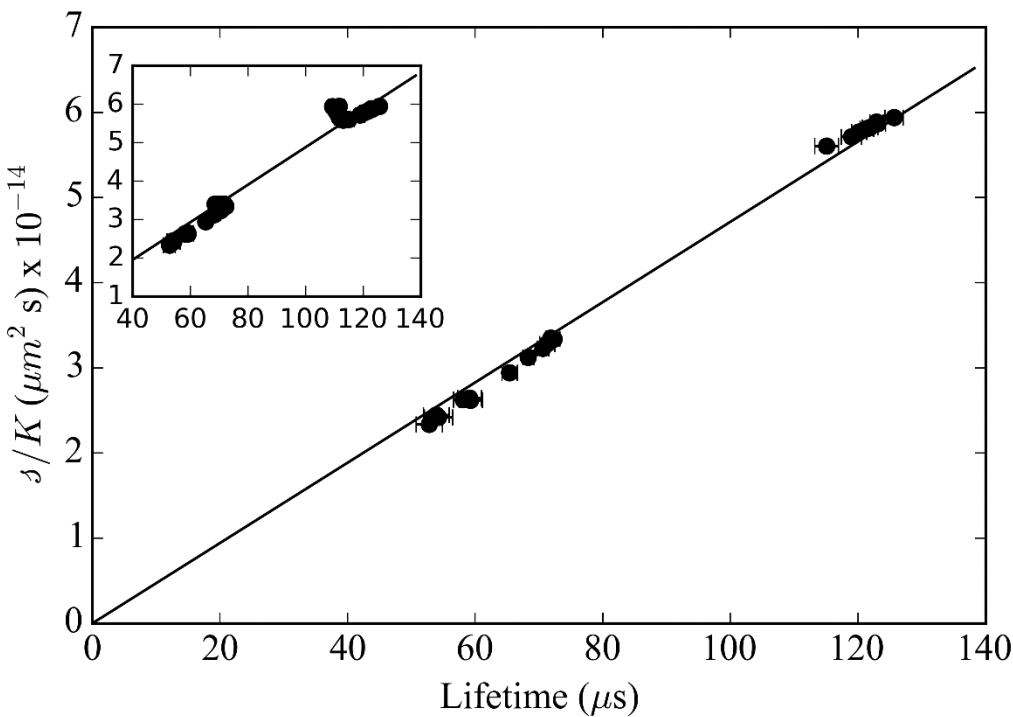
Figure 7.2: Plot of normalized signal vs roll-off lifetime for El-Cat 2_9 sample (dataset on the left) and for the thick wafer (dataset on the right). Straight line is best-fit line through zero. The highest injected carrier density in the El-Cat 2_9 and the thick wafer data are $1.62 \times 10^{16} cm^{-3}$ and $2.62 \times 10^{15} cm^{-3}$, respectively. Inset: Normalized signal vs roll-off lifetime over a wider range of injected carrier densities. The highest injected carrier density in the El-Cat 2_9 and the thick wafer data are $2.19 \times 10^{16} cm^{-3}$ and $1.19 \times 10^{16} cm^{-3}$, respectively.

For each lifetime that is measured, the QSS signal $\mathcal{S}_{qss}$ is divided by K to form the *normalized signal*. The normalized signals are plotted as a function of roll-off frequency in Figure 7.2.

Equation (7.14) predicts a linear trend of $\mathscr{s}/K$ with τ, which is confirmed in Figure 7.2. The slope of best-fit line is the FCA cross section, which I measure to be $\sigma_{FCA} = (4.71 \pm 0.25) \times 10^{-10} \; \mu m^2$. The value of this cross section and how it compares to values from the literature is discussed in 7.4. In essence, the plot in Figure 7.2 is a calibration procedure for the QSS-FCA technique, where the slope of the line of best-fit is the calibration coefficient. Alternatively, the value of σ_{FCA} can be determined by a single datapoint measurement. Once the calibration coefficient has been measured, the lifetime of an arbitrary wafer can be measured in quasi-steady state. To do this the experimenter measures the AC and DC amplitude of the probe signal and forms the reduced signal $\mathscr{s}$, and then calculates the value of the experimental factor K. Then using the calibration coefficient σ_{FCA}, the lifetime is computed as $\tau_{qss} = \mathscr{s}/K\sigma_{FCA}$. This is a single datapoint measurement acquired at low frequency. If the factors in K do not change between measurements then K remains constant and does not need to be recomputed. K depends on parameters set by the experimenter, which can be held fixed, and depends on the optical properties of the wafer under test (f_a in Equation (7.15)), which can vary if different types of wafers are examined. It is reasonable to expect that wafers on a production line will have identical optical properties and thickness, so K will remain unchanged. If K remains fixed from measurement to measurement, then it can be bundled together with σ_{FCA} during calibration. The advantage of this is that the factors that go into K would not need to be explicitly known.

One feature that distinguishes QSS-FCA from other QSS techniques like QSSPC and ILM/CDI is that calibration unambiguously resolves the relationship between the quasi-steady state amplitude, and the lifetime. Calibration with the other techniques does not involve an actual lifetime measurement, but a measurement of free-carrier density on a reference wafer. The reference wafer has a known free-carrier density and is used to calibrate the measurement apparatus to be able to measure the free-carrier density in absolute units. Then to measure the lifetime of an arbitrary wafer, the free-carrier density n of the wafer under optical injection is measured and knowing the optical generation rate G, the lifetime is given by $\tau = n/G$ (Equation (3.16)). This reason why this reference wafer is required is because the QSSPC and ILM/CDI measurement apparatuses do not have a secondary means of measuring lifetime. QSS-FCA on the other hand is basically the MFCA

technique, except the lifetime is extracted from the amplitude and not the roll-off curve. A MFCA frequency sweep simultaneously determines the QSS amplitude and roll-off lifetime (Figure 7.1), so the amplitude can be directly related to the true lifetime. This ensures that lifetimes measured by the QSS-FCA technique are accurate. It is reasonable to question why calibration is required at all since σ_{FCA} is a material constant that can be looked up. It turns out that values of σ_{FCA} from the literature are unreliable, and it is more practical to measure σ_{FCA} directly as I have done in Figure 7.2. This is discussed further in 7.4. It has also been assumed that σ_{FCA} is a constant. The inset of Figure 7.2 shows datapoints collected at higher injected carrier densities (beyond $1.62 \times 10^{16} \mathrm{cm}^{-3}$ for El-Cat 2_9 wafer and $2.62 \times 10^{15} \mathrm{cm}^{-3}$ for the thick wafer). It is clear that at higher carrier densities s/K vs τ begins deviating from linearity. The explanation for this is that the free-carrier absorption cross section is not a constant, but actually varies with injected carrier density. This effect and how to correct for it will be addressed in 7.6.

Another point to address is the fact that QSS-FCA requires an initial measurement of the frequency dependence of the probe signal in order to determine lifetime and calibrate the apparatus (see Figure 7.1). I have mentioned a few times now that an advantage of QSS-FCA over the MFCA technique is that the apparatus does not require the high bandwidth necessary to map out the frequency-dependence. However, high-bandwidth *is* required in this work as can be seen in Figure 7.1 where a modulation bandwidth on the order of 100 kHz has been used to measure the frequency-dependence. In practice one only needs to map out a portion of the roll-off curve, say up to the 3dB point, in order to extract the lifetime. At the 3dB point, $f_{3dB} = 1/2\pi\tau$. The lifetime from the dataset in Figure 7.1 is about 69 μs which corresponds to a 3dB frequency of 2.31 kHz. One could use a wafer with a long recombination lifetime for calibration instead. If the wafer has a lifetime of 1 ms, then $f_{3dB} = 159$ Hz. Thus even though I have used a wide measurement bandwidth in this work to demonstrate QSS-FCA, wide measurement bandwidth would not be required in a practical QSS-FCA apparatus, preserving the technique's low-frequency advantage.

7.4   The Free-Carrier Absorption Cross Section

The parameter σ_{FCA} is dependent on probe wavelength, carrier density, carrier type, the ratio of free-electrons and holes, and electronic mobility, among other factors [58]. This is a wide parameter space which is accompanied by a wide variation in values for σ_{FCA} across the literature. Baker-Finch et al. [71] summarized several parameterizations for σ_{FCA}[30] from various authors. They use a model where σ_{FCA} is constant with carrier density and parameterized by the probe wavelength and two empirically determined constants. Using this parameterization, the total cross section due to electrons and holes is:

$$\sigma_{FCA} = C_e \lambda^{\gamma_e} + C_h \lambda^{\gamma_h} \tag{7.21}$$

where C_i & γ_i are empirically determined constants. The subscripts 'e' and 'h' denote constants derived for electrons and holes, respectively. A summary of these constants is given in Table I of their work, which is recreated here in Table II.

---

[30] The cross-section parameter σ_{FCA} does not explicitly appear in Refs [71], and in fact it does not appear in most free-carrier absorption literature. A related parameter, the free-carrier absorption coefficient α_{FCA} is what is usually used in the literature. α_{FCA} is related to cross section σ_{FCA} and the free-carrier density n via $\alpha_{FCA} = \sigma_{FCA} n$.

Table II: Free Carrier Absorption Coefficient Parameters from across the literature.

Reference	C Parameter (p-type, n-type)	γ parameter	λ range (μm)	N range (cm^{-3})	σ_{FCA}(x10^{-10} μm^2)
[58]	$2.7x10^{-10}$ $1x10^{-10}$	2 2	>4	$< 10^{19}$	8.89
[88]	$2.6x10^{-10}$ $2.7x10^{-6}$	2 3	>2.5	$\sim10^{18}$	16.3
[89]	$1.04x10^{-8}$ $4.52x10^{-8}$	2.4 2.6	1-2	$10^{17} - 10^{20}$	13.1
[90]	$3.2x10^{-6}$ $3.0x10^{-6}$	3 3	1-1.2	$10^{17} - 10^{20}$	23.1
[71]	$(1.80 \pm 0.83)x10^{-9}$ $(1.68 \pm 0.62)x10^{-6}$	2.18 ± 0.01 2.88 ± 0.08	1-1.5	$\sim10^{18} - 5x10^{20}$	26.8 ± 14.8

Table II shows $C_{e,h}$ & $\gamma_{e,h}$ parameters derived from the work of several different publications. The range of wavelengths λ and carrier density N over which the parameters are acquired is also listed.

Examining the last three rows of Table II, it can be seen that the C parameter varies across orders of magnitude between different authors, even though the wavelength and doping range are similar. The corresponding σ_{FCA} for electrons and holes is shown in the right column of Table II, which shows a factor of 3 difference between the lowest and highest values for σ_{FCA}. Baker-Finch hypothesized that the reason for the spread of σ_{FCA} values across the literature is due to high experimental uncertainty. Indeed their work was the first to quantify the precision of their apparatus and they show high uncertainty in the empirically derived parameters. Using error propagation I estimate the uncertainty of σ_{FCA} from their measurements to be about 55% (with a 95% confidence interval). All of the other σ_{FCA} values shown in Table II fall within this range, except for Refs [58]. However, if the uncertainty in σ_{FCA} from Refs [58] was as high as Baker-Finch then their cross-section would fall within the range of Baker-Finch's value too. The origin of the high uncertainty is due to the nature of how FCA is measured in Table II, as well as the fact that FCA is very weak. In Refs [58], [71], [89], [90] the FCA *coefficient* is measured on lightly-doped wafers with front and/or backside diffusions of n and p-type dopants. Assuming that the peak carrier density is 10^{20} cm^{-3}, and the cross section $\sigma_{FCA} = 10 \ x \ 10^{-10}$ μm^2, the FCA coefficient calculated by Equation (3.2) is $\alpha_{FCA} = 1000$ cm^{-1}. This is actually quite large[31], but since the width of diffused profiles is so small the total attenuation due to FCA is small. If the width of the profile is 100 nm (consider Figure 3 of Refs [89]), the attenuation due to FCA at 1550 nm would be about 1% of the full power of the beam[32]. FCA is measured experimentally by determining the total reflectance R and transmittance T of a monochromatic light source incident upon the wafer, with the absorption given by $1 - (R + T)$. Since $R + T \sim 1$ it is difficult to extract a precise value for the FCA cross-section from this difference measurement. Another issue is that since the measurements are carried out on samples with diffused dopants, the dopant profile is

---

[31] For reference, the band-to-band absorption coefficient of silicon at 1064 nm is only 9.85 cm^{-1}.

[32] The attenuation is estimated using the Beer Lambert Law, which gives the fraction of power remaining as $e^{-\sigma_{FCA}nW}$ where W is the width of the diffused dopant profile.

required in order to determine the average FCA coefficient and thus cross-section. This is because in order to determine α_{FCA} the carrier concentration and width of the profile are required. Uncertainty in the shape and magnitude of the profile will contribute to the overall uncertainty of the FCA coefficient measurement [71].

It is interesting to note that in this work I am able to determine σ_{FCA} to a much higher degree of precision than the works shown in Table II. One of the reasons for this is the fundamental difference between how FCA is measured in Table II and how I measure FCA. The Table II measurements are carried out on samples with fixed dopant concentrations, and is determined based on the difference between two quantities (the incident power, and the reflected and transmitted powers) which are within a few percent of each other. In my work, the carriers are injected periodically and the resultant FCA signal is demodulated on a lock-in amplifier. The signal is *only* sensitive to the periodic change in the FCA population due to injection. This permits the extraction of the FCA cross-section to a much higher degree of precision.

All of the FCA cross sections from Table II are higher than the value of 4.71×10^{-10} μm^2 that I measure in 7.3. This can perhaps be explained by the fact that the cross-section depends on the carrier density [45], [46], [58]. In Table II most of the cross-sections are determined for carrier concentrations in excess of 10^{18} cm^{-3} whereas for the data in Figure 7.2 the maximum carrier density is about 10^{16} cm^{-3}. Another reason for the discrepancy is that the measurements in Table II are performed on samples with fixed carrier concentrations where the carriers originate from dopants. In my work the carriers originate from dopants and from optical injection. As far as I am aware no one has explicitly studied the difference in the FCA cross section due to dopant-carriers and optically-injected carriers, though it has been hinted at [45]. It has been suggested offhandedly that the absorption is equivalent between these two cases [91]. I do not believe that this is correct, however. The process of light absorption by free-carriers is facilitated by carrier scattering since intraband transitions are only permitted alongside a momentum-conserving scattering event. Thus the magnitude of the FCA cross-section must depend in some way on the underlying scattering mechanism affecting the free-carriers. The relevant scattering mechanisms for silicon in the range

of carrier densities under investigation here and Table II are lattice scattering, ionized impurity scattering, and electron-hole scattering [69]. Ionized impurity scattering is due to carriers interacting with charged donor and acceptor impurity atoms, whereas electron-hole scattering are free-carriers interacting with each other. It is discussed by Klaassen that the scattering cross-sections for impurity-scattering are a few times higher than electron-hole scattering [69]. From this it is expected that the FCA cross section in heavily doped samples is fundamentally different than heavily-injected samples with modest or intrinsic doping. In the former the primary scattering mechanism will be impurity scattering, and in the latter the mechanism will be electron-hole scattering. A simplified model for the variation of σ_{FCA} with injected carrier density n is presented in 7.5, which is partially validated in 7.6. This model predicts[33] that σ_{FCA} should be a factor of 6.13 times smaller at 10^{16} cm^{-3} than 10^{18} cm^{-3}. If it is assumed that the Baker-Finch parameterization is correct, this correction leads to $\sigma_{FCA} = (4.37 \pm 2.41)$ x 10^{-10} μm^2 which falls within the range of the value I computed for measurements where $n \sim 10^{16}$ cm^{-3}.

It is clear that quantitative values of the free-carrier absorption cross section from the literature are not reliable. Therefore it advisable that the FCA cross section constant be determined empirically. In the ILM/CDI lifetime measurement techniques (discussed in Chapter 2), the free-carrier absorption cross section is measured by calibrating the experimental apparatus using wafers of known carrier density. For example, Isenberg et al. use p-type silicon wafers to establish a calibration curve and extract the free-carrier absorption coefficient [6]. Since this value is only applicable to holes, it must be corrected to account for FCA by electrons and holes. In their work they use a proportionality factor from Refs [58] to make this correction. This correction is not well motivated, however. In their work the probe is a blackbody source with a distribution of wavelengths. Their correction assumes that the ratio of the electron to hole FCA cross section is

---

[33] I used the model to compute σ_{FCA} at $n = 10^{18}$ cm^{-3} assuming that the free-carrier population is entirely due donors and acceptors. This value of σ_{FCA} is divided by σ_{FCA} computed at $n = 10^{16}$ cm^{-3}, where the free-carrier population is due entirely to optical-injection.

constant as a function of wavelength, which is not supported by empirical evidence [91]. This brings into question the accuracy of ILM/CDI lifetime measurements. These accuracy concerns are not applicable to QSS-FCA where the relationship between measured signal and the true lifetime is determined directly.

The plot in Figure 7.2 illustrates the calibration methodology of QSS-FCA. The reduced signal s divided by the experimental factor K is measured directly and plotted against the lifetime measured by the roll-off technique. The slope of this line is the FCA cross section σ_{FCA} via Equation (7.14), which can then be used to determine the QSS lifetime for a sample with unknown lifetime. This calibration methodology is superior to ILM/CDI since it directly establishes the relationship between the signal measured in QSS and the lifetime. As far as I am aware, no other QSS lifetime technique is calibrated in such a way. Other techniques calibrate the measurement apparatus to measure the free-carrier density, and then hope that the free-carrier density measured on arbitrary wafers is accurate.

7.5   Injection Level Dependence of Free-Carrier Absorption Cross Section

The use of Equation (7.14) to measure lifetime assumes that the FCA cross section is constant with varying excess carrier density n. However from both a theoretical and empirical point of view this is not correct. Higher carrier densities lead to an increase in carrier scattering which leads to an increase in the absorption cross section. The FCA absorption coefficient as given by the Drude model is given by Equation (3.1). It predicts the absorption coefficient for a free electron and hole population of n & p, respectively. Using the fact that $\sigma_{FCA} = \alpha_{FCA}/n$ and that under optical injection $n = p$, the FCA cross section predicted by the Drude model is given by:

$$\sigma_{FCA} = \frac{q^3 \lambda^2}{4\pi^2 \varepsilon_0 c^3 n} \left[\frac{1}{m_n^{*2} \mu_n} + \frac{1}{m_p^{*2} \mu_p} \right] \tag{7.22}$$

The carrier concentration dependence of σ_{FCA} is due to the charge carrier mobilities μ_n & μ_p. As discussed in 3.1, the underlying physics behind free-carrier absorption is the absorption of light by electrons or holes and an accompanying momentum-conserving scattering event. The scattering mechanisms are lattice scattering, electron-hole scattering, and ionized impurity scattering [69]. Charge carrier mobility is a function of scattering, so it is reasonable for the σ_{FCA} to depend on mobility. As carrier concentration increases, so does the scattering rate which leads to a decrease in electron and hole mobility and an increase in σ_{FCA}. To model μ_n & μ_p I have used a general mobility model by Klaassen [69]. This model calculates the electron and hole mobilities for an arbitrary charge carrier and doping concentration. In this way the total mobility due to dopant impurities and optically injected carriers can be accounted for. Accounting for optical injection is not possible in simpler formulations such as the Caughey-Thomas model where the charge carrier concentration is fixed to the dopant concentration, and the difference between electron-hole scattering and ionized impurity scattering is not considered [92].

From Equation (7.14) it is clear that the FCA cross section can be measured directly if $\mathscr{s}, K$ & τ_{qss} are known. This measurement was performed on El-Cat 2_9 and the thick wafer as a function of free-carrier density. The free-carrier density is controlled by the setting the incident power of the pump. Data is collected with an average power ranging from about 10-650 mW for each sample.
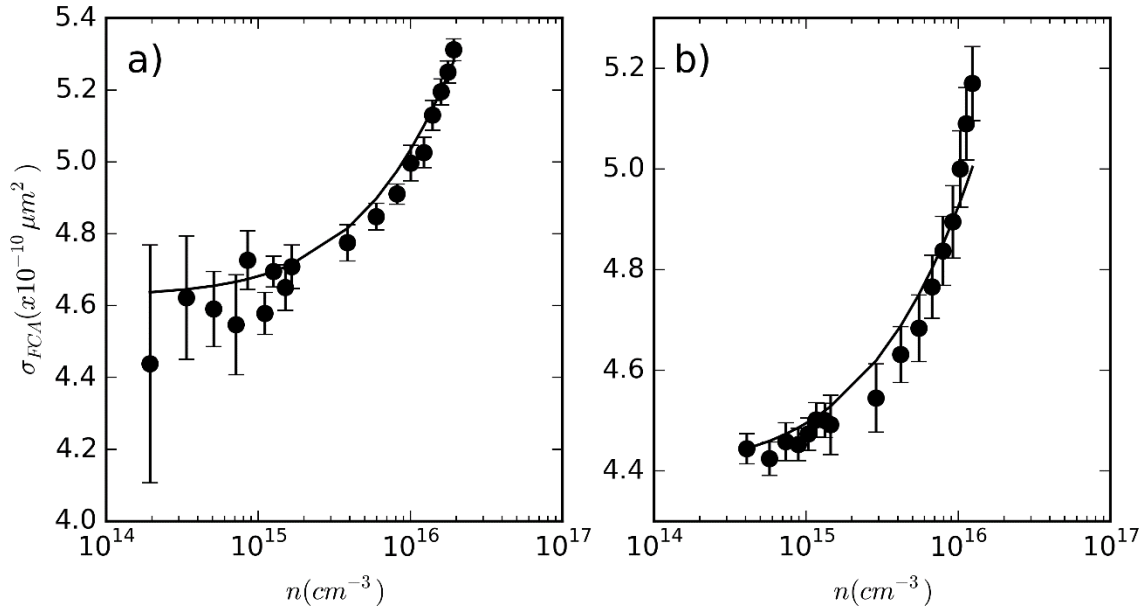
Figure 7.3: Injection level dependent free-carrier absorption cross section for El-Cat 2_9 (a) and Thick wafer (b). The continuous line is a plot of the variation in σ_{FCA} predicted by the Drude model. Note that this curve is scaled to overlap with the experimental data, since the Drude model itself does not quantitatively predict σ_{FCA}. It does however predict the trend of σ_{FCA} with n.

Figure 7.3 shows a plot of σ_{FCA} vs n for the El-Cat 2_9 (a) and Thick (b) wafers. The AC injected carrier density n_{AC} is computed using Equation (7.17) then corrected to the DC carrier density n by dividing by the modulation depth of the pump, m_{pu}. Overlaid on both σ_{FCA} vs n curves is the variation in σ_{FCA} predicted by the Drude model (Equation (7.22)). The curves are scaled using one of the empirically derived σ_{FCA} values from each dataset, since the Drude model underestimates the true value of the FCA cross section [71]. Using Equation (7.22) I calculate a value of $\sigma_{FCA} = 0.962 \times 10^{-10}$ μm² when $n = 10^{15}$ cm⁻³ and $N_d = 3.2x10^{15}$ cm⁻³ (donor density of El-Cat 2_9 wafer). This is about 4.8 times smaller than the value determined experimentally in Figure 7.3 a). However, the relative value of σ_{FCA} does appear to be well-described by the Drude model as evidenced in Figure 7.3 a). There is reasonable overlap between the Drude curve and the experimental data in Figure 7.3 b), though the experimental values are rising more rapidly at higher carrier densities. Further investigation is required to understand this discrepancy.

One reason for the quantitative discrepancy between the model and the experiment is that the Drude model is purely classical and assumes that the energy of the light undergoing FCA is small with respect to the average thermal energy kT [72], which is about 25 meV at room temperature. This condition is obviously violated at 1550 nm where the energy is 0.8 eV. It is assumed in the derivation of the model that the charge-carriers in the semiconductor have a parabolic dispersion relationship between energy and momentum. When the energy of the light is comparable to the bandgap, the non-parabolicity of the energy bands needs to be accounted for [73] as well as intervalley transitions [93]. It is reasonable to question whether or not the Drude model is actually useable at 1550 nm. The relative values of σ_{FCA} from the model match the experimentally derived values quite well for the El-Cat 2_9 wafer, but don't agree as well for the thick wafer. It is possible that the agreement for the El-Cat 2_9 sample is simply a coincidence. Further investigation is required in order to elucidate the true nature of FCA near the bandgap of silicon and the appropriate model in which to describe it. This is beyond the scope of this work. However, this work provides a very good starting point since QSS-FCA allows for the precise experimental measurement of σ_{FCA}!

7.6   Accounting for the Variation in σ_{FCA}

In Figure 7.2 I plotted data for the El-Cat 2_9 and thick wafer which was taken at various pump powers, and thus different injected carrier densities. Each datapoint in the figure is collected at a different power, and has a different lifetime due to the injection-level dependent lifetime of silicon. I intentionally cut off datapoints taken at higher powers due to the breakdown in linearity in the plot. The same plot with all of the datapoints in place is shown in the inset of Figure 7.2. Clearly there is a breakdown in linearity, especially for the thick sample, which I attribute to the non-constancy of σ_{FCA}. This complicates the use of QSS-FCA for extracting lifetime since it can no longer be assumed that the relationship between $\mathcal{S}_{qss}/K$ and τ is linear if σ_{FCA} is not constant. The carrier concentration dependence of σ_{FCA} must be accounted for. Examining Equation (7.20), the goal is to determine the injected carrier density n so that the recombination lifetime can be measured via Equation (7.18). The problem now is that σ_{FCA} itself is a function of n so how can n

be isolated from a measurement of S_{qss}? First, rewrite this equation in terms of the free-carrier absorption coefficient, α_{FCA}, which is simply $\sigma_{FCA}n$:

$$s = m_{pu}\alpha_{FCA}(n)W \tag{7.23}$$

Since σ_{FCA} is monotonically increasing with n, $\alpha_{FCA}(n)$ is a unique function of n (*i.e.* α_{FCA} takes on a unique value for each value of n). Thus if the relationship $\alpha_{FCA}(n)$ is known *a priori*, the value of n can be determined from the experimental measurement of $\alpha_{FCA}(n)$. As discussed in 7.5, the relative (but not absolute) value of σ_{FCA} as a function of n can be predicted with Drude theory. This means that the relative value of $\alpha_{FCA}(n)$ may also be described by Drude theory. Thus if the absolute value of $\alpha_{FCA}(n)$ is known at some point n_0, then α_{FCA} can be predicted quantitatively for any arbitrary n.

Let $\alpha_{Dr}(n, N_d, N_a)$ be the FCA coefficient predicted by Equation (3.1), which of course is a function of the injected and background doping carrier densities. Since only the relative value of α_{Dr} is reliable, an absolute value is required in order to scale the α_{Dr} curve to the absolute α_{FCA} curve. To do this α_{FCA} is directly measured at some point n_0. The scaling factor k to convert α_{Dr} to α_{FCA} is then given by:

$$k = \frac{\alpha_{FCA}(n_0)}{\alpha_{Dr}(n_0, N_d, N_a)} \tag{7.24}$$

In order to compute the scaling factor, both $\alpha_{FCA}(n_0)$ and n_0 must be known. Of course $\alpha_{FCA}(n_0)$ can be measured directly from the signal's quasi-steady state amplitude using Equation (7.23). n_0 is measured using Equation (7.18), which requires that the lifetime be known. The lifetime is measured *in situ* using the traditional MFCA approach. With k known the absolute value FCA coefficient curve is given by:

$$\alpha_{FCA}(n) = k\alpha_{Dr}(n_0, N_d, N_a) \tag{7.25}$$

With α_{FCA} determined, the lifetime can now be measured in quasi-steady state. S_{qss} is measured experimentally and used to determine $\alpha_{FCA}(n)$ via Equation (7.23). Since $\alpha_{FCA}(n)$ is known for all n after calibration, the experimentally measured α_{FCA} can be inverted to determine n. Once n is known the lifetime is extracted using Equation (7.18).
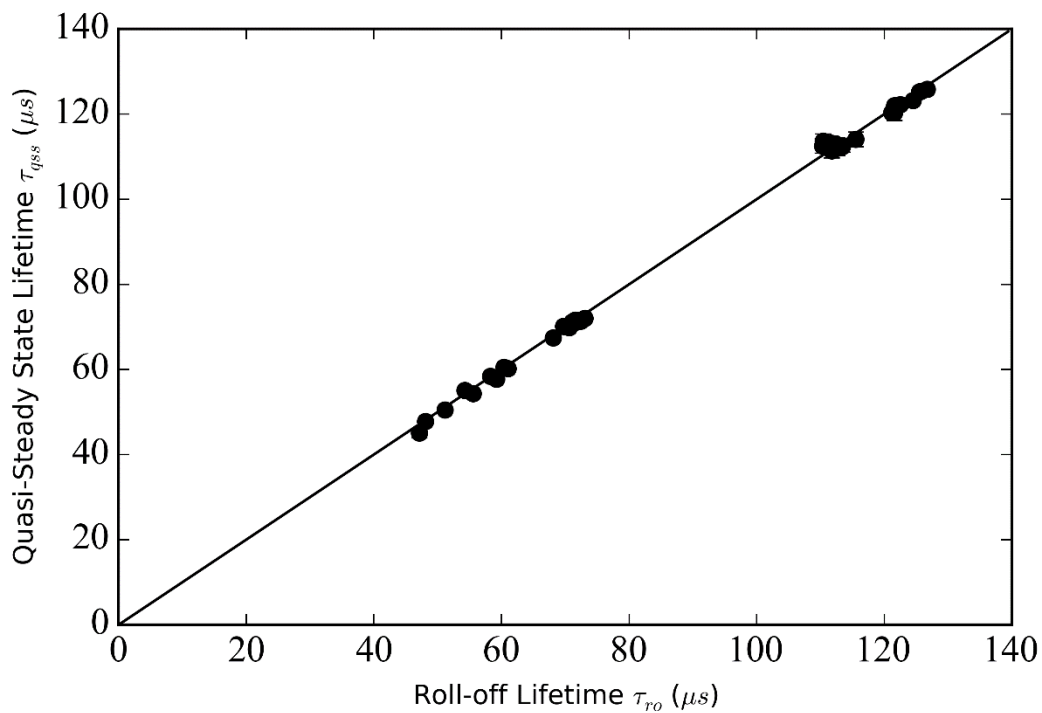
Figure 7.4: Steady-state lifetime measured via Equation (7.20) vs roll-off lifetime for El-Cat 2_9 wafer (left data set) and thick wafer (right dataset). The solid line has unity slope

I have analyzed the data from the inset of Figure 7.2 using the new procedure outlined in this section. The scaling factor k is determined for each wafer using a single experimental point in Figure 7.3. Once the scaling factor is known, the lifetime can be predicted from a quasi-steady state measurement of the FCA signal using the procedure described in this section. The lifetime

149

determined in the quasi-steady state is plotted vs the roll-off lifetime in Figure 7.4. The ordinate of the straight-line in the figure is the roll-off lifetime. Clearly there is excellent agreement between the lifetimes measured in quasi-steady state and using the traditional MFCA technique. This demonstrates that even in the case where σ_{FCA} is a function of carrier density, the lifetime may still be measured! It worth reiterating here that each datapoint's position along the x-axis in Figure 7.4 is determined by a roll-off measurement which requires sweeping the modulation frequency from low to high frequencies in order to map out the roll-off curve. This requires multiple datapoints and bandwidth comparable to the inverse of the recombination lifetime. Each datapoint's position along the y-axis is determined by a single, low frequency measurement. Thus QSS-FCA can be applied even if σ_{FCA} is changing. Generally if the injected carrier density is small or even comparable to the doping level, it is expected that σ_{FCA} will remain constant and the analysis applied in 7.2 should be sufficient for extracting the lifetime. When the injected carrier density is swept from values lower than to values greater than the doping density, it is expected that σ_{FCA} will change and this change should be accounted for using the analysis of this section.

7.7   Summary

In this chapter I have developed Quasi-Steady State Free-Carrier Absorption for measuring recombination lifetime in semiconductors. The theory for the technique is derived in 7.2. In 7.3 I validate the model over a range of injected carrier densities that are $\leq 10^{16} \text{cm}^{-3}$. In this range the calibration factor σ_{FCA}, the free-carrier absorption cross-section, may be treated as constant. The model predicts a linear dependence between the QSS-FCA signal and recombination lifetime, which is demonstrated. The slope of this relationship is the FCA cross section, which is determined from the plot. Once this is known, arbitrary lifetimes may be measured with a single measurement of the QSS-FCA amplitude. In 7.4 I discuss the FCA cross section that I have measured, and compare it to other values in the literature. σ_{FCA} values from the literature exhibit a significant amount of variation which is due to poor experimental precision [71], which is at least in excess of 50%. In my work QSS-FCA is measured to within a precision of about 5%. The higher precision in my measurements is due to a fundamental difference in how FCA is measured in my work, and

in the literature. In my work the measured signal is due to the AC modulation of free-carriers and the signal arises entirely from FCA, with minimal background effects. In the literature, FCA is measured on wafers with a fixed doping concentration and is extracted by separating the power that is incident upon the wafer from the power that is reflected and transmitted. Since these powers are very close to another (typically within 1%), there is a large uncertainty after subtracting them. In 7.5 I explore the injected-carrier dependence of the FCA cross-section σ_{FCA}. To my knowledge this has never actually been demonstrated experimentally for optical injection. I find that this dependence can be modelled with the Drude model. Though the Drude model underestimates the magnitude of FCA, a feature that is well-known in the literature [71], the relative free-carrier dependence of σ_{FCA} that it predicts matches experiment reasonably well. In 7.6 I show how to generalize the technique described in 7.3 to account for an injection-dependent σ_{FCA}, and demonstrate that the lifetime measured in quasi-steady state matches the lifetime measured with the traditional MFCA technique. This proves that QSS-FCA can measure the recombination lifetime under quasi-steady state conditions, and with the advantages offered by its superior calibration it could compete with QSSPC, the most popular commercial apparatus for measuring lifetime.

8 Conclusion and Future Work

In this dissertation I have developed new and improved techniques for the measurement of recombination lifetime in semiconductors, particularly silicon. The first technique, single-beam pump/probe, is the first of its kind capable of measuring lifetime in silicon using only a single laser as both pump and probe beam. Though single-beam pump/probe techniques have been reported elsewhere [59], [60], they were extremely limited in their scope and to my knowledge were never explored further from their original publications. These techniques required splitting the laser beam so that a portion could be used in a feedback loop to suppress stray background signals. This is not required in my implementation, making it fundamentally simpler and exemplifying that the technique is truly a *single* beam technique. The significance of being able to remove the second beam cannot be overstated. There are several issues associated with dual-beam pump/probe techniques that are simplified, reduced, or completely eliminated with single-beam pump/probe. Alignment is one of the most challenging issues when implementing a pump/probe experiment. Both pump and probe beam have to be guided to the sample under study and aligned so that they overlap on the sample. In silicon lifetime measurements where the pump beam diameter is on the order of millimeters [3], the alignment must be very precise. If the pump and probe beams are guided over a long distance, lasers and optical components with high pointing stability are a necessity since small angular deviations translate into large displacements at the sample. Another issue is that both pump and probe beams will need separate supporting optics in order to condition the beams before striking the sample. Power, polarization, and beam width are all parameters that an experimenter might need to control with supporting optics. In addition to this, these components, including both pump and probe sources, take up valuable space on a laboratory bench. A single-beam pump/probe apparatus eliminates the alignment of a second beam, reduces the number of components required to implement the experiment, and occupies less real-estate than its dual-beam counterpart. In addition to this, single-beam pump/probe will almost always be less costly to implement since fewer components are needed. In this work I have demonstrated that the results obtained with single-beam pump/probe are consistent with its dual-beam counterpart. This

is proof-of-concept demonstration that single-beam pump/probe can supersede dual/beam pump/probe as a lifetime characterization tool for semiconductors.

Beyond what has been presented here, the most obvious application for single-beam pump/probe is for *in situ* semiconductor process monitoring. Ellipsometry [94], [95], x-ray diffraction [96], [97], electron-microscopy [98], [99], and Fourier-Transform Infrared Spectroscopy (FTIR) [100], [101] have all been used to study film growth *in situ* in Chemical Vapor Deposition (CVD) or Atomic-Layer Deposition (ALD) reaction chambers. Using these techniques it is possible to elucidate information about the growth kinetics, stoichiometry, electronic properties, and crystal structure of films being grown in real-time. What these techniques all have in common is that they study the film being grown, and not the substrate it is being grown on. Single-beam pump/probe is uniquely suited to measuring the substrate, in particular its electronic properties. By probing the substrate it is possible to study the interface between the substrate and film. As discussed in 3.3.2, the effective lifetime of a semiconductor is a function of the surface recombination velocity at the semiconductor's surface, which is affected by the electronic quality[34] of the interface between substrate and film [9], [43], [102]. Therefore with single-beam pump/probe an experimenter can now probe additional information about the CVD process, which can be used for process optimization. For photovoltaic devices, very high quality interfaces between semiconductor and dielectric films are required to reduce recombination and achieve high energy conversion efficiency. There has been an extensive amount of work devoted to studying and optimizing the interface quality of these dielectric layers [103]−[111]. All of the optimization studies that I have encountered in the literature perform measurements of surface recombination velocity *ex situ* after the deposition of the film is complete. For CVD-deposited films, there are typically a great number of process parameters that can be tuned. For plasma-assisted CVD, parameters such as RF power, gas flow rate, gas flow ratios, deposition temperature, and deposition pressure can all affect the

---

[34] In this case 'quality' refers to the density of electrically-active trap states at the surface, with higher quality interfaces have a lower density.

quality of an interface [109]. Optimization of this wide parameter space can be very costly in terms of time and resources, especially when measurements of the interface quality are taken after the sample is removed from the CVD chamber. With single-beam pump/probe, the lifetime of the wafer can be measured *in situ* and information about the semiconductor-dielectric interface can be extracted in real-time. Real-time information of the interface quality could be used as feedback for optimizing process conditions. An annealing step follows the deposition of silicon nitride, with the annealing time and temperature also affecting the interface quality [109]. In this case the quality as a function of time is assessed at discrete times since the wafer has to be removed from the annealing furnace before it can be measured. With single-beam pump/probe, the quality as a function of time could be easily measured *in situ.*

Though there are several commercial tools available for in-line measurement of lifetime on a photovoltaic production line (see Footnote 4), I am not aware of any tools that can measure the lifetime of a wafer undergoing CVD *in situ*. One reason for this is that it is impractical to incorporate lifetime measurement into a CVD reaction chamber using the current technologies available. Commercial lifetime technologies like QSSPC and μ-PCD use RF and microwave-based physics for measuring the photoconductivity of silicon. It is not clear if the plasma in a CVD chamber would interfere with these measurements. Since the plasma is charged, it is likely to screen the silicon wafer from RF/microwave-based probes. In addition to this both techniques require that the wafer be in close proximity to the measurement apparatus, which would be quite invasive to the CVD reaction chamber. Dual-beam pump/probe is also impractical due to the alignment challenges of overlapping the pump and probe beams inside the reaction chamber. Camera-based techniques such as ILM/CDI could potentially be used, but they require imaging optics which could be impractical to place within a CVD chamber. Single-beam pump/probe seems uniquely suited for *in situ* lifetime measurements. As long as there is a line of sight between the laser source, wafer, and detector, single-beam pump/probe can be implemented.

The second technique that I have developed, Quasi-Steady State Free-Carrier Absorption, measures lifetime in quasi-steady state and simplifies the traditional frequency-resolved MFCA

technique. Where MFCA requires sweeping the pump modulation frequency from low to high values and recording data over that range, QSS-FCA requires a single datapoint measured at low frequency in order to extract the recombination lifetime. The advantage of this is that it relaxes the bandwidth constraints of frequency-resolved measurements. This reduces the complexity and cost of the QSS-FCA apparatus[35] since bandwidth comparable to the inverse lifetime of the wafer is not required. QSS-FCA improves upon competing QSS techniques such as QSSPC and ILM/CDI in several ways. Firstly, QSS-FCA is able to establish a direct relationship between the QSS signal and the lifetime since the true lifetime can be measured *in situ* with the QSS measurement using MFCA. This is in contrast to the QSSPC and ILM/CDI methods which use a reference wafer to calibrate the instrument to measure free-carrier density, which is then used to measure lifetime. Independent verification of the lifetime using another experimental apparatus is required in order to assess the accuracy of the calibration. In QSS-FCA, the relationship between quasi-steady state and the true lifetime can be measured directly. The calibration factor for QSS-FCA is the FCA cross section, which is a material constant. Once calibrated, the QSS-FCA apparatus needn't ever be calibrated again. This is in contrast to QSSPC where the calibration factor is composed of geometrical factors relating to the positioning of the wafer with respect to the photoconductivity sensor. This means that wafers under test must be positioned in precisely the same position relative to the apparatus' photoconductivity sensor as the reference wafer was during calibration, in order for the calibration to hold. Another advantage of QSS-FCA over QSSPC is that since QSS-FCA is entirely optical, there is no restriction as to where the pump/probe sources and the probe detector can be positioned relative to the sample under test. As long as the pump and probe light can be overlapped on the sample and the probe light collected by a detector, QSS-FCA can measure

---

[35] I designed and built the first QSS-FCA apparatus for a course project. The instructions were to build an optical device to perform some kind of measurement, so I decided to build a discount version of my Ph.D research. I used a DVD laser diode for the pump, an incandescent flashlight for the probe, and an InGaAs photodiode for the detector. A custom circuit was built to drive the laser and amplify the photodiode signal. The laser was driven by and data was collected on an MSP432 microcontroller and fed to a computer. This apparatus was able to measure a signal proportional to the effective recombination lifetime, and only cost $150 to build.

lifetime. This provides more flexibility when building a QSS-FCA apparatus. In QSSPC, the photoconductivity sensor must be placed in close proximity (on the order of centimeters) to the wafer.

Beyond lifetime measurement applications, QSS-FCA can be used to measure the free-carrier absorption cross section of silicon directly, and to a higher precision than has been reported in the literature. As I have discussed in 7.4, σ_{FCA} values found in the literature vary considerably. One of the reasons for this is that the FCA is very small (the power absorbed due to FCA is about 1 part per thousand of the total probe power) so the experimental error arising from a DC measurement of the absorption is high, as deduced by Baker-Finch et al. [71]. The QSS-FCA technique allows σ_{FCA} to be measured to a high degree of precision since it is an AC measurement and can take advantage of lock-in detection. This permits measurements of σ_{FCA} at low carrier densities ($< 10^{16}$ cm^{-3}). There is a lot of underlying physics that goes into σ_{FCA} such as several scattering mechanisms (acoustic and optical phonon scattering, as well as inter-carrier and ionized impurity scattering), as well as specifics about the band-structure and transition of carriers inside and between energy bands. There are many models in the literature that account for these effects in isolation, but to my knowledge a general theory consolidating all effects, including experimental validation, has never been presented. Since QSS-FCA can make precise measurements of σ_{FCA}, it is the perfect tool for experimentally validating a general FCA theory.

QSS-FCA can also be used to make absolute measurements of the injected free-carrier density n in an arbitrary wafer via Equation (7.20). Indeed this is the principle behind QSS-FCA lifetime measurements! Another way of looking at this is that measurement of n is an alternative way of quantifying the total amount of optical absorption in a silicon wafer since n results directly from optical absorption. One application where this is useful is for studying the effectiveness of plasmonic light-trapping structures on silicon. Plasmonic light-trapping involves metal nanoparticles placed on top of a silicon wafer (or on top of a thin dielectric spacer on silicon) that

enhance light absorption in the wafer[36][112]–[116]. These metal nanoparticles capture light that is incident on the silicon wafer by coupling it into quantized oscillations of the free-electrons in the metal (*plasmons*). This energy is then coupled into silicon in either the near or far-field, producing electron-hole pairs that can be harnessed for photocurrent. A drawback of plasmonic nanoparticles is that some of the energy of the light is lost in the metal itself as heat. This parasitic absorption hampers the effectiveness of the plasmonic structures for light-trapping and they must be designed to minimize it. It is difficult to experimentally measure and separate the absorption in the silicon wafer from the parasitic absorption in the plasmonic particles using optical measurements alone. Traditionally, the total optical absorption in a structure can be measured using an integrating sphere configured to capture all of the light reflected from and transmitted through a sample. Any energy deficit between the incident light and the light coupled out of the sphere is due to absorption in the structure. An integrating sphere measurement deduces the total absorption from the silicon wafer and plasmonic particles, but it does not discriminate between the two. The absorption contributions can be decoupled with a separate measurement of n which determines the absorption in the silicon wafer alone.

To support my experimental techniques I have developed a general mathematical model that can be used to predict the signal measured from a semiconductor wafer with arbitrary electronic properties, measured using an apparatus of arbitrary configuration. The solution, provided in Appendix C, predicts the free-carrier concentration $n(r, z, t)$ within a semiconductor as a function of space and time. The solution is highly general, describing three-dimensional carrier transport and recombination within the semiconductor, both in the bulk and at the surface of the wafer. There is no assumption made about the bulk recombination lifetime, surface recombination velocity, diffusion coefficient, or thickness of the wafer. The solution is also completely analytic, and relatively simple from an algebraic point of view. The only part of the solution that is not closed

---

[36] Typical nanoparticle diameters are 10-100 nm, and the dielectric spacing layer is on the order of 10s of nm.

form are two transcendental equations of the form $\tan x = ax$ and $\cot x = ax$, which are easily solved numerically using a computer. I have not seen a solution to the 3D continuity equation presented in a form as simple and succinct as I have presented it here. Though I have not found this particular solution elsewhere, it would not be surprising if it does exist in this form. Using my 3D solution for $n(r, z, t)$, I developed a general equation to predict the probe power that transmits through a silicon wafer and into a detector for a given modulation of $n(r, z, t)$ via a pump source. The transmitted power is modulated by $n(r, z, t)$ due to free-carrier absorption, and information about n and the recombination dynamics of the wafer can be determined by isolating this modulation term. This pump/probe equation is also highly general, completely analytic and relatively succinct. It also reveals a very elegant symmetry between the pump and probe beams. It is applicable to a very broad range of pump/probe experiments involving semiconductors. No assumption is made about the wavelength, power, beam radius, or reflectance and transmittance of the pump or probe beams, nor about the recombination and transport properties of the wafer being investigated. In addition to this, the equation is derived under the assumption that the beam has a Gaussian shape. This makes it applicable to any pump/probe studies involving single-mode lasers, which covers a vast range of applications. From this theory I was able to derive the complete models behind single-beam pump/probe and QSS-FCA with just a few variable substitutions. This equation should be very useful to authors studying charge carrier transport and recombination in semiconductors. Certainly I would have found this equation useful before I derived it, instead of equations that take an entire page [42] just to write down!

The experimental techniques that I have developed in this work are promising. Single-beam pump/probe opens up a wide range of possibilities for *in situ* process monitoring that would be impractical with dual-beam techniques. I have proposed several ideas of where single-beam pump/probe could be applied. It cannot be overstated how much single-beam pump/probe simplifies traditional pump/probe measurements in terms of time, space and cost. QSS-FCA has been demonstrated to be superior to other quasi-steady state measurement techniques in several ways such as guaranteed accuracy, and flexibility in implementation. QSS-FCA also provides a mechanism for measuring the free-carrier absorption cross section to a much greater precision (at

least 10 times) than has been reported elsewhere [71]. Being able to measure this cross-section provides experimenters with a means of probing the underlying physics of carrier scattering and intraband transitions in a semiconductor. There is no unified theory of free-carrier absorption in silicon that accounts for all of the underlying physics consolidated into a single equation. QSS-FCA is the tool to validate such a theory experimentally.

References

[1]   S. Rein, Lifetime spectroscopy: a method of defect characterization in silicon for photovoltaic applications ; with 29 tables. Berlin: Springer, 2005.

[2]   A. Luque and S. Hegedus, Eds., Handbook of photovoltaic science and engineering. Hoboken, NJ: Wiley, 2003.

[3]   J. Linnros, "Carrier lifetime measurements using free carrier absorption transients. I. Principle and injection dependence," J. Appl. Phys., vol. 84, no. 1, p. 275, 1998.

[4]   V. Grivickas and J. Linnros, Carrier Lifetime-Free Carrier Absorption, Photoconductivity and Photoluminescence. John Wiley & Sons, Inc., 2012.

[5]   R. A. Sinton and A. Cuevas, "Contactless determination of current–voltage characteristics and minority-carrier lifetimes in semiconductors from quasi-steady-state photoconductance data," Appl. Phys. Lett., vol. 69, no. 17, pp. 2510–2512, Oct. 1996.

[6]   J. Isenberg, S. Riepe, S. W. Glunz, and W. Warta, "Imaging method for laterally resolved measurement of minority carrier densities and lifetimes: Measurement principle and first applications," J. Appl. Phys., vol. 93, no. 7, pp. 4268–4275, Apr. 2003.

[7]   J. Linnros, "Carrier lifetime measurements using free carrier absorption transients. II. Lifetime mapping and effects of surface recombination," J. Appl. Phys., vol. 84, no. 1, pp. 284–291, Jul. 1998.

[8]   F. Sanii, F. P. Giles, R. J. Schwartz, and J. L. Gray, "Contactless nondestructive measurement of bulk and surface recombination using frequency-modulated free carrier absorption," Solid-State Electron., vol. 35, no. 3, pp. 311–317, 1992.

[9]   S. W. Glunz, A. B. Sproul, W. Warta, and W. Wettling, "Injection-level-dependent recombination velocities at the Si-SiO$_2$ interface for various dopant concentrations," J. Appl. Phys., vol. 75, no. 3, pp. 1611–1615, Feb. 1994.

[10]   M. Kunst and G. Beck, "The study of charge carrier kinetics in semiconductors by microwave conductivity measurements," J. Appl. Phys., vol. 60, no. 10, p. 3558, 1986.

[11]   A. P. Ramsa, H. Jacobs, and F. A. Brand, "Microwave Techniques in Measurement of Lifetime in Germanium," J. Appl. Phys., vol. 30, no. 7, pp. 1054–1060, Jul. 1959.

[12]   R. Brendel, "Note on the interpretation of injection-level-dependent surface recombination velocities," Appl. Phys. A, vol. 60, no. 5, pp. 523–524, 1995.

[13] A. G. Aberle, J. Schmidt, and R. Brendel, "On the data analysis of light-biased photoconductance decay measurements," J. Appl. Phys., vol. 79, no. 3, pp. 1491–1496, Feb. 1996.

[14] R. Schieck and M. Kunst, "Frequency modulated microwave photoconductivity measurements for characterization of silicon wafers," Solid-State Electron., vol. 41, no. 11, pp. 1755–1760, 1997.

[15] G. Ferenczi, T. Pavelka, and P. Tutto, "Injection Level Spectroscopy-A Novel Contact Contamination Analysis Technique in Silicon.pdf," Jpn. J. Appl. Phys., vol. 30, no. 12B, pp. 3630–3633, Dec. 1991.

[16] G. Citarella, S. von Aichberger, and M. Kunst, "Microwave photoconductivity techniques for the characterization of semiconductors," Mater. Sci. Eng. B, vol. 91, pp. 224–228, 2002.

[17] M. E. Rodríguez, A. Mandelis, G. Pan, J. A. García, V. Gorodokin, and Y. Raskin, "Minority carrier lifetime and iron concentration measurements on p -Si wafers by infrared photothermal radiometry and microwave photoconductance decay," J. Appl. Phys., vol. 87, no. 11, pp. 8113–8121, Jun. 2000.

[18] M. Wilson et al., "QSS-μPCD measurement of lifetime in silicon wafers: advantages and new applications," Energy Procedia, vol. 8, pp. 128–134, 2011.

[19] A. Buczkowski, Z. J. Radzimski, G. A. Rozgonyi, and F. Shimura, "Separation of the bulk and surface components of recombination lifetime obtained with a single laser/microwave photoconductance technique," J. Appl. Phys., vol. 72, no. 7, pp. 2873–2878, Oct. 1992.

[20] Y. Lv, N. Wang, C. Zhuang, P. Li, B. Han, and H. Gong, "The uniformity of InGaAs in InP/InGaAs/InP by microwave photoconductivity decay (μ-PCD) carrier lifetime measurement," Semicond. Sci. Technol., vol. 21, no. 6, pp. 771–774, Jun. 2006.

[21] Z. Wang and Y. Chu, "Use of microwave photoconductivity to measure semiconductor properties," Solid-State Electron., vol. 34, no. 7, pp. 735–740, 1991.

[22] R. K. Ahrenkiel, N. Call, S. W. Johnston, and W. K. Metzger, "Comparison of techniques for measuring carrier lifetime in thin-film and multicrystalline photovoltaic materials," Sol. Energy Mater. Sol. Cells, vol. 94, no. 12, pp. 2197–2204, Dec. 2010.

[23] J. S. Swirhun, R. A. Sinton, M. K. Forsyth, and T. Mankad, "Contactless measurement of minority carrier lifetime in silicon ingots and bricks," Prog. Photovolt. Res. Appl., vol. 19, no. 3, pp. 313–319, May 2011.

[24] J. Schmidt, M. Kerr, and P. P. Altermatt, "Coulomb-enhanced Auger recombination in crystalline silicon at intermediate and high injection densities," J. Appl. Phys., vol. 88, no. 3, pp. 1494–1497, Aug. 2000.

[25] S. Bowden and R. A. Sinton, "Determining lifetime in silicon blocks and wafers with accurate expressions for carrier density," J. Appl. Phys., vol. 102, no. 12, p. 124501, Dec. 2007.

[26] J. Schmidt and A. Cuevas, "Electronic properties of light-induced recombination centers in boron-doped Czochralski silicon," J. Appl. Phys., vol. 86, no. 6, pp. 3175–3180, Sep. 1999.

[27] S. Rein and S. W. Glunz, "Electronic properties of the metastable defect in boron-doped Czochralski silicon: Unambiguous determination by advanced lifetime spectroscopy," Appl. Phys. Lett., vol. 82, no. 7, pp. 1054–1056, Feb. 2003.

[28] R. Lago-Aurrekoetxea, I. Tobías, C. del Cañizo, and A. Luque, "Lifetime Measurements by Photoconductance Techniques in Wafers Immersed in a Passivating Liquid," J. Electrochem. Soc., vol. 148, no. 4, p. G200, 2001.

[29] K. Sopian, S. L. Cheow, and S. H. Zaidi, "An overview of crystalline silicon solar cell technology: Past, present, and future," 2017, p. 020004.

[30] L. Huldt, "Optical Method for Determining Carrier Lifetimes in Semiconductors," Phys. Rev. Lett., vol. 2, no. 1, p. 3, 1959.

[31] N. G. Nilsson, "Determination of carrier lifetime, diffusion length, and surface recombination velocity in semiconductors from photo-excited infrared absorption," Solid-State Electron., vol. 7, no. 6, pp. 455–463, 1964.

[32] F. Sanii, R. J. Schwartz, R. F. Pierret, and W. . Au, "The Measurement of Bulk and Surface Recombination by Means of Modulated Free Carrier Absorption," IEEE J. Photovolt., p. 575.

[33] Y.-S. Chang, S. S. Li, and P.-C. Yang, "Determination of interface recombination velocities and carrier lifetimes in SOI materials by a contactless optical modulation technique," Solid-State Electron., vol. 38, no. 7, pp. 1359–1366, 1995.

[34] A. Schönecker, J. A. Eikelboom, A. R. Burgers, P. Lölgen, C. Leguijt, and W. C. Sinke, "Sensitivity analysis for the determination of recombination parameters in Si wafers using harmonic carrier generation," J. Appl. Phys., vol. 79, no. 3, pp. 1497–1504, Feb. 1996.

[35] X. Zhang and B. Li, "Carrier Diffusivity Measurement in Silicon Wafers Using Free Carrier Absorption," Int. J. Thermophys., vol. 34, no. 8–9, pp. 1721–1726, Sep. 2013.

[36] A. G. Aberle, "Surface passivation of crystalline silicon solar cells: a review," Prog. Photovolt. Res. Appl., vol. 8, no. 5, pp. 473–487.

[37] E. Yablonovitch, D. L. Allara, C. C. Chang, T. Gmitter, and T. B. Bright, "Unusually low surface-recombination velocity on silicon and germanium surfaces," Phys. Rev. Lett., vol. 57, no. 2, p. 249, 1986.

[38] S. W. Glunz and W. Warta, "High-resolution lifetime mapping using modulated free-carrier absorption," J. Appl. Phys., vol. 77, no. 7, pp. 3243–3247, Apr. 1995.

[39] M. Li, Y. Dai, W. Ma, B. Yang, and Q. Chu, "Review of New Technology for Preparing Crystalline Silicon Solar Cell Materials by Metallurgical Method," IOP Conf. Ser. Earth Environ. Sci., vol. 94, p. 012016, Nov. 2017.

[40] W. Seifert, G. Morgenstern, and M. Kittler, "Influence of dislocation density on recombination at grain boundaries in multicrystalline silicon," Semicond. Sci. Technol., vol. 8, no. 9, p. 1687, 1993.

[41] X. Zhang and C. Gao, "Influence of Reflectance on Determination of Free Carrier Absorption of Silicon Wafer," Int. J. Thermophys., vol. 36, no. 5–6, pp. 973–979, Jun. 2015.

[42] S. Ren, B. Li, and Q. Huang, "Three-dimensional transient model for time-domain free-carrier absorption measurement of excess carriers in silicon wafers," J. Appl. Phys., vol. 114, no. 24, p. 243702, Dec. 2013.

[43] S. S. Suvanam et al., "4H-silicon carbide-dielectric interface recombination analysis using free carrier absorption," J. Appl. Phys., vol. 117, no. 10, p. 105309, Mar. 2015.

[44] W. D. Eades and R. M. Swanson, "Calculation of surface generation and recombination velocities at the Si-SiO$_2$ interface," J. Appl. Phys., vol. 58, no. 11, pp. 4267–4276, Dec. 1985.

[45] J. Meitzner, F. G. Moore, B. M. Tillotson, S. D. Kevan, and G. L. Richmond, "Time-resolved measurement of free carrier absorption, diffusivity, and internal quantum efficiency in silicon," Appl. Phys. Lett., vol. 103, no. 9, p. 092101, Aug. 2013.

[46] J. Isenberg and W. Warta, "Free carrier absorption in heavily doped silicon layers," Appl. Phys. Lett., vol. 84, no. 13, pp. 2265–2267, Mar. 2004.

[47] R. J. Schwartz and J. L. Gray, "Contactless measurement of lifetime by free carrier infrared absorption," in 13th Photovoltaic Specialists Conference, 1978, pp. 83–88.

[48] T. Warabisako, T. Saitoh, T. Motooka, and T. Tokuyama, "Contactless Measurement of Wafer Lifetime by Free Carrier Infrared Absorption," Jpn. J. Appl. Phys., vol. 22, no. S1, p. 557, 1983.

[49] S. M. Johnson and L. G. Johnson, "Contactless measurement of bulk free-carrier lifetime in cast polycrystalline silicon ingots," J. Appl. Phys., vol. 60, no. 6, pp. 2008–2015, Sep. 1986.

[50] J. Waldmeyer, "A contactless method for determination of carrier lifetime, surface recombination velocity, and diffusion constant in semiconductors," J. Appl. Phys., vol. 63, no. 6, pp. 1977–1983, Mar. 1988.

[51] K. L. Luke and L. Cheng, "Analysis of the interaction of a laser pulse with a silicon wafer: Determination of bulk lifetime and surface recombination velocity," J. Appl. Phys., vol. 61, no. 6, pp. 2282–2293, Mar. 1987.

[52] J. Linnros and V. Grivickas, "Carrier-diffusion measurements in silicon with a Fourier-transient-grating method," Phys. Rev. B, vol. 50, no. 23, p. 16943, 1994.

[53] P. Ščajev and K. Jarašiūnas, "Temperature- and excitation-dependent carrier diffusivity and recombination rate in 4H-SiC," J. Phys. Appl. Phys., vol. 46, no. 26, p. 265304, Jul. 2013.

[54] N. J. Harrick, "Lifetime Measurements of Excess Carriers in Semiconductors," J. Appl. Phys., vol. 27, no. 12, pp. 1439–1442, Dec. 1956.

[55] D. L. Polla, "Determination of carrier lifetime in Si by optical modulation," IEEE Electron Device Lett., vol. 4, no. 6, pp. 185–187, 1983.

[56] P.-C. Yang and S. S. Li, "Measurements of substrate carrier lifetimes in silicon-on-insulator wafers by a contactless dual-beam optical modulation technique," Solid-State Electron., vol. 35, no. 7, pp. 927–932, 1992.

[57] M. Bail, J. Kentsch, R. Brendel, and M. Schulz, "Lifetime mapping of Si wafers by an infrared camera [for solar cell production]," in Photovoltaic Specialists Conference, 2000. Conference Record of the Twenty-Eighth IEEE, 2000, pp. 99–103.

[58] D. K. Schroder, R. N. Thomas, and J. C. Swartz, "Free carrier absorption in silicon," IEEE J. Solid-State Circuits, vol. 13, no. 1, pp. 180–187, 1978.

[59] M. B. Suddendorf and M. G. Somekh, "Single beam photoreflectance microscopy system with electronic feedback," Electron. Lett., vol. 30, no. 5, pp. 398–399, 1994.

[60] H. P. Ho, S. Y. Wu, and P. K. Chu, "A simplified surface photoreflectance measurement system," Meas. Sci. Technol., vol. 11, no. 9, p. 1348, 2000.

[61] K. G. Svantesson and N. G. Nilsson, "Determination of the Absorption and the Free Carrier Distribution in Silicon at High Level Photogeneration at 1.06 μm and 294 K," Phys. Scr., vol. 18, pp. 405–409.

[62] P.-C. Heisel et al., "Free charge carrier absorption in silicon at 800 nm," Appl. Phys. B, vol. 122, no. 3, Mar. 2016.

[63] W. I. Ndebeka, P. H. Neethling, E. G. Rohwer, C. M. Steenkamp, J. Bergmann, and H. Stafast, "Interband and free charge carrier absorption in silicon at 800 nm: experiments and model calculations," Appl. Phys. B, vol. 123, no. 10, Oct. 2017.

[64] K. G. Svantesson, "Determination of the interband and the free carrier absorption constants in silicon at high-level photoinjection," J. Phys. Appl. Phys., vol. 12, no. 3, p. 425, 1979.

[65] K. G. Svantesson and N. G. Nilsson, "The temperature dependence of the Auger recombination coefficient of undoped silicon," J. Phys. C Solid State Phys., vol. 12, no. 23, p. 5111, 1979.

[66] K. G. Svantesson and N. G. Nilsson, "Determination of the temperature dependence of the free carrier and interband absorption in silicon at 1.06 μm," J. Phys. C Solid State Phys., vol. 12, no. 18, p. 3837, 1979.

[67] C. Battaglia, A. Cuevas, and S. De Wolf, "High-efficiency crystalline silicon solar cells: status and perspectives," Energy Environ. Sci., vol. 9, no. 5, pp. 1552–1576, 2016.

[68] J. García-Martín, J. Gómez-Gil, and E. Vázquez-Sánchez, "Non-Destructive Techniques Based on Eddy Current Testing," Sensors, vol. 11, no. 3, pp. 2525–2565, Feb. 2011.

[69] D. B. M. Klaassen, "A unified mobility model for device simulation—I. Model equations and concentration dependence," Solid-State Electron., vol. 35, no. 7, pp. 953–959, 1992.

[70] P. Zheng, F. E. Rougieux, D. Macdonald, and A. Cuevas, "Measurement and Parameterization of Carrier Mobility Sum in Silicon as a Function of Doping, Temperature and Injection Level," IEEE J. Photovolt., vol. 4, no. 2, pp. 560–565, Mar. 2014.

[71] S. C. Baker-Finch, K. R. McIntosh, D. Yan, K. C. Fong, and T. C. Kho, "Near-infrared free carrier absorption in heavily doped silicon," J. Appl. Phys., vol. 116, no. 6, p. 063106, Aug. 2014.

[72] B. K. Ridley, Quantum Processes in Semiconductors. OUP Oxford, 2013.

[73] G. N. Koskowich, M. Soma, and R. B. Darling, "Near-infrared free-carrier optical absorption in silicon: effect of first-order phonon-assisted scattering in a nonparabolic conduction band," Phys. Rev. B, vol. 41, no. 5, p. 2944, 1990.

[74] T. Trupke, R. A. Bardos, M. C. Schubert, and W. Warta, "Photoluminescence imaging of silicon wafers," Appl. Phys. Lett., vol. 89, no. 4, p. 044107, Jul. 2006.

[75] J. Iveland, L. Martinelli, J. Peretti, J. S. Speck, and C. Weisbuch, "Direct Measurement of Auger Electrons Emitted from a Semiconductor Light-Emitting Diode under Electrical

Injection: Identification of the Dominant Mechanism for Efficiency Droop," Phys. Rev. Lett., vol. 110, no. 17, Apr. 2013.

[76] S. M. Sze and K. K. Ng, Physics of Semiconductor Devices. Wiley, 2006.

[77] M. Z. Rahman and S. I. Khan, "Advances in surface passivation of c-Si solar cells," Mater. Renew. Sustain. Energy, vol. 1, no. 1, Dec. 2012.

[78] T. Lauinger, J. Schmidt, A. G. Aberle, and R. Hezel, "Record low surface recombination velocities on 1 Ω cm p -silicon using remote plasma silicon nitride passivation," Appl. Phys. Lett., vol. 68, no. 9, pp. 1232–1234, Feb. 1996.

[79] J. Zhao, A. Wang, M. A. Green, and F. Ferrazza, "19.8% efficient 'honeycomb' textured multicrystalline and 24.4% monocrystalline silicon solar cells," Appl. Phys. Lett., vol. 73, no. 14, pp. 1991–1993, Oct. 1998.

[80] M. A. Green, K. Emery, Y. Hishikawa, W. Warta, and E. D. Dunlop, "Solar cell efficiency tables (version 44): Solar cell efficiency tables," Prog. Photovolt. Res. Appl., vol. 22, no. 7, pp. 701–710, Jul. 2014.

[81] M. Rosling, H. Bleichner, P. Jonsson, and E. Nordlander, "The ambipolar diffusion coefficient in silicon: Dependence on excess-carrier concentration and temperature," J. Appl. Phys., vol. 76, no. 5, pp. 2855–2859, Sep. 1994.

[82] T. E. Tiwald, A. D. Miller, and J. A. Woollam, "Measurement of silicon doping profiles using infrared ellipsometry combined with anodic oxidation sectioning," 1998, pp. 221–225.

[83] N. F. Scherer, J. L. Knee, D. D. Smith, and A. H. Zewail, "Femtosecond photofragment spectroscopy: The reaction ICN→ CN+ I," J. Phys. Chem., vol. 89, no. 24, pp. 5141–5143, 1985.

[84] M. Drescher, M. Hentschel, R. Klenberger, M. Ulberacker, and others, "Time-resolved atomic inner-shell spectroscopy," Nature, vol. 419, no. 6909, p. 802, 2002.

[85] F. Vetrone et al., "Temperature Sensing Using Fluorescent Nanothermometers," ACS Nano, vol. 4, no. 6, pp. 3254–3258, Jun. 2010.

[86] K. E. Schmidt et al., "Time-resolved protein nanocrystallography using an X-ray free-electron laser," 2011.

[87] J. R. Goldman and J. A. Prybyla, "Ultrafast Dynamics of Laser-Excited Electron Distributions in Silicon," Phys. Rev. Lett., vol. 72, no. 9, pp. 1364–1367, 1994.

[88] M. A. Green, Silicon solar cells: advanced principles & practice. Centre for photovoltaic devices and systems, University of New South Wales, 1995.

[89] M. Rudiger, J. Greulich, A. Richter, and M. Hermle, "Parameterization of Free Carrier Absorption in Highly Doped Silicon for Solar Cells," IEEE Trans. Electron Devices, vol. 60, no. 7, pp. 2156–2163, Jul. 2013.

[90] G. Xu et al., "An improved optical simulation method for crystalline silicon solar cells," in Photovoltaic Specialists Conference (PVSC), 2013 IEEE 39th, 2013, pp. 2677–2680.

[91] R. Soref and B. Bennett, "Electrooptical effects in silicon," IEEE J. Quantum Electron., vol. 23, no. 1, pp. 123–129, 1987.

[92] D. M. Caughey and R. E. Thomas, "Carrier mobilities in silicon empirically related to doping and field," Proc. IEEE, vol. 55, no. 12, pp. 2192–2193, 1967.

[93] E. Barta, "Optical constants of various heavily doped p-and n-type silicon crystals obtained by Kramers-Kronig analysis," Infrared Phys., vol. 17, no. 5, pp. 319–329, 1977.

[94] E. Langereis, S. B. S. Heil, M. C. M. van de Sanden, and W. M. M. Kessels, "In situ spectroscopic ellipsometry study on the growth of ultrathin TiN films by plasma-assisted atomic layer deposition," J. Appl. Phys., vol. 100, no. 2, p. 023534, Jul. 2006.

[95] J. W. Klaus, A. W. Ott, A. C. Dillon, and S. M. George, "Atomic layer controlled growth of Si3N4 films using sequential surface reactions," Surf. Sci., vol. 418, no. 1, pp. L14–L19, 1998.

[96] P. R. Kidambi et al., "In Situ Observations during Chemical Vapor Deposition of Hexagonal Boron Nitride on Polycrystalline Copper," Chem. Mater., vol. 26, no. 22, pp. 6380–6392, Nov. 2014.

[97] B. Bein et al., "In situ X-ray diffraction and the evolution of polarization during the growth of ferroelectric superlattices," Nat. Commun., vol. 6, no. 1, Dec. 2015.

[98] M. L. Taheri et al., "Current status and future directions for in situ transmission electron microscopy," Ultramicroscopy, vol. 170, pp. 86–95, Nov. 2016.

[99] Z.-J. Wang et al., "Direct Observation of Graphene Growth and Associated Copper Substrate Dynamics by in Situ Scanning Electron Microscopy," ACS Nano, vol. 9, no. 2, pp. 1506–1519, Feb. 2015.

[100] M. M. Frank, Y. J. Chabal, and G. D. Wilk, "Nucleation and interface formation mechanisms in atomic layer deposition of gate oxides," Appl. Phys. Lett., vol. 82, no. 26, pp. 4758–4760, Jun. 2003.

[101] V. Hopfe et al., "In-situ monitoring for CVD processes," Thin Solid Films, vol. 442, no. 1–2, pp. 60–65, Oct. 2003.

[102] A. G. Aberle, T. Lauinger, J. Schmidt, and R. Hezel, "Injection-level dependent surface recombination velocities at the silicon-plasma silicon nitride interface," Appl. Phys. Lett., vol. 66, no. 21, pp. 2828–2830, May 1995.

[103] H. T. T. Nguyen et al., "Al$_2$O$_3$/SiON stack layers for effective surface passivation and anti-reflection of high efficiency n-type c-Si solar cells," Semicond. Sci. Technol., vol. 32, no. 2, p. 025005, Feb. 2017.

[104] J. Yoo, S. Kumar Dhungel, and J. Yi, "Annealing optimization of silicon nitride film for solar cell application," Thin Solid Films, vol. 515, no. 19, pp. 7611–7614, Jul. 2007.

[105] W. Soppe, H. Rieffe, and A. Weeber, "Bulk and surface passivation of silicon solar cells accomplished by silicon nitride deposited on industrial scale by microwave PECVD," Prog. Photovolt. Res. Appl., vol. 13, no. 7, pp. 551–569, Nov. 2005.

[106] Y. Wan, K. R. McIntosh, and A. F. Thomson, "Characterisation and optimisation of PECVD SiN$_x$ as an antireflection coating and passivation layer for silicon solar cells," AIP Adv., vol. 3, no. 3, p. 032113, Mar. 2013.

[107] M. J. D, H. Jürgen, S. Jan, and H. Rudolf, "High-quality surface passivation of silicon solar cells in an industrial-type inline plasma silicon nitride deposition system," Prog. Photovolt. Res. Appl., vol. 12, no. 1, pp. 21–31.

[108] S.-S. Han, L. Cai, G. S. May, and A. Rohatgi, "Modeling the growth of PECVD silicon nitride films for solar cell applications using neural networks," IEEE Trans. Semicond. Manuf., vol. 9, no. 3, pp. 303–311, 1996.

[109] J. Schmidt, M. Kerr, and A. Cuevas, "Surface passivation of silicon solar cells using plasma-enhanced chemical-vapour-deposited SiN films and thin thermal SiO$_2$/plasma SiN stacks," Semicond. Sci. Technol., vol. 16, no. 3, p. 164, 2001.

[110] G. Agostinelli et al., "Very low surface recombination velocities on p-type silicon wafers passivated with a dielectric with fixed negative charge," Sol. Energy Mater. Sol. Cells, vol. 90, no. 18–19, pp. 3438–3443, Nov. 2006.

[111] P. Saint-Cast, D. Kania, M. Hofmann, J. Benick, J. Rentsch, and R. Preu, "Very low surface recombination velocity on p-type c-Si by high-rate plasma-deposited aluminum oxide," Appl. Phys. Lett., vol. 95, no. 15, p. 151502, Oct. 2009.

[112]   P. Spinelli, M. Hebbink, R. de Waele, L. Black, F. Lenzmann, and A. Polman, "Optical Impedance Matching Using Coupled Plasmonic Nanoparticle Arrays," Nano Lett., vol. 11, no. 4, pp. 1760–1765, Apr. 2011.

[113]   K. R. Catchpole et al., "Plasmonics and nanophotonics for photovoltaics," MRS Bull., vol. 36, no. 06, pp. 461–467, Jun. 2011.

[114]   H. A. Atwater and A. Polman, "Plasmonics for improved photovoltaic devices," Nat. Mater., vol. 9, no. 3, pp. 205–213, Mar. 2010.

[115]   S. Pillai and M. A. Green, "Plasmonics for photovoltaic applications," Sol. Energy Mater. Sol. Cells, vol. 94, no. 9, pp. 1481–1486, Sep. 2010.

[116]   F. J. Beck, A. Polman, and K. R. Catchpole, "Tunable light trapping for solar cells using localized surface plasmons," J. Appl. Phys., vol. 105, no. 11, p. 114310, Jun. 2009.

Appendix A   Writing Luke and Cheng Solution in terms of $\mathfrak{T}$

According to Luke and Cheng [51] the solution to (3.18) subject to the boundary conditions (3.22) & (3.23) for a temporal impulse excitation $g(z, t)$ is:

$$n(t) = \phi_0 \frac{(1 - R)}{1 - Re^{-\alpha\eta W}} \frac{8\alpha\eta e^{-\frac{\alpha\eta W}{2}}}{W} \text{X} \tag{A.1}$$

$$\sum_{n=1}^{\infty} \frac{\sin\left(\frac{\alpha_n W}{2}\right)}{((\alpha\eta)^2 + \alpha_n^2)(\alpha_n W + \sin\alpha_n W)} \left[\alpha\eta \sinh\left(\frac{\alpha\eta W}{2}\right)\cos\left(\frac{\alpha_n W}{2}\right)\right.$$

$$\left. + \alpha_n \cosh\left(\frac{\alpha\eta W}{2}\right)\sin\left(\frac{\alpha_n W}{2}\right)\right] e^{-\frac{t}{\tau_n}}$$

The frequency-domain representation of this equation is just the Fourier transform of $n(t)$:

$$N(\omega) = \int_0^\infty n(t)e^{-i\omega t}dt \tag{A.2}$$

The Fourier transform limits are from 0 to infinity and not negative to positive infinity, since $\Delta n(t) = 0$ for $t < 0$. The time-dependent term in e^{-t/τ_n} which has the Fourier transform $\tau_n/(1 + i\omega\tau_n)$. Therefore:

$$N(\omega) = \phi_0 \frac{(1-R)}{1-Re^{-\alpha\eta W}} \frac{8\alpha\eta e^{-\frac{\alpha\eta W}{2}}}{W} \text{ X} \tag{A.3}$$

$$\sum_{n=1}^{\infty} \frac{\sin\left(\frac{\alpha_n W}{2}\right)}{((\alpha\eta)^2 + \alpha_n^2)(\alpha_n W + \sin \alpha_n W)} \left[\alpha\eta \sinh\left(\frac{\alpha\eta W}{2}\right)\cos\left(\frac{\alpha_n W}{2}\right)\right.$$
$$\left. + \alpha_n \cosh\left(\frac{\alpha\eta W}{2}\right)\sin\left(\frac{\alpha_n W}{2}\right)\right] \frac{\tau_n}{1 + i\omega\tau_n}$$

For an excitation source with absorption coefficient α, and an initial photon flux ϕ_0' entering the wafer, the photon flux inside the wafer is given by:

$$\phi(x) = \phi_0' \, e^{-\alpha x} \tag{A.4}$$

The volumetric generation rate G is then given by:

$$G(x,\omega) = A(\omega)\left[-\frac{d\phi}{dx}\right] \tag{A.5}$$

where $A(\omega)$ is the amplitude of the modulation. In this experiment $A(\omega)$ is flat across all of the frequencies of interest, so $A(\omega) = 1$. The average volumetric generation rate is given by $\frac{1}{W}\int_{-W/2}^{W/2} G(x,\omega)dx$, so:

$$G(\omega) = \frac{1}{W}[\phi(-W/2) - \phi(W/2)] \tag{A.6}$$

The factor in square brackets is just the photon flux absorbed into the wafer, which is $\phi_0 f_a$. Therefore the average generation rate, in terms of the incident photon flux, is:

$$G(\omega) = \frac{\phi_0 f_a}{W} \tag{A.7}$$

where f_a is the fraction of incident light absorbed into the wafer, which is given by (Appendix I):

$$f_a = (1 - R)\frac{1 - e^{-\alpha\eta W}}{1 - Re^{-\alpha\eta W}} \tag{A.8}$$

. $\mathfrak{T}$ is defined as $N(\omega)/G(\omega)$ (Equation (3.19)), so the $\mathfrak{T}$ factor for the Luke and Cheng solution is given by:

$$\mathfrak{T} = \frac{8\alpha\eta e^{-\frac{\alpha\eta W}{2}}}{1 - e^{-\alpha\eta W}} \sum_{n=1}^{\infty} \frac{\sin\left(\frac{\alpha_n W}{2}\right)}{((\alpha\eta)^2 + \alpha_n^2)(\alpha_n W + \sin\alpha_n W)}\left[\alpha\eta \sinh\left(\frac{\alpha\eta W}{2}\right)\cos\left(\frac{\alpha_n W}{2}\right)\right. \tag{A.9}$$
$$\left. + \alpha_n \cosh\left(\frac{\alpha\eta W}{2}\right)\sin\left(\frac{\alpha_n W}{2}\right)\right]\frac{\tau_n}{1 + i\omega\tau_n}$$

Appendix B   Writing Sanii Solution in Terms of

$\mathfrak{T}$

According to Sanii et.al., amplitude of the excess carrier density $N(\omega)$ is given by (Equation 22 in Refs [8]):

$$N(\omega) = \frac{\phi_0}{WD(\alpha^2 L^2 - 1)} L^2 [\alpha L C_1(1 - e^{-x}) - \alpha L C_2(1 - e^x) - (1 - e^{-\alpha W})] \qquad \text{(B.1)}$$

where ϕ_0 is the incident photon flux density, D is the diffusion coefficient, C_1 & C_2 are coefficients, x is a factor given by W/L, and L is the *effective diffusion length*. The C coefficients and L are given by:

$$C_1 = \frac{1}{2} \frac{\left[(\alpha D + S_f)\left(\frac{D}{L} - S_r\right) - (\alpha D - S_r)\left(\frac{D}{L} + S_f\right) e^{-\alpha W} e^x \right]}{\left(\frac{D^2}{L^2} + S_f S_r\right) \sinh x + \frac{D}{L}(S_f + S_r) \cosh x} \qquad \text{(B.2)}$$

$$C_2 = \frac{1}{2} \frac{\left[(\alpha D + S_f)\left(\frac{D}{L} + S_r\right) - (\alpha D - S_r)\left(\frac{D}{L} - S_f\right) e^{-\alpha W} e^{-x}\right]}{\left(\frac{D^2}{L^2} + S_f S_r\right) \sinh x + \frac{D}{L}(S_f + S_r) \cosh x} \tag{B.3}$$

$$L = \sqrt{\frac{D\tau_b}{1 + i\omega\tau_b}} \tag{B.4}$$

Note that the lifetime appearing in L is the bulk lifetime, and not an effective lifetime. The generation rate is given by Equation (A.7) (Appendix A), so by dividing (B.4) by (A.7) we get $\mathfrak{T}$:

$$\mathfrak{T} = \frac{1}{D(\alpha^2 L^2 - 1)(1 - e^{-\alpha W})} L^2 [\alpha L C_1 (1 - e^{-x}) - \alpha L C_2 (1 - e^x) - (1 - e^{-\alpha W})] \tag{B.5}$$

$$= \frac{L^2}{D(\alpha^2 L^2 - 1)(1 - e^{-\alpha W})} \Gamma$$

where we have written the terms in square brackets in (B.5) as a factor Γ:

$$\Gamma = [\alpha L C_1(1 - e^{-x}) - \alpha L C_2(1 - e^x) - (1 - e^{-\alpha W})] \tag{B.6}$$

We now simplify the factor Γ. Rearranging (B.6) we get:

$$\Gamma = -\alpha L(C_2 - C_1) + \alpha L(C_2 e^x - C_1 e^{-x}) - (1 - e^{-\alpha W}) \tag{B.7}$$

Examine the factor $(C_2 e^x - C_1 e^{-x})$. Expand the exponentials into their Taylor series:

$$(C_2 e^x - C_1 e^{-x}) \tag{B.8}$$
$$= C_2\left(1 + x + \frac{x^2}{2!} + \frac{x^3}{3!} + \frac{x^4}{4!} \cdots\right) - C_1\left(1 - x + \frac{x^2}{2!} - \frac{x^3}{3!} + \frac{x^4}{4!}\right.$$
$$\left. - \cdots\right)$$

$$(C_2 e^x - C_1 e^{-x}) \tag{B.9}$$
$$= (C_2 - C_1) + (C_2 + C_1)\left[x + \frac{x^3}{3!} + \cdots\right]$$
$$+ (C_2 - C_1)\left[\frac{x^2}{2!} + \frac{x^4}{4!} + \cdots\right]$$

The first series in square brackets is that of $\sinh x$, and the second is $\cosh x - 1$:

$$(C_2 e^x - C_1 e^{-x}) = (C_2 - C_1) + (C_2 + C_1)\sinh x + (C_2 - C_1)(\cosh x - 1) \qquad \text{(B.10)}$$

$$(C_2 e^x - C_1 e^{-x}) = (C_2 + C_1)\sinh x + (C_2 - C_1)\cosh x \qquad \text{(B.11)}$$

Now we evaluate the expressions for $C_2 \pm C_1$. Assume that the front and rear surface recombination velocities are identical (*i.e.* $S = S_f = S_r$).

$$C_2 + C_1 = \frac{1}{2}\frac{\left[\frac{2D}{L}(\alpha D + S) - (\alpha D - S)e^{-\alpha W}\left[\left(\frac{D}{L} + S\right)e^x + \left(\frac{D}{L} - S\right)e^{-x}\right]\right]}{\left(\frac{D^2}{L^2} + S^2\right)\sinh x + 2S\frac{D}{L}\cosh x} \qquad \text{(B.12)}$$

$$C_2 + C_1 = \frac{1}{2}\frac{\left[\frac{2D}{L}(\alpha D + S) - (\alpha D - S)e^{-\alpha W}\left[\frac{2D}{L}\cosh x + 2S\sinh x\right]\right]}{\left(\frac{D^2}{L^2} + S^2\right)\sinh x + 2S\frac{D}{L}\cosh x} \qquad \text{(B.13)}$$

$$C_2 + C_1 = \frac{\frac{D}{L}(\alpha D + S) - (\alpha D - S)e^{-\alpha W}\left[\frac{D}{L}\cosh x + S\sinh x\right]}{\left(\frac{D^2}{L^2} + S^2\right)\sinh x + 2S\frac{D}{L}\cosh x} \tag{B.14}$$

$$C_2 - C_1 = \frac{1}{2}\frac{\left[2S(\alpha D + S) - (\alpha D - S)e^{-\alpha W}\left[\left(\frac{D}{L} - S\right)e^{-x} - \left(\frac{D}{L} + S\right)e^{x}\right]\right]}{\left(\frac{D^2}{L^2} + S^2\right)\sinh x + 2S\frac{D}{L}\cosh x} \tag{B.15}$$

$$C_2 - C_1 = \frac{1}{2}\frac{\left[2S(\alpha D + S) + (\alpha D - S)e^{-\alpha W}\left[\frac{2D}{L}\sinh x + 2S\cosh x\right]\right]}{\left(\frac{D^2}{L^2} + S^2\right)\sinh x + 2S\frac{D}{L}\cosh x} \tag{B.16}$$

$$C_2 - C_1 = \frac{S(\alpha D + S) + (\alpha D - S)e^{-\alpha W}\left[\frac{D}{L}\sinh x + S\cosh x\right]}{\left(\frac{D^2}{L^2} + S^2\right)\sinh x + 2S\frac{D}{L}\cosh x} \tag{B.17}$$

Substitute the final expressions for $C_2 \pm C_1$ into Equation (B.11):

$$(C_2 e^x - C_1 e^{-x}) \tag{B.18}$$

$$= \left[\frac{\frac{D}{L}(\alpha D + S) - (\alpha D - S)e^{-\alpha W}\left[\frac{D}{L}\cosh x + S\sinh x\right]}{\left(\frac{D^2}{L^2} + S^2\right)\sinh x + 2S\frac{D}{L}\cosh x}\right]\sinh x$$

$$+ \left[\frac{S(\alpha D + S) + (\alpha D - S)e^{-\alpha W}\left[\frac{D}{L}\sinh x + S\cosh x\right]}{\left(\frac{D^2}{L^2} + S^2\right)\sinh x + 2S\frac{D}{L}\cosh x}\right]\cosh x$$

Group the denominator into a factor γ:

$$(C_2 e^x - C_1 e^{-x}) \tag{B.19}$$

$$= \frac{1}{\gamma}\left[(\alpha D + S)\left(\frac{D}{L}\sinh x + S\cosh x\right)\right.$$

$$\left. + (\alpha D - S)e^{-\alpha W}[S(\cosh^2 x - \sinh^2 x)]\right]$$

$$(C_2 e^x - C_1 e^{-x}) = \frac{\left[(\alpha D + S)\left(\frac{D}{L}\sinh x + S\cosh x\right) + S(\alpha D - S)e^{-\alpha W}\right]}{\left(\frac{D^2}{L^2} + S^2\right)\sinh x + 2S\frac{D}{L}\cosh x} \tag{B.20}$$

Let's condense the above expressions by introducing some dimensionless parameters μ & ν:

$$\mu \equiv \frac{\alpha D}{S} \tag{B.21}$$

$$\nu \equiv \frac{D}{LS} \tag{B.22}$$

Divide the top and bottom of $C_2 - C_1$ by S^2: Now $C_2 - C_1$ becomes:

$$C_2 - C_1 = \frac{\left(\frac{\alpha D}{S} + 1\right) + \left(\frac{\alpha D}{S} - 1\right)e^{-\alpha W}\left[\frac{D}{LS}\sinh x + \cosh x\right]}{\left(\frac{D^2}{L^2 S^2} + 1\right)\sinh x + 2\frac{D}{LS}\cosh x} \tag{B.23}$$

$$C_2 - C_1 = \frac{(\mu + 1) + (\mu - 1)e^{-\alpha W}[\nu \sinh x + \cosh x]}{(\nu^2 + 1)\sinh x + 2\nu\cosh x} \tag{B.24}$$

Dividing the top and bottom of $(C_2 e^x - C_1 e^{-x})$ by S^2:

$$(C_2 e^x - C_1 e^{-x}) = \frac{\left[\left(\frac{\alpha D}{S} + 1\right)\left(\frac{D}{LS}\sinh x + \cosh x\right) + \left(\frac{\alpha D}{S} - 1\right)e^{-\alpha W}\right]}{\left(\frac{D^2}{L^2 S^2} + 1\right)\sinh x + 2\frac{D}{LS}\cosh x} \tag{B.25}$$

$$(C_2 e^x - C_1 e^{-x}) = \frac{[(\mu + 1)(\nu \sinh x + \cosh x) + (\mu - 1)e^{-\alpha W}]}{(\nu^2 + 1)\sinh x + 2\nu\cosh x} \tag{B.26}$$

Letting $\gamma = (\nu^2 + 1) \sinh x + 2\nu \cosh x$, substitute (B.24) and (B.26) into (B.7):

$$\Gamma = -\alpha L \left[\frac{(\mu + 1) + (\mu - 1)e^{-\alpha W}(\nu \sinh x + \cosh x)}{\gamma} \right] \tag{B.27}$$

$$+ \alpha L \left[\frac{(\mu + 1)(\nu \sinh x + \cosh x) + (\mu - 1)e^{-\alpha W}}{\gamma} \right] - (1 - e^{-\alpha W})$$

$$\Gamma = -\frac{\alpha L}{\gamma} [(\mu + 1) + (\mu - 1)e^{-\alpha W}(\nu \sinh x + \cosh x) \tag{B.28}$$

$$- (\mu + 1)(\nu \sinh x + \cosh x) - (\mu - 1)e^{-\alpha W}] - (1 - e^{-\alpha W})$$

Let $\beta = (\nu \sinh x + \cosh x)$

$$\Gamma = -\frac{\alpha L}{\gamma} [(\mu + 1) + (\mu - 1)e^{-\alpha W}\beta - (\mu + 1)\beta - (\mu - 1)e^{-\alpha W}] - (1 - e^{-\alpha W}) \tag{B.29}$$

$$\Gamma = -\frac{\alpha L}{\gamma}[(\mu + 1) + (\mu - 1)e^{-\alpha W}(\beta - 1) - (\mu + 1)\beta] - (1 - e^{-\alpha W}) \tag{B.30}$$

$$\Gamma = -\frac{\alpha L}{\gamma}[\mu + 1 + \mu e^{-\alpha W}(\beta - 1) - e^{-\alpha W}(\beta - 1) - \mu\beta - \beta] - (1 - e^{-\alpha W}) \tag{B.31}$$

$$\Gamma = -\frac{\alpha L}{\gamma}[\mu(1 + e^{-\alpha W}(\beta - 1) - \beta) + (1 - e^{-\alpha W}(\beta - 1) - \beta] - (1 - e^{-\alpha W}) \tag{B.32}$$

$$\Gamma = -\frac{\alpha L}{\gamma}[\mu(1 - e^{-\alpha W})(1 - \beta) + (1 + e^{-\alpha W})(1 - \beta)] - (1 - e^{-\alpha W}) \tag{B.33}$$

$$\Gamma = \frac{\alpha L}{\gamma}(\beta - 1)[\mu(1 - e^{-\alpha W}) + (1 + e^{-\alpha W})] - (1 - e^{-\alpha W}) \tag{B.34}$$

Substitute Γ into Equation (B.5):

$$\mathfrak{T} = \frac{L^2}{D(\alpha^2 L^2 - 1)} \frac{\frac{\alpha L}{\gamma}(\beta - 1)[\mu(1 - e^{-\alpha W}) + (1 + e^{-\alpha W})] - (1 - e^{-\alpha W})}{(1 - e^{-\alpha W})} \tag{B.35}$$

$$\mathfrak{T} = \frac{L^2}{D(\alpha^2 L^2 - 1)}\left[\frac{\alpha L}{\gamma}(\beta - 1)\left[\mu + \frac{1 + e^{-\alpha W}}{1 - e^{-\alpha W}}\right] - 1\right] \tag{B.36}$$

$$\mathfrak{T} = \frac{L^2}{D(\alpha^2 L^2 - 1)}\left[\frac{\alpha L}{\gamma}(\beta - 1)\left(\mu + \coth\frac{\alpha W}{2}\right) - 1\right] \tag{B.37}$$

Let's examine the factor $\frac{\beta-1}{\gamma}$. Substitute in the values for β and γ:

$$\frac{\beta - 1}{\gamma} = \frac{v \sinh x + \cosh x}{(v^2 + 1) \sinh x + 2v \cosh x} \tag{B.38}$$

This simplifies to:

$$\frac{\beta - 1}{\gamma} = \frac{1}{v + \coth\frac{x}{2}} \tag{B.39}$$

Substituting this into (B.37) we get:

$$\mathfrak{I} = \frac{L^2}{D(\alpha^2 L^2 - 1)} \left[\frac{\mu + \coth\frac{\alpha W}{2}}{v + \coth\frac{x}{2}} \alpha L - 1 \right] \tag{B.40}$$

184

Appendix C   Solution to 3D Continuity Equation

In this appendix I derive a solution to the excess carrier density $n(r, z, t)$ as a function of 3D position and time for the case of an impulse-response optical generation rate with a Gaussian spatial distribution of power. This derivation is a generalization of the 1D solution given by Luke and Cheng [51]. The derivation uses separation of variables to separate the equation into two differential equations: one that depends only on the radial coordinate, and one that depends on the axial coordinate and time. The axial/time dependent equation is solved following the procedure used by Luke and Cheng. The resulting solution for $n(r, z, t)$ depends on the Luke and Cheng solution, as well as a radial component.

The 3D continuity equation in cylindrical coordinates is given by:

$$\frac{\partial n}{\partial t} = D\frac{\partial^2 n}{\partial r^2} + \frac{D}{r}\frac{\partial n}{\partial r} + D\frac{\partial^2 n}{\partial z^2} - \frac{n}{\tau_b} \tag{C.1}$$

where n is the excess carrier density, τ_b is the bulk recombination lifetime, and D is the diffusion coefficient. The goal is to solve this equation in the time domain for an impulse-response generation, and then convert to the frequency-domain via Fourier transform. Let the solution be given by:

$$n(r, z, t) = \Theta(z, t)R(r) \tag{C.2}$$

Substituting into (C.2) into (C.1):

$$\Theta_t = D\Theta R_{rr} + \frac{D}{r}\Theta R_r + D\Theta_{zz}R - \frac{\Theta R}{\tau_b} \tag{C.3}$$

$$\frac{1}{D}\frac{\Theta_t}{\Theta} = \frac{R_{rr}}{R} + \frac{1}{r}\frac{R_r}{R} + \frac{\Theta_{zz}}{\Theta} - \frac{1}{D\tau_b} \tag{C.4}$$

$$\left[\frac{1}{D}\frac{\Theta_t}{\Theta} - \frac{\Theta_{zz}}{\Theta} + \frac{1}{D\tau_b}\right] - \left[\frac{R_{rr}}{R} + \frac{1}{r}\frac{R_r}{R}\right] = 0 \tag{C.5}$$

The first term in square brackets in (C.5) depends only on z, t, whereas the second term only depends on r. Since these terms vary independently of each other, the only way for (C.5) to be satisfied is for each term to be equal to a constant $-\gamma_m^2$ (we incorporate the index m since this term will be summed over later on). Let's start with the first term:

$$\frac{1}{D}\frac{\Theta_t}{\Theta} - \frac{\Theta_{zz}}{\Theta} + \frac{1}{D\tau_b} = -\gamma_m^2 \tag{C.6}$$

$$\frac{\partial \Theta}{\partial t} = D \frac{\partial^2 \Theta}{\partial z^2} - \left[\frac{1}{\tau_b} + D\gamma_m^2\right]\Theta \tag{C.7}$$

According to Luke and Cheng [51], the solution to an equation of the form in (C.7) is given by:

$$\Theta(z,t) = e^{-t\left(\frac{1}{\tau_b} + D\gamma_m^2\right)}\left[A_n e^{-\alpha_n^2 Dt}\cos\alpha_n z + B_n e^{-\beta_n^2 Dt}\sin\beta_n z\right] \tag{C.8}$$

where $A_n, B_n, \alpha_n, \& \beta_n$ are constants determined by the boundary conditions. Now consider the second term in (C.5):

$$\frac{R_{rr}}{R} + \frac{1}{r}\frac{R_r}{R} = -\gamma^2 \tag{C.9}$$

$$r^2 \frac{\partial^2 R}{\partial r^2} + r\frac{\partial R}{\partial r} + r^2\gamma^2 R = 0 \tag{C.10}$$

The solution to this equation is given by:

$$R(r) = c_1 J_0(\gamma r) + c_2 Y_0(\gamma r) \tag{C.11}$$

where c_1 & c_2 are constants, and J_0 & Y_0 are zeroth order Bessel functions of the first and second kind, respectively. Since the solution must be finite as $r \to 0$, we can take c_2 as 0. We take $c_1 = c_m$, since we will sum over the solution later on:

$$R(r) = c_m J_0(\gamma_m r) \tag{C.12}$$

The total solution for $n(z, r, t)$ is:

$$n(z, r, t) = e^{-\frac{t}{\tau_b}} \sum_m \sum_n \left[A_{mn} e^{-\alpha_n^2 Dt} \cos \alpha_n z + B_{mn} e^{-\beta_n^2 Dt} \sin \beta_n z \right] e^{-\gamma_m^2 Dt} J_0(\gamma_m r) \tag{C.13}$$

where the c_m coefficient in (C.12) has been bundled into the A_n & B_n coefficients which become A_{mn} & B_{mn}. The carrier density $n(r, z, t)$ is subject to two boundary conditions for the z variable, two for the r variable, and an initial condition for $t = 0$. The boundary conditions along z are for surface recombination:

$$D \frac{\partial n}{\partial z}\bigg|_{-\frac{W}{2}} = S\, n \tag{C.14}$$

$$D \left. \frac{\partial n}{\partial z} \right|_{\frac{W}{2}} = -S \, n \tag{C.15}$$

where W is the wafer thickness, and S is the surface recombination velocity. If the entire solution (C.13) satisfies the boundary conditions of (C.14) and (C.15) then each individual term will as well. Substituting the mn^{th} term from (C.13) into (C.14) and (C.15) we get:

$$D \left[A_{mn} e^{-\alpha_n^2 Dt} \alpha_n \sin \frac{\alpha_n W}{2} + B_{mn} e^{-\beta_n^2 Dt} \beta_n \cos \frac{\beta_n W}{2} \right] \tag{C.16}$$
$$= S \left[A_{mn} e^{-\alpha_n^2 Dt} \cos \frac{\alpha_n W}{2} - B_{mn} e^{-\beta_n^2 Dt} \sin \frac{\beta_n W}{2} \right]$$

$$D \left[-A_{mn} e^{-\alpha_n^2 Dt} \alpha_n \sin \frac{\alpha_n W}{2} + B_{mn} e^{-\beta_n^2 Dt} \beta_n \cos \frac{\beta_n W}{2} \right] \tag{C.17}$$
$$= -S \left[A_{mn} e^{-\alpha_n^2 Dt} \cos \frac{\alpha_n W}{2} + B_{mn} e^{-\beta_n^2 Dt} \sin \frac{\beta_n W}{2} \right]$$

Subtracting and adding (C.16) and (C.17) together yield conditions for the α_n & β_n coefficients, respectively. For the α_n coefficient we get:

$$2D A_{mn} e^{-\alpha_n^2 t} \alpha_n \sin \frac{\alpha_n W}{2} = 2S A_{mn} e^{-\alpha_n^2 Dt} \cos \frac{\alpha_n W}{2} \tag{C.18}$$

$$\frac{\alpha_n D}{S} = \cot \frac{\alpha_n W}{2} \tag{C.19}$$

For the β_n coefficient:

$$2DB_{mn}e^{-\beta_n^2 Dt}\beta_n \cos\frac{\beta_n W}{2} = -2SB_{mn}e^{-\beta_n^2 Dt}\sin\frac{\beta_n W}{2} \tag{C.20}$$

$$\frac{\beta_n D}{S} = -\tan\frac{\beta_n W}{2} \tag{C.21}$$

We define δ_{n1} & δ_{n2} as:

$$\delta_{n1} = \frac{\alpha_n W}{2} \tag{C.22}$$

$$\delta_{n2} = \frac{\beta_n W}{2} \tag{C.23}$$

Substituting δ_{n1} & δ_{n2} into (C.19) & (C.21), respectively, we get:

$$\cot\delta_{n1} = \frac{2D}{SW}\delta_{n1} \tag{C.24}$$

$$\tan\delta_{n2} = -\frac{2D}{SW}\delta_{n2} \tag{C.25}$$

Thus the coefficients α_n & β_n are solutions to the transcendental equations (C.24) & (C.25) . This is the exact result obtained by Luke and Cheng [51]. For the radial direction, we require that the solution goes to 0 as $r \to \infty$, and that the flux about $r = 0$ is also 0, due to radial symmetry. Both of these conditions are satisfied by $J_0(\gamma_m r)$.

Now that $n(r,z,t)$ satisfies all of the boundary conditions, we can solve for the initial condition. For an impulse-response generation, the initial value of $n(r,z,t)$ is given by:

$$n(r,z,0) = \left[\frac{2P_0\lambda}{\pi w^2 hc}e^{-\frac{2r^2}{w^2}}\right]\alpha\eta\frac{\left(e^{-\alpha\eta\left(z+\frac{W}{2}\right)} + R_{ref}e^{-\alpha\eta W}e^{-\alpha\eta\left(-z+\frac{W}{2}\right)}\right)}{1-\left(R_{ref}e^{-\alpha\eta W}\right)^2} \tag{C.26}$$

where α is the band-to-band absorption coefficient of the pump, w is the pump beam radius, and R_{ref} is the reflectance at the air-silicon interface. The term in square brackets is the radial photon flux density, and the remaining term is due to band-to-band absorption of the laser in the wafer.

Substituting in the solution (C.13) at $t = 0$:

$$\sum_m \sum_n [A_{mn}\cos\alpha_n z + B_{mn}\sin\beta_n z]J_0(\gamma_m r) \tag{C.27}$$

$$= g_0''\frac{\left(e^{-\alpha\eta\left(z+\frac{W}{2}\right)} + R_{ref}e^{-\alpha\eta W}e^{-\alpha\eta\left(-z+\frac{W}{2}\right)}\right)}{1-\left(R_{ref}e^{-\alpha\eta W}\right)^2}e^{-\frac{2r^2}{w^2}}$$

$$\sum_m \sum_n [A_{mn} \cos \alpha_n z + B_{mn} \sin \beta_n z] J_0(\gamma_m r) = g(z)h(r) \qquad \text{(C.28)}$$

where g_0'' is given by:

$$g_0'' = \left[\frac{2P_0 \lambda}{\pi w^2 hc}\right] \alpha \eta \qquad \text{(C.29)}$$

$$g(z) = g_0'' \frac{\left(e^{-\alpha \eta \left(z+\frac{W}{2}\right)} + R_{ref} e^{-\alpha \eta W} e^{-\alpha \eta \left(-z+\frac{W}{2}\right)}\right)}{1 - \left(R_{ref} e^{-\alpha \eta W}\right)^2} \qquad \text{(C.30)}$$

$$h(r) = e^{-\frac{2r^2}{w^2}} \qquad \text{(C.31)}$$

To solve for the coefficients A_{mn} & B_{mn} we need to use the orthogonality of $\cos \alpha_n z$ & $J_0(\gamma_m z)$. The orthogonality relationship for Bessel functions on an infinite domain is given by:

$$\int_0^\infty r J_0(\gamma_m r) J_0(\gamma_n r) dr = \frac{\delta(\gamma_m - \gamma_n)}{\gamma_m} \tag{C.32}$$

where δ is the Dirac Delta Function. We determine A_{mn} by multiplying both sides of (C.27) by $r J_0(\frac{\zeta_m}{a} r)$ and $\cos \alpha_n z$ and integrating:

$$\iint\limits_{r=0,z=-\frac{W}{2}}^{r=\infty,z=\frac{W}{2}} \left(\sum_m \sum_n [A_{mn} \cos \alpha_n z + B_{mn} \sin \beta_n z] J_0(\gamma_m r) \right) J_0(\gamma_m r) \cos \alpha_n z \, dr dz \tag{C.33}$$

$$= \iint\limits_{r=0,z=-\frac{W}{2}}^{r=\infty,z=\frac{W}{2}} h(r) g(z) dr dz$$

Since $\cos \alpha_n z$ & $\sin \beta_n z$ are orthogonal, the B_{mn} terms drops out.

$$A_{mn} \frac{1}{\gamma_m} \int_{-W/2}^{W/2} \cos^2 \alpha_n z \, dz = \left[\int_0^\infty r h(r) J_0(\gamma_m r) \, dr \right] \left[\int_{-W/2}^{W/2} g(z) \cos \alpha_n z \, dz \right] \tag{C.34}$$

To isolate B_{mn} we multiply by $rJ_0(\frac{\zeta_m}{a} r)$ and $\sin \alpha_n z$ and integrate, which leads to:

$$B_{mn} \frac{1}{\gamma_m} \int_{-W/2}^{W/2} \sin^2 \beta_n z \, dz = \left[\int_0^\infty rh(r)J_0(\gamma_m r) \, dr \right] \left[\int_{-W/2}^{W/2} g(z) \sin \beta_n z \, dz \right] \tag{C.35}$$

We can write A_{mn} & B_{mn} in terms of the radial Bessel coefficient, and the axial Luke and Cheng coefficients:

$$A_{mn} = A_m^{Bes} A_n^{ax} \tag{C.36}$$

$$B_{mn} = A_m^{Bes} B_n^{ax} \tag{C.37}$$

where A_m^{Bes}, A_n^{ax} and B_n^{ax} are given by:

$$A_m^{Bes} = \gamma_m \int_0^\infty rh(r)J_0(\gamma_m r) \, dr = \int_0^\infty re^{-\frac{2r^2}{w^2}} J_0(\gamma_m r) dr \tag{C.38}$$

$$A_n^{ax} = \frac{\int_{-W/2}^{W/2} g(z) \cos \alpha_n z \, dz}{\int_{-W/2}^{W/2} \cos^2 \alpha_n z \, dz} \tag{C.39}$$

$$= \frac{4g_0' \alpha_n e^{-\frac{\alpha \eta W}{2}} \left(1 + R_{ref} e^{-\frac{\alpha \eta W}{2}}\right)}{((\alpha\eta)^2 + \alpha_n^2)(\alpha_n W + \sin \alpha_n W)} \left[\alpha\eta \sinh \left(\frac{\alpha \eta W}{2}\right) \cos \left(\frac{\alpha_n W}{2}\right) \right.$$
$$\left. + \alpha_n \cosh \left(\frac{\alpha \eta W}{2}\right) \sin \left(\frac{\alpha_n W}{2}\right) \right]$$

$$B_n^{ax} = \frac{\int_{-W/2}^{W/2} g(z) \sin \beta_n z \, dz}{\int_{-W/2}^{W/2} \sin^2 \beta_n z \, dz} \tag{C.40}$$

$$= \frac{-4g_0' \alpha_n e^{-\frac{\alpha \eta W}{2}} \left(1 - R_{ref} e^{-\frac{\alpha \eta W}{2}}\right)}{((\alpha\eta)^2 + \beta_n^2)(\alpha_n W + \sin \beta_n W)} \left[\alpha\eta \cosh \left(\frac{\alpha \eta W}{2}\right) \sin \left(\frac{\beta_n W}{2}\right) \right.$$
$$\left. - \beta_n \sinh \left(\frac{\alpha \eta W}{2}\right) \cos \left(\frac{\beta_n W}{2}\right) \right]$$

where g_0' is a prefactor given by:

$$g_0' = \frac{\phi_0 \alpha \eta (1 - R_{ref})}{1 - \left(R_{ref} e^{-\alpha \eta W}\right)^2} \tag{C.41}$$

where ϕ_0 is the incident photon flux per unit area and R_{ref} is the reflectance coefficient of the air-semiconductor interface. A_n^{ax} & B_n^{ax} are the axial coefficients of the 3D solution, and are given by Equations 1d and 1e of [51]. Substitute (C.36) & (C.37) into (C.13), interchange the order of summation and isolate m & n terms:

$$n(z,r,t) = e^{-\frac{t}{\tau_b}} \sum_n \left[A_n^{ax} e^{-\alpha_n^2 Dt} \cos \alpha_n z \right. \tag{C.42}$$
$$\left. + B_n^{ax} e^{-\beta_n^2 Dt} \sin \beta_n z\right] \sum_m A_m^{Bes} e^{-\gamma_m^2 Dt} J_0(\gamma_m r)$$

The Bessel coefficient is given by:

196

$$A_m^{Bes} = \frac{w^2 \gamma_m}{4} e^{\frac{-w^2 \gamma_m^2}{8}} \qquad \text{(C.43)}$$

Substituting (C.43) into (C.42):

$$n(z, r, t) = e^{-\frac{t}{\tau_b}} \sum_n \left[A_n^{ax} e^{-\alpha_n^2 Dt} \cos \alpha_n z \right. \qquad \text{(C.44)}$$

$$\left. + B_n^{ax} e^{-\beta_n^2 Dt} \sin \beta_n z \right] \sum_m \frac{w^2 \gamma_m}{4} e^{\frac{-w^2 \gamma_m^2}{8}} e^{-\gamma_m^2 Dt} J_0(\gamma_m r)$$

The Bessel function orthogonality relationship imposes no conditions on the value of γ_m, so we may use any real number for γ_m. With this in mind, we convert the summation into an integration:

$$\sum_m e^{-\gamma_m^2 Dt} \frac{w^2 \gamma_m}{4} e^{\frac{-w^2 \gamma_m^2}{8}} J_0(\gamma_m r) = \int_0^\infty e^{-\gamma^2 Dt} \frac{w^2 \gamma}{4} e^{\frac{-w^2 \gamma^2}{8}} J_0(\gamma r) d\gamma \qquad \text{(C.45)}$$

$$\sum_m e^{-\gamma_m^2 Dt}\frac{w^2\gamma_m}{4}e^{\frac{-w^2\gamma_m^2}{8}}J_0(\gamma_m r) = \frac{w^2}{4}\int_0^\infty \gamma e^{-\gamma^2\left(Dt+\frac{w^2}{8}\right)}J_0(\gamma r)d\gamma \qquad (C.46)$$

Since the integral is over an odd function, we take the integral from 0 to infinity. If taken from negative to positive infinity, the result is 0 which is a trivial solution. This integral is given by:

$$\frac{w^2}{4}\int_0^\infty \gamma e^{-\gamma^2\left(Dt+\frac{w^2}{8}\right)}J_0(\gamma r)d\gamma = \frac{w^2}{8\left(Dt+\frac{w^2}{8}\right)}e^{-\frac{r^2}{4\left(Dt+\frac{w^2}{8}\right)}} \qquad (C.47)$$

$$\frac{w^2}{4}\int_0^\infty \gamma e^{-\gamma^2\left(Dt+\frac{w^2}{8}\right)}J_0(\gamma r)d\gamma = \frac{1}{\frac{t}{\tau_D}+1}e^{-\frac{2r^2}{w^2\left(\frac{t}{\tau_D}+1\right)}} \qquad (C.48)$$

where τ_D is the *diffusion time constant*, given by:

$$\tau_D = \frac{w^2}{8D} \tag{C.49}$$

Substituting (C.48) into the summation over m in (C.44), we arrive at the full solution to the 3D continuity equation:

$$n(z,r,t) = e^{-\frac{t}{\tau_b}} \frac{1}{\frac{t}{\tau_D}+1} e^{\frac{-2r^2}{w^2\left(\frac{t}{\tau_D}+1\right)}} \sum_n \left[A_n^{ax} e^{-\alpha_n^2 Dt} \cos \alpha_n z + B_n^{ax} e^{-\beta_n^2 Dt} \sin \beta_n z\right] \tag{C.50}$$

Equation (C.50) is a fully general solution to the 3D continuity equation in cylindrical coordinates for a Gaussian-shaped excitation beam. The solution was derived by assuming that the generation rate is a Dirac-Delta function in time. The solution for an arbitrary temporal generation rate may be computed by convolving (C.50) with the generation rate. This equation is fully general, accounting for the 3D transport of free-carriers in a semiconductor, as well as recombination in the bulk and at the surface. Furthermore, because the equation was solved for a Gaussian-shaped excitation it is applicable to any experiment employing single-mode lasers.

Appendix D   Evaluation of Triple Integral over $n(r,z,t)$

The following integral is evaluated in this Appendix:

$$\Im = \int_{r=0}^{r=\infty} \int_{z=-\frac{W}{2}}^{z=\frac{W}{2}} \int_{t=0}^{\infty} r e^{-\frac{2r^2}{w_{pr}^2}} n(r,z,t) e^{-i\omega t} dt\, dz\, dr \tag{D.1}$$

where $n(r,z,t)$ is given by:

$$n(r,z,t) = e^{-\frac{t}{\tau_b}} \frac{1}{\frac{t}{\tau_D}+1} e^{\frac{-2r^2}{w_{pu}^2\left(\frac{t}{\tau_D}+1\right)}} \sum_n \left[A_n^{ax} e^{-\alpha_n^2 Dt} \cos\alpha_n z + B_n^{ax} e^{-\beta_n^2 Dt} \sin\beta_n z\right] \tag{D.2}$$

where w_{pu} is the radius of the pump beam and the diffusion time constant is given by $\tau_D = w_{pu}^2/8D$ The integral of the excess carrier density over the axial direction of the wafer is given by:

$$n_{2D}(r,t) = \int_{-W/2}^{W/2} n(r,z,t) dz \tag{D.3}$$

200

$$n_{2D}(r,t) = e^{-\frac{t}{\tau_b}} \frac{1}{\frac{t}{\tau_D}+1} e^{\frac{-2r^2}{w_{pu}^2\left(\frac{t}{\tau_D}+1\right)}} \int_{-W/2}^{W/2} \sum_n \left[A_n^{ax} e^{-\alpha_n^2 Dt} \cos \alpha_n z \right. \tag{D.4}$$

$$\left. + B_n^{ax} e^{-\beta_n^2 Dt} \sin \beta_n z \right] dz$$

Since the second term in square brackets is odd, it will not contribute to the integral and may be neglected:

$$n_{2D}(r,t) = e^{-\frac{t}{\tau_b}} \frac{1}{\frac{t}{\tau_D}+1} e^{\frac{-2r^2}{w_{pu}^2\left(\frac{t}{\tau_D}+1\right)}} \int_{-W/2}^{W/2} \sum_n A_n^{ax} e^{-\alpha_n^2 Dt} \cos \alpha_n z \, dz \tag{D.5}$$

Multiply the top and bottom of (D.5) by the wafer thickness W and bring the exponential time dependencies together:

$$n_{2D}(r,t) = \frac{1}{\frac{t}{\tau_D}+1} e^{\frac{-2r^2}{w_{pu}^2\left(\frac{t}{\tau_D}+1\right)}} W \left[\frac{1}{W}\int_{-\frac{W}{2}}^{\frac{W}{2}} \sum_n A_n^{ax} e^{-(\tau_b^{-1}+\alpha_n^2 D)t} \cos\alpha_n z \, dz\right] \tag{D.6}$$

The term in square brackets is Equation 3a in Refs [51] (reproduced in Equation (3.24) in Chapter 3). Substituting this into $n_{2D}(r,t)$ we get:

$$n_{2D}(r,t) = \frac{1}{\frac{t}{\tau_D}+1} e^{\frac{-2r^2}{w^2\left(\frac{t}{\tau_D}+1\right)}} W \text{ X} \tag{D.7}$$

$$\left[\frac{8g_0\alpha\eta e^{-\frac{\alpha\eta W}{2}}}{W} \sum_n \frac{\sin\left(\frac{\alpha_n W}{2}\right)}{((\alpha\eta)^2+\alpha_n^2)(\alpha_n W+\sin\alpha_n W)}\left[\alpha\eta\sinh\left(\frac{\alpha\eta W}{2}\right)\cos\left(\frac{\alpha_n W}{2}\right)\right.\right.$$

$$\left.\left.+\alpha_n\cosh\left(\frac{\alpha\eta W}{2}\right)\sin\left(\frac{\alpha_n W}{2}\right)\right]e^{-(\tau_b^{-1}+\alpha_n^2 D)t}\right]$$

$$n_{2D}(r,t) = 8g_0\alpha\eta e^{-\frac{\alpha\eta W}{2}} \frac{1}{\frac{t}{\tau_D}+1} e^{\frac{-2r^2}{w^2\left(\frac{t}{\tau_D}+1\right)}} \sum_n e^{-(\tau_b^{-1}+\alpha_n^2 D)t} A_n^{lc} \tag{D.8}$$

202

where A_n^{lc} is the Luke and Cheng coefficient, given by:

$$A_n^{lc} = \frac{\sin\left(\frac{\alpha_n W}{2}\right)}{((\alpha\eta)^2 + \alpha_n^2)(\alpha_n W + \sin \alpha_n W)}\left[\alpha\eta \sinh\left(\frac{\alpha\eta W}{2}\right)\cos\left(\frac{\alpha_n W}{2}\right)\right.$$
$$\left. + \alpha_n \cosh\left(\frac{\alpha\eta W}{2}\right)\sin\left(\frac{\alpha_n W}{2}\right)\right]$$

(D.9)

and g_0 is:

$$g_0 = \frac{2P_{pu}\lambda_{pu}}{\pi w_{pu}^2 hc}\frac{1 - R_{pu}}{1 - R_{pu}e^{-\alpha\eta W}}$$

(D.10)

where P_{pu} is the incident pump power, R_{pu} is the pump reflectance from the surface, and α_{pu} is the band-to-band absorption coefficient of the pump.

The signal integral is now given by:

$$\Im = 8g_0\alpha\eta e^{-\frac{\alpha\eta W}{2}}\ X \tag{D.11}$$

$$\int_{r=0}^{r=\infty}\int_{t=0}^{t=\infty} re^{-\frac{2r^2}{w_{pr}^2}}\left[\frac{1}{\frac{t}{\tau_D}+1}e^{\frac{-2r^2}{w_{pu}^2\left(\frac{t}{\tau_D}+1\right)}}\sum_n e^{-(\tau_b^{-1}+\alpha_n^2 D)t}A_n^{lc}\right]dre^{-i\omega t}dt$$

$$\Im = 8g_0\alpha\eta e^{-\frac{\alpha\eta W}{2}}\ X \tag{D.12}$$

$$\int_{t=0}^{t=\infty}\left[\frac{1}{\frac{t}{\tau_D}+1}\int_0^{\infty} re^{-2r^2\left[\frac{1}{w_{pu}^2}\left(\frac{t}{\tau_D}+1\right)^{-1}+\frac{1}{w_{pr}^2}\right]}dr\sum_n e^{-(\tau_b^{-1}+\alpha_n^2 D)t}A_n^{lc}\right]e^{-i\omega t}dt$$

$$\Im = 8g_0\alpha\eta e^{-\frac{\alpha\eta W}{2}}\ X \tag{D.13}$$

$$\int_{t=0}^{t=\infty}\left[\frac{1}{\frac{t}{\tau_D}+1}\int_0^{\infty} re^{-\frac{2r^2}{w_{pr}^2}\left[\left(\frac{w_{pr}}{w_{pu}}\right)^2\left(\frac{t}{\tau_D}+1\right)^{-1}+1\right]}dr\sum_n e^{-(\tau_b^{-1}+\alpha_n^2 D)t}A_n^{lc}\right]e^{-i\omega t}dt$$

$$\Im = 8g_0\alpha\eta e^{-\frac{\alpha\eta W}{2}}\,\mathrm{X} \tag{D.14}$$

$$\int_{t=0}^{t=\infty}\left[\frac{1}{\left(\frac{t}{\tau_D}+1\right)\left(\frac{w_{pr}}{w_{pu}}\right)^2\left(\frac{t}{\tau_D}+1\right)^{-1}+1}\frac{-\frac{w_{pr}^2}{4}}{}e^{-\frac{2r^2}{w_{pr}^2}\left[\left(\frac{w_{pr}}{w_{pu}}\right)^2\left(\frac{t}{\tau_D}+1\right)^{-1}+1\right]}\Bigg|_0^\infty \sum_n e^{-(\tau_b^{-1}+\alpha_n^2 D)t}A_n^{lc}\right]e^{-i\omega t}dt$$

$$\Im = w_{pr}^2 2g_0\alpha\eta e^{-\frac{\alpha\eta W}{2}}\int_{t=0}^{t=\infty}\frac{1}{\left(\frac{t}{\tau_D}+\left(1+\frac{w_{pr}^2}{w_{pu}^2}\right)\right)}\sum_n e^{-(\tau_b^{-1}+\alpha_n^2 D)t}A_n^{lc}\,e^{-i\omega t}dt \tag{D.15}$$

Now we can evaluate the integral over time:

$$\Im = w_{pr}^2 2g_0\alpha\eta e^{-\frac{\alpha\eta W}{2}}\sum_n\int_{t=0}^{t=\infty}\frac{1}{\left(\frac{t}{\tau_D}+\left(1+\frac{w_{pr}^2}{w_{pu}^2}\right)\right)}e^{-(\tau_b^{-1}+\alpha_n^2 D+i\omega)t}A_n^{lc}dt \tag{D.16}$$

Factor all of the exponential time terms into a parameter τ_n' and isolate t in the denominator:

$$\Im = w_{pr}^2 2 g_0 \alpha \eta e^{-\frac{\alpha \eta W}{2}} \int\limits_{t=0}^{t=\infty} \frac{\tau_D}{\left(t + \tau_D \left(1 + \frac{w_{pr}^2}{w_{pu}^2}\right)\right)} e^{-\frac{t}{\tau_n'}} A_n^{lc} dt \tag{D.17}$$

where τ_n' is given by:

$$\tau_n' = (\tau_b^{-1} + \alpha_n^2 D + i\omega)^{-1} = \frac{\tau_n}{1 + \omega_{pu}\tau_n} \tag{D.18}$$

The integral in (D.17) is given by the incomplete Gamma function:

$$\int\limits_0^{\infty} \frac{1}{(t+a)} e^{-bt} dt = e^{ab} \Gamma(0, ab) \tag{D.19}$$

Thus the signal integral is:

$$\Im = 2w_{pr}^2 \tau_D g_0 \alpha \eta e^{-\frac{\alpha \eta W}{2}} \sum_n e^{\frac{\tau_D}{\tau_n'}\left(1+\frac{w_{pr}^2}{w_{pu}^2}\right)} \Gamma\left(0, \frac{\tau_D}{\tau_n'}\left(1+\frac{w_{pr}^2}{w_{pu}^2}\right)\right) A_n^{lc} \tag{D.20}$$

Substituting in $\tau_D = w_{pu}^2/8D$ and then switching the symbol τ_D to τ_D^{pu}:

$$\Im = 2w_{pr}^2 \tau_D^{pu} g_0 \alpha \eta e^{-\frac{\alpha \eta W}{2}} \sum_n e^{\frac{\tau_D^{pu}+\tau_D^{pr}}{\tau_n'}} \Gamma\left(0, \frac{\tau_D^{pu}+\tau_D^{pr}}{\tau_n'}\right) A_n^{lc} \tag{D.21}$$

where τ_D^{pu} and τ_D^{pr} are the pump and probe diffusion time constants, respectively. They are given by:

$$\tau_D^{pu(pr)} = \frac{w_{pu(pr)}^2}{8D} \tag{D.22}$$

As a quick consistency check, we can verify that the units of (D.1) & (D.20) are the same. In (D.1) the carrier density $n(r, z, t)$ has units of m^{-3}, which is then integrated over a volume and is thus dimensionless. In (D.20) the exponential and Gamma functions are dimensionless. g_0 has units of $m^{-2}s^{-1}$, where the s^{-1} is cancelled by τ_D and m^{-2} is cancelled by w_{pr}^2. α has units of m^{-1}, and A_n^{lc} has units of m so (D.21) is dimensionless, consistent with (D.1).

Appendix E   Computing the Diffusive Factor

Experimentally, the recombination lifetime measured in single-beam pump/probe is related to peak of the imaginary component of the signal via the following equation:

$$\tau = \frac{\mathcal{D}}{\omega_p} \tag{E.1}$$

In this section I derive an implicit equation that can be used for evaluating $\mathcal{D}$. The frequency-dependence of the signal in the pump/probe experiment is given by the factor $\mathcal{F}$:

$$\mathcal{F} = e^{\frac{2\tau_D}{\tau'}} \Gamma\left(0, \frac{2\tau_D}{\tau'}\right) \tag{E.2}$$

For simplicity I only consider the first term of the summation. This is justified in the limit when the surface recombination velocity is low. Substituting in the expression for τ':

$$\mathcal{F} = e^{\frac{2\tau_D}{\tau}(1+i\omega\tau)} \Gamma\left(0, \frac{2\tau_D}{\tau}(1 + i\omega\tau)\right) \tag{E.3}$$

We can rewrite the argument in as z:

$$z \equiv \frac{2\tau_D}{\tau'} = \frac{2\tau_D}{\tau}(1 + i\omega\tau) \tag{E.4}$$

Therefore (E.3) becomes:

$$\mathcal{F} = e^z \Gamma(0, z) \tag{E.5}$$

The derivative of (E.5) with respect to frequency is given by:

$$\frac{d\mathcal{F}}{d\omega} = e^z \frac{dz}{d\omega} \Gamma(0, z) - \frac{e^{-z}}{z} \frac{dz}{d\omega} e^z \tag{E.6}$$

$$\frac{d\mathcal{F}}{d\omega} = \frac{dz}{d\omega}\left[e^z \Gamma(0, z) - \frac{1}{z}\right] \tag{E.7}$$

$$\frac{d\mathcal{F}}{d\omega} = 2\tau_D i \left[e^z \Gamma(0, z) - \frac{1}{z}\right] \tag{E.8}$$

The frequency spectrum of the imaginary component of (E.5) has a characteristic peak at the angular frequency ω_p which can be easily measured experimentally. The goal here is to establish the relationship between ω_p and the diffusive factor $\mathcal{D}$ so that the effective lifetime can be determined. The peak position can be determined by finding the value ω that makes the imaginary component of (E.8) equal to 0. This means Equation (E.8) should be completely real at ω_p, which means that the term in square brackets is completely imaginary. The component in square brackets is purely imaginary when the real parts of the individual terms are equal to each other:

$$\text{Re}\left[e^{z(\omega_p)} \Gamma\left(0, z(\omega_p)\right)\right] = \text{Re}\left[\frac{1}{z(\omega_p)}\right] \tag{E.9}$$

The factor $\frac{1}{z(\omega_p)}$ is given by:

$$\frac{1}{z(\omega_p)} = \frac{\tau}{2\tau_D}\frac{1}{1 + i\omega_p\tau} = \frac{\tau}{2\tau_D}\frac{1 - i\omega_p\tau}{\left(1 + \omega_p^2\tau^2\right)} \tag{E.10}$$

The real part of $1/z(\omega_p)$ is then given by:

$$\text{Re}\left[\frac{1}{z(\omega_p)}\right] = \frac{1}{\frac{2\tau_D}{\tau}\left(1 + \omega_p^2\tau^2\right)} \tag{E.11}$$

Substituting Equation (E.11) into Equation (E.9):

$$\text{Re}\left[e^{\frac{2\tau_D}{\tau}(1+i\omega_p\tau)}\,\Gamma\left(0,\frac{2\tau_D}{\tau}\left(1+i\omega_p\tau\right)\right)\right]=\frac{1}{\frac{2\tau_D}{\tau}\left(1+\omega_p^2\tau^2\right)} \tag{E.12}$$

Multiply the top and bottom of all $\frac{2\tau_D}{\tau}$ factors by ω_p and use the fact that the diffusive factor $\mathcal{D}=\omega_p\tau$:

$$\text{Re}\left[e^{\frac{2\tau_D\omega_p}{\mathcal{D}}(1+i\mathcal{D})}\,\Gamma\left(0,\frac{2\tau_D\omega_p}{\mathcal{D}}(1+i\mathcal{D})\right)\right]=\frac{1}{\frac{2\tau_D\omega_p}{\mathcal{D}}(1+\mathcal{D}^2)} \tag{E.13}$$

Equation (E.13) is an equation that implicitly relates the diffusive factor $\mathcal{D}$ to the factor $2\tau_D\omega_p$. Given a specified value of $2\tau_D\omega_p$, $\mathcal{D}$ is the value that then satisfies (E.13). The factor τ_D is usually known *a priori* and the factor ω_p is easily measured experimentally. With $2\tau_D\omega_p$ known, the diffusive factor can be determined and the lifetime τ extracted via Equation (E.1)
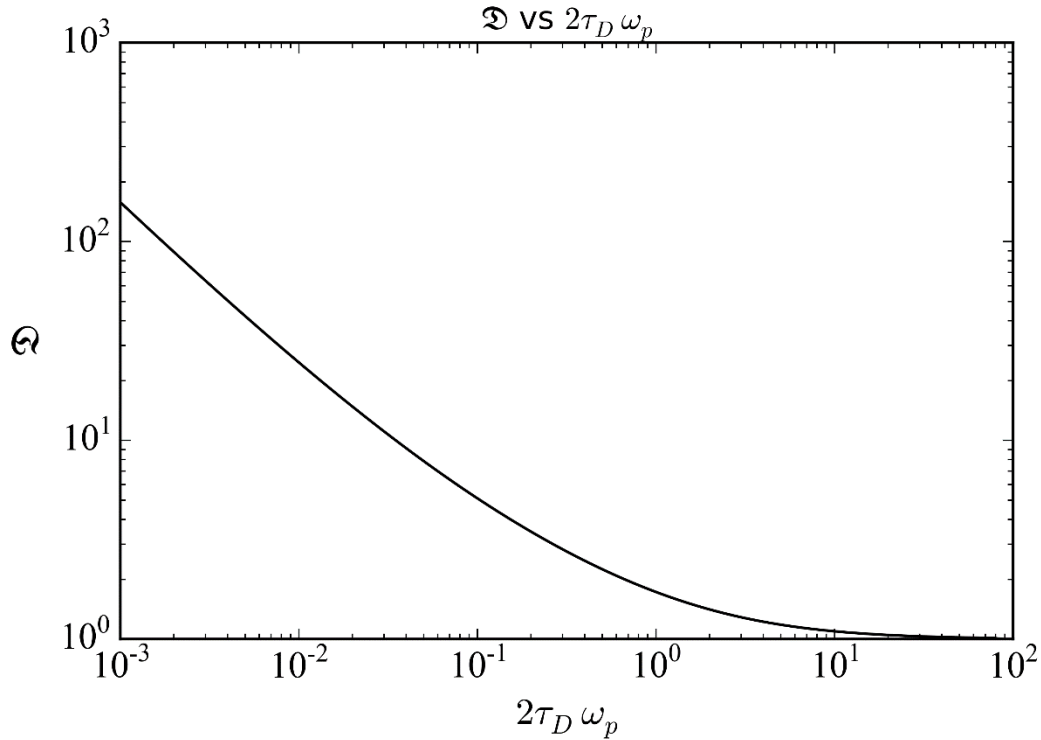
Figure E.1: Plot of diffusive factor $\mathcal{D}$ vs $2\tau_D\omega_p$

Figure E.1 plots $\mathcal{D}$ vs $2\tau_D\omega_p$. Using this curve, and knowing the beam radius w and diffusion coefficient D, the effective lifetime τ_n can be extracted given the experimentally measured peak frequency ω_p. The algorithm for finding τ_n is simple:

1. ω_p is measured and the product $2\tau_D\omega_p$ is computed.
2. The curve in Figure F.2 is used to find the diffusive factor $\mathcal{D}$
3. τ_n is determined by dividing $\mathcal{D}$ by ω_p

The functional behavior of Figure E.1 can be explained as follows. When the beam radius is large, diffusion effects are negligible and $\mathcal{D} = 1$. This is the case corresponding to a simple Lorentzian roll-off, as is expected (see Chapter 3). A large beam radius corresponds to a large $2\tau_D\omega_p$, hence the asymptotic region. When the beam radius is small, diffusion effects can no longer be neglected. Diffusion effects result in a faster carrier decay since carriers diffuse out the volume being probed.

The shorter time constant corresponds to a higher roll-off frequency and thus a higher ω_p value. This results in the product $\mathcal{D} > 1$.

Appendix F   Mapping the Peak of the Imaginary Component of the Signal to the Effective Lifetime

In the generalized equation for pump/probe experiments, the factor ξ contains all of the physical information about recombination lifetime, surface recombination velocity, and diffusion. ξ is a function of modulation frequency, and by sweeping the modulation frequency the relevant physical information in ξ may be extracted. In particular, there is a characteristic peak in the imaginary spectrum of $\xi(\omega)$ at ω_p that is related to the lifetime and diffusion parameters of the pump/probe experiment. This relationship is given by:

$$\tau = \frac{\mathfrak{D}}{\omega_p} \tag{F.1}$$

where $\mathfrak{D}$ is the *diffusive factor*, which is a dimensionless parameter that is always ≥ 1. In the limit where diffusion is negligible, $\mathfrak{D} \to 1$. In this Appendix, $\mathfrak{D}$ is determined numerically.

Let $\xi_n{}'$ be a factor that contains only the terms related to lifetime and diffusion:

$$\xi_n' = e^{\frac{2\tau_D}{\tau_n'}}\Gamma\left(0,\frac{2\tau_D}{\tau_n'}\right) = e^{\frac{w^2}{4L_n^2}(1+i\omega\tau_n)}\Gamma\left(0,\frac{w^2}{4L_n^2}(1+i\omega\tau_n)\right) \tag{F.2}$$

where w is the beam radius, L_n is the effective diffusion length, τ_n is the effective lifetime, and ω is the modulation frequency. Since ξ'_n is a complex number it may be written in terms of its real and imaginary components $\xi'_{n,re}$ & $\xi'_{n,im}$, respectively:

$$\xi'_n = \xi'_{n,re} + i\xi'_{n,im} \tag{F.3}$$

Taking the derivative with respect to ω and evaluating at the frequency where the imaginary component peaks ω_p:

$$\left.\frac{d\xi'_n}{d\omega}\right|_{\omega_p} = \left.\frac{d\xi'_{n,re}}{d\omega}\right|_{\omega_p} + i\left.\frac{d\xi'_{n,im}}{d\omega}\right|_{\omega_p} = \left.\frac{d\xi'_{n,re}}{d\omega}\right|_{\omega_p} \tag{F.4}$$

where $\left.\frac{d\xi'_{n,im}}{d\omega}\right|_{\omega_p} = 0$ since the imaginary component has a characteristic peak at ω_p. Taking the derivative of (F.2) with respect to ω and evaluating at ω_p:

$$\frac{d\xi'}{d\omega}\bigg|_{\omega=\omega_p} = \frac{w^2}{4L_n^2} i\tau_n e^{\frac{w^2}{4L_n^2}(1+i\omega_p\tau_n)}\Gamma\left(0,\frac{w^2}{4L_n^2}\left(1+i\omega_p\tau_n\right)\right) \tag{F.5}$$

$$-\frac{w^2}{4L_n^2} i\tau_n \frac{e^{-\frac{w^2}{4L_n^2}(1+i\omega_p\tau_n)}}{\frac{w^2}{4L_n^2}\left(1+i\omega_p\tau_n\right)}e^{\frac{w^2}{4L_n^2}(1+i\omega_p\tau_n)}$$

$$\frac{w^2}{4L_n^2}\tau_n i\left[e^{\frac{w^2}{4L_n^2}(1+i\omega_p\tau_n)}\Gamma\left(0,\frac{w^2}{4L_n^2}\left(1+i\omega_p\tau_n\right)\right)-\frac{1}{\frac{w^2}{4L_n^2}\left(1+i\omega_p\tau_n\right)}\right] = C \tag{F.6}$$

where C is some constant. From Equation (F.4) it can be seen that $\frac{d\xi'}{d\omega}\bigg|_{\omega=\omega_p}$ (and thus C) is purely real. Therefore the function in square brackets in Equation (F.6) must be purely imaginary. Let this function be represented by ρ:

$$\rho = e^{\frac{w^2}{4L_n^2}(1+i\omega\tau_n)}\Gamma\left(0,\frac{w^2}{4L_n^2}\left(1+i\omega\tau_n\right)\right)-\frac{1}{\frac{w^2}{4L_n^2}\left(1+i\omega\tau_n\right)} \tag{F.7}$$

Let's examine the function argument in (F.7):

$$z = \frac{w^2}{4L_n^2}(1 + i\omega\tau_n) \tag{F.8}$$

where $L_n^2 = D\tau_n$. Multiplying this through we get:

$$z = \frac{w^2}{4L_n^2} + i\frac{w^2}{4D}\omega \tag{F.9}$$

$$z = \frac{w^2}{4L_n^2} + i2\tau_D\omega \tag{F.10}$$

where $\tau_D = w^2/8D$. Bundle the factors in (F.10) into a real and imaginary coefficients a & b:

$$z = a + ib \tag{F.11}$$

where a & b are given by:

$$a = \frac{w^2}{4L_n^2} \qquad \text{(F.12)}$$

$$\ell = 2\tau_D \omega \qquad \text{(F.13)}$$

Now ρ becomes:

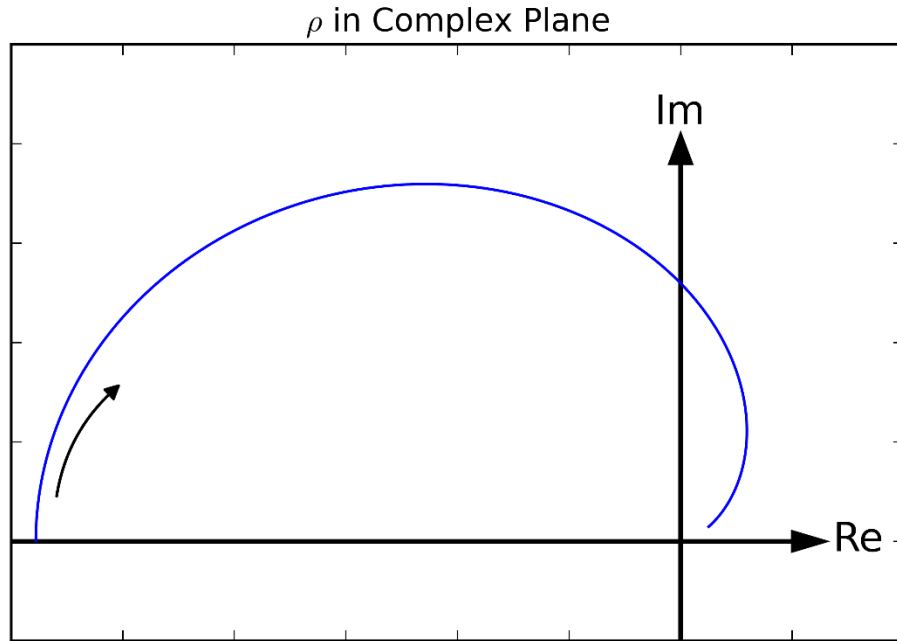$$\rho = e^z \Gamma(0,z) - \frac{1}{z} \qquad \text{(F.14)}$$

Figure F.1: Plot of ρ in the complex plane. The curved arrow points along the direction of increasing imaginary component b in z

Figure F. shows a plot of ρ in the complex plane as a function of z, where a is kept fixed while b increases. This corresponds to the experimental case where a is fixed by the sample and experimental parameters, and b is swept from low to high values by increasing the modulation frequency ω. The curved arrow points in the direction of increasing b. When $b = 0$, ρ is purely real. As b increases ρ takes on an imaginary component and eventually it crosses the imaginary axis. The value of b where ρ crosses the imaginary axis corresponds to ω_p, where the imaginary component of ξ' peaks. For a given a, the value of b, where ρ crosses the imaginary axis is unique. Let this value be given by b_p, where $b_p = 2\tau_D\omega_p$. Therefore, by establishing the relationship between a and b_p we relate the value ω_p to the experimental parameters w, D & τ_n. I have not been able to determine an analytic relationship between a & b_p, so this relationship is established numerically. To do this, a set of a values are selected that correspond to a wide range of $\frac{w}{L_n}$ values. For each a in the set, b is increased until ρ crosses the imaginary axis. The value of b where this

occurs is given by ℓ_p. Since for each value of a there is a corresponding ℓ_p, then for each value ℓ_p there is a unique $\frac{\ell_p}{a}$. According to Equations (F.12) & (F.13) this ratio is given by:

$$\frac{\ell_p}{a} = \omega_p \tau_n = \mathfrak{D}_n \qquad\qquad (F.15)$$
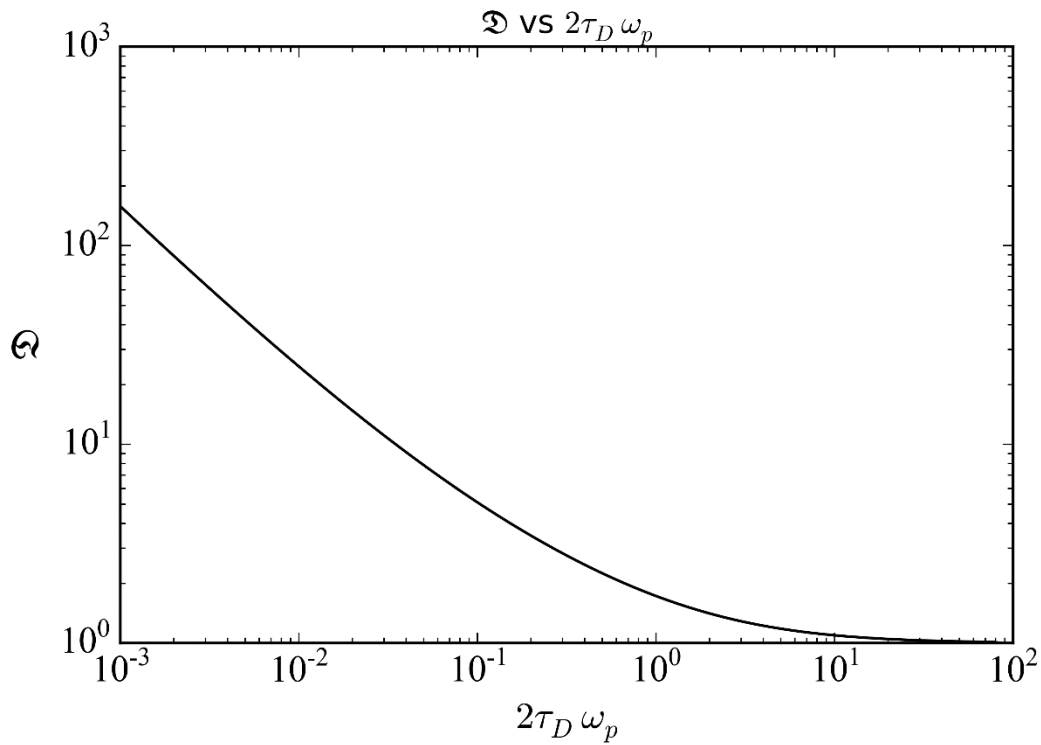

Figure F.2: Plot of $\mathfrak{D}$ vs $2\tau_D \omega_p$

Figure F.2 plots $\mathfrak{D}_n$ vs $2\tau_D \omega_p$ $\left(\frac{\ell_p}{a} \text{ vs } \ell_p\right)$. The a values that are used in generating this curve vary from $10^{-4} - 10^2$, which corresponds to a w/L_n range of 0.02 to 20. This covers three orders of magnitude of pump radius to diffusion length, and essentially all practical experimental

configurations. Using this curve, and knowing the beam radius w and diffusion coefficient D, the effective lifetime τ_n can be extracted given the experimentally measured peak frequency ω_p. The algorithm for finding τ_n is simple:

4. ω_p is measured and the product $2\tau_D\omega_p$ is computed.
5. The curve in Figure F.2 is used to find the diffusive factor $\mathfrak{D}_n$
6. τ_n is determined by dividing $\mathfrak{D}_n$ by ω_p

The functional behavior of Figure F.2 can be explained as follows. When the beam radius is large, diffusion effects are negligible and $\mathfrak{D}_n = 1$. This is the case corresponding to a simple Lorentzian roll-off, as is expected (see Chapter 3). A large beam radius corresponds to a large $2\tau_D\omega_p$, hence the asymptotic region. When the beam radius is small, diffusion effects can no longer be neglected. Diffusion effects result in a faster carrier decay since carriers diffuse out the volume being probed. The shorter time constant corresponds to a higher roll-off frequency and thus a higher ω_p value. This results in the product $\mathfrak{D}_n > 1$.

Appendix G   Background Removal Strategies for Single-Beam Pump/Probe

The simplest way (conceptually) of decoupling pump and probe signals is to acquire a frequency spectra with and without a sample in place and then subtract the two. The acquisition of these spectra requires a serial sweep of modulation frequency where each data point is collected at a different point in time. This approach is at the mercy of non-idealities in the measurement equipment, and is extremely susceptible to experimental drift. For example, if the signal being measured is a factor $< 10^{-3}$ of the pump signal then the pump signal itself must be stable to within this factor in order for subtraction to reliably decouple pump and probe. This is certainly not the case with the experimental setup used in this work, where the signal will wander by several percent over time. I used this approach in the earliest iterations of the single-beam experiment but to no avail. The next attempt to decouple the signals used a balanced-photodetector. The pump beam was split prior to illuminating the sample and one beam is passed through the silicon wafer while the other is used as reference beam. The balanced-photodetector subtracts the reference signal from the sample signal. In principle this technique should be more robust against drift since any variation in the pump beam (whether it originates in the laser power itself, the EOM or the drive signal) should occur equally in both reference and signal arms, which is then cancelled. Indeed the balanced photodetector that was used has a common mode rejection of 40 dB (or 1 part per 10^{-4}) so this should provide sufficient rejection for the isolation of the probe signal. Unfortunately this too was subject to an unacceptably high level of drift and the desired signal could not be resolved. I believe the origin of the drift was the wandering of the beam position on the detector.

The first strategy I used that was successful was a dual-frequency demodulation scheme. Taking advantage of the fact that the Zurich lock-in amplifier can modulate and demodulate several signals simultaneously, I impressed two sinusoidal signals on the pump beam. One signal was kept fixed at a frequency of 100 kHz, while the other frequency was swept from low to high frequencies to trace out the carrier decay curve. The fixed frequency signal played the role of a reference which

could be used to monitor the drift of the pump over time. Assuming that the drift in the sample signal and the reference signal were perfectly correlated, the reference signal could be used to correct for drift in the sample signal, allowing the FCA to be separated from a background spectrum without any sample in place. This strategy was somewhat successful and I was able to demonstrate agreement between single and dual beam pump/probe. Unfortunately the degree of correlation between sample signal and reference signal was not always 100%, and was not always repeatable. The result was that I could usually extract a roll-off curve similar to those in Figure 3.5, but not consistently.

I finally settled on the separation technique described in Equation (6.9) by observing that when the sample spectrum is divided by a background spectrum without FCA, the detector response is completely removed. This means that any imaginary component that remains is due to free-carrier absorption, from which the lifetime can be extracted. Another advantage of measuring the imaginary component is that there is a characteristic peak that corresponds to the lifetime.

Appendix H   Special Cases of ξ

The ξ factor derived in Chapter 5 is given by:

$$\xi(\omega_{pu}) = \sigma_{FCA}\tau_D^{pu}g_0\alpha\eta e^{-\frac{\alpha\eta W}{2}}\sum_n e^{\frac{\tau_D^{pu}+\tau_D^{pr}}{\tau_n'}}\Gamma\left(0,\frac{\tau_D^{pu}+\tau_D^{pr}}{\tau_n'}\right)A_n^{lc} \tag{H.1}$$

where g_0 is given by:

$$g_0 = \frac{2P_{pu}\lambda_{pu}}{\pi w_{pu}^2 hc}\frac{1-R_{pu}}{1-R_{pu}e^{-\alpha\eta W}} \tag{H.2}$$

And A_n^{lc} is given by:

$$A_n^{lc} = \frac{\sin\left(\frac{\alpha_n W}{2}\right)}{((\alpha\eta)^2 + \alpha_n^2)(\alpha_n W + \sin\alpha_n W)}\left[\alpha\eta\sinh\left(\frac{\alpha\eta W}{2}\right)\cos\left(\frac{\alpha_n W}{2}\right)\right. \tag{H.3}$$
$$\left. + \alpha_n\cosh\left(\frac{\alpha\eta W}{2}\right)\sin\left(\frac{\alpha_n W}{2}\right)\right]$$

In this Appendix I will derive several special cases of ξ for both single-beam and two-beam pump probe. First I will examine the case when the surface recombination velocity of the wafer is 0. In this case, $\alpha_n \to 0$:

$$\lim_{\alpha_n \to 0} A_n^{lc} = \frac{1}{4\alpha\eta} \sinh \frac{\alpha\eta W}{2} \tag{H.4}$$

Substituting this into Equation (H.1):

$$\xi(\omega_{pu}) = \sigma_{FCA}\tau_D^{pu} g_0 \alpha\eta e^{-\frac{\alpha\eta W}{2}} e^{\frac{\tau_D^{pu}+\tau_D^{pr}}{\tau'}} \Gamma\left(0, \frac{\tau_D^{pu}+\tau_D^{pr}}{\tau'}\right) \left[\frac{1}{4\alpha\eta} \sinh \frac{\alpha\eta W}{2}\right] \tag{H.5}$$

$$\xi(\omega_{pu}) = \frac{1}{8} \sigma_{FCA}\tau_D^{pu} g_0 (1-e^{-\alpha\eta W}) e^{\frac{\tau_D^{pu}+\tau_D^{pr}}{\tau'}} \Gamma\left(0, \frac{\tau_D^{pu}+\tau_D^{pr}}{\tau'}\right) \tag{H.6}$$

Here the lifetimes τ'_n have been replaced by τ' since the summation over n disappears in the limit of 0 surface recombination velocity. Thus for both single and dual-beam pump/probe experiments in the limit where surface recombination in the wafer is negligible, the ξ factors are given by:

$$\xi_{SB} = \frac{1}{8}\sigma_{FCA}\tau_D g_0 (1 - e^{-\alpha\eta W})e^{\frac{2\tau_D}{\tau'}}\Gamma\left(0, \frac{2\tau_D}{\tau'}\right) \tag{H.7}$$

$$\xi_{DB} = \frac{1}{8}\sigma_{FCA}\tau_D^{pu} g_0 (1 - e^{-\alpha\eta W})e^{\frac{\tau_D^{pu}+\tau_D^{pr}}{\tau'}}\Gamma\left(0, \frac{\tau_D^{pu} + \tau_D^{pr}}{\tau'}\right) \tag{H.8}$$

I have used the fact that in the single beam experiment $\tau_D^{pu} = \tau_D^{pr} = \tau_D$. Another important case is when the pump or probe beam is much larger than the other beam. First, multiply the top and bottom of (H.1) by τ_D^{pr}:

$$\xi(\omega_{pu}) = \frac{1}{\tau_D^{pr}}\sigma_{FCA}g_0\alpha\eta e^{-\frac{\alpha\eta W}{2}}\tau_D^{pu}\tau_D^{pr}\sum_n e^{\frac{\tau_D^{pu}+\tau_D^{pr}}{\tau'_n}}\Gamma\left(0, \frac{\tau_D^{pu} + \tau_D^{pr}}{\tau'_n}\right)A_n^{lc} \tag{H.9}$$

It is also assumed that $\tau_D \gg \tau'_n$. This is equivalent to saying that the beam is sufficiently large that radial diffusion can be neglected. Using the fact that $\lim_{z \to \infty} z e^z \Gamma(0, z) = 1$ we can write expressions for the single and dual-beam case where the pump or probe is large enough for radial diffusion to be neglected:

$$\xi_{SB} = \frac{1}{2} \sigma_{FCA} g_0 \alpha \eta e^{-\frac{\alpha \eta W}{2}} \sum_n \frac{\tau}{1 + i \omega \tau} A_n^{lc} \tag{H.10}$$

$$\xi_{DB} = \begin{cases} \frac{\tau_D^{pu}}{\tau_D^{pr}} \sigma_{FCA} g_0 \alpha \eta e^{-\frac{\alpha \eta W}{2}} \sum_n \frac{\tau}{1 + i \omega \tau} A_n^{lc}, & \tau_D^{pr} \gg \tau_D^{pu} \\ \sigma_{FCA} g_0 \alpha \eta e^{-\frac{\alpha \eta W}{2}} \sum_n \frac{\tau}{1 + i \omega \tau} A_n^{lc}, & \tau_D^{pu} \gg \tau_D^{pr} \end{cases} \tag{H.11}$$

Here I used the fact that $\tau' = \frac{\tau}{1 + i \omega \tau}$. The limiting cases for $\tau_D^{pr} \gg \tau_D^{pu}$ and $\tau_D^{pu} \gg \tau_D^{pr}$ are functionally the same, though the prefactor is different.

Finally, we can examine the case when both the radial diffusion effects are negligible, and when surface recombination is negligible. The equations for single and dual beam cases are then:

$$\xi_{SB} = \frac{1}{16}\sigma_{FCA}g_0(1 - e^{-\alpha\eta W})\frac{\tau}{1 + i\omega\tau}$$ (H.12)

$$\xi_{DB} = \begin{cases} \dfrac{1}{8}\dfrac{\tau_D^{pu}}{\tau_D^{pr}}\sigma_{FCA}g_0(1 - e^{-\alpha\eta W})\dfrac{\tau}{1 + i\omega\tau}, \tau_D^{pr} \gg \tau_D^{pu} \\ \dfrac{1}{8}\sigma_{FCA}g_0(1 - e^{-\alpha\eta W})\dfrac{\tau}{1 + i\omega\tau}, \tau_D^{pu} \gg \tau_D^{pr} \end{cases}$$ (H.13)

Appendix I   Fraction of Pump Power Absorbed

When light strikes a semiconductor interface, a fraction of the incident power is reflected while the rest is transmitted. If the absorption coefficient of the semiconductor is weak then the light that enters the semiconductor will bounce around inside multiple times, partially transmitting out of the semiconductor each time it reaches an interface. The total light that emerges from the front surface is the reflected light, while the total light that emerges from the back surface is the transmitted light. In this appendix I will quantify the reflection and transmitted power in the presence of multiple bounces through the wafer. This information will be used to derive a mathematical expression for the fraction of incident power absorbed in a wafer of arbitrary thickness and reflection coefficient, and to derive a correction factor to the amplitude measured in a pump/probe experiment. Note that this analysis is valid double-side polished silicon only, where all reflections are specular. For unpolished or textured silicon, the diffuse reflectance must be accounted for.

The reflectance and transmittance of a slab is given by an infinite number of bounces. Each light ray that traverses the wafer is attenuated by a factor $e^{-\eta\beta}$. Here β is an absorption factor which in general has contributions from band-to-band and free-carrier absorption. η is a factor describing the increase in pathlength through the wafer due to a non-normal angle of propagation. $\eta = \sec\theta$, where θ is the angle of propagation through the wafer.

For an incident power of P_0, the reflected power from the first surface is:

$$P_{r0} = RP_0 \tag{I.1}$$

where R is the interfacial reflection coefficient. The second reflected beam is given by:

$$P_{r1} = T^2 R e^{-2\eta\beta} P_0 \tag{I.2}$$

Here T is the transmission coefficient, which is squared because the initial light ray has to transmit into the wafer, then transmit out again. The factor of '2' in the attenuation factor accounts for two passes through the wafer. The next reflected beam is:

$$P_{r2} = T^2 R^3 e^{-4\eta\beta} P_0 \tag{I.3}$$

Generalizing to the mth reflected ray:

$$P_{rm} = T^2 R^{2m-1} e^{-2m\eta\beta} P_0 \tag{I.4}$$

where $m = 1, 2, \ldots$

For the transmitted power:

$$P_{t1} = T^2 e^{-\eta\beta} P_0$$

$$P_{t2} = T^2 R^2 e^{-3\eta\beta} P_0$$

$$P_{tm} = T^2 R^{2(m-1)} e^{-(2m-1)\eta\beta} P_0$$

The total reflection and transmission are then given by:

$$P_{ref} = RP_0 + \frac{T^2}{R}P_0 \sum_{m=1}^{\infty}\left[R^2 e^{-2\eta\beta}\right]^m \qquad (I.5)$$

$$P_{trans} = \frac{T^2}{R^2 e^{-\eta\beta}}P_0 \sum_{m=1}^{\infty}\left[R^2 e^{-2\eta\beta}\right]^m \qquad (I.6)$$

The summation is just that of a geometric series, where:

$$\sum_{m=0}^{\infty} x^m = \frac{1}{1-x}$$

Therefore:

$$\sum_{m=1}^{\infty}\left[R^2 e^{-2\eta\beta}\right]^m = \sum_{m=0}^{\infty}\left[R^2 e^{-2\eta\beta}\right]^m - 1 = \frac{1}{1-R^2 e^{-2\eta\beta}} - 1 = \frac{R^2 e^{-2\eta\beta}}{1-R^2 e^{-2\eta\beta}} \qquad (I.7)$$

Therefore the total reflection and transmission become:

$$P_{ref} = RP_0 + \frac{T^2 R e^{-2\eta\beta}}{1 - R^2 e^{-2\eta\beta}} P_0 = RP_0 \left[1 + \frac{T^2 e^{-2\eta\beta}}{1 - R^2 e^{-2\eta\beta}} \right] \qquad (I.8)$$

$$P_{trans} = \frac{T^2 e^{-\eta\beta}}{1 - R^2 e^{-2\eta\beta}} P_0 \qquad (I.9)$$

The   fraction   of   power   absorbed   in   the   wafer   is   defined   as:

$$f_a = 1 - \frac{P_{ref} + P_{trans}}{P_0} \qquad (I.10)$$

$$f_a = 1 - \left(R + \frac{T^2 e^{-2\eta\beta} R}{1 - R^2 e^{-2\eta\beta}} + \frac{T^2 e^{-\eta\beta}}{1 - R^2 e^{-2\eta\beta}} \right) \qquad (I.11)$$

$$f_a = 1 - R - \frac{T^2 e^{-\eta\beta}}{1 - R^2 e^{-2\eta\beta}} \left(1 + R e^{-\eta\beta} \right) \qquad (I.12)$$

Factoring the denominator:

$$f_a = 1 - R - \frac{T^2 e^{-\eta\beta}}{(1 - Re^{-\eta\beta})(1 + Re^{-\eta\beta})}\left(1 + Re^{-\eta\beta}\right) \tag{I.13}$$

$$f_a = 1 - R - \frac{T^2 e^{-\eta\beta}}{1 - Re^{-\eta\beta}} \tag{I.14}$$

Using the fact that the interfacial transmission coefficient is $T = 1 - R$:

$$f_a = 1 - R - \frac{(1 - R)^2 e^{-\eta\beta}}{1 - Re^{-\eta\beta}} \tag{I.15}$$

$$f_a = (1 - R)\left[1 - \frac{(1 - R)e^{-\eta\beta}}{1 - Re^{-\eta\beta}}\right] \tag{I.16}$$

$$f_a = \frac{1 - R}{1 - Re^{-\eta\beta}}\left[1 - Re^{-\eta\beta} - (1 - R)e^{-\eta\beta}\right] \tag{I.17}$$

$$f_a = \frac{1 - R}{1 - Re^{-\eta\beta}}\left(1 - e^{-\eta\beta}\right) \tag{I.18}$$

In general, $\beta = \alpha W + \beta_{FCA}$ where the former term quantifies absorption due to band-to-band absorption, and β_{FCA} quantifies FCA. Since $\beta_{FCA} \ll \alpha W$, $\beta \approx \alpha W$. Therefore the fraction of power absorbed into the wafer is given by:

$$f_a = \frac{1-R}{1-Re^{-\alpha\eta W}}(1-e^{-\alpha\eta W}) \tag{I.19}$$

Appendix J   Correction Factor from Multiple Reflection/Transmission

In lifetime measurement experiments we measure the probe power that transmits through the wafer, and isolate the component due to FCA. According to Appendix I, the power transmitted through the wafer is given by:

$$P_{trans} = \frac{T^2 e^{-\eta\beta}}{1 - R^2 e^{-2\eta\beta}} P_0 \tag{J.1}$$

where β is an absorption factor. In general, this factor is given by:

$$\beta = \beta_{bb} + \beta_{FCA} \tag{J.2}$$

where β_{bb} is the contribution due to band-to-band absorption, and β_{FCA} is the contribution to FCA. It is the β_{FCA} factor that contains all of the lifetime information. Substitute Equation (J.2) into (I.9) and split the exponentials:

$$P_{trans} = \frac{T^2}{1 - R^2 e^{-2\eta\beta_{bb}} e^{-2\eta\beta_{FCA}}} P_0 e^{-\eta\beta_{bb}} e^{-\eta\beta_{FCA}} \tag{J.3}$$

Bundle the band-to-band exponentials into the power and reflection terms:

$$P_{trans} = \frac{T^2}{1 - R'^2 e^{-2\eta\beta_{FCA}}} P_0' e^{-\eta\beta_{FCA}} \tag{J.4}$$

Applying a first order Taylor approximation:

$$P_{trans} = \frac{T^2}{1 - R'^2(1 - 2\eta\beta_{FCA})} P_0'(1 - \eta\beta_{FCA}) \tag{J.5}$$

Rearranging the denominator:

$$P_{trans} = \frac{T^2}{1 - R'^2} \left[\frac{1}{1 + \frac{2R'^2\eta\beta_{FCA}}{1 - R'^2}} \right] P_0'(1 - \eta\beta_{FCA}) \tag{J.6}$$

Using the binomial approximation to flip the denominator into the numerator:

$$P_{trans} = \frac{T^2}{1 - R'^2} P_0' \left(1 - \frac{2R'^2\eta\beta_{FCA}}{1 - R'^2} \right)(1 - \eta\beta_{FCA}) \tag{J.7}$$

$$P_{trans} = \frac{T^2}{1 - R'^2} P_0' \left(1 - \eta\beta_{FCA} - \frac{2R'^2\eta\beta_{FCA}}{1 - R'^2} + \frac{2R'^2\eta^2\beta_{FCA}^2}{1 - R'^2} \right) \tag{J.8}$$

The term that is second order in β_{FCA} can be neglected since $\beta_{FCA} \ll 1$:

$$P_{trans} = \frac{T^2}{1 - R'^2} P_0' \frac{1}{1 - R'^2} \left(1 - \eta\beta_{FCA} + R'^2\eta\beta_{FCA} - R'^2 - 2R'^2\eta\beta_{FCA} \right) \tag{J.9}$$

$$P_{trans} = \frac{T^2}{1 - R'^2} P_0' \frac{1}{1 - R'^2} \left(1 - \eta\beta_{FCA} - R'^2 - R'^2\eta\beta_{FCA} \right) \tag{J.10}$$

$$P_{trans} = \frac{T^2}{1 - R'^2} P_0' \frac{1}{1 - R'^2} \left(1 - R'^2 - (1 + R'^2)\eta\beta_{FCA} \right) \tag{J.11}$$

$$P_{trans} = \frac{T^2}{1 - R'^2} P_0' \left(1 - \frac{1 + R'^2}{1 - R'^2} \eta\beta_{FCA} \right) \tag{J.12}$$

Letting $\Re = \frac{1 + R'^2}{1 - R'^2}$ we get the final expression for the power transmitted in the presence of both band-to-band and free-carrier absorption:

$$P_{trans} = \frac{T^2}{1 - R'^2} P_0'(1 - \Re\eta\beta_{FCA}) \tag{J.13}$$

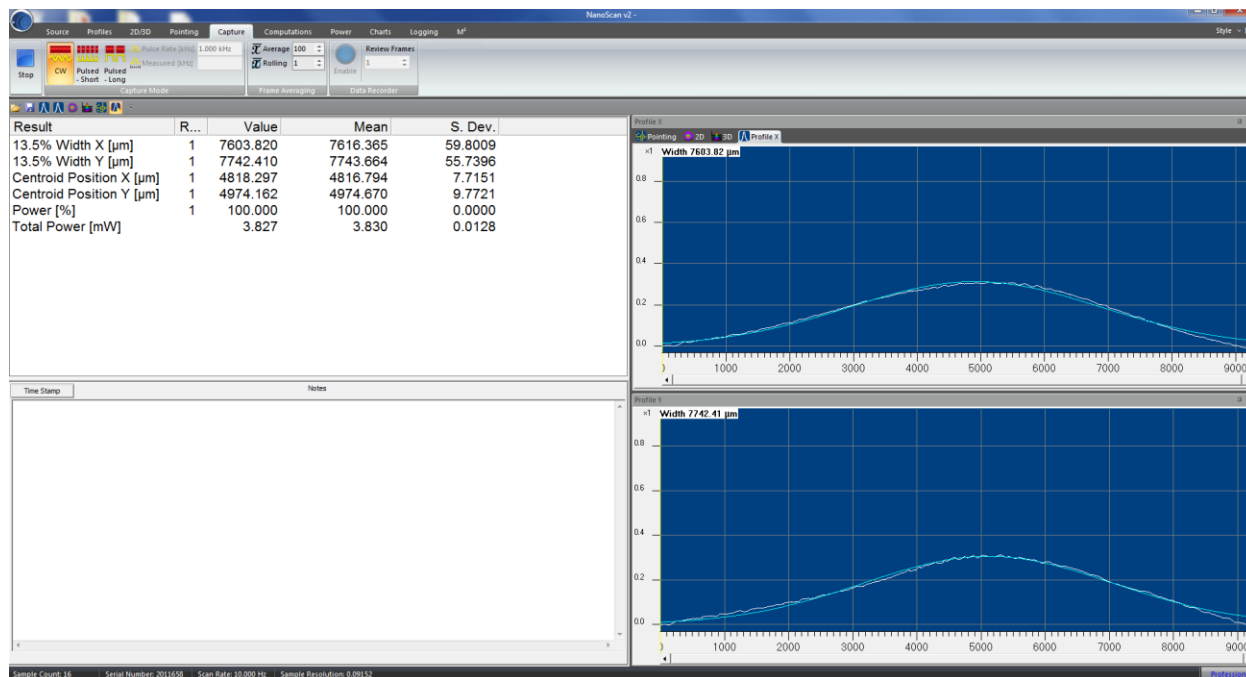# Appendix K   Nanoscan Beam Profiles

Figure K.1: Screenshot of Nanoscan Beam Profiler interface, showing the characteristics of the pump beam used in 6.3.2
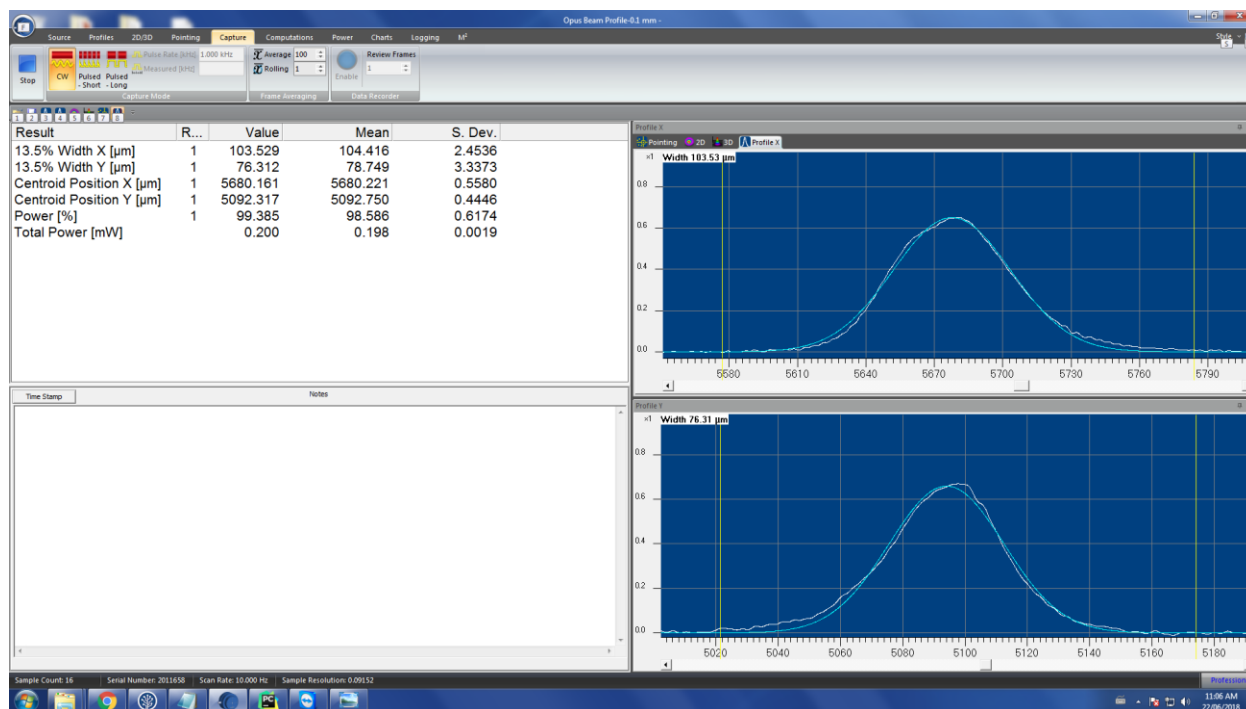
Figure K.2: Screenshot of Nanoscan Beam Profiler interface, showing the characteristics of the pump beam used for the 46 micron radius dataset in 6.6.
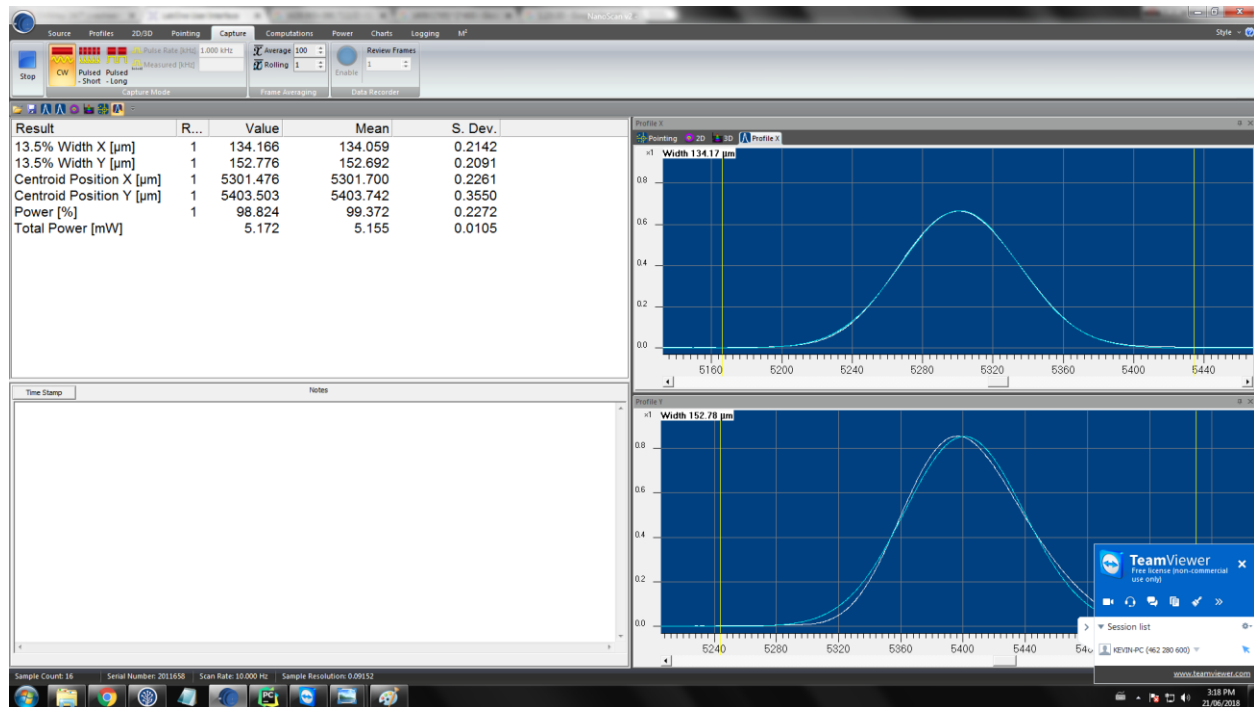
Figure K.3: Screenshot of Nanoscan Beam Profiler interface, showing the characteristics of the pump beam used for the 72 micron radius dataset in 6.6.